The Synthesis and Characterization of Hydrophilic Gold Nanoparticles via a DEN-MPC Method and their Evaluation as Biphasic Catalysts

by Jezreel Cloete

Dissertation presented for the Degree of Doctor of Chemistry at Stellenbosch University

Promotor: Dr Rehana Malgas-Enus

Co-Promotor: Prof. Selwyn F. Mapolie

Faculty of Science

December 2017

Declaration

By submitting this thesis/dissertation electronically, I declare that the entirety of the work contained therein is my own, original work, that I am the sole author thereof (save to the extent explicitly otherwise stated), that reproduction and publication thereof by Stellenbosch University will not infringe any third party rights and that I have not previously in its entirety or in part submitted it for obtaining any qualification.

_____

Jezreel Cloete

December 2017

Abstract

The synthesis of hydrophilic gold nanoparticles, by using a dendrimer template method to produce dendrimer encapsulated nanoparticles (DENs), in combination with a monolayer protected cluster (MPC) method is reported on. This was achieved by forming the DENs in chloroform and then extracting the nanoparticles into water. The extraction of the nanoparticles was facilitated by a water-soluble ligand (1,3,5-triaza-7-phosphaadamantane) which subsequently also provided the particles with a protective layer to limit agglomeration. In addition, the catalytic performance in the transformation of styrene of the water-soluble gold nanoparticles is described.

The use of the combined DENs-MPC method was driven by an attempt to tightly control the initial size of the synthesized nanoparticles (DENs method) and afterwards provide a means of maintaining the particle size over an extended period of time (weeks or months) using the MPC method. It was aimed to control nanoparticle size by means of varying the Au:dendrimer ratio in order to produce Au atom clusters of a certain number and thus nanoparticles of a certain size. During our initial synthetic attempts utilizing a Au:dendrimer ratio of 55:1, we managed to synthesize nanoparticles with an average size of 1.5 nm ± 0.9 which is the equivalent of an Au_{55} atom cluster and thus appeared to validate our proposed synthesis method. However, studies using UV/vis spectroscopy and transmission electron microscopy (TEM) in an attempt to monitor the growth evolution of the nanoparticles over time revealed that the gold to dendrimer ratio was not the only factor that plays a role in the formation of stable nanoparticles. Based on the information gained from the size evolution studies, it was found that when Au:dendrimer ratios were used which would theoretically produce specific atomic cluster sizes possessing closed shell configurations (such as Au_{55} and Au_{13}), DENs with sizes larger than the specific cluster size would form. However, upon extraction into the aqueous phase, the particles would reduce in size closer to the expected atomic cluster size. Conversely, Au:dendrimer ratios which would not result in closed shell configurations (*e.g.* Au_{31}), did not exhibit this reduction in size upon extraction from the organic into the aqueous phase. The mechanistic pathway, which was hypothesized to be facilitated by the 1,3,5-triaza-7-phosphaadamantane (PTA) ligand, is therefore elucidated.

It was subsequently aimed to tailor nanoparticle size (with the further aim of potentially tailoring catalytic performance). However, although the mechanism of size reduction upon extraction of the nanoparticles from the organic into the aqueous layer appeared to hold for each synthetic attempt, the extent of nanoparticle size reduction was found to be variable for successive synthetic procedures. This observation prompted a more in-depth study into the exact nature of the facilitation of gold nanoparticle size reduction by the water-soluble PTA ligand. This study was enabled by the utilization of dynamic light scattering (DLS) equipment in conjunction with nanoparticle zeta potential determination, and resulted in devising a more optimum PTA concentration in the aqueous layer required for nanoparticle size reduction and stabilization. In addition to this, the re-evaluation of the gold salt reduction procedure further improved on achieving nanoparticle size and shape reproducibility. However, although these results yielded improvements in synthesis repeatability in terms of nanoparticle size, it was still not satisfactory.

With improvements in synthetic repeatability showing promise, yet still not being satisfactory, the effect of process conditions such as stirring and manner of reagent addition were evaluated. This was done utilizing a custom made nanoparticle synthesis reactor set-up and led to the revelation that the inconsistency in size produced for successive synthetic procedures was due to the lack of retention and scaffolding properties of the dendrimer in preventing uncontrolled nucleation and nanoparticle growth. Based on this it was found that addition of the stabilizing ligand along with the reducing agent before extraction into the aqueous layer proved to arrest any uncontrolled growth and resulted in addressing the synthetic inconsistency in terms of nanoparticle size.

The ability to now tailor nanoparticle size, and produce them consistently, therefore enabled the evaluation of the synthesized aqueous gold nanoparticles in the attempted biphasic catalytic oxidation of styrene. Interestingly however, the catalyst showed overwhelming selectivity toward polystyrene with conversion surprisingly also not appearing to be dependent on nanoparticle size. In addition, it was found that additives such as H_2O_2 and *t*-butyl-hydroperoxide (TBHP) which were intended to act as oxidizing agents, instead influenced polystyrene properties. The various aspects resulting in the observed catalytic behavior is discussed and an overall mechanism proposed.

Opsomming

Die sintese van hidrofielise goud nanopartikels, deur die gebruik van 'n dendrimer templaat metode om dendrimeer enkapsileerde nanopartikels (DENs) to vorm, in kombinasie met 'n monolaag beskermde groepeering (MBG) metode word oor berig. Dit was bereik deur die DENs in klorofoom te vorm and daarna die nanopartikels te ekstrak na water. Die ekstraksie van die nanopartikels was aangehulp deur 'n wateroplosbaare ligand (1,3,5-triaza-7-phosphaadamantane) wat daarna die partikels met 'n beskermde laag aangebied het om agglomerassie te voorkom. Daarbenewens word die prestasie van die wateroplosbare goud nanopartikels as katalisator in die transformeering van stireen bekryf.

Die gebruik van die gekombineerde DENs-MBG metode was aangedryf deur die poging of streng beheer oor die aanvanklike groote van die gesintiseerde nanopartikels (DENs metode) te hê en daarna a manier te skep om die partikel groote te handaaf oor verlengde tyd periodes (weke of maande) deur gebruik van die MBG metode. Dit was beoog om nanopartikel groote te kontroleer deur die Au:dendrimeer verhouding te wissel om so Au atoom groepeeringe van 'n sekere nommer, en dus 'n sekere groote te bekom. Gedeurende ons aanvanklike pogings om 'n Au:dendrimeer verhouding van 55:1 te gebruik, het ons daarin geslaag om nanopartikels te vorm met 'n gemiddelde groote van 1.5 nm ± 0.9 wat die ekwivalent van 'n Au_{55} atoom groepeering is. Dit het daarom voorgekom dat ons voorgestelde sintetise metode gewalideer is. UV/vis spectroscopie en transmissie elektroon microskopie (TEM) wat gebruik is om die groeie evolusie met tyd van die nanopartikels te monitor het egter aangedui dat die verhouding van goud na dendrimeer nie die enigste faktor was wat 'n rol in die formasie van stabiele nanopartikels speel nie. Gebaseer op informasie van die groote evolusie studies wat ogedoen is, is daar gevind dat wanneer Au:dendrimeer verhoudings wat teoreties atomise groepeerings met 'n toe dop konfigurasie sou vorm, DENs groter dan die spesifieke atomiese gropeering gevorm het. Nanopartikels met grotes nader aan wat verwag is het egter gevorm na ekstraksie van die orgaanise fase na die water fase toe. Aan die teenoorgestelde kant, het verhoudinge wat nie toe dop konfigurasies so vorm nie (*e.g.* Au_{31}), nie verminder in groote na ekstraksie nie. Die meganistiese paaie wat aangehulp is deur die PTA ligand is dus verduidelik.

Gevolglik is daar beam om nanopartikel groote te beheer (met die verdure beaaming om potensieel kataliesise verrigting te beheer). Alhoewel die meganisme vir die vermindering van nanopartikel groote gebluik het om te hou vir elke sintetiese poging, is dit egter gevind dat nanopartikel grote gewissel het. Hierdie waarneming het 'n meer in diepte studie meegebring na die fasiliteering van nanopartikel groote vermindering deur die PTA ligand. Hierdie studie was in staat gestel deur die benut van dinamiese lig strooiing (DLS) toerusting in samewerking met zeta potensiaal bepaaling. Die resultaat was dat 'n meer optimum PTA konsentrasie in die water lag, wat benodig is vir nanopartikel groote vermindering en stabiliseering bedink was. Nietemin, alhoewel die resultate verbeteringe in sintetise herhaaldelikheid aangebring het in terme van nanopartikel groote, was dit nog steeds nie na wense nie.

Met verbetering aan sintetiese herhaaldelikheid wat bemoedigend was, maar nog steeds nie heeltemal na wense nie, was die effek van proses kondiesies geëvalueer. Dit was gedoen deur 'n oorspronlike reactor stelsel te gebruik en gelui het na die onthuling dat die teenstrydigheid in partikel groote vir opeenvolgende sintetiese prosedures weens die gebrek aan behoudings and steierwerk eienskape van die dendrimeer was om onbeheerde kernvorming en groeie te voorkom. Gebaseer hierop, is dit gevind dat die byvoeging van die stabiliseerende ligand tesame met die reduseermiddel voor ekstraksie na die water laag, voorkom het dat onbeheerde groeie vertraag is en gelei het na beter herhaaldelikheid in terme van nanopartikel groote.

Die vermoë om nou nanopartikel groote te beheer, en om hulle herhaaldelik te vorm, het ons dus in plaas gestel om die waterige goud nanopartikels in die gepoogde bifasiese kataliesiese oksidasie van stireen te evalueer. Verbaasend egter het die katalisator oorweldigende selektiwiteit na polystireen gewys met omskakeling wat ook verbaasend nie verskyn of dit afhanklik van nanopartikel grote was nie. Daarbenewens is di took gevind dat toevoeg middels soos H_2O_2 en *t*-butyl-hydroperoksied (TBHP) wat veronderstel was om op te tree as oksideermiddels, in stede die eienskape van die polystireen beinvloed het. Die verskeie aspekte wat gelei het na die waargeneemde katalitiese gedrag is bespreek en 'n algehele meganisme word voorgestel.

Acknowledgments

I would like to thank the following people and organisations for their help and support throughout this study:

The National Research Foundation (NRF) for financial support.

Dr. Rehana Malgas-Enus for her assistance, guidance and motivation as supervisor.

Prof. Selwyn F. Mapolie for his contribution as co-supervisor.

Stellenbosch University and especially the technical staff and colleagues within Inorganic Chemistry. I also extend thanks to the Central Analytical Facility (CAF) of Stellenbosch University.

Electron Microscope Unit at the University of the Western Cape for assistance with transmission electron microscopy (TEM) imaging.

Mr Charles Noakes from Poretech for the use of Dynamic Light Scattering (DLS) equipment.

Mr Dewald Vosloo from Devos Laboratory Consultants for assistance in designing and supplying of the nanoparticle synthesis reactor and providing technical support in ensuring the smooth operation of the system.

Finally I would like to extend a special thanks to my family for their love and support and understanding throughout. I especially thank my wife, Kim, and four legged son Hash, for keeping me sane and motivating me.

Publications

Jezreel Cloete, Selwyn F. Mapolie, Rehana Malgas-Enus, Facile synthesis and characterization of PTA stabilized hydrophilic Au_{55} nanoparticles via a DEN-MPC method, *Polyhedron*, 2015, **102**, 469-478

Conference Contributions

- Jezreel Cloete, Selwyn F. Mapolie and Rehana Malgas-Enus

  Oral Presentation: ***The Synthesis of Hydrophilic Narrow Sized Au_{55} Nanoparticles***. The South African Chemical Institute and the Royal Society of Chemistry Western Cape Young Chemists' Symposium, University of Cape Town, South Africa, 2014.

- Jezreel Cloete, Selwyn F. Mapolie and Rehana Malgas-Enus

  Poster Presentation: ***Synthesis and Extraction of Au Nanoparticles using Dendrimer Micelles as Templates and their Application in Oxidation Reactions***. Catalysis South Africa (CATSA) Conference, Pretoria, South Africa, 2014.

- Jezreel Cloete, Selwyn F. Mapolie and Rehana Malgas-Enus

  Poster Presentation: ***The Synthesis of Hydrophilic Narrow Sized Au_{55} Nanoparticles and their Application as Styrene Oxidation Catalysts***. IUPAC International Symposia on Organometallic Chemistry Directed Towards Organic Synthesis (OMCOS), Barcelona, Spain, 2015.

- Jezreel Cloete, Selwyn F. Mapolie and Rehana Malgas-Enus

  Poster Presentation: ***The use of Dynamic Light Scattering and Zeta Potential as a Tool for determining Nanoparticle Stabilization Properties***. Catalysis South Africa (CATSA) Conference, Kleinmond, South Africa, 2015.

List of Abbreviations

^{1}H NMR	: proton nuclear magnetic resonance
ATR	: attenuated total reflectance
C_{crit}	: critical concentration of monomer
C_{sol}	: monomer saturation point
DAB-PPI	: diaminobutane poly(propylene imine)
DCE	: 1,2-dichloroethane
DENs	: dendrimer encapsulated nanoparticles
DFT	: density-functional theory
DLS	: dynamic light scattering
DOS	: density of one-electron states
EDX	: energy-dispersive X-ray spectroscopy
FEG	: field emission gun
GC	: gas chromatography
GC-MS	: gas chromatograph coupled to a mass spectrometer
GPC	: gel permeation chromatography
ICP	: inductively coupled plasma spectroscopy
ICP-OES	: inductively coupled plasma coupled to optical emission spectroscopy
IR	: infrared
LFRP	: living free radical polymerization
LMCT	: ligand-to-metal charge-transfer
M_n	: number average molecular weight
M_P	: molecular weight of highest peak
MPCs	: monolayer-protected clusters
M_W	: weight average molecular weight
M_W/M_n	: polydispersity index
M_Z and M_{Z+1}	: higher average molecular weights
nm	: nanometre
PAMAM	: poly(amidoamine)
PPh_3	: triphenylphosphine
PPI	: poly(propylene imine)
PTA	: 1,3,5-triaza-7-phosphaadamantane

SAXS : X-ray scattering spectroscopy

SPR : surface plasmonic resonance

TBHP : *t*-butyl-hydroperoxide

TEM : transmission electron microscopy

THF : tetrahydofuran

TOAB : tetraoctylammonium bromide

TOF : turnover frequency

TPPMS : triphenylphosphine monosulfonate

TPPTS : triphenylphosphine thiosulfonate

UV-vis : ultraviolet-visible light spectroscopy

XAFS : X-ray absorption fine structure

XANES : X-ray absorption near-edge spectroscopy

Table of Contents

List of Figures

List of Schemes

List of Tables

List of Equations

Chapter 1

The Application of Gold Nanoparticles and Methods of Synthesis

---

1.1 Introduction

In this chapter we look at the factors resulting in the reactivity of gold nanoparticles and how this reactivity comes about especially when considering the inert nature of bulk metallic gold. A short review of various gold nanoparticle synthesis methods is then given before setting out the scope of the research undertaken based on the resultant findings from literature.

The resilience of metallic gold towards oxidation (even when heated), as well as its tendency to be inert to strong alkalis and acids (except to *aqua regia* and selenic acid) makes it one of the least chemically reactive metals and, as such, is classified as a noble metal.[1] Hammer and Nørskov (1995) in fact contended that it could be considered the most inert of the noble metals.[2]

Their argument was based on density-functional theory (DFT) calculations indicating the calculated minimum potential energy of the H-H bond as it approaches the surface of a metal (Figure 1.1). Compared to the noble metals Ni, Cu and Pt, they found that energetically, it was most unfavourable for H_2 to approach the surface of metallic Au which would therefore severely limit H_2 dissociation from occurring. On the other hand, they found that the approach of H_2 to the surfaces of especially Pt and Ni were energetically more favourable and therefore greatly enhanced the probability of dissociation occurring.

The cause for the observed differences in H-H potential energy as the molecule approaches the different metal surfaces, were reasoned to be as a result of the differing outer electron shell configurations of each metal and the nature of their bonding and antibonding states. Specifically, this behaviour is related to a combination of three properties characteristic to each metal; the degree of filling of the antibonding H_2-metal *d* states, the magnitude of the *s*-*d* coupling matrix element (a measure of the energy required for long distance electron transfer reactions during bonding)[3] and the metal cohesive energy (a measure of how strongly the atoms of the metal are bound).

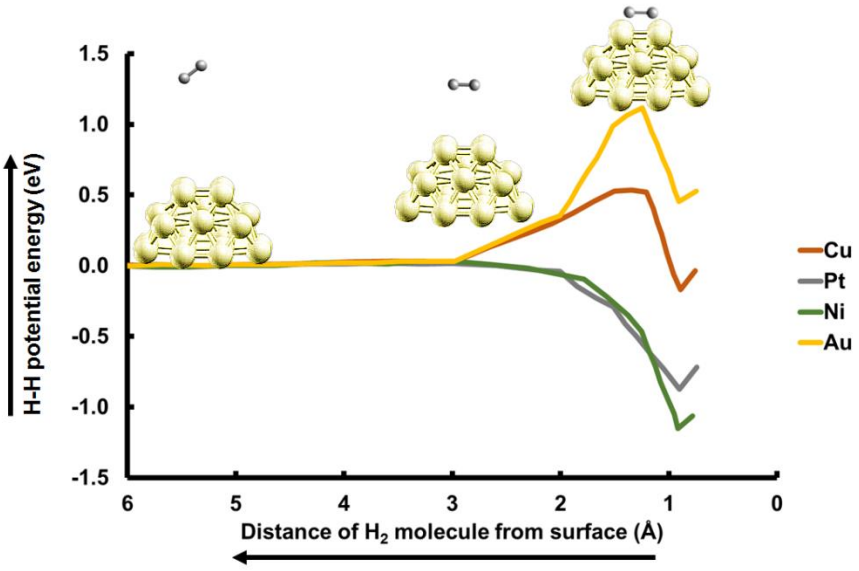

Figure 1.1 Comparison of potential energy of H-H bond as it approaches the surfaces of Au, Cu, Pt and Ni (adapted from reference 2).

Considering the degree of filling of the antibonding H_2-metal *d* states, Figure 1.2 depicts the density of one-electron states (DOS) for a H-atom chemisorbed on the (111) surfaces of Ni, Cu, Pt and Au. It can be seen that for Cu and Au, there is an energy associated with the H 1*s*-*d* antibonding state (red dashed band) which is not present for Ni and Pt. Bearing in mind the valence electron shell configuration of each metal, the energy observed can be associated with filled antibonding states on Cu and Au (d^{10} orbitals) which are essentially empty on Ni and Pt (d^9 orbitals). Thus on Ni and Pt, the potential coupling of the H-atom ($1s^1$ electron configuration) to the metal *d*-band gives rise to an extra attraction in addition to the contribution attributable to the interaction with the metal *s*-band. On Cu and Au, the interaction results in repulsion due to their filled *d*-orbitals.[2,4] Although there is still an interaction of the H-atom with the Cu and Au metal *s*-bands, the repulsive interaction with the *d*-bands gives rise to a H-Cu bond which is marginally stable relative to the H-H bond with the H-Au bond completely unstable relative to the H-H bond. This therefore explains the increase in energy seen in Figure 1.1 as the H_2 molecule approaches the surfaces of Cu and Au compared to the decrease seen for Ni and Pt.

Subsequently, in order to understand why Au is "more noble" than Cu, the magnitude of the *s*-*d* coupling matrix elements and the metal cohesive energies should be considered. Figure 1.3 shows values of these two properties along with the discussed filling of valence *d*-orbitals (expressed as a ratio – 1.0 representing d^{10} electron configuration) for metals in the vicinity of

Au in the periodic table. Since the effect of filled *d*-orbitals on impeding adsorption of a H-atom to a metal surface has already been established, we consider how Au compares to other metals with *d*-band filling ratios of 1.0 (highlighted red squares in Figure 1.3). Of these metals, it is apparent from the graph in Figure 1.4 that Au has the highest cohesive energy and coupling matrix element. This is thus an indication that compared to Cu (and other metals with a filled *d*-band), it would require the highest energy for bond formation to occur in Au and hence establishing its unreactive nature and being considered the "most noble" of noble metals.

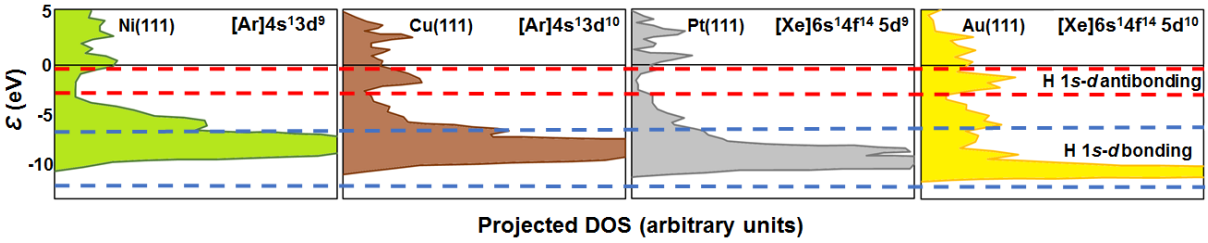

Figure 1.2 Density of one-electron states (DOS) for a hydrogen atom chemisorbed on the (111) surfaces of Ni, Cu, Pt and Au (adapted from references 2 and 5).

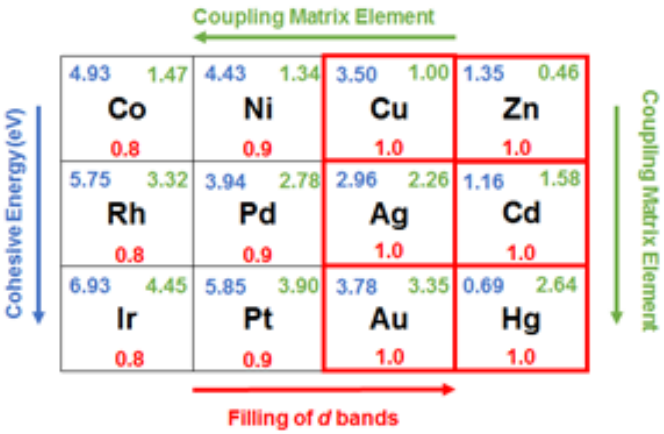

Figure 1.3 Values of cohesive energies, coupling matrix elements and *d*-orbital filling (expressed as a ratio – 1.0 representing d^{10} electron configuration) for metals in the vicinity of Au in the periodic table (adapted from reference 2).

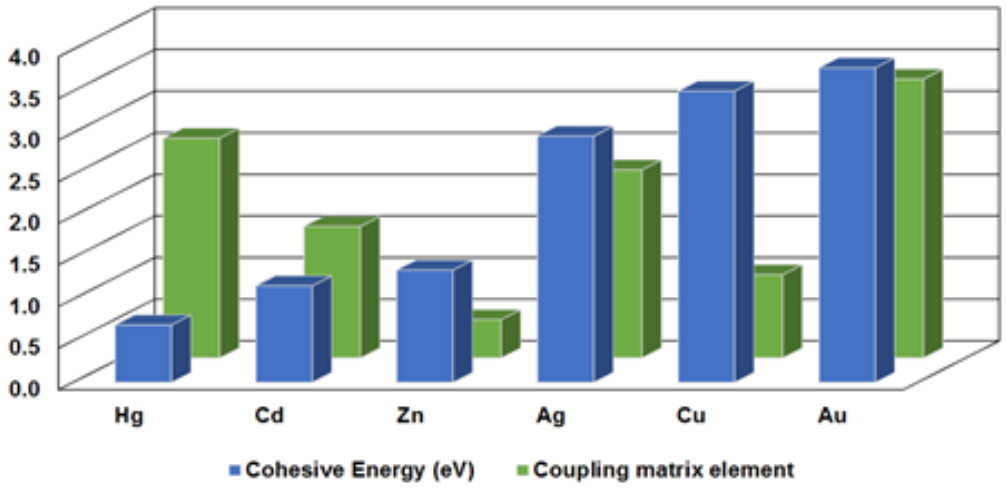

Figure 1.4 Comparisons of cohesive energies and coupling matrix elements for metals having *d*-band filling values of 1.0 which are higlighted by red squares in Figure 1.3.[2]

Similarly, gold complexes were for many years considered to be largely catalytically inactive. Even on occasion when certain Au complexes were shown to exhibit some activity, they proved to be inferior to other catalysts catalysing the same reaction.[6–8] However, since the discovery in the late 1990s that gold complexes could be utilized as efficient catalysts for the activation and functionalization of π-C-C bonds, their development and application in catalysis has grown rapidly.[6,7,9] A comprehensive review by Joost *et al* (2015) highlights the developments in catalysis by gold complexes. The review systematically demonstrates how these complexes, after historically being thought to be inactive, exhibit the elementary steps of organometallic chemistry.[6] They therefore delve into oxidative addition, reductive elimination, transmetallation/metallation and migratory insertion reactions exhibited by numerous gold complexes. They conclude that despite their ability to undergo the major elementary organometallic chemistry step, the reactivity does not parallel that of other transition metal complexes and requires the design of appropriate ligands and complexes to achieve the aforementioned organometallic chemistry steps. This difference in reactivity of the gold complexes compared to complexes of other metals thus mirrors the unique chemical behaviour described above for metallic gold.

In a further review by Hashmi (2004)[10], examples of gold complexes utilized in homogeneous catalysis for oxidation reactions, C-C bond formation, activation of C-C multiple bonds for the addition of N- and O-nucleophiles, reactions with organoboron compounds, dihydrogen, organostannanes and organosilanes and the trans/cis-isomerisation

of Pd(II) diaryl complexes, are also given. Selected examples of some reactions, catalyst precursors and gold oxidation states are shown in Table 1.1.

The majority of the applications of the listed gold (I) and gold (III) complexes in Table 1.1 can be seen to be in the organic synthesis of fine chemicals with the reactions of stannanes and Pd(II) complexes having applications in the field of inorganic synthesis. More recent review articles by Patil (2013)[11] and Dorel and Echavarren (2015)[12] show that research into numerous homogeneous organic transformations catalysed by gold continues to garner much interest.

Despite the ongoing interest around homogeneous organic transformations catalysed by gold complexes, in the review by Patil, the use of gold nanoparticles as catalysts for reactions only previously known to occur using homogeneous catalysts is eluded to as a trend leading to new studies in the arena of organic transformations. An example of this is the nanoparticle catalysed addition of nucleophiles to alkenes or alkynes to form addition products or cascade products.[13] This therefore leads us to the introduction of gold nanoparticles and their reactivity, applications and synthesis.

The activity of gold nanoparticles is due to what is known as the quantum size effect resulting in single electron transitions. It had been predicted by physicists working on semiconductor clusters that nanoparticles in the intermediate size between small molecules and bulk metal (approximate diameter range of 1 to 100 nm) would display electronic structures owing to quantum-mechanical rules.[14] This would result in physical properties which would be neither those of a bulk metal or a molecular compound, but would be strongly dependent on the nanoparticle size, interparticle distance, the nature of the protecting organic shell and shape of the nanoparticles.[15]

In practice this would mean that, depending on its size, the physical properties of a gold nanoparticle could be altered to be more or less reactive. Thus by altering the size of a gold nanoparticle, it can be tailored to be as (or more) reactive than corresponding gold (III) catalyst precursors or show less reactivity comparable to that of gold (I) catalyst precursors. Therefore, gold nanoparticles could be utilized in a wide variety of catalytic processes depending on the reactivity required and the nature of the protecting organic shell. This was

demonstrated by Quinn *et al* (2003) where they were able to electrochemically resolve fifteen oxidation states for various types of thiol protected gold nanoparticles.[16]

However, while organic gold complexes and inorganic gold ions are mainly used as homogeneous catalysts for the production of high-value organic fine chemicals, gold nanoparticle catalysts are usually used as heterogeneous catalysts on much larger scales in processes such as air cleaning, low light-off auto catalysts and in the purification of hydrogen streams used for fuel cells. Examples of supported heterogeneous gold catalyst reactions are given in Table 1.2.

The uniqueness of Au nanoparticle catalysts are that they are active under mild conditions and even at ambient temperature or less. They therefore have the potential to be effective in reducing running costs of chemical plants and the ability to increase the selectivity of reactions. Furthermore, it has been shown that gold nanoparticle catalysts are more durable and resistant to catalyst poisons, with mixed metal/gold catalysts having been shown to produce even higher activities than with the use of gold alone.[19, 20]

When gold nanoparticles less than approximately 5 nm are supported on base metal oxides or carbon, very active catalysts are produced. An example of this is seen in Figure 1.5 where the turnover frequency (TOF) for the oxidation of CO over a Au/TiO_2 catalyst significantly increases for particle diameters less than 5 nm.[18,21]

In addition it has been demonstrated that the catalytic performance of supported gold nanoparticles can be further tailored by selecting specific support materials, in addition to controlling nanoparticle size. An extensive set of examples demonstrating the size specificity of gold clusters for chemical reactions is shown in Table 1.3.

What is apparent is that in most cases, catalyst activity is as a result of electronic effects brought about by interaction with specific supports or ligands/capping agents. With the effect of Au nanoparticle size on reactivity being clearly demonstrated, it thus follows that it would be of interest to have control over cluster size during nanoparticle synthesis. The following section thus addresses Au nanoparticle synthesis and the various methods developed enabling sizes to be varied or limited within a certain range. This is also one of the major focal points

of the thesis and will lead into our hypothesis of how to attempt to synthesize Au nanoparticles while exercising size control.

Table 1.1 Summary of gold (I) and gold (III) complexes utilized in homogeneous catalysis.[10]

Reaction	Gold Oxidation State	Catalyst	Reaction Example
Oxidation	III	$Bu_4N[AuCl_4]$	Selective oxidation of thioethers
	I	$AuCl(PPh_3)$	Synthesis of formamides from CO under oxidative conditions
C-C bond formation	III	$AuCl_3$	Selective cross-dimerization of allenyl ketones and Michael acceptors
	I	$[Au(c\text{-}C_6H_{11}\text{-}NC)_2]BF_4$	Catalytic asymmetric aldol reaction
C-C bond activation for nucleophile addition	III	$Na[AuCl_4]$	Intramolecular addition of N-nucleophiles to alkynes
	I	$Au(CH_3)(PPh_3)$	Hydroamination under solvent-free conditions
Reactions with organoboron compounds	I	$AuCl[P(C_2H_5)_3]$	Diborylation of styrenes
Reactions with dihydrogen	*	Au coated Pd nanoparticles (20 to 56 nm)*	Hydrogenation of alkynes to (*Z*)-alkenes
Reactions with organnostannanes	I	$Au(CH_3)(PPh_3)$	Dehydrogenative dimerization of trialkylstannanes
Reactions with organosilanes	I	$AuCl(PPh_3)/PBu_3$	Hydrosilylation of aldehydes and imines

* Catalyst precursor not a Au complex but catalytic activity due to synergistic effects of Au and Pd with Au^0 being the most likely starting oxidation state.[17]

Table 1.2 Examples of Au catalyst applications.[18]

Fields of applications	Reactants or Reactions	Support materials
Indoor air quality control	odour (commercialized) CO sick house gases	Fe_2O_3, TiO_2
Pollutant abatement	dioxin oxidation-decomposition NO reduction N_2O decomposition	Fe_2O_3, Al_2O_3, Co_3O_4
H_2 energy carrier	water-gas shift CO removal fuel cell anode	ZrO_2, CeO_2, Al_2O_3, Mn_2O_3, Fe_2O_3, carbon black
Chemical process	hydrochlorination hydrogenation liquid-phase selective oxidation propylene epoxidation	$AuCl_3$/activated carbon, ZnO, activated carbon, TiO_2(anatase) and Ti-SiO_2

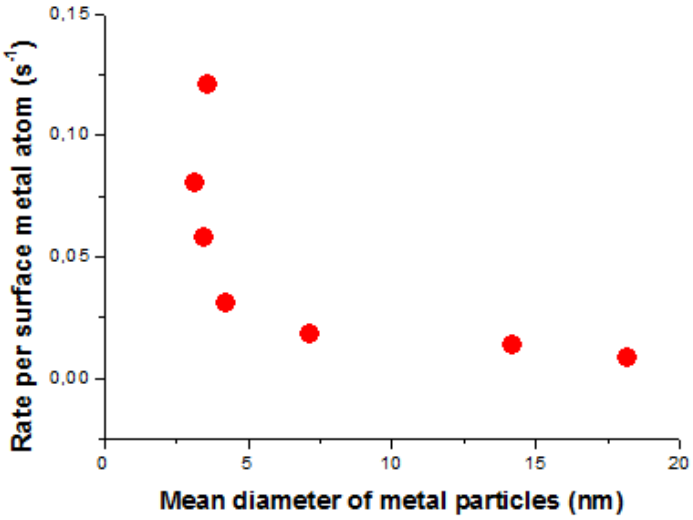

Figure 1.5 Turnover frequency (TOF) for CO oxidation over Au/TiO_2 demonstrating the effect of gold nanoparticle size on activity.[18,21]

Table 1.3 Size specificity of gold clusters for chemical reactions.[19]

Phase of clusters	Specific No. of atoms	State of gold	Effect (electronic or geometric)	Chemical reactions	Reaction conditions	Temp./K
In liquid	35	Au clusters formed in situ	e	ester-assisted hydration of alkynes	H_2O	rt
	1.1 nm	Au:PVP	e	aerobic oxidation of p-hydroxybenzyl alcohol	K_2CO_3 (300 mol%), H_2O, air	300
On solid support	6-10	Au/amorphous Al_2O_3	e	propene epoxidation	$C_3H_6/O_2/H_2O$ = 2/1/1, 133 kPa, 30 mL min^{-1}	473
	8≤	Au/MgO (F-center-defective)	e	CO oxidation	CO, O_2 0.2 Langmuir	140-280
	0.6-1.0 nm (13 atoms)	Icosahedron $Mg(OH)_2$	e, g	CO oxidation	1 vol% CO in air, SV = 20000 $h^{-1}mLg_{cat-1}$	203
	39	Au/HAP	e	aerobic oxidation of cyclohexane	TBHP, O_2 (1 MPa)	423
	55	Au/Si wafers	g	resistive against oxidation	oxygen plasma, 10min, 50W, 0.5 Pa	
	55	Au/SiO_2	e	aerobic oxidation of styrene)	in toluene, O_2 (0.15 MPa	373
	2 atoms thick	Au/TiO_2/Mo	e	CO oxidation	$CO:O_2$ = 2:1, total P = 5 Tor	rt

1.2 Gold Nanoparticle Synthesis

Since the reduction of a tetrachloroaurate solution by phosphorus in carbon disulfide (a biphasic reaction) to produce gold nanoparticles was first reported by Faraday in 1857 [22], the preparation of gold nanoparticles with controlled sizes and shapes has garnered considerable attention.

Gold nanoparticles can be prepared by both "top down" and "bottom up" approaches. The "top down" approach involves the systematic break down of bulk gold to generate gold nanoparticles of desired dimensions. Examples producing nanoparticles from a bulk gold source is ion irradiation in air or arc discharge in water. These types of nanoparticles are usually used in suspension with further surfactants added to stabilize them. The "top down" method is however limited in that it is difficult to control the size and shape of particles as well as there being difficulty in obtaining narrow size distributions.[23]

In contrast, the "bottom up" strategy uses wet chemical processes to prepare nanoparticles. This includes chemical reduction of gold salts, electrochemical pathways and decomposition of organometallic compounds. Of these methods, the chemical reduction method is relatively simple and controllable in the preparation of nanoparticles of various shapes and sizes.[23] This chemical reduction method involves two steps: nucleation and successive growth. When the nucleation and successive growth are completed in the same process, it is called *in situ* synthesis or the seed-growth method.[24]

1.2.1 Mechanisms and Theories of Nucleation and Growth in Solution

The most generally accepted mechanism, the LaMer Mechanism of nucleation and growth, is based on the study of sulphur sol synthesis from the decomposition of sodium thiosulfate and is separated into three stages as depicted in Figure 1.6.[25, 26]

The first stage (**I**) is the rapid increase in concentration of monomers which, in the case of gold nanoparticle synthesis, is the generation of Au^0 atoms upon reduction of a gold salt such as $HAuCl_4$. The concentration of the monomer increases until a saturation point, C_{sol}, is reached where after they are no longer soluble. The concentration of monomer further increases until a critical concentration (C_{crit}) is reached where rapid nucleation occurs (stage **II**). The rate of nucleation is described as "effectively infinite" and this rapid nucleation (or

"burst nucleation") continues until the monomer concentration decreases and stabilizes (stage **III**). This stabilization is brought about by the growth of the seeds or nuclei produced during stage (**II**). Depending on reaction conditions, growth during stage (**III**) can occur in a controlled or anisotropic fashion.

Nanoparticle growth proceeds either in a kinetically or thermodynamically controlled fashion.[27] Thermodynamic growth results in the uniform growth of all crystal facets and thus the subsequent formation of spherical or near-spherical structures. In the case of kinetic growth, the energetically preferential orientation of crystal facets favours directional growth and thus results in the formation of polyhedron shaped nanoparticles.[28]

During controlled (isotropic) growth, spherical clusters of atoms are formed by means of the addition of successive shells of atoms to the nucleus generated in stage (**II**). The stability of these atomic clusters formed after nucleation has been found to be dependent on electronic and geometric shell closing. The first stable cluster consists of 13 atoms which is arranged with 12 atoms in a geometrically closed icosahedron shell and the 13th positioned in the centre.[29,30] This configuration represents the first geometric shell closing for both icosahedral and cuboctahedral structures.[31] Stable geometric cluster sizes then increase by the successive addition of further shells which correspond to atom numbers 55, 147, 309 etc. These stable cluster arrangement of atoms are often referred to as "magic number" clusters.[32,33] The arrangement of atoms in these increasing magic number configurations are shown in Figure 1.7, where the contrasting outer colours depict the addition of a shell of atoms around the preceding core. The isotropic formation of "magic number" clusters can thus be seen to be thermodynamically governed.

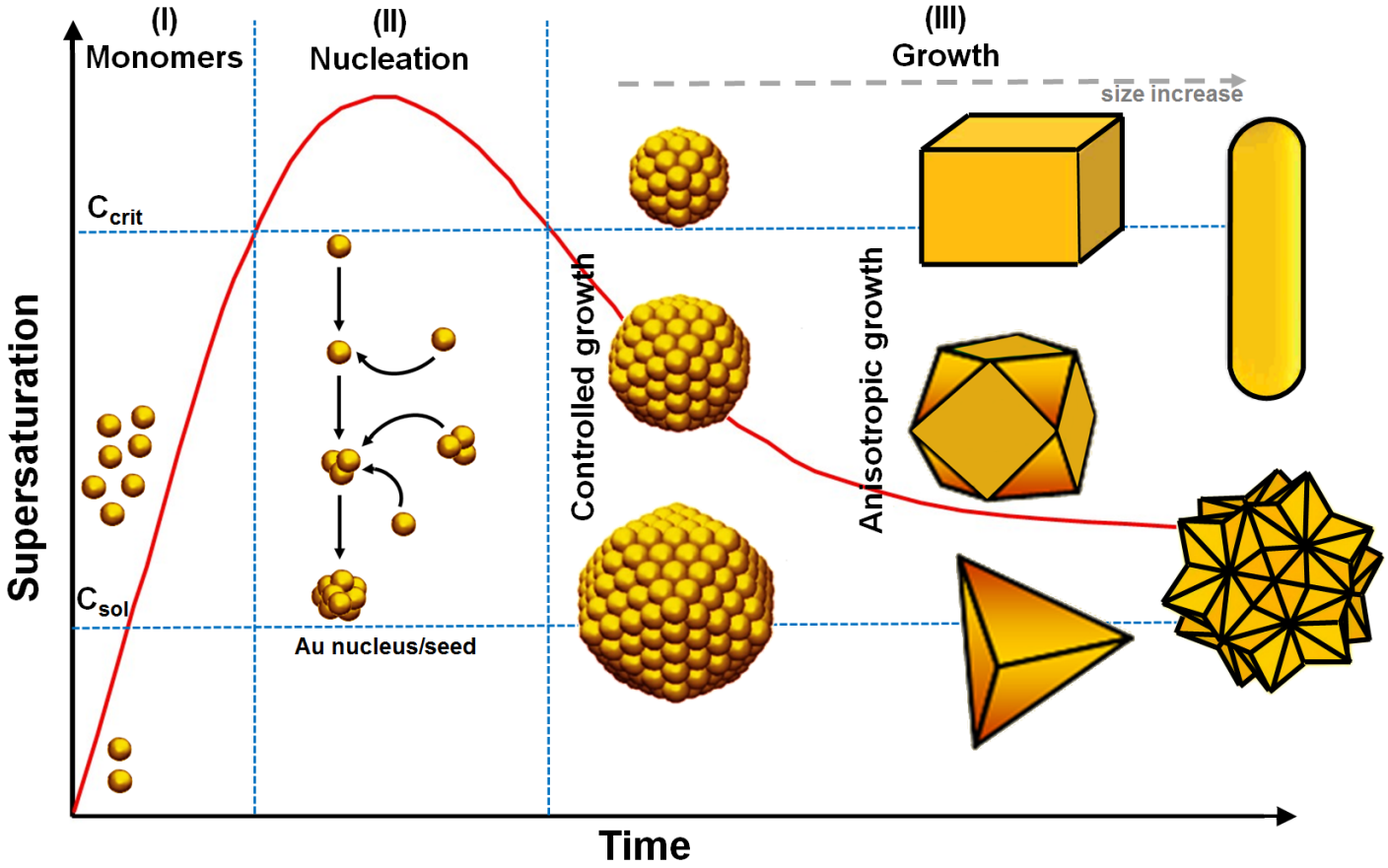

Figure 1.6 LaMer diagram depicting the various stages of nucleation and growth and types of nanoparticles produced.[25]

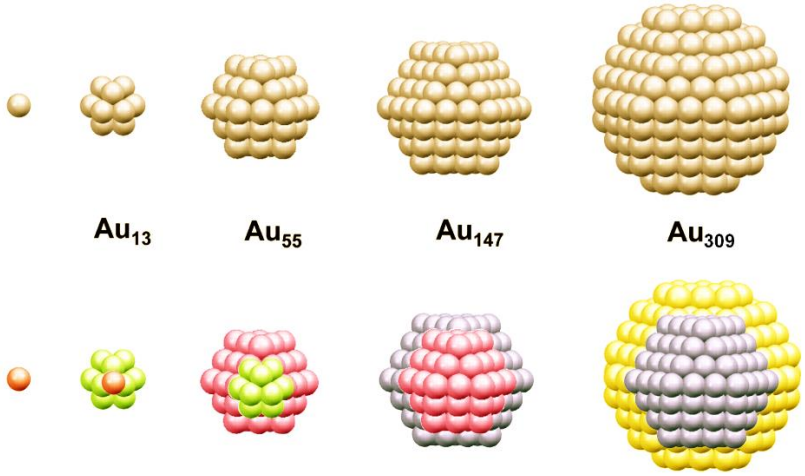

Figure 1.7 Atom arrangement with addition of successive shells to form "magic number" clusters (adapted from reference 30).

These isotropically formed clusters can in turn potentially act as seeds for anisotropic growth which produces polyhedron shaped nanoparticles; the seeds being either single "magic number" clusters or multiply twinned particles (a collection of tetrahedral clusters adjoined on identical faces).[34,35] Different seeds give rise to various polyhedron shaped particles which can grow even further to potentially form rods and star shaped structures. In general, anisotropic growth is kinetically governed. The process of anisotropic growth is depicted in Figure 1.8.

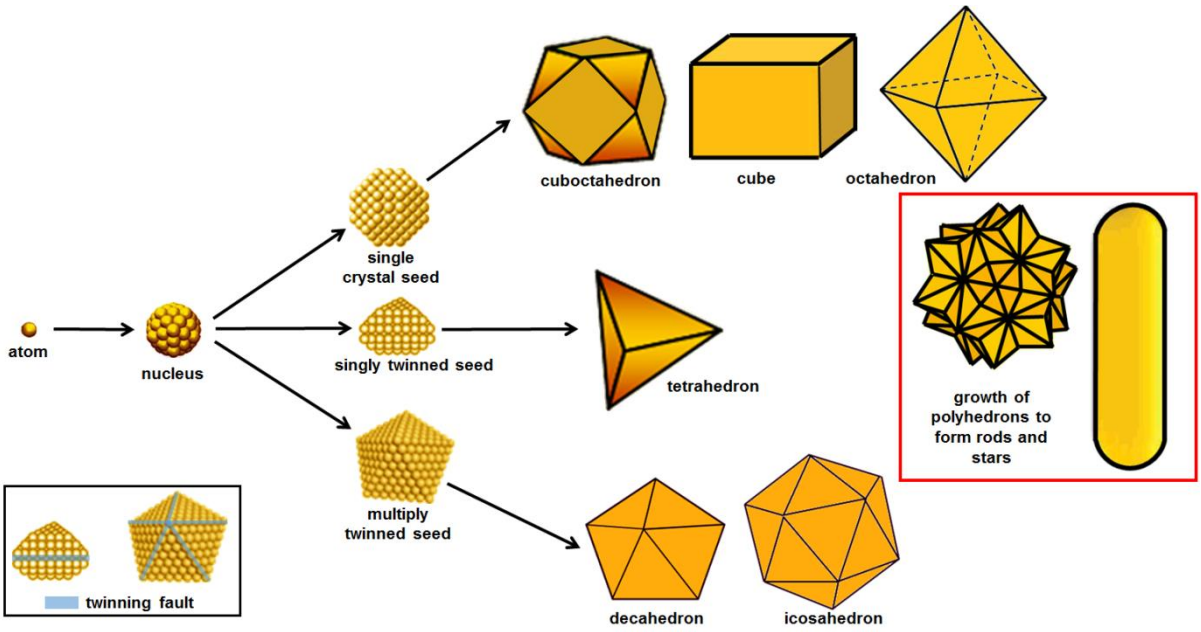

Figure 1.8 Process of anisotropic growth (adapted from reference 34).

Controlling which of thermodynamic or kinetic growth is dominant is a matter of adjusting reaction conditions, with tiny variations in growth conditions such as sequence of addition of reducing and capping agents and concentrations thereof being of critical importance. However, synergistic effects of both thermodynamic and kinetic aspects is of further importance in determining final nanoparticle shape and size.[27,28,36] Hence, due to the number of slight variations in reaction conditions which could result in variations in the final morphology of nanoparticles formed, an overall mechanism taking into account synergistic effects of kinetic and thermodynamic aspects governing nanoparticle growth, is yet to be proposed.[28] However, general equations exist which are able to describe nucleus/seed formation and subsequent nanoparticle growth as a function of reaction conditions.

The thermodynamic growth of homogeneous seeds can be considered by looking at the total free energy of constituent nanoparticles. For a spherical particle with radius *r*, this total free energy ΔG is defined as the sum of the surface (γ) and bulk (ΔGv) free energies of the nanoparticle as expressed in Equation 1.1.[37]

$$\Delta G = 4\pi r^2\gamma + \frac{4}{3}\pi r^2 \Delta Gv$$

(Equation 1.1)

Where $$\Delta Gv = \frac{-k_B T\, ln(S)}{v}$$

(Equation 1.2)

(k_B= Boltzmann's constant, S = supersaturation of the solution, v = molar volume and T = temperature)

These equations thus clearly highlight and confirm how variations in growth conditions are critical for the control of which of thermodynamic or kinetic growth is dominant and also demonstrates the synergy which exists between them. This is because even though (Equation 1.1 describes thermodynamic growth of a seed, it incorporates the kinetic bulk free energy term which is shown to be dependent on temperature, the concentration of monomers generated upon reduction, and the resultant supersaturation of the solution of these monomers.

The rate of nucleation is subsequently given by an Arrhenius type equation (Equation 1.3) where A is a pre-exponential factor.

$$\frac{dN}{dt} = A\, exp\left(\frac{16\pi\gamma^3 v^2}{3{k_B}^3(\ln S)^3}\right)$$

(Equation 1.3)

Once more the effect of nucleation conditions are clear, with supersaturation, temperature and surface free energy being critical parameters. However the greatest effect on nucleation rate is the supersaturation. Kwon and Hyeon (2011) found that a doubling of the supersaturation caused an approximate 10^{70} times increase in the rate of nucleation.[38]

The control of nucleation is important in determining the final size distribution. Fast monomer consumption during nucleation ensures that additional nucleation at latter stages during the reaction time is suppressed and therefore results in better control of final nanoparticle size.[38]

When the nuclei formed reach a point of critical supersaturation during stage (**II**), nucleation is complete and growth begins (see Figure 1.6) and occurs *via* two steps. For a spherical particle, the first step is the transference of monomers from the bulk solution onto the surface of a crystal, with the second step being the reaction of the monomers on the surface which, subsequently, results in growth.[38] The first step can be described by Fick's law of diffusion

$$J = -D\frac{d[M]}{dx}$$

(Equation 1.4)

where J = the monomer flux, D = the diffusion constant and $[M]$ = the monomer concentration. If x is the radius of the spherical particle ($x = r$), $[M]_s$ is the surface concentration of monomer and $[M]_b$ the bulk concentration the total movement of the monomer onto the surface can be described by

$$J = 4\pi Dr([M]_b - [M]_s]$$

(Equation 1.5)

From the equations describing growth, it becomes apparent once more that supersaturation is critical to the rate at which it occurs. Thus it follows that limiting $[M]_b$ would in turn retard migration of monomer to the surface which would result in surface reaction and subsequent

growth. What this highlights is the critical role of reduction of the metal salt in determining final nanoparticle size and morphology. In addition, the role of capping agents can also be seen to be as critical, as it would also limit the surface concentration of monomers leading to growth.

The general mechanisms by which nucleation and growth occur in solution as described by the above equations, have been proposed to occur according to four major theories. The first of these is by means of Ostwald ripening and digestive ripening.[39] In Ostwald ripening, the growth is caused by the change of solubility of nanoparticles depending on their size. Due to the high surface energy of smaller particles within solution, they re-dissolve which allows for larger particles to grow more. Digestive ripening is essentially the inverse of Ostwald ripening. Here high energy small particles lower their energy by growing at the expense of larger particles.

The Finke-Watzky Two Step Mechanism is a process whereby nucleation and growth happen simultaneously.[40] The first step is a slow continuous nucleation followed by autocatalytic surface growth which is not diffusion controlled.

Another mechanism is coalescence and orientated attachment. These mechanisms are similar, but differ in the orientation of the crystal lattice at the grain boundary. For coalescence there is no particular preference in the attachment, whereas for orientated attachment, there is a common crystallographic alignment which allows for continuous crystallographic planes.[37]

The fourth mechanism is intraparticle growth. This is the diffusion of monomers along the surface of a nanomaterial to change the shape of the particle with time. This occurs where the energy of monomers within solution are lower than that of one of the crystal facets of the nanoparticles already formed.[41, 42]

As previously mentioned and illustrated by Figure 1.5 and Table 1.3, gold nanoparticle size plays a decisive role in their catalytic activity. Therefore, if the nanoparticles were to be utilized in catalysis, controlling particle size during synthesis is thus crucial in producing a potentially highly active catalyst. The following section therefore highlights various methods of gold nanoparticle synthesis in which sizes are tailored to within ever decreasing ranges.

1.2.2 Methods of Gold Nanoparticle Synthesis

1.2.2.1 Turkevich Method

The Turkevich method of gold nanoparticle synthesis is considered to be the most popular method of synthesis since its introduction by Turkevich in 1951.[43] In general, a $HAuCl_4$ solution is boiled, and trisodium citrate dihydrate is quickly added under vigorous stirring. Trisodium citrate both reduces the $HAuCl_4$ and acts a stabilizer for the nanoparticles formed. After a few minutes, a wine-red colloidal suspension is obtained. The gold nanoparticles subsequently produced are approximately 20 nm in size. Frens (1973) improved on this method by being able to control the sizes of nanoparticles obtained in a range from 15 to 150 nm by controlling the trisodium citrate to $HAuCl_4$ ratio.[44] Kumar *et al* (2007) explained this discovery by Frens through the development of a kinetic model for the formation of gold nanoparticles by the citrate method and showed that unlike the usual balance between nucleation and growth which determines particle size, it is the balance between the rate of nucleation and degradation of dicarboxy acetone that determines the particle size in the citrate process.[45]

The process of gold nanoparticle formation by the traditional Turkevich method had been investigated in detail by Kimling *et al* (2006) compared variations of the method using UV initiated reduction and ascorbate reduction[46]. As presented by Frens, they found a general relation between the gold-to-reductant ratio and the final size of the particles and in addition that, in general, the relationship is independent of the absolute concentrations. However they identified that the limit for the production of stable particles over an extended period was below 2 mM of gold, and that between 1 and 2 mM gold concentration the particle sizes are sensitive to the concentration. The size definition was found to be best below 0.8 mM, where a size dispersion of 13 – 16 % could be achieved for particles smaller than 40 nm. Larger particles tended to develop an elongated shape, while the size polydispersity also worsened. The UV initiated particle growth in contrast resulted in more spherical like particles, even at larger sizes. A small abundance of triangles and/or platelets were also found to be present. They further found that ascorbate reduction ensured the best spherical definition of the particles. These results not only demonstrates how changes in reaction conditions vastly influence final nanoparticle size and morphology, but that size variations are generally not influenced by a single parameter.

Uppal *et al* (2010) further demonstrated that the size of gold nanoparticles produced *via* the Turkevich method could be controlled by two methods. Firstly they showed a systematic decrease in nanoparticle size from 15 nm at synthesis, to 11 – 12 nm after 14 days.[47] This was found to occur consistently independently of whether samples were stored in light or dark. Furthermore, the observation was made irrespective of whether excess un-reacted citrate and $HAuCl_4$ was present and was thus independent of excess reactant chemistries and charge stabilities. Their study therefore suggested that gold nanoparticle sizes between 15 and 11 nm could be obtained by simply harvesting them at a specific time after synthesis. At the conditions employed in this work it therefore appeared that digestive ripening was the dominant mechanism.

Uppal *et al* (2010) then went on to demonstrate how to vary, within certain ranges, the average size of nanoparticles formed by the Turkevich method.[48] Depending on the method by which the growth of the gold nanoparticles were initiated (either thermally, by sonolysis, microwave or hard ultra-violet irradiation), nanoparticles in the range of 8.0 – 18.0 nm were obtained. For thermal initiation of growth, gold nanoparticles of 11.0 – 11.9 nm were obtained, for sonolysis 16.9 – 18.0 nm was achieved, 11.3 – 17.2 nm nanoparticles were found for microwave initiated growth and 8.0 – 11.2 nm for hard ultra-violet irradiation mediated growth initiation. Although they found that gold nanoparticle solutions did not form unless tri-sodium citrate was present, regardless of the initiation method used, the formation was not affected by citrate concentration increases between 0 and 3.88 mM (with the concentration of $HAuCl_4$ kept constant at 0.28 mM) in the case of thermal and sonolysis initiated growth. Microwave assisted reactions were concentration dependent from 0.96 mM, at which point nanoparticles 17.2 nm in size were formed. As the citrate concentrations were then increased, smaller nanoparticles of 11.3 – 11.6 nm in size were formed. Hard ultra-violet light initiated reactions were concentration dependent from 0.84 mM with particles also becoming more elliptical in nature with an increase in citrate concentration up to 3.88 mM.

The variations in the Turkevich method described above, although bringing about better control in the size ranges of the nanoparticles produced, did not produce particles below the threshold of 5 nm at which gold nanoparticle catalysts show the best activity (Figure 1.5). Brown *et al* (1996) however, reached just above this threshold by obtaining 6 nm particles.[49] They did this by utilizing a further modification of the Turkevich method where a

$NaBH_4$/citrate mixture was added into a $HAuCl_4$ solution at room temperature. In this case then, $NaBH_4$ acted as the reducing agent with citrate acting only as the nanoparticle stabilizer.

Sivaraman *et al* (2011) further approached the 5 nm threshold by simply reversing the order of addition in the Turkevich method *i.e.* adding $HAuCl_4$ to a citrate solution.[50] By doing this they showed that gold nanoparticles in the 5 – 10 nm range could be synthesized.

Whereas the above repeatedly demonstrated the effect of the interplay between various parameters, Ftouni *et al* (2012) then demonstrated that with a high control of the synthesis parameters such as reactant mixing, temperature and reaction time control using a microfluidic set-up, gold nanoparticles protected by sodium citrate with an average diameter < 2 nm could be produced.[51] It was found that the mixing in the microfluidic system produced smaller nanoparticles compared to using classical glassware such as a round bottomed flask. In addition, the time of mixing (residence time) also had an effect on particle size. Interestingly though, there was no direct correlation of nanoparticle size with residence time. What this suggests is that the microfluidic system allowed for greater control over the nucleation stage and therefore limited further growth with time. In particular, it allowed for fast monomer consumption resulting in the suppression of growth.

The above examples give an indication as to why the Turkevich method is considered to be one of the more popular methods of nanoparticle synthesis. It is relatively simple, in general requiring the addition of sodium citrate to a boiling solution of $HAuCl_4$. By slight alterations of the method (altering gold/citrate ratios, concentrations, order of addition *etc.*) nanoparticle sizes can be widely varied. This is an important factor when considering the application of the synthesised nanoparticles, and in the case of catalysis, their reactivity.

1.2.2.2 Brust-Schiffrin Method

The Brust-Schiffrin method of gold nanoparticle synthesis produces highly monodisperse nanoparticles of controlled size (ranging in diameter between 1.5 and 5.2 nm) which are thermally and air-stable. This allows the gold nanoparticles to be re-dissolved in common organic solvents without irreversible aggregation or decomposition, and they can be easily handled and functionalized similarly to simple organic and molecular compounds.[52] The technique of synthesis was inspired by Faraday's two-phase system and uses thiol ligands that strongly bind gold due to the soft character of both Au and S.[53] In this method, $AuCl_4^-$ is

transferred to toluene using tetraoctylammonium bromide (TOAB) as the phase-transfer reagent and reduced by $NaBH_4$ in the presence of dodecanethiol. The organic phase changes colour from orange to deep brown within a few seconds upon addition of $NaBH_4$.

The Brust-Schiffrin method was extended in 1995 to an improved procedure upon which the p-mercaptophenol-stabilized gold nanoparticles were synthesized in a methanol solution without the phase transfer agent TAOB.[54] In this way, the introduction of TAOB impurities were avoided. Methanol was found to be an excellent solvent for a single-phase system since both $HAuCl_4$ and p-mercaptophenol are soluble in it. In general, any thiol that is soluble in the same solvent as $HAuCl_4$ such as methanol, ethanol or water allows the use of a single phase system for gold nanoparticle synthesis.

Later refinements of the method by several groups have enabled high-quality synthesis of a few particularly stable "magic number" compounds in the size range 1 – 3 nm, with a few having been determined up to molecular precision. These include $Au_{20}(SR)_{16}$, $Au_{25}(SR)_{18}$, $Au_{38}(SR)_{24}$, $Au_{40}(SR)_{24}$, $Au_{68}(SR)_{34}$, $Au_{102}(SR)_{44}$ and compounds with around 144 Au atoms and 60 thiolates.[55] It had further been established that the gold–sulfur interface in these clusters consists of oligomeric $RS(AuSR)_n$ units. This changed the understanding of the internal atomic structure of these systems and redefined the concepts of the "metal core" and the "passivating ligand layer". At variance with early theoretical models that considered an atomically smooth Au–S interface and compact Au cores, Au atoms at the centre of the particle and in the thiolate layer were now considered to be in two distinct chemical states (metallic and oxidized).[55]

In an attempt to investigate the mechanism of gold nanoparticle formation by the Brust−Schiffrin two-phase method, Yu *et al* (2014) characterized the polymeric gold(I) thiolates that precipitated from the intermediate solutions during the synthesis process.[56] Solution ^1H NMR confirmed the complete reduction from Au(III) to Au(I) with the addition of the first two equivalents of thiols, while only the third and fourth equivalents of thiols were found to participate in forming gold(I) thiolates. Gold(I) thiolates, [Au(I)SR]n, precipitated from these solutions were further characterized by ^1H solid-state NMR spectroscopy under fast magic angle spinning (MAS), Raman spectroscopy, and thermogravimetric analysis. Further quantitative studies revealed that the composition of [Au(I)SR]n could be controlled by changing the order of addition of the third and fourth equivalents of thiols.

Uehara *et al* (2015) further elucidated the mechanism of the Brust−Schiffrin gold nanoparticle synthesis through the use of ion transfer voltammetry at the water/1,2-dichloroethane (DCE) solution interface, combined with X-ray absorption fine structure (XAFS) of the reaction between $AuCl_4^-$ and thiol (RSH) in a homogeneous toluene solution.[57] Their ion transfer calculations indicated the formation of $AuCl_2^-$ at RSH/Au ratios from 0.2 – 2 with a time-dependent variation observed over several days. At RSH/Au ratios above 2 and after time periods greater than 24 h, the formation of Au(I)SR was also observed. The relative concentrations of reaction products observed at the liquid/liquid interface were in excellent agreement with those observed by XAFS for the corresponding reaction in a single homogeneous phase. BH_4^- ion transfer reactions between water and DCE indicated that the reduction of $AuCl_4^-$ or $AuCl_2^-$ to Au nanoparticles by BH_4^- proceeded in the bulk organic phase. On the other hand, BH_4^- was unable to reduce the insoluble [Au(I)SR]n species to Au nanoparticles. The number and size of the nanoparticles formed were dependent on the concentration ratio of RSH/Au, as well as the experimental duration because of the competing formation of the [Au(I)SR]n precipitate. Higher concentrations of nanoparticles, with diameters of 1.0 – 1.5 nm, were formed at RSH/Au ratios from 1 to 2.

Although there are advantages in the small and narrow size distribution of the nanoparticles formed by the Brust-Schiffrin, it is apparent that the synergy of reaction conditions allowing for this is quite complex. As previously mentioned and observed, tiny variations in reaction parameters could lead to large disparities in nanoparticle size and morphology. Thus, the apparent complexity could potentially allow for little or no room for deviation and thus make nanoparticle synthesis repeatability challenging.

1.2.2.3 Martin Method

In another biphasic chemical synthesis method, Martin *et al* (2010) described a simple, fast, highly reproducible, and size-tunable (from 3.2 – 5.2 nm diameter) technique for alkanethiolate coated gold nanoparticles production.[58] Gold nanoparticles were synthesized in water and then phase-transferred to hexane by coating them with insulating 1-dodecanethiol molecules. This was achieved in less than 10 minutes, without post synthesis cleaning and using minimal amounts of chemicals.

Being negatively charged in nonpolar solvents was proposed to be the key property of gold nanoparticles coated with hydrophobic 1-dodecanethiol molecules for 2D self-assembly at the air-liquid interface of a toluene droplet, which is also strongly dependent on the size of nanoparticles. A monolayer film of close-packed gold nanoparticles at the air-liquid interface of a toluene droplet could be deposited to any substrate with no limit in size. This provided a very simple and effective construction method for 2D monolayer films of close-packed nanoparticles. Therefore, unlike with the Brust-Schiffrin method, gold nanoparticles produced in this biphasic manner could potentially be used in heterogeneous catalysis.

In a refinement to the method, Martin *et al* (2012) produced hexanethiolate-coated gold nanoclusters with a diameter of < 2 nm (< 250 atoms per nanocluster) taking only 2 min and which could be easily reproduced.[59] The ultrafast synthesis was made possible by minimizing the reaction of Au(III) ions with thiol molecules before their reduction to nanoclusters. This is also critical for controlling the diameter of the nanoparticles to < 2 nm. In addition, no post-synthesis cleaning was needed, since two immiscible solvents of methanol and hexane were used for easy and fast separation of the final product of gold nanoclusters in hexane from the reaction by-products in mostly methanol. The only impurity in the hexane solution of gold nanoclusters is free, unreacted alkanethiol molecules at very low concentrations. These could potentially be removed by a post-synthesis size-filtering ultracentrifugation process.[59]

With the thiol molecules responsible having a major influence on the resultant nanoparticle size, a potential drawback of nanoparticles synthesized through this method is that the thiols would limit access the access of reactants to the catalytic surface and thereby negate some of the advantage that would be gained by the small size achievable.

1.2.2.3 Dendrimer Template Method

Dendrimers are branched, tree-like polymers that are comprised of three main components: a central core, repeating units with branched structures and surface functionalities.[60–62] Because they have properties such as mono-dispersity, nanoscale size and possess large numbers of surface functionalities and interior cavities, dendrimers have gained great interest in fields ranging from polymer- and material chemistry, to industrial and biomedical applications.[63,64] These structural components and properties are illustrated in Figure 1.9. Among these

investigations, the host−guest interaction (or inclusion chemistry) of dendrimers toward a list of guests such as drugs, dyes, surfactants, catalysts, bio-macromolecules, and metal nanoparticles have held great scientific interest due to their key roles in the broad applications of dendrimers.[65]

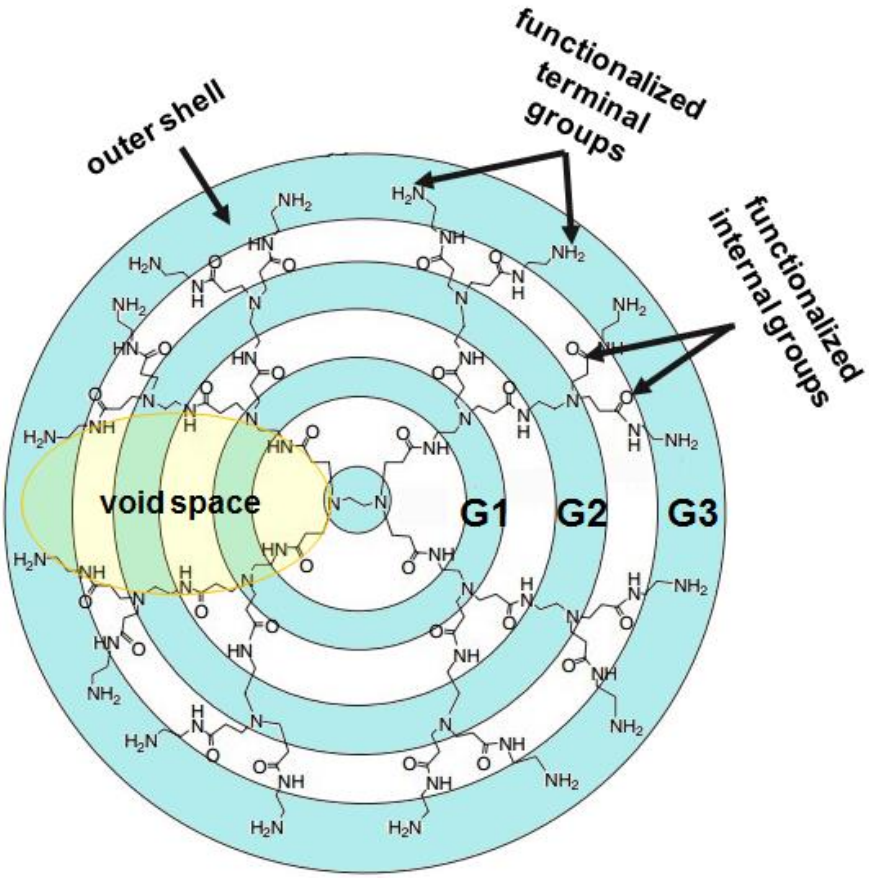

Figure 1.9 Illustration of dendrimer structural components and properties illustrated using a generation 3 (G3) poly(amidoamine) (PAMAM) dendrimer (adapted from reference 66).

The inclusion chemistry of metal nanoparticles enclosed within dendrimers was exploited by Zhao *et al* (1998), who introduced a template synthesis strategy for preparing metal nanoclusters within dendrimers.[67] Proof of concept was demonstrated by preparation of Cu clusters, but the approach was said to be applicable to any transition metal ions that could be extracted into the interior of a dendrimer and subsequently reduced. With the demonstration using Cu, clusters from 4 to 64 atoms (nanoparticle sizes of < 2.0 nm) were prepared by partitioning Cu^{2+} into the interior of poly(amidoamine) (PAMAM) dendrimers and the subsequent reduction of the metal ions. They further found that the Cu clusters were extremely stable despite their small size. This provided strong evidence that the clusters were located within the dendrimer interior. Thus by using dendrimers as monodisperse templates

for cluster growth, they achieved both cluster stability and full control over size and size distribution.

The manner in which dendrimers stabilize nanoparticles within their interiors differ to where lowering of the surface energy to limit agglomeration (by absorption of stabilizers with polymers and surfactants) is applied. The problem with traditional stabilizers is that by lowering the surface energy, they are in effect poisoning the surface of the cluster thereby reducing their catalytic potential. Dendrimers on the other hand do not entirely co-ordinate to the nanoparticle surface, but mostly sterically retain nanoparticles within the dendrimer interior.[68,69] The dendrimer template method therefore restricts aggregation while also limiting any reduction in the potential catalytic activity.[67]

1.2.2.3.1 Properties of Dendrimers Required for Nanoparticle Synthesis *via* the Template Method

PAMAM and poly(propylene imine) (PPI) (Figure 1.10) are two of the most studied and characterized dendrimers and were subsequently the first to be commercialized.[70,71] As a consequence, both have been used as effective templates for preparing nearly monodisperse metal nanoparticles contained within the dendrimer interior.[67,72–74] Thus the vast majority of studies involving the templating method thus utilize these two dendrimers.[69,75]

An important distinction between PPI and PAMAM dendrimers is that PPI is smaller than PAMAM for equivalent generations. This is illustrated in Figure 1.11 which shows that a PPI dendrimer requires to reach generation 5 in order to have an equivalent radius to a generation 3 PAMAM dendrimer (≈ 1.8 nm).[76] This difference in dendrimer size can affect the sizes of corresponding inter- and intra-dendrimer stabilized nanoclusters.[77] As is further illustrated in Figure 1.10, this is due to the PPI dendrimer having a shorter repeating unit (-$CH_2CH_2CH_2$-) compared to a PAMAM dendrimer repeating unit (-$CH_2CH_2COCH_2CH_2$-).[78]

Furthermore it can be seen from Figure 1.10 that the nature of the repeating units result in the interior of a PPI dendrimer being less hydrophilic than that of a PAMAM dendrimer; the less polar (–CH_2-)$_3$ repeating units rendering the PPI dendrimer more hydrophobic compared to the more polar, oxygen containing repeating units of the PAMAM dendrimer. Another distinguishing characteristic is that the PPI dendrimer is stable at very high temperatures (the

onset of weight loss for G4 PPI is 470 °C), whereas PAMAM dendrimers undergo retro-Michael addition (*i.e.* loss of amide linkages) at temperatures higher than about 100 °C.[77,79]

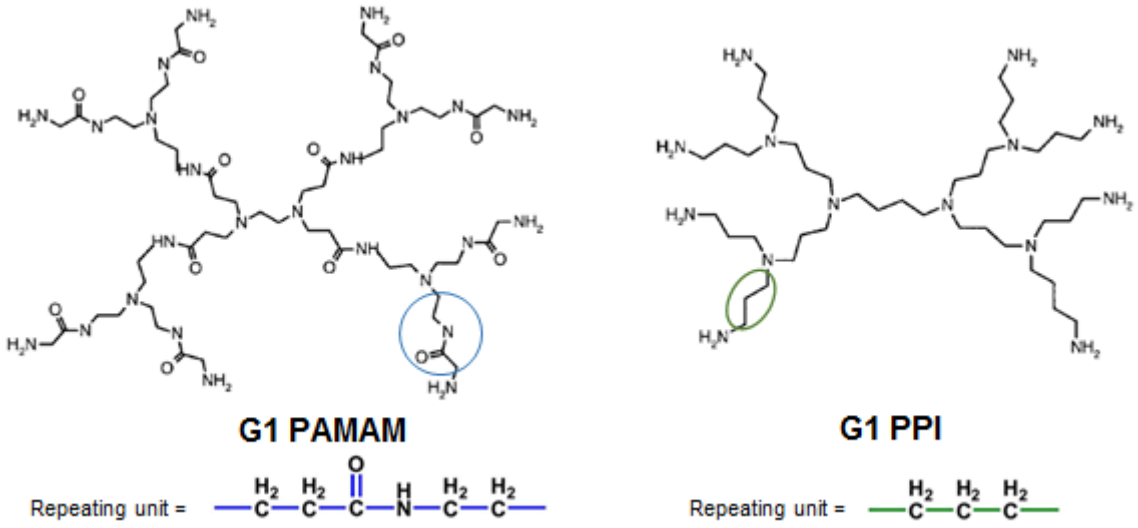

Figure 1.10 Structures of G1 PAMAM and G1 PPI dendrimers.[69,78]

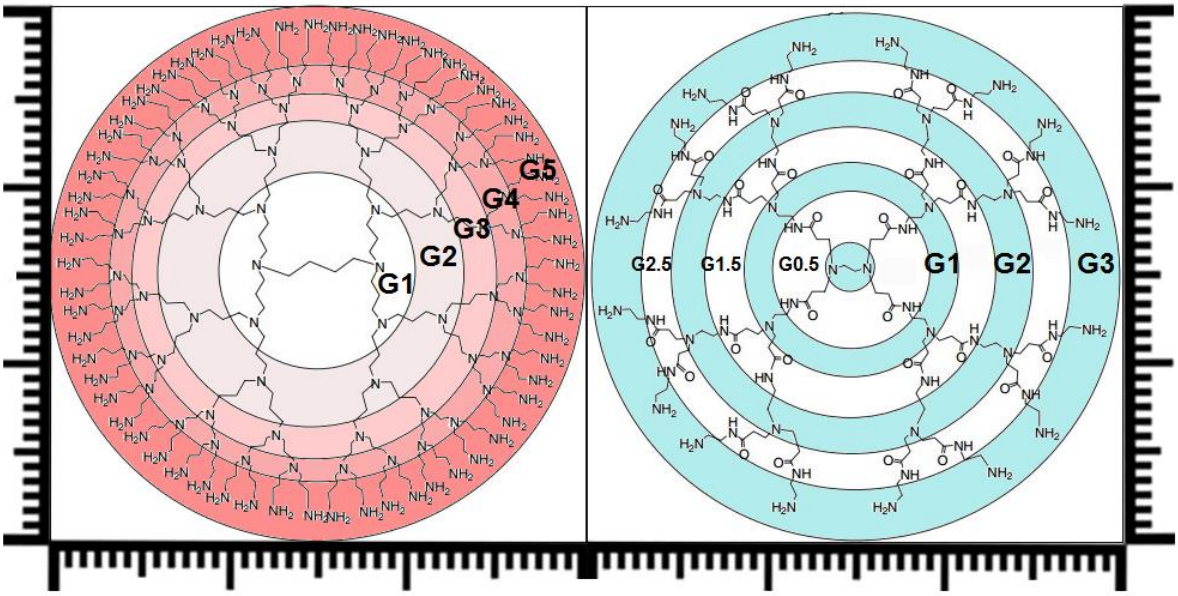

Figure 1.11 Comparison of equivalent dendrimer generation radii of PPI (left) and PAMAM (right).

In general, for the dendrimer template method to be effective, the surface density should be low enough to allow incoming metal ions to enter the interior of the dendrimer, but not too open allowing for the entrained species to be easily dislodged from the interior.[77,62] These properties were referred to by Tomalia *et al.* as their container and scaffolding behaviour and

are determined by the size, shape, and multiplicity of the construction components that are used for the core, interior and surface of the dendrimer.[62] The changes in molecular shape, two-dimensional branch cell amplification, number of surface branch cells, surface groups and molecular weights as a function of generation from 0 to 5 of PAMAM is shown in Figure 1.*12*.

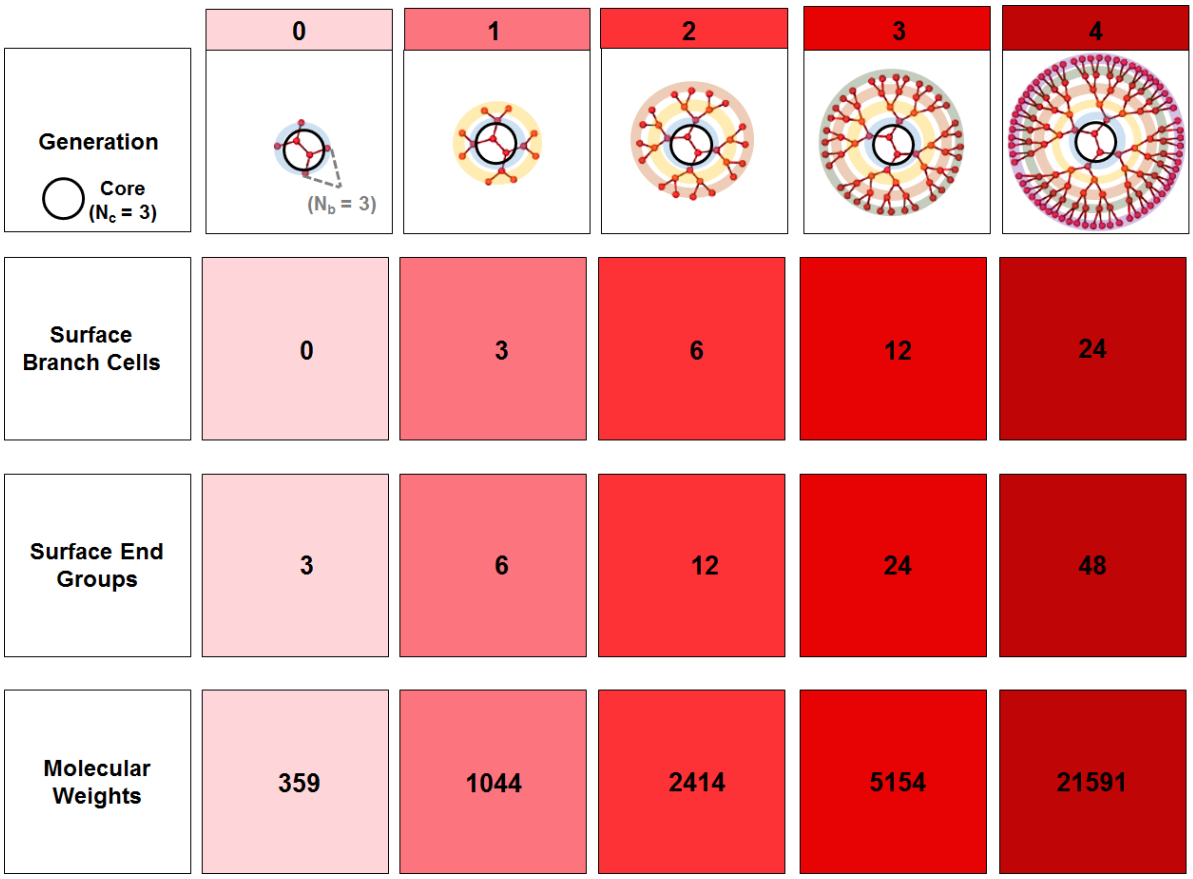

Figure 1.12 Changes in molecular shape, two-dimensional branch cell amplification, number of surface branch cells, surface groups and molecular weights as a function of generation from 0 to 4 of PAMAM where N_c = core multiplicity and N_b = branch cell multiplicity (adapted from reference 71).

Container and scaffolding properties are specific to each dendrimer series. Within the PAMAM dendrimer series, containing and scaffolding generally occur in three phases. Generations 0 to 3 do not exhibit well-defined interior cavities, therefore limiting retention of metal ions within the interior. However, this changes from generation 4 to 7 where de Gennes dense packing, which are the distances between dendrimer surface groups, is open enough to allow incoming metal ions to enter the interior while having well-defined interior architectures capable of retaining the metal ion. Above generation 7, the de Gennes dense

packing becomes too severe to allow entry for any incoming metal ions.[62,77] The concept is illustrated in Figure 1.13. Thus for PAMAM, the ideal generations for application in the templating method of nanoparticle synthesis would be between 4 and 6.

The ability to prepare well-defined intra-dendrimer metal nanoclusters was also shown to depend strongly on the chemical composition of the dendrimer. Crooks *et al* (2001) showed spectroscopic results that indicated when amine-terminated fourth generation (G4) PAMAM dendrimers (G4-NH_2) were used as templates, they sorb a maximum of 36 Cu^{2+} ions which bind primarily to the terminal primary amine groups. Reduction of a solution containing 0.6 mM $CuSO_4$ and 0.05 mM G4-NH_2 resulted in a clearly observable plasmon resonance band at 570 nm, which indicated that the Cu clusters prepared in this way are >5 nm in diameter. This larger size was thought to be a consequence of agglomeration of Cu particles adsorbed to the unprotected dendrimer exterior. They then further showed how the size of nanoparticles synthesized by the dendrimer template method was dependent on the number of metal ions initially loaded into the dendrimer.[80]

Depending on reaction conditions and end groups, co-ordination can be *via* the internal tertiary amine groups, a combination of amine and end groups or as a salt. This is depicted as (i), (ii) and (iii) respectively in Scheme 1.1. A mixture of the three aforementioned co-ordination modes could also occur.[68] Reduction subsequently results in the formation of dendrimer encapsulated nanoparticles (DENs) which may form internal, external or mixed composite structures (Scheme 1.2).

Because the dendrimer template is uniform in structure, each one contains the same number of interior co-ordination sites. As a result, an equal number of metal ions should co-ordinate within each dendrimer and hence the encapsulated nanoparticles that form after reduction should all contain approximately the same number of atoms. This is particularly advantageous when targeting specific atom clusters such as Au_{55} for example; a dendrimer with a sufficient number of end groups resulting in 55 interior co-ordination sites would result in nearly monodisperse Au_{55} atom clusters forming. Nanoparticle encapsulation is maintained predominantly by steric effects, but chemical interactions between the dendrimer and metal particle surface may also play a role.[68, 81]

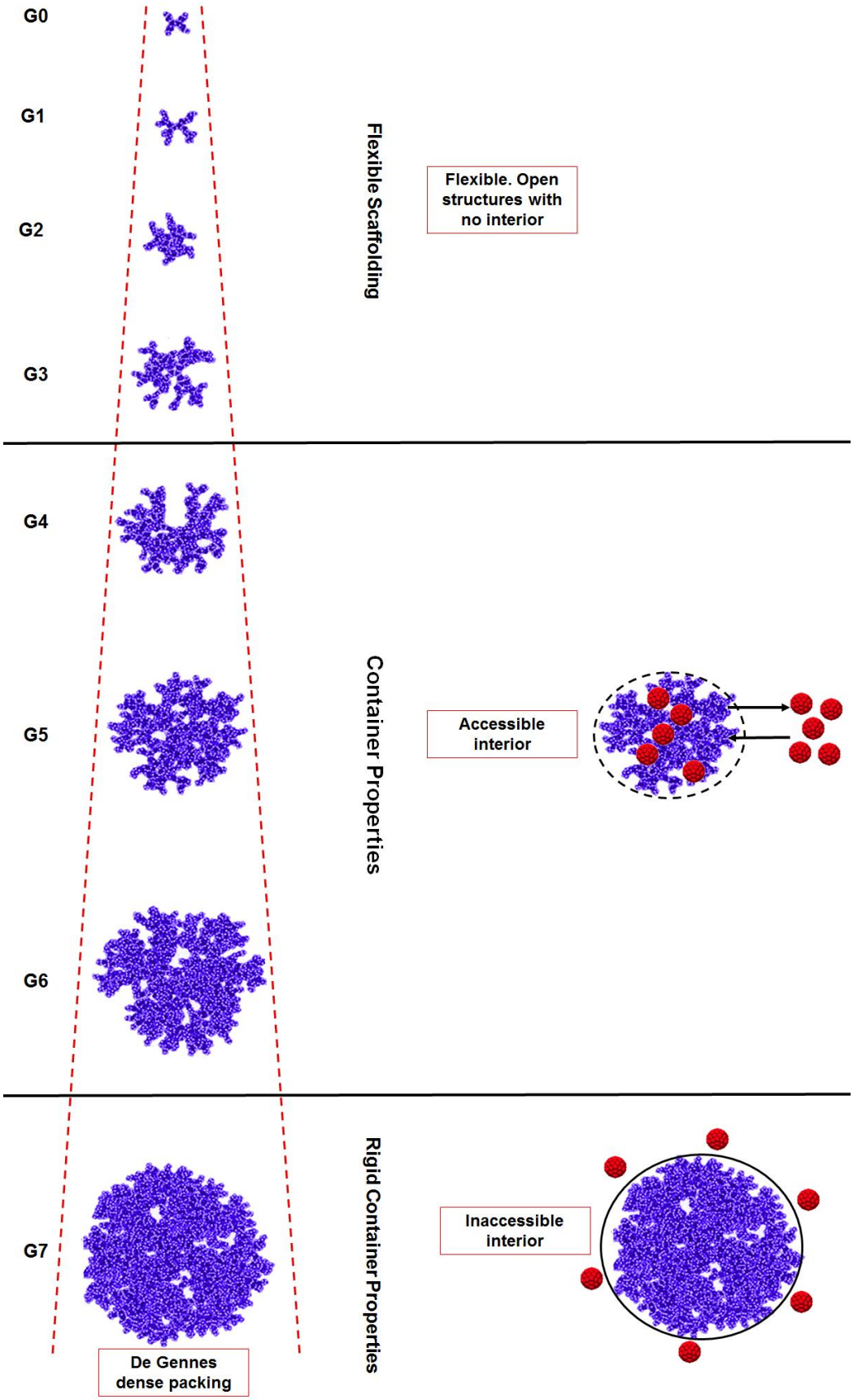

Figure 1.13 Container and scaffolding properties of successive generations of PAMAM dendrimers (adapted from reference 62).

Scheme 1.1 Representation of possible co-ordination sites of metal ions, reduction and formation of nanoparticle in a generic amine-type dendrimer.

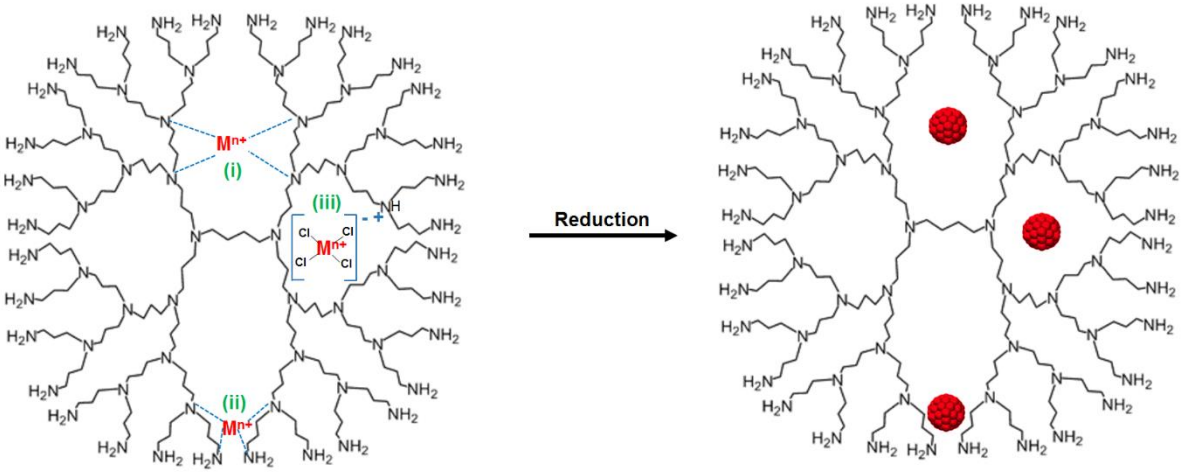

Scheme 1.2 Internal, external and mixed dendrimer nanocomposites (adapted from reference 68).

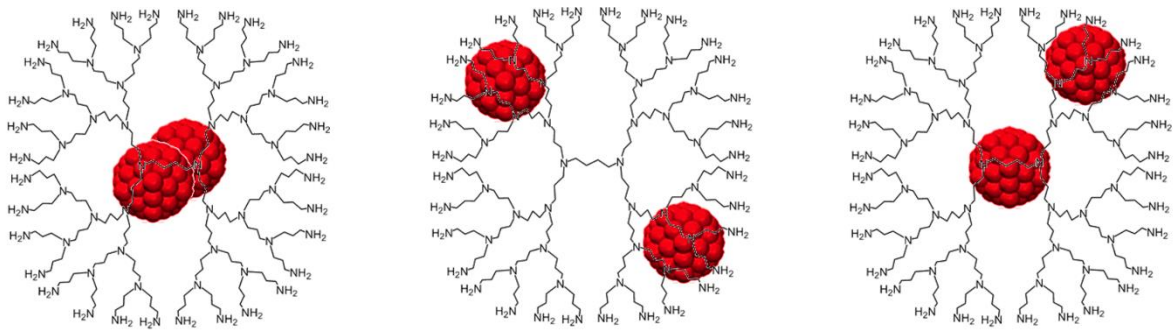

In a further development of this method, Garcia-Martinez (2003), reported on the extraction of intact monodisperse Pd nanoparticles from dendrimer templates using *n*-alkanethiols.[82] This was considered a significant discovery for several reasons. First, it demonstrated that nanometer-scale materials prepared within a molecular template can be removed, leaving both the replica and template undamaged. Second, it provided a straightforward approach for preparing highly monodisperse metallic and bimetallic monolayer-protected clusters (MPCs) without the need for subsequent purification. Third, it demonstrated that multiple, fairly complex operations, including formation of covalent bonds, electron-transfer, molecular transport, heterogeneous self-assembly, and nanoparticle transport could all be executed within the interior of a 4.5 nm dendrimer. These points were demonstrated by templating the formation of 1.7 nm Pd nanoparticles within PAMAM dendrimers and then extracting the Pd

into a toluene phase while leaving the dendrimer in the aqueous phase. The general procedure is shown in Figure 1.14.

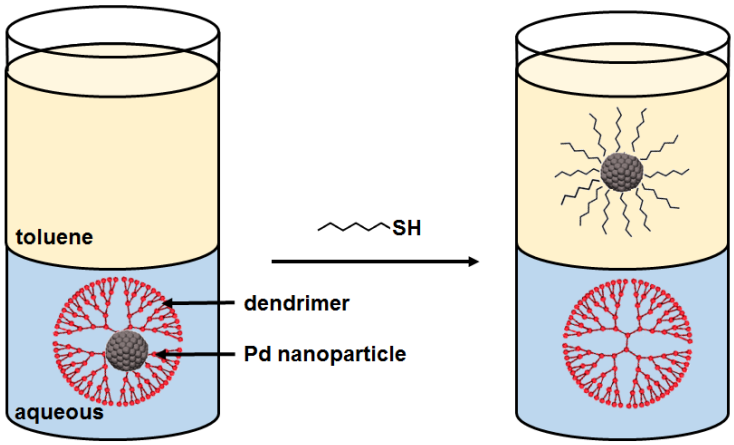

Figure 1.14 General procedure for extraction of metal nanoparticle from dendrimer template in an aqueous phase to an organic phase to produce MPCs (modified from reference 82).

In further work Garcia-Martinez and Crooks (2004) performed the extraction of gold nanoparticles having narrow size distributions from dendrimer templates.[83] The extracted nanoparticles had diameters of less than 2.2 nm and were extracted from within the interior of PAMAM dendrimers using n-alkanethiol. Extraction was found to proceed quickly regardless of the size of the nanoparticle, the dendrimer generation or the peripheral functionalization of the dendrimer. The extraction rate was fastest for the lowest generation dendrimers, the smallest nanoparticles, and the shortest chain-length n-alkanethiols. Other important results of the reported study were that, firstly, within the accuracy of absorbance spectroscopy, the extraction yield is quantitative. Secondly, NMR and FT-IR spectroscopy indicated that after extraction the dendrimer remains in the aqueous phase and could be used to template additional metal particles. Thirdly, the size and optical characteristics of the extracted nanoparticles were the same as the precursor dendrimer-encapsulated nanoparticles (DENs). Fourthly, a 100-fold excess of n-alkanethiol molecules is required to prevent aggregation of DENs during extraction.

In a modification of the nanoparticle synthesis method from a dendrimer template, Niu and Crooks (2003) demonstrated the preparation of dendrimer encapsulated nanoparticles using organic solvents.[68] Normally, and as shown above, dendrimer encapsulated nanoparticles are prepared in water using dendrimers that have hydrophilic amine or hydroxyl end groups. However, in the method described by Niu and Crooks, the PAMAM dendrimers were

modified according to a method described by Esumi *et al*[84] so that the periphery was ester-terminated, thereby rendering the PAMAM dendrimers soluble in organic solvents. The significance of synthesizing dendrimer encapsulated nanoparticles using organic solvents was that differences in metal-ion solubility between the solvent and the dendrimer interior could be used to drive metal ion encapsulation, instead of depending on the number of coordination sites available in a particular dendrimer generation. Subsequent chemical reduction of the dendrimer/metal ion composite then resulted in formation of dendrimer encapsulated nanoparticles. This approach contrasted with the previously reported method for preparing dendrimer encapsulated nanoparticles which relied on specific interactions between metal ions and intra-dendrimer functional groups for metal-ion encapsulation. Because reliance on specific metal/ligand interactions were relaxed, this approach provided a means for increasing both the type and size of nanoparticles that could be encapsulated within dendrimers *i.e.* nanoparticle size was not dependent on dendrimer generation and the number of corresponding functional groups.

Considering gold specifically, Knecht *et al* (2005) then went on to demonstrate the synthesis, characterization and extraction dendrimer encapsulated nanoparticles composed of 31 and 55 atoms using organic solvents.[85] Previous attempts to synthesize Au nanoparticles in organic solvents using dendrimers had resulted in the formation of materials that were most likely stabilized by multiple dendrimers.[86,87] Such materials were termed "dendrimer-stabilized nanoparticles", because they consisted of a relatively large metal core (with a diameter often nearly as large as or even larger than the diameter of the stabilizing dendrimer) surrounded by multiple dendrimers. In the synthesis and extraction of the Au_{31} and Au_{55} nanoparticles demonstrated by Knecht *et al*, an amine-terminated, fourth-generation PAMAM dendrimer modified on its periphery with dodecyl groups was employed for the synthesis (Figure 1.15). The use of an analogous fifth-generation PPI dendrimer, also modified at the periphery (as also shown in Figure 1.15) to render it soluble in organic solvents, was however not successful with large Au nanoparticles forming. For the modified PAMAM dendrimer, a single-phase synthesis in toluene was used to prepare Au dendrimer encapsulated nanoparticles having diameters of < 1.3 nm and standard deviations ranging from 0.3 to 0.4 nm. The particles were characterized before and after extraction using UV-vis spectroscopy, transmission electron microscopy (TEM), and near-IR fluorescence spectroscopy. The results indicated that the extraction process lead to the formation of nearly monodisperse Au_{31} and

Au_{55} MPC's regardless of the nature of the thiolate extractant used. The MPC's were found to be stable in aqueous solutions and are not fluorescent.

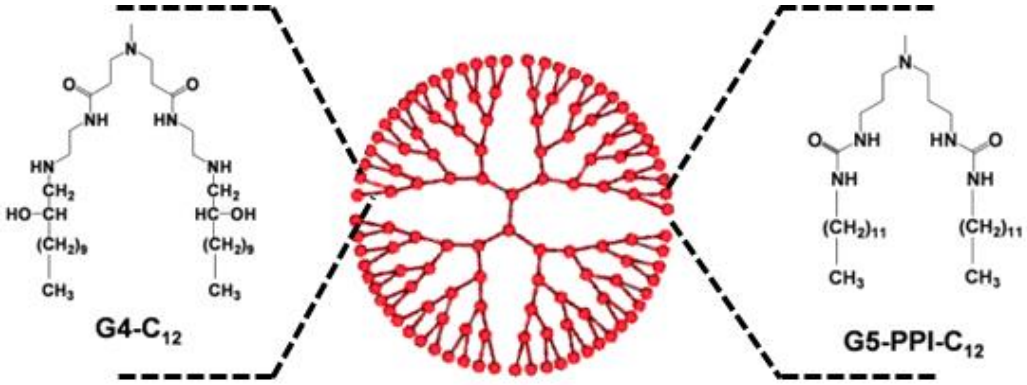

Figure 1.15 Modification of the peripheries of fourth-generation PAMAM and fifth generation PPI dodecyl groups to render it soluble in organic solvents (modified from reference 85).

1.3 Summary and Scope of Thesis

From the above it was seen that although it is generally inert as a bulk metal, gold (I) and (III) complexes are active and have found applications in homogeneous catalysis. Furthermore, gold nanoparticles have found applications in a far wider range of heterogeneous catalysis applications. What makes gold nanoparticles so versatile is their ability to exhibit properties characteristic of a number of oxidation states depending on their size (as a result of the cluster configuration and number of surface atoms available, different size nanoparticles exhibit varying electronic properties) which correspond to certain oxidation states. Thus, an important aspect of determining the application of gold nanoparticles is the tailoring of their size during synthesis.

For the purposes of this thesis, we will focus on the synthesis of gold nanoparticles and specifically on a method to produce uniform nanoparticles (in shape and size) which are ideally $\leq$ 5nm; the size below which a marked increase in catalytic activity is observed. As such, the catalytic performance of the synthesized nanoparticles would subsequently be evaluated.

Various methods of nanoparticle synthesis are highlighted, with subtle variations to each method resulting in ever smaller and monodisperse nanoparticles being synthesised. In

addition, each method demonstrates an aspect which adds to an ease of synthesis and also ever decreasing gold nanoparticle size.

It was seen how good control for various ranges of nanoparticle sizes were obtained for the Turkevich method, but that at best the 5 nm threshold was just about achieved. However, when this method was modified to enable the use of a microfluidic reactor set-up, gold nanoparticles < 2 nm in size were produced.

The Brust-Schiffrin method showed an improvement in reproducibly being able to synthesise gold nanoparticles in the range of 1.5- to 5.2 nm, although it required a few reaction steps with a subsequent reaction mechanism which appeared somewhat complex. In contrast, the Martin method, although also having a few steps in the synthesis procedure, had through iterative alterations to the method, been modified to be completed in under 2 minutes and still produce gold nanoparticles of < 2 nm in size.

With the dendrimer template method, versatility was seen to be the major advantage. Firstly, a range of transition metal nanoparticles could be synthesised following the same synthetic principals. Secondly, nanoparticle size could be controlled by varying the generation of dendrimer and functional groups. Furthermore the manner of uptake of the metal into the interior of the dendrimer could be modified by changing the periphery of it to render it soluble in different solvents. Where the periphery is modified using an alkyl chain, a dendrimer micelle is formed and renders the usually water-soluble PAMAM or PPI dendrimers soluble in organic solvents. This then allows for a choice of metal/dendrimer interactions which are either driven by metal ion/dendrimer co-ordination (in the case of unmodified PAMAM or PPI dendrimers) or by solubility differences in the case where the dendrimer is modified with an alkyl chain to form a dendrimer micelle. When encapsulation is driven by solubility, nanoparticle size is no longer dependent on coordinating to a certain number of functional groups within the dendrimer or at its periphery, and hence nanoparticle size is not dependent on dendrimer generation. Instead nanoparticle size can be controlled by varying the metal:dendrimer ratio and in effect, a dendrimer of one specific generation can be used to produce nanoparticles of various sizes. Furthermore, it has also been demonstrated that nanoparticles could be extracted from the dendrimer interior to produce monolayer protected clusters (MPC's). Once extracted, the dendrimer template could be re-used to co-

ordinate more metal. With these factors in mind, the aims and objectives of the thesis are set out below.

The first aim of the study was to attempt the synthesis of Au nanoparticles using a dendrimer micelle which is soluble in an organic phase and thereafter extracting the nanoparticles from the interior of the dendrimer micelle, out of the organic phase and into an aqueous phase. In the aqueous phase, the extracted gold nanoparticles will be stabilized by a water-soluble ligand to prevent agglomeration. Encapsulation of the nanoparticles would ideally be solubility driven. With this being the case, the need to utilize various dendrimer generations in order to achieve varying nanoparticle sizes would be eliminated. Instead it was hoped that nanoparticle size could be tailored by varying the Au:dendrimer ratio. In this manner, it was hoped that a certain number of Au atoms would be taken up within the dendrimer micelle and form atom clusters of that specific number. Consequently, varying the atom cluster number would result in nanoparticles of varying sizes.

The extraction of the nanoparticles from the dendrimer micelle in the organic phase into an aqueous phase where it is stabilized by a water-soluble ligand, would have a two-fold purpose. Firstly, since the nanoparticles would not be retained within the dendrimer micelle by coordination but due to solubility, the potential exists for nanoparticle agglomeration to occur inside the dendrimer micelle. By extracting them and capping it with a ligand, it was hoped that nanoparticle agglomeration would be retarded or, ideally eliminated. Secondly, we would have a water-soluble catalyst system which could potentially be used in a biphasic manner. This would then have the further potential of the catalyst being easily separated from any organic substrate and re-used.

Whereas a similar nanoparticle synthesis method was described in the review of the literature, we attempted this with a third-generation PPI dendrimer which had been modified at the periphery to render it soluble in an organic medium. This contrasts to the work by Knecht *et al* in which a modified fourth-generation PAMAM dendrimer was used successfully to synthesise Au_{31} and Au_{55} nanoparticles of less than 1.3 nm in size.

The reason for selecting PPI is that, as mentioned, the interior of PPI is less hydrophilic than that of PAMAM. With this being the case, it was hoped that the nanoparticles encapsulated

would thus preferentially and more readily leave the interior of the PPI dendrimer micelle and migrate to the aqueous phase.

Furthermore, a generation three PPI dendrimer would be utilized instead of the generation four used in the literature. Utilizing a lower generation dendrimer has the potential in lowering synthesis costs since the cost of dendrimers increases exponentially with increased generation. In addition, as previously mentioned, by utilizing a dendrimer micelle, this single low generation could be used to potentially produce nanoparticles of varying sizes without varying dendrimer generation. Therefore, in this manner, synthesis costs are also restricted.

Although it was previously shown that for PAMAM, retention properties are apparent from generation 4, it appears that a generation 3 PPI dendrimer might have sufficient de Gennes dense packing to allow for retention. Furthermore, the tethers which will be added to render it soluble in an organic medium will further aid retention within the dendrimer interior. A potential challenge might however be that the generation 3 PPI dendrimer will most likely have a more flexible, open structure thus limiting nanoparticle retention. However, this may be beneficial for more ready extraction of the nanoparticles from the interior into the aqueous phase.

With the above scope in mind, the following aims and objectives were set:

- Modifying the periphery of a G3 PPI dendrimer to produce a G3 PPI dendrimer micelle which is soluble in an organic medium.
- Synthesize gold nanoparticles of varying size which are encapsulated within the dendrimer micelle. The size would be controlled by varying the Au:dendrimer micelle ratio.
- Extract the encapsulated nanoparticles from the dendrimer found in the organic medium and into an aqueous phase where they are then stabilized by a water-soluble ligand.
- Evaluate the catalytic performance of the water-soluble gold nanoparticles in the biphasic oxidation of styrene.

Consequently, Chapter 2 outlines our initial attempts at synthesizing hydrophilic gold nanoparticles of specific sizes, by simply varying the metal to dendrimer micelle ratio.

Results showed that certain ratios resulted in atom clusters which were unstable and accelerated agglomeration. The results obtained enabled the subsequent proposal of a mechanism whereby the gold nanoparticles are transported from an organic to an aqueous medium and the process leading to the eventual attaining of the desired nanoparticle sizes. An observation made following our initial synthesis procedure was that there appeared to be an inconsistency in the sizes of nanoparticles obtained using the same synthesis procedure. This was thought to be due to differences in the immediacy of obtaining transmission electron microscopy (TEM) analysis for determining size, and that the sizes determined varied due to the extent of nanoparticle agglomeration during the various time lengths before analysis. Chapter 3 therefore delves into the evaluation of dynamic light scattering (DLS) as a more immediate method for nanoparticle size determination. In addition to the evaluation results of DLS as a suitable nanoparticle size determination tool, a greater understanding of the nature of the nanoparticle environment in the aqueous phase once extracted was obtained.

The insight gained in Chapter 3 subsequently directed our investigations into refining the nanoparticle synthesis procedure in terms of limiting agglomeration over time in order to obtain consistent particle sizes irrespective of the length of time between synthesis and obtaining size information. This is described in Chapter 4.

In Chapter 5 the catalytic performance in the attempted biphasic oxidation of styrene of the synthesized nanoparticles are evaluated and reported on. The results obtained were extremely unexpected and interesting in terms of the effect of nanoparticle size on styrene conversion and the selectivity obtained. Based on further investigations into the unexpected results, reaction mechanisms leading to the observations made are proposed.

1.4 References

(1) Thakor, S.; Jokerst, J.; Zavaleta, C.; Massoud, T. F.; Gambhir, S. S. *Nano Lett.* **2011**, *11*, 4029.

(2) Hammer, B.; Nørskov, J. K. *Nature* **1995**, *376* (6537), 238.

(3) Cave, R. J.; Newton, M. D. *J. Chem. Phys.* **1997**, *106* (22), 9213.

(4) Hammer, B.; Scheffler, M. *Phys. Rev. Lett.* **1995**, *74* (17), 3487.

(5) Hammer, B.; Norskov, J. K. *Adv. Catal.* **2000**, *45*, 71.

(6) Joost, M.; Amgoune, A.; Bourissou, D. *Angew. Chemie - Int. Ed.* **2015**, *54* (50),

15022.

(7) Hashmi, A. S. K.; Hutchings, G. J. *Angew. Chemie - Int. Ed.* **2006**, *45* (47), 7896.

(8) Bond, G. C. *Gold Bull.* **1972**, *5* (1), 11.

(9) Teles, J. H.; Brode, S.; Chabanas, M. *Angew. Chemie - Int. Ed.* **1998**, *37* (10), 1415.

(10) Hashmi, A. S. K. *Gold Bull.* **2004**, *37*, 51.

(11) Patil, N. T. *Curr. Sci.* **2013**, *104* (12), 1671.

(12) Dorel, R.; Echavarren, A. M. *Chem. Rev.* **2015**, *115* (17), 9028.

(13) Patil, N. T. *ChemCatChem* **2011**, *3* (7), 1121.

(14) Alivisatos, P. *Science* **1996**, *271* (5251), 933.

(15) Kiely, C. J. *Col. Surf. A Physic. Eng. Asp.* **2002**, *202*, 175.

(16) Quinn, B. M.; Liljeroth, P.; Ruiz, V.; Laaksonen, T.; Kontturi, K. *J. Am. Chem. Soc.* **2003**, *125*, 6644.

(17) Schmid, G.; West, H.; Malm, J.-O.; Bovin, J.-O.; Grenthe, C. *Chem. - A Eur. J.* **1996**, *2* (9), 1099.

(18) Haruta, M. *Gold Bull.* **2004**, *37*, 27.

(19) Taketoshi, A.; Haruta, M. *Chem. Lett.* **2014**, *43*, 380.

(20) Thompson, D. T. *Nano Today* **2007**, *2* (4), 40.

(21) Haruta, M.; Daté, M. *Appl. Catal. A Gen.* **2001**, *222*, 427.

(22) Faraday, M. *Philos. Trans.* **1857**, *147*, 145.

(23) Nguyen, D. T.; Kim, D. J.; Kim, K. S. *Micron* **2011**, *42* (3), 207.

(24) Zhao, P.; Li, N.; Astruc, D. *Coord. Chem. Rev.* **2013**, *257*, 638.

(25) LaMer, V. K.; Dinegar, R. H. *J. Am. Chem. Soc.* **1950**, *72* (11), 4847.

(26) LaMer, V. K. *Ind. Eng. Chem.* **1952**, *44* (6), 1270.

(27) Berhault, G.; Bausach, M.; Bisson, L.; Becerra, L.; Thomazeau, C.; Uzio, D. *J. Phys. Chem. C* **2007**, *111* (16), 5915.

(28) Sajanlal, P. R.; Sreeprasad, T. S.; Samal, A. K.; Pradeep, T. *Nano Rev.* **2011**, *2*, 5883.

(29) Khanna, S. N.; Jena, P. *Phys. Rev. Lett.* **1992**, *69* (11), 1664.

(30) Qian, H.; Zhu, Y.; Jin, R. *Proc. Natl. Acad. Sci. U. S. A.* **2012**, *109* (3), 696.

(31) Gruber, M.; Heimel, G.; Romaner, L.; Brédas, J. L.; Zojer, E. *Phys. Rev. B - Condens. Matter Mater. Phys.* **2008**, *77* (16), 165411.

(32) Mackay, A. L. *Acta Crystallogrphica* **1962**, *15*, 916.

(33) Shafai, G.; Hong, S.; Bertino, M.; Rahman, T. S. *J. Phys. Chem. C* **2009**, *113* (28), 12072.

(34) Lu, X.; Rycenga, M.; Skrabalak, S. E.; Wiley, B.; Xia, Y. *Annu. Rev. Phys. Chem.*

2009, *60* (1), 167.

(35) Marks, L. D. *Philos. Mag. A* **1984**, *49* (1), 81.

(36) Burrows, N. D.; Vartanian, A. M.; Abadeer, N. S.; Grzincic, E. M.; Jacob, L. M.; Lin, W.; Li, J.; Dennison, J. M.; Hinman, J. G.; Murphy, C. J. *J. Phys. Chem. Lett.* **2016**, *7* (4), 632.

(37) Thanh, N. T. K.; Maclean, N.; Mahiddine, S. *Chem. Rev.* **2014**, *114*, 7610.

(38) Kwon, S. G.; Hyeon, T. *Small* **2011**, *7* (19), 2685.

(39) Ostwald, W. *Z. Phys. Chem* **1900**, *34*, 495.

(40) Watzky, M. a; Watzky, M. a; Finke, R. G.; Finke, R. G. *Chem. Mater.* **1997**, *9* (12), 3083.

(41) Peng, X. G.; Manna, L.; Yang, W. D.; Wickham, J.; Scher, E.; Kadavanich, A.; Alivisatos, A. P. *Nature* **2000**, *404* (6773), 59.

(42) Peng, Z.; Peng, X. *J. Am. Chem. Soc.* **2001**, *123* (7), 1389.

(43) Turkevich, J.; Stevenson, P. C.; Hillier, J. *Discuss. Faraday Soc.* **1951**, *11* (c), 55.

(44) Frens, G. *Nat. Phys. Sci.* **1973**, *241*, 20.

(45) Kumar, S.; Gandhi, K. S.; Kumar, R. *Ind. Eng. Chem. (Analytical Ed.* **2007**, *46*, 3128.

(46) Kimling, J.; Maier, M.; Okenve, B.; Kotaidis, V.; Ballot, H.; Plech, A. *J. Phys. Chem. B* **2006**, *110*, 15700.

(47) Uppal, M.; Kafizas, A.; Lim, T.; Parkin, I. *New J. Chem.* **2010**, *34* (7), 1401.

(48) Uppal, M.; Kafizas, A.; Ewing, M. B.; Parkin, I. P. *New J. Chem.* **2010**, *34* (12), 2906.

(49) Brown, K. R.; Fox, A. P.; Natan, M. J. *J. Am. Chem. Soc.* **1996**, *118* (5), 1996.

(50) Sivaraman, S. K.; Kumar, S.; Santhanam, V. *J. Colloid Interface Sci.* **2011**, *361* (2), 543.

(51) Ftouni, J.; Penhoat, M.; Addad, A.; Payen, E.; Rolando, C.; Girardon, J.-S. *Nanoscale* **2012**, *4* (15), 4450.

(52) Brust, M.; Walker, M.; Bethell, D.; Schiffrin, D. J.; Whyman, R. *J. Chem. Soc. Chem. Commun.* **1994**, *1994* (7), 801.

(53) Daniel, M.-C.; Astruc, D. *Chem. Rev.* **2004**, *104* (1), 293.

(54) Brust, M.; Fink, J.; Bethell, D.; Schiffrin, D. J.; Kiely, C. *J. Chem. Soc. Chem. Commun.* **1995**, *1995* (16), 1655.

(55) Häkkinen, H. *Nat. Chem.* **2012**, *4* (6), 443.

(56) Yu, C.; Zhu, L.; Zhang, R.; Wang, X.; Guo, C.; Sun, P.; Xue, G. *J. Phys. Chem. C* **2014**, *118*, 10434.

(57) Uehara, A.; Booth, S. G.; Chang, S. Y.; Schroeder, S. L. M.; Imai, T.; Hashimoto, T.;

Mosselmans, J. F. W.; Dryfe, R. A. W. *J. Am. Chem. Soc.* **2015**, *137*, 15135.

(58) Martin, M. N.; Basham, J. I.; Chando, P.; Eah, S. *Langmuir* **2010**, *26* (10), 7410.

(59) Martin, M. N.; Li, D.; Dass, A.; Eah, S.-K. *Nanoscale* **2012**, *4*, 4091.

(60) Stanwix, H. *Nanomedicine* **2012**, *7* (7), 953.

(61) Tomalia, D. A. *New J. Chem.* **2012**, *36* (2), 264.

(62) Tomalia, D. A. *Prog. Polym. Sci.* **2005**, *30*, 294.

(63) Menjoge, A. R.; Kannan, R. M.; Tomalia, D. A. *Drug Discov. Today* **2010**, *15* (5-6), 171.

(64) Cheng, Y.; Zhao, L.; Xu, T. *Chem. Soc. Rev.* **2011**, *40*, 2673.

(65) Hu, J.; Xu, T.; Cheng, Y. *Chem. Rev.* **2012**, *112*, 3856.

(66) Wang, X.; Guerrand, L.; Wu, B.; Li, X.; Boldon, L.; Chen, W. R.; Liu, L. *Polymers (Basel).* **2012**, *4* (1), 600.

(67) Zhao, M.; Sun, L.; Crooks, R. M. *J. Am. Chem. Soc.* **1998**, *120* (19), 4877.

(68) Niu, Y. H.; Crooks, R. M. *Chem. Mater.* **2003**, *15* (18), 3463.

(69) Crooks, R. M.; Zhao, M.; Sun, L. I.; Chechik, V.; Yeung, L. E. E. K. *Acc. Chem. Res.* **2001**, *34* (3), 181.

(70) Helms, B.; Meijer, E. W. *Science (80-.).* **2006**, *313*, 929.

(71) Tomalia, D. A.; Frechect, J. M. J. *Dendrimers and Other Dendritic Polymers*; Scheirs, J., Ed.; John Wiley & Sons, Ltd: Chichester, UK, 2001; Vol. 1.

(72) Zhao, B. M.; Crooks, R. M. *Adv. Mater.* **1999**, *1* (11), 217.

(73) Yeung, L. K.; Crooks, R. M. *Nano Lett.* **2001**, *1* (1), 14.

(74) Floriano, P. N.; Noble, C. O.; Schoonmaker, J. M.; Poliakoff, E. D.; Mccarley, R. L. *J. Am. Chem. Soc.* **2001**, *123*, 10545.

(75) Astruc, D.; Lemo, J.; Heuze, K. *Inorganica Chim. Acta* **2006**, *359*, 4909.

(76) Hayakawa, K.; Yoshimura, T.; Esumi, K. *Langmuir* **2003**, No. 25, 5517.

(77) Vohs, J. K.; Fahlman, B. D. *New J. Chem.* **2007**, *31*, 1041.

(78) Li, T.; Shao, N.; Liu, Y.; Hu, J.; Wang, Y.; Zhang, L.; Wang, H.; Chen, D.; Cheng, Y. *J. Phys. Chem. B* **2014**, *118* (11), 3074.

(79) Zhao, M.; Liu, Y.; Crooks, R. M.; Bergbreiter, D. E. *J. Am. Chem. Soc.* **1999**, *121* (5), 923.

(80) Zhao, B. M.; Crooks, R. M. *Acc. Chem. Res.* **1999**, *1* (3), 1997.

(81) Niu, Y.; Crooks, R. M. *Comptes Rendus Chim.* **2003**, *6*, 1049.

(82) Garcia-Martinez, J. C.; Scott, R. W. J.; Crooks, R. M. *J. Am. Chem. Soc.* **2003**, *125* (37), 11190.

(83) Garcia-Martinez, J. C.; Crooks, R. M. *J. Am. Chem. Soc.* **2004**, *126* (49), 16170.

(84) Esumi, K.; Nakamura, R.; Suzuki, A.; Torigoe, K. *Langmuir* **2000**, *16*, 7842.

(85) Knecht, M. R.; Garcia-Martinez, J. C.; Crooks, R. M. *Langmuir* **2005**, *21* (25), 11981.

(86) Esumi, K.; Hosoya, T.; Suzuki, a; Torigoe, K. *J. Colloid Interface Sci.* **2000**, *229* (1), 303.

(87) Torigoe, K.; Suzuki, A.; Esumi, K. *J. Colloid Interface Sci.* **2001**, *241*, 346.

Chapter 2

Facile Synthesis and Characterization of PTA-stabilized Hydrophilic Gold Nanoparticles via a DEN-MPC Method

---

2.1 Introduction

In most reports, dendrimer encapsulated nanoparticles (DENs) are prepared in water, since both poly(amido amine) (PAMAM) and poly(propylene imine) (PPI) dendrimers are water soluble. There are however a few reported cases of DENs being prepared in organic solvents.[1] In these cases the terminal groups of the dendrimer had been tailored with a carbon chain of a certain length to render it soluble in organic solvents.

The synthesis of DENs in an organic medium and subsequent extraction into an aqueous medium would result in the formation of hydrophilic nanoparticles. As briefly outlined in Chapter 1, one of the advantages of hydrophilic nanoparticles is its potential use as catalyst in bi-phasic catalytic processes. With bi-phasic catalysis there would be the potential advantage of easy recovery and subsequent re-usability of the catalyst. A further positive aspect of the dendrimer template method of nanoparticle synthesis as discussed in Chapter 1, is that the dendrimer does not fully co-ordinate to the nanoparticle surface, but retain nanoparticles mostly due to steric considerations. With the more open geometry of the G3 PPI dendrimer also discussed in the introductory chapter, it was hypothesized that extraction of the nanoparticles from the organic phase into the aqueous phase would be more facile.

However, once extracted into the aqueous, the nanoparticles would have to be stabilized by a suitable ligand to prevent or mitigate agglomeration. In a search of literature to identify a suitable water-soluble ligand, phosphine ligands with polar substituents such as hydroxyl or amino functionalities; or ionic groups such as sulfonates or carboxylates emerged as potentially suitable candidates. Examples of such ligands are the sulfonated analogues of triphenylphosphine (PPh_3) triphenylphosphine monosulfonate (TPPMS), triphenylphosphine thiosulfonate (TPPTS) as well as glutathione and tiopronin.[2,3] These ligands are shown in Figure 2.1. Another ligand which was of particular interest was 1,3,5-triaza-7-phosphaadamantane (PTA). It has been proven to solubilize transition metal complexes in the aqueous phase allowing for Rh-, Ru- and Pd-PTA complexes to be utilized in aqueous phase

or bi-phasic catalysis.[3–6] Ru and Pt nanoparticles prepared in organic solvents and then transferred into water due the solubility in both media has also been demonstrated.[7]

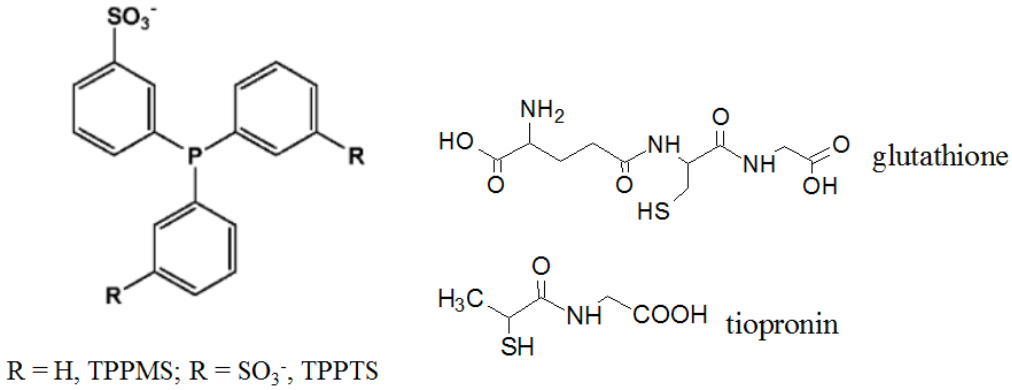

R = H, TPPMS; R = SO_3^-, TPPTS

Figure 2.1 Examples of water-soluble phosphine ligands

Au-PTA complexes have also been synthesized.[3] The structure of PTA, and subsequent steric considerations when co-ordinating to the nanoparticle surface as compared to those depicted in Figure 2.1, potentially makes PTA an attractive option as a ligand to be used in the extraction and stabilization of the Au nanoparticles to be synthesized. In Scheme 2.1 it can be seen that the relatively compact nature of PTA compared to the other ligands, could allow for easier access of substrates to the nanoparticle surface, thereby possibly enhancing catalytic activity.

In this chapter we therefore report on the facile synthesis of Au_{55} nanoparticles *via* a combined DENs-MPC method. Synthesis of dendrimer micelle encapsulated nanoparticles (DENs) consisting of Au_{55}, Au_{31} and Au_{13} cluster sizes was attempted. This was done in an organic medium after which the nanoparticles were extracted from the dendrimer micelle template into water using PTA as a stabilizing ligand which resulted in monolayer protected cluster (MPC) formation. Using this DEN-MPC method, we managed to synthesize hydrophilic Au_{55} nanoparticles with an average particle size of 1.5 nm ± 0.9, which is much simpler and more economical than previously reported methods for Au_{55} cluster formation. Based on this, as well as the results obtained when attempting synthesis of Au_{13} and Au_{31}, we were able to propose possible mechanistic pathways by which nanoparticle formation occurs using the specific DEN-MPC method described.

An important characteristic of Au nanoparticles, which allowed for the monitoring of nanoparticle formation and size evolution in both the organic and aqueous phase, is that of

Surface Plasmon Resonance (SPR). Surface plasmons are collective excitations of the electrons at the interface of the nanoparticle surface and its environment. These excitations can be detected through the optical response of, for example, UV-vis and allows for the ability to monitor growth of nanoparticles and therefore enable design of complex nanostructures which can be identified by a signature optical response.[8,9] These optical techniques can also be used as a complimentary structural characterization tool to techniques such as transmission electron microscopy.[8]

Scheme 2.1 Possible differences in ligand co-ordination of PTA to the Au nanoparticle (b) compared to other water-soluble phosphines (a).

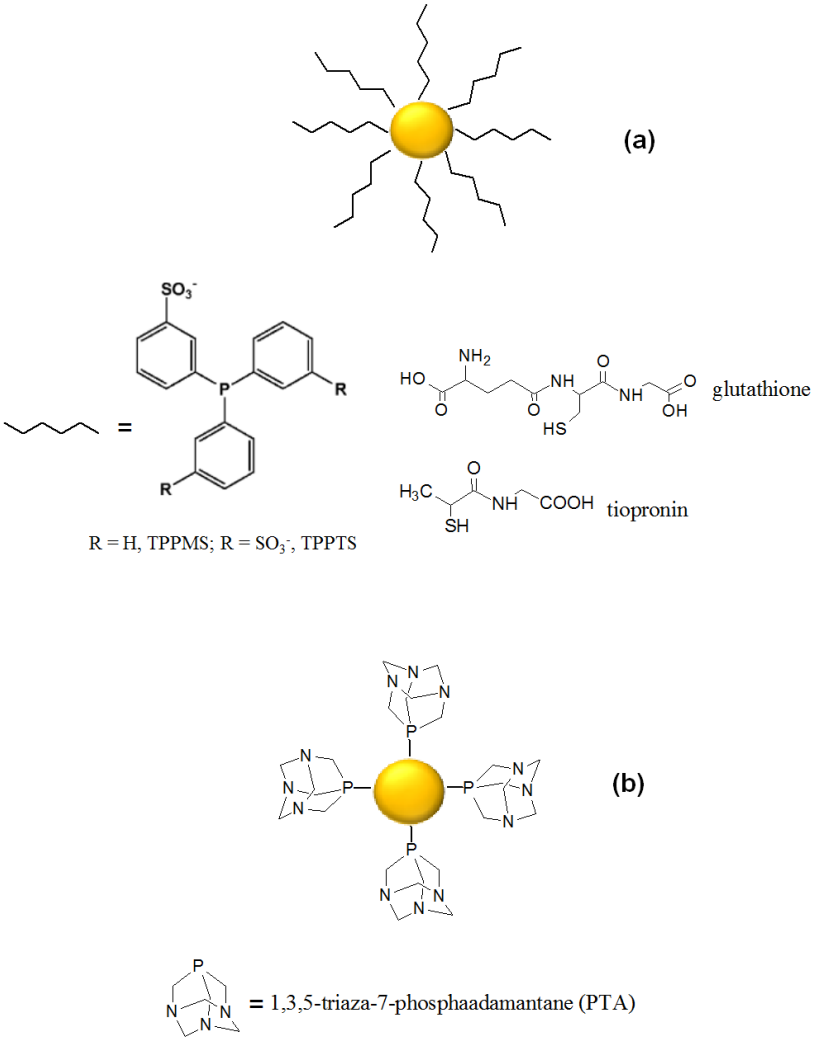

Examples of metals exhibiting plasmon resonance are Cr, Pd, Ni, Pt and Au. Each have UV-vis absorption bands due to plasmon resonance at unique wavenumbers and can therefore be identified in this way.[10] This is shown in Table 2.1. Thus by monitoring shifts in the position of the plasmon resonance bands in the region of approximately 550 nm, information can be

gathered about nanoparticle shape and size. In addition to the position of the plasmon resonance peak, the shape thereof (broad or narrow) also provides structural information about the nanoparticle.[11]

Table 2.1 Transition metals and approximate regions of plasmon resonance bands in UV-vis.[10]

Transition Metal	Approximate Wavenumber Region of Absorption due to Plasmon Resonance
Cr	300 nm
Pd	250 nm
Ni	400 nm
Pt	350 nm
Au	550 nm

2.2 Results and Discussion

2.2.1 Synthesis of Au DENs

A third generation diaminobutane poly(propylene imine) (DAB-PPI) dendrimer (which had been modified at the periphery with palmitoyl chloride in order to render it soluble in an organic solvents as depicted in Scheme 2.2), was used as a template. Previous reports of DENs prepared in an organic medium focused on fourth generation PAMAM dendrimers modified at the periphery with a C_{12} group.[12] In these dendrimer micelles (now known as a dendrimer micelle after being modified at the periphery through the use of aliphatic chains to render it soluble in organic media), the metal strongly complexes with interior tertiary amine groups.[13] In contrast, for a DAB-PPI dendrimer micelle, metal ions are attracted to the hydrophilic interior by weaker Van Der Waals forces.[14] Extraction of the weaker bound nanoparticles was thus thought to be potentially advantageous with regards to the concentration of gold being present in the aqueous phase.

A range of Au DENs were prepared in chloroform by stoichiometric addition of $HAuCl_4$ (0.1 mmol) to a vigorously stirred solution of G3 PPI dendrimer micelle. It has previously been demonstrated that DENs of a desired cluster size could be synthesised by utilising a dendrimer/$AuCl_4^-$ ratio of, or close to, the desired size.[15] The concentration of micelle was therefore varied according to which of either Au_{55}, Au_{31} or Au_{13} atomic cluster size were being aimed for (0.009, 0.017 and 0.045 µM respectively). Reduction with an excess of $NaBH_4$ (0.26 mmol) (in order to ensure complete reduction) resulted in a deep purple solution which is indicative of the presence of Au nanoparticles.[16–18]

The size, shape and concentration of the extracted Au nanoparticles were monitored at intervals of 2, 4, 8, 16 and 24 hours of extraction using UV-vis spectroscopy, transmission electron microscopy (TEM) and inductively coupled plasma spectroscopy (ICP). Nanoparticle size information using TEM was obtained within 24 h of sampling. It therefore provided as close as possible to an instantaneous result in terms of nanoparticle size. This was done in order to monitor the evolution of nanoparticle characteristics with time. The results indicate that the described synthesis and extraction process produces nearly monodisperse nanoparticles in the attempted synthesis of Au_{55} and Au_{13} MPCs with attempted synthesis of Au_{31} nanoparticles exhibiting higher polydispersity. The Au_{55} nanoparticles were also the smallest (1.5 nm ± 0.9) followed by Au_{13} (3.3 nm ± 1.0), with that of Au_{31} being much larger (9.4 nm ± 4.7) after 24 h of extraction.

Figure 2.2 compares the UV-vis spectra of each of the steps from micelle dissolution to reduction of Au. It can be seen that upon addition of the Au salt to the micelle solution, the weak intensity absorption band of the micelle in solution (at approximately 290 nm) disappears with the emergence of a strong peak in the region of 330 nm which is characteristic of the ligand-to-metal charge-transfer (LMCT) band of $AuCl_4^-$.[19,20] The absence of an absorption band at approximately 280 nm (which would indicate complexing between the dendrimer micelle and $AuCl_4^-$) with only the LMCT band present indicates the solvent driven encapsulation of the Au ions.[21] After reduction, a strong plasmon resonance peak in the region of 540 nm materializes. This is characteristic of the presence of Au nanoparticles greater than two nanometres in diameter.[1,22,23] The disappearance of the $AuCl_4^-$ LMCT band at around 330 nm was indicative of complete reduction occurring; stirring the solution for 30 min proving sufficient for this to occur.

Differences in the UV – Vis spectra of the reduction solutions of the aimed for Au_{55}, Au_{31} and Au_{13} atomic cluster nanoparticles are clearly visible in Figure 2.2. This is an indication of the differences in the size, shape and stability of the initial nanoparticles formed within the dendrimer framework. After reduction of the Au salt, atoms are generated which then undergo self-nucleation.[14,13] Figure 2.3 shows the differing shapes and sizes obtained for Au_{55}, Au_{31} and Au_{13} DENs. Due to their more stable core atom shell configurations the aimed for Au_{55} and Au_{13} atom clusters form seeds having distinct polyhedron and spherical shapes respectively. This is clearly depicted in Figure 2.4.

Scheme 2.2 Synthesis of dendrimer micelle

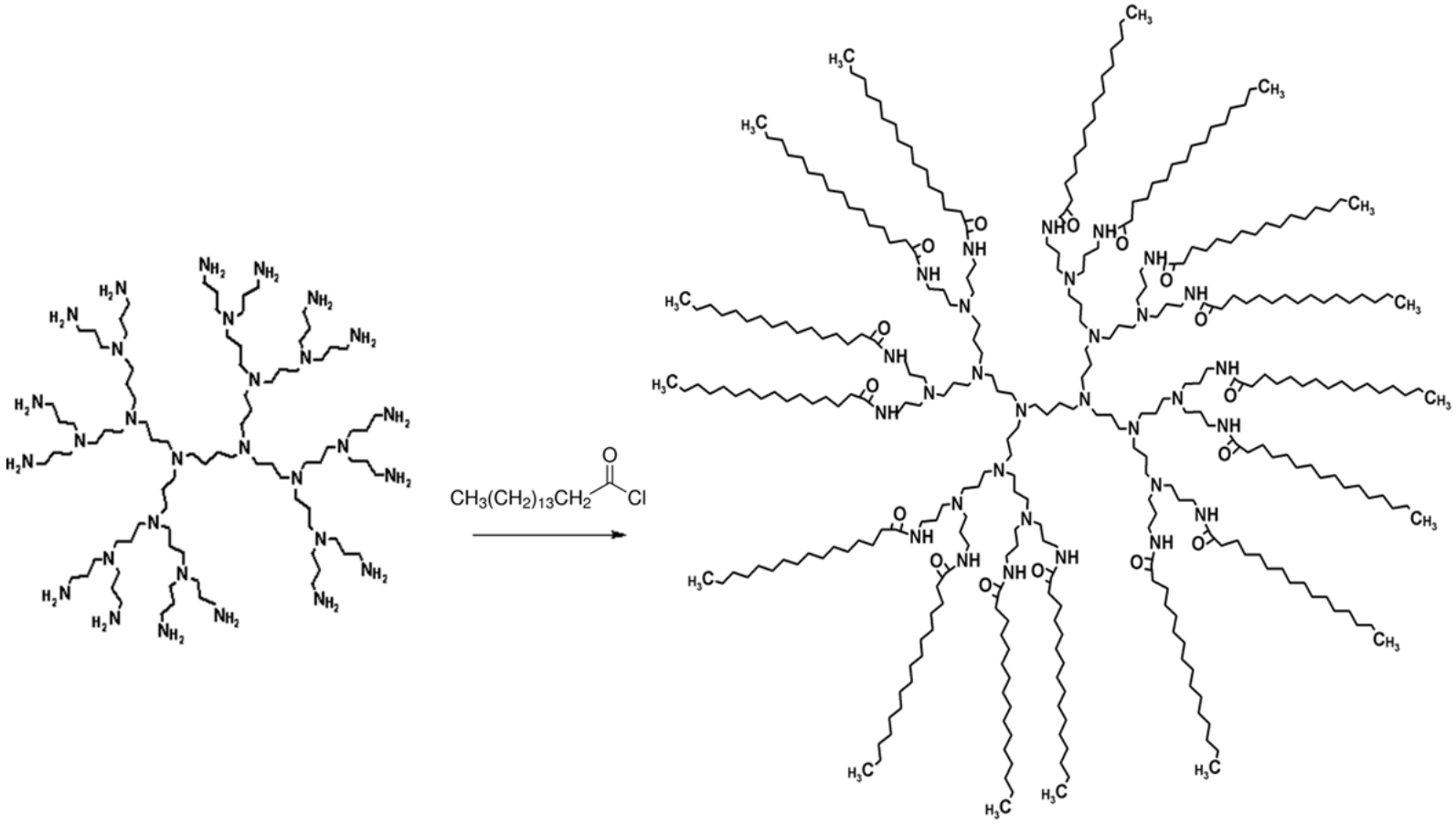

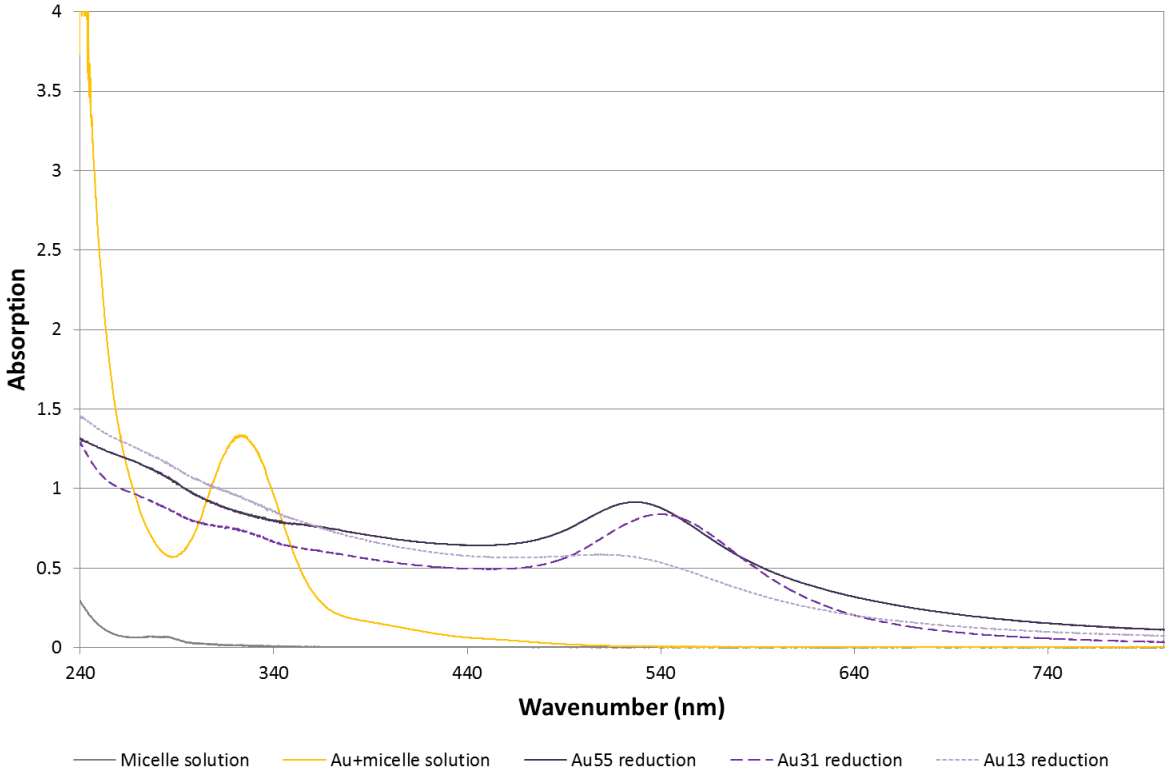

Figure 2.2 Changes in the UV – vis spectrum of micelle solution after addition of Au salt and reduction.

In contrast it can be seen in Figure 2.3 that for the desired Au_{31} atom cluster, the incomplete core shell hampers efficient seeding and results in anisotropic cluster seeds which in turn form quite a number of irregularly shaped nanoparticles having modified Wulff constructions.[24] A hypothetical depiction of this occurring is given in Scheme 2.3.

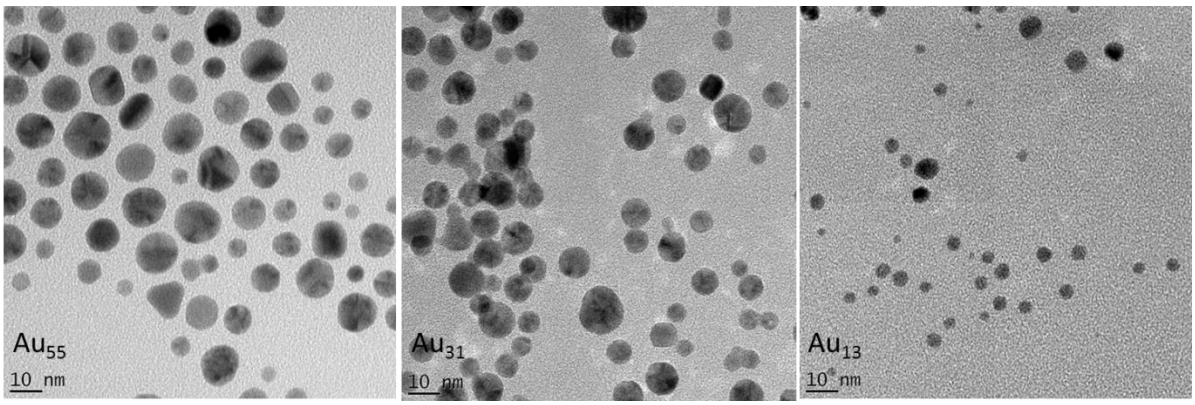

Figure 2.3 Comparison of nanoparticle shape and size for Au_{55}, Au_{31} and Au_{13} DENs

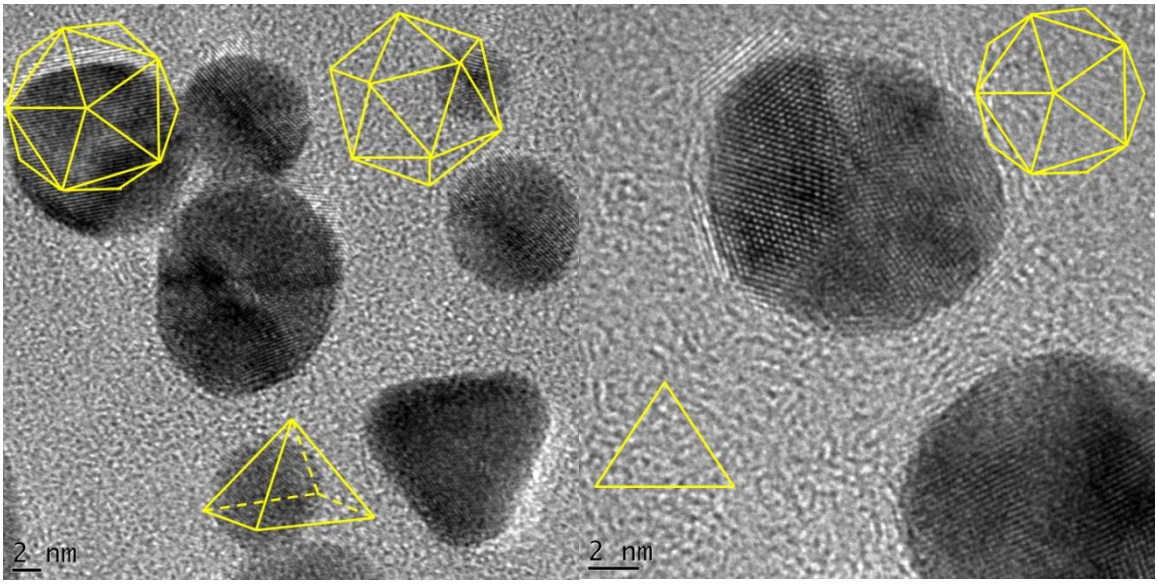

Figure 2.4 TEM images showing distinct polyhedron shaped DENs of Au_{55}

Scheme 2.3 Proposed formation of a nanoparticle having a hypothetical modified Wulff construction derived from an incomplete Au_{31} shell

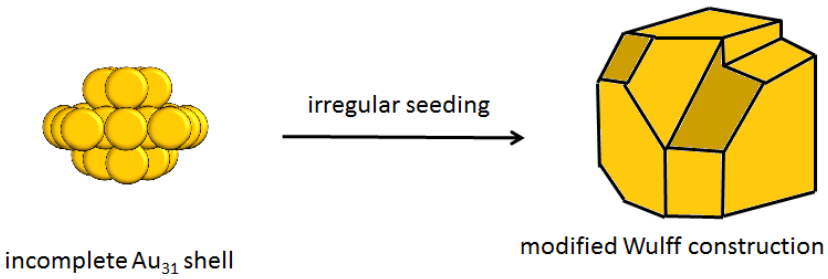

It has been reported that particle shape affects the wavelength at which UV – Vis bands absorb; the more irregular, the shape the higher the wavelength of absorption.[25] There is thus a clear correlation between the UV – Vis spectra of the reduction solutions in Figure 2.2 and the depicted particle shapes in Figure 2.3. The overwhelmingly spherical Au_{13} atom cluster nanoparticles results in the absorption band being found at the lowest wavelength. The varying but distinct shapes of the Au_{55} atom cluster nanoparticles results in a slightly higher shift of the absorption band with the irregularly shaped Au_{31} atom cluster nanoparticles resulting in this absorption band being found at the highest wavelengths.

Furthermore the difference in intensity of the absorption bands can be attributed to the sizes of the initially formed nanoparticles. TEM results obtained show that the average DENs size for Au_{13} was found to be 3.9 nm ± 1.6 compared to 6.0 nm ± 1.8 for Au_{31} and 8.9 nm ± 3.1

for Au_{55} (Figure 2.5). This corresponds to the lowest to highest absorption band intensity of Au_{13}, Au_{31} and Au_{55} respectively.

2.2.2 Extraction of Au nanoparticles from the dendrimer template

After reduction, 1,3,5-triaza-7-phosphaadamantane (PTA) was dissolved in 20 ml distilled water and added to the reduction solution. The best ratio of Au to PTA ligand was determined for the extraction of Au_{55} nanoparticles, but applied in the extraction of Au_{13} and Au_{31} as well.

The postulated mechanisms of nanoparticles from a hydrophilic dendrimer and hydrophobic dendrimer micelle differ slightly. For extraction of a nanoparticle from a hydrophilic dendrimer, it is thought that the ligand penetrates the interior of the dendrimer and attaches to the metal nanoparticle. This weakens the interactions of the dendrimer and the nanoparticle as more ligands attach and subsequently the nanoparticle exits the dendrimer framework and is extracted into the organic phase. For a hydrophobic dendrimer micelle however, it is believed that the hydrophobic extremities distort at the organic/aqueous interface where it exposes the hydrophilic interior containing the nanoparticles. The hydrophilic ligands in the aqueous phase can then easily attach to the nanoparticle surface and subsequently form a stable monolayer protected cluster (MPC) which is then transported into the aqueous layer.[1,26]

Since the mechanism of hydrophobic/hydrophilic micelle conformity at the interface has been proposed, it was therefore thought that smaller amounts of ligand might be necessary to extract the nanoparticles as compared to where larger amounts of ligand would be needed to penetrate a dendrimer and render the nanoparticle water-soluble. We therefore started at the lowest possible ratios of Au to ligand in order to determine the least amount of ligand that would be necessary for optimal extraction.

By starting at a ratio of 1:0.1 Au:PTA, and incrementally increasing the amount of PTA to 1:1, an incremental increase in the amount of Au extracted was observed. This however only occurred up to a ratio of 1:0.4 Au:PTA. The amount of Au extracted above this ratio showed a decrease in extraction of gold, in addition to higher ratios resulting in what appears to be the masking of the plasmon resonance peak by excess PTA.[2] The aforementioned trend is

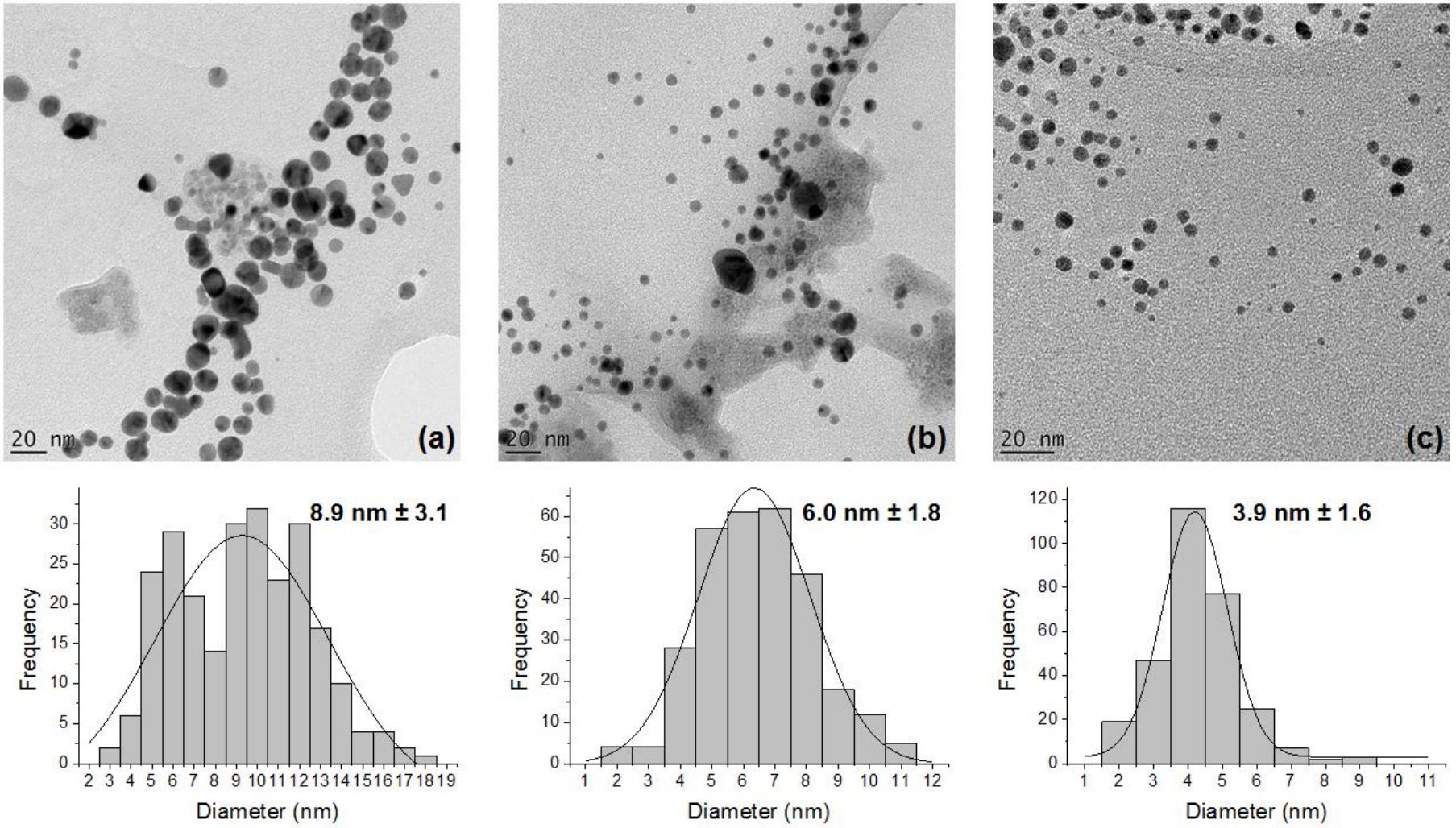

Figure 2.5 TEM images, histograms and particle size distributions of Au_{55}, Au_{31} and Au_{13} DENs (a, b and c) respectively

reflected in the UV-vis spectra for samples extracted after 24 h (Figure 2.6) and confirmed by ICP (Figure 2.7). Each nanoparticle size will be discussed below individually.

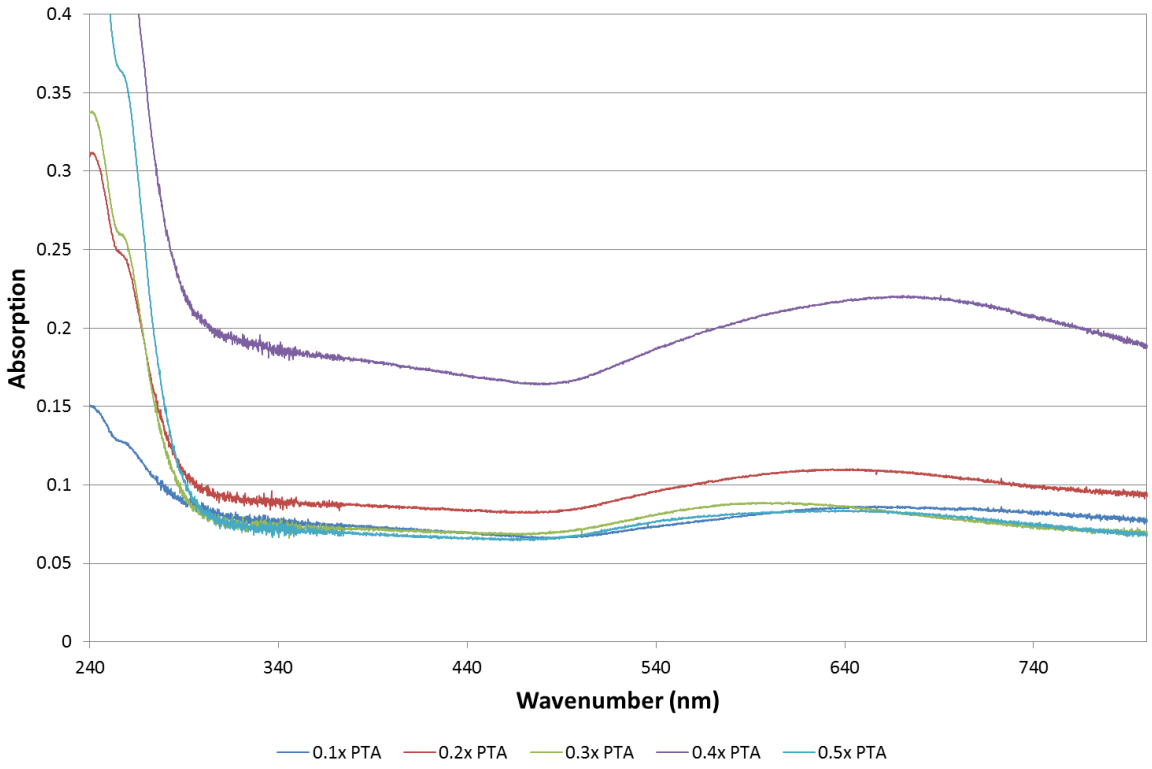

Figure 2.6 UV – vis spectra of aqueous layer after 24 h of extraction with increasing PTA concentration.

2.2.3 Extraction and Characterization of Au_{55} MPCs

Figure 2.8 shows the UV-vis spectra for samples taken at 2, 4, 8, 16 and 24 h of extraction (Au:PTA = 1:0.4). Analysed in conjunction with ICP (Figure 2.9) and TEM (Figure 2.10), an increase in the amount of gold extracted into the aqueous layer up to 16 h can be observed. After 24 h a similar concentration is maintained.

What is apparent from the TEM results is that there is a decrease in nanoparticle size with the progression of extraction time. The average particle size decreased from 10.5 nm ± 2.9 after 2 h of extraction to 1.5 nm ± 0.9 at the end of 24 h which is close to the size of 1.4 nm of a single Au_{55} cluster.[27,28]

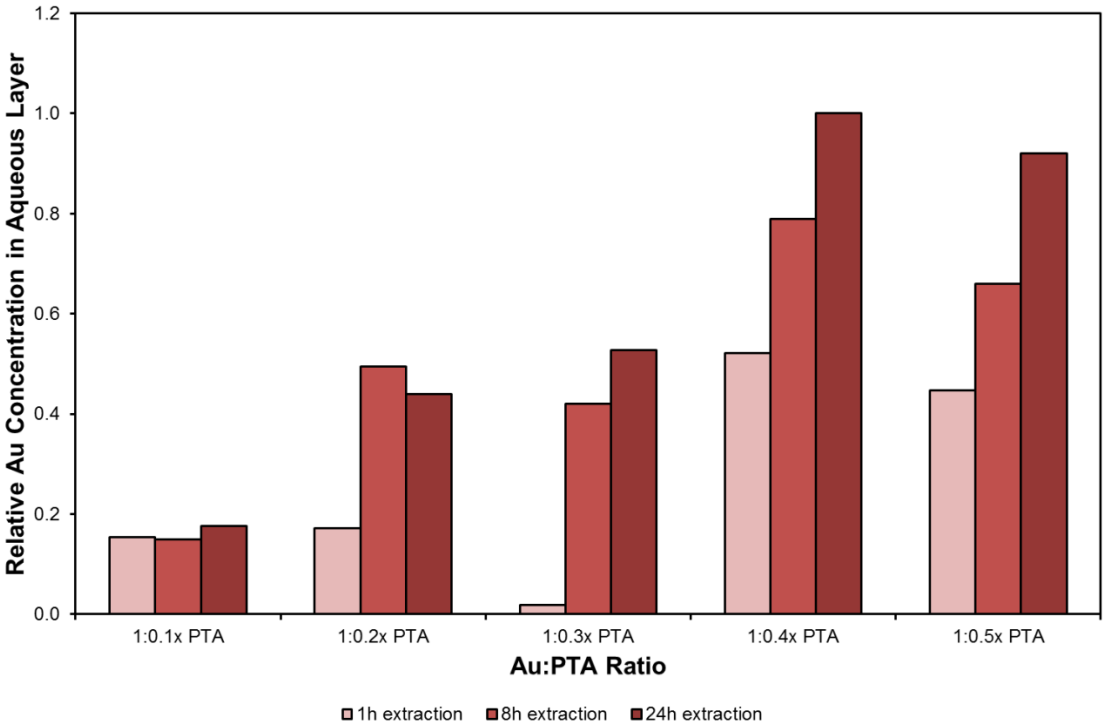

Figure 2.7 ICP showing optimum extraction of Au with varying amounts of PTA.

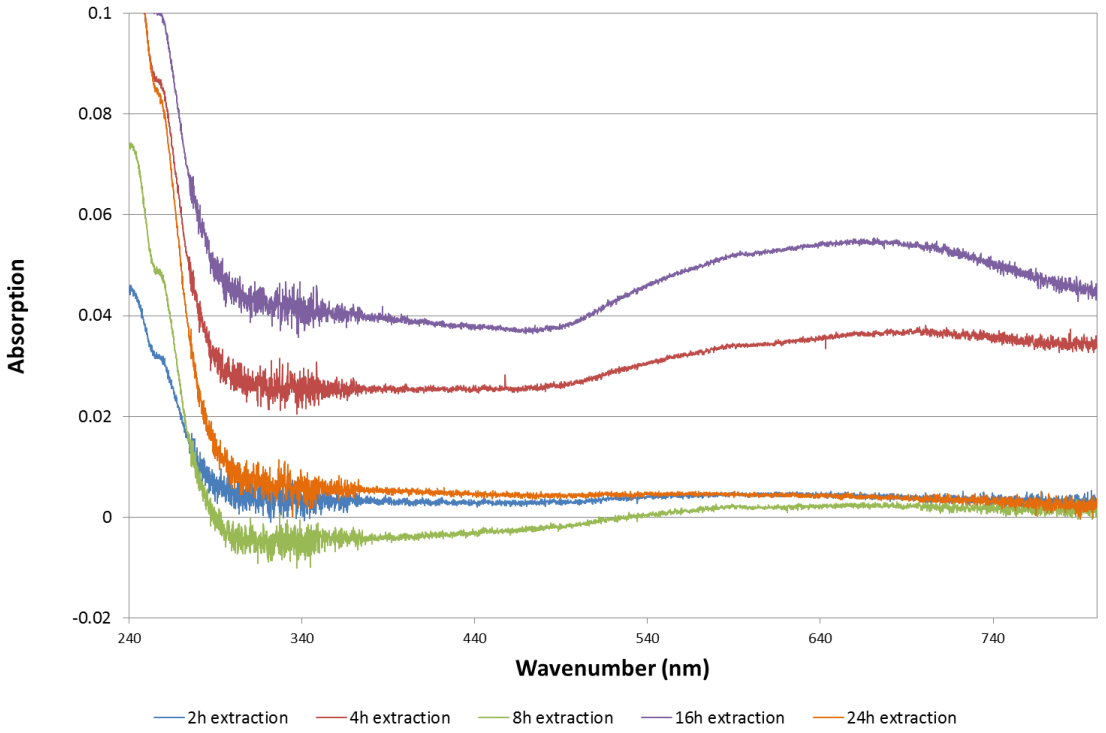

Figure 2.8 UV – vis spectra of samples taken after 2, 4, 8, 16 and 24 h extraction of Au_{55}.

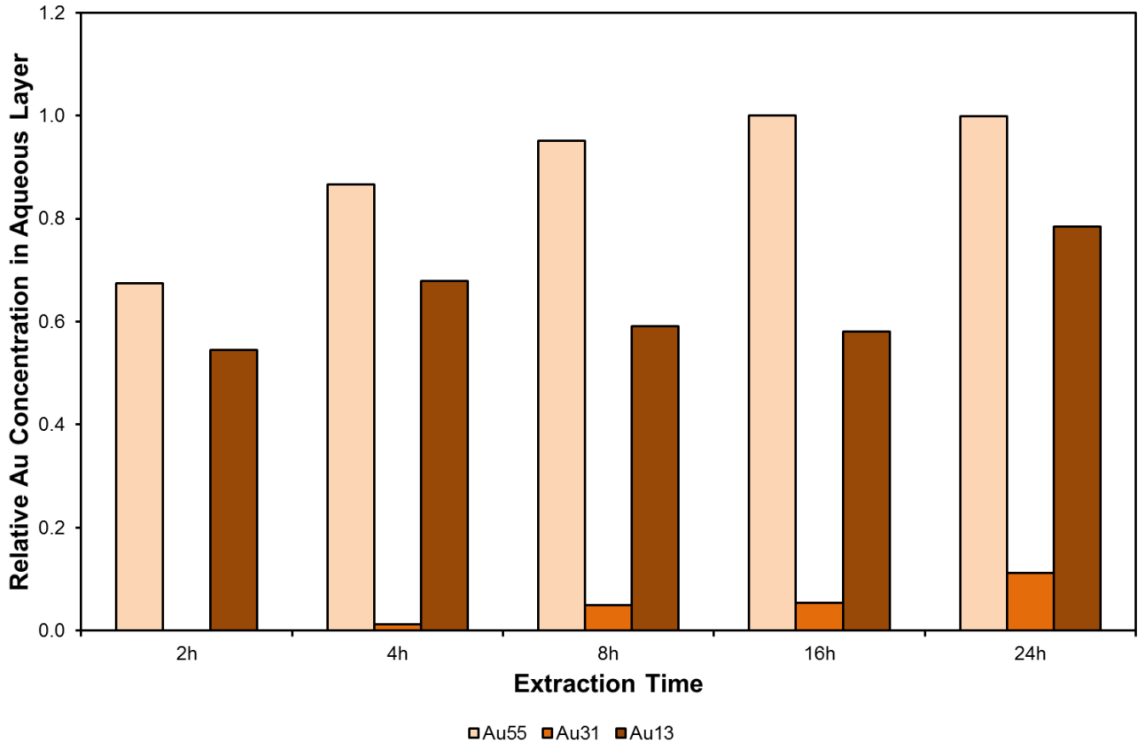

Figure 2.9 Relative Au concentrations in aqueous layer after 2, 4, 8, 16 and 24 h of extraction for Au_{55}, Au_{31} and Au_{13}.

The proposed migration of Au nanoparticles is summarised in Scheme 2.4. As previously mentioned, it has been postulated that extraction occurs when the hydrophobic extremities of the micelle distorts at the organic/aqueous interface to expose the hydrophilic interior where the Au nanoparticles had been formed. The nanoparticles are now exposed and are able to come into contact with the ligand at the interface where it attaches and renders the nanoparticle soluble in the aqueous phase

Thus, following the proposed mechanism, it can be reasoned that the initial larger particles which are formed, as observed by TEM, are as a result of the Au being exposed by the micelle and being at the organic/aqueous phase interface. Once exposed at the interface, seeded growth can more easily occur since dendrimer micelle no longer offers a degree of protection from seeds coming into proximity of each other allowing for growth. This appears to occur during the first 2 h of extraction resulting in the observed nanoparticle size of 10.5 nm ± 2.9 after this time. Singly or multiply twinned seeds have been observed to contain at least one twin defect. The strain energy caused by twin defects greatly increase as the seed grows in size. This in turn results in the free energy of the system to go up. As a consequence,

twinned seeds are only favoured thermodynamically at relatively small sizes. It therefore appears that after extraction, seed growth occurs to 10.5 nm ± 2.9 after which they become unstable and revert to forming smaller seeds.[25] The regression to smaller seeds and stabilization thereof is most likely aided by what is referred to as the "divide-and-protect" mechanism. Walter *et al* proposed this mechanism for the capping of gold nanoclusters[29] which states that a ligand and certain cluster of Au atoms will form, if possible, a nanoparticle having a closed shell noble-gas configuration. It is thus possible that with time, the co-ordination of the ligands along and within the various twin defects can lead to more stable seeds resulting in an increase of smaller, stabilized nanoparticles with time as depicted in Scheme 2.5. The maximum concentration of Au in the aqueous phase using a Au:PTA ratio of 1:0.4 was found to be approximately 70 ppm. This equates to approximately 7.0 % of the Au initially reduced migrating into the aqueous layer. It therefore appears that the Au:PTA ratio in the aqueous layer resulting in a closed shell noble gas configuration and stable Au_{55} nanoparticles of size 1.5 nm ± 0.9 at the end of 24 h is approximately 1:6. Although the concentration of gold extracted is low, subsequent extraction from the same organic phase yields a further approximately 70 ppm of gold. The histogram and wide particle size distribution after 4 h of extraction depicted in Figure 2.10 is a clear indication of the intermediate sizes of particles formed before equilibrium in stabilization by PTA and formation of smaller nanoparticles is achieved.

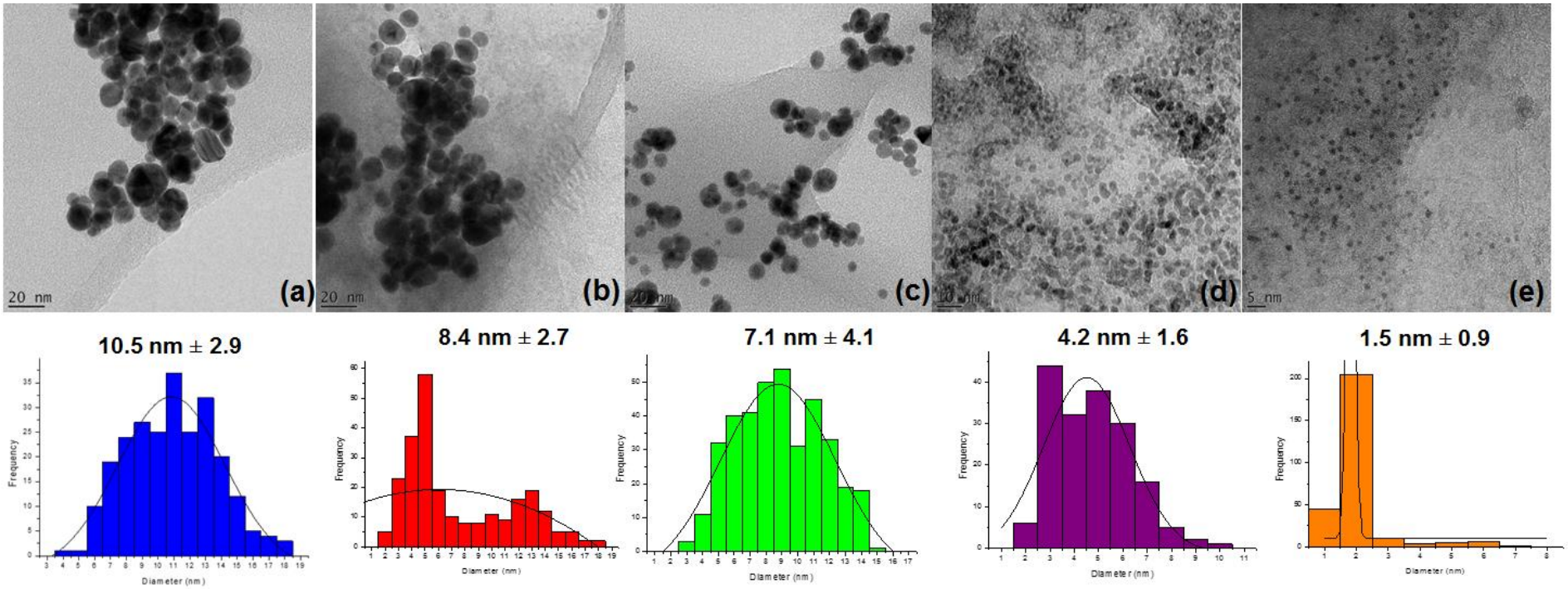

Figure 2.10 TEM images, histograms and particle size distributions of Au_{55} after 2, 4, 8, 16 and 24 h extraction (a, b, c, d and e respectively).

Scheme 2.4 Graphic representation of nanoparticle migration.

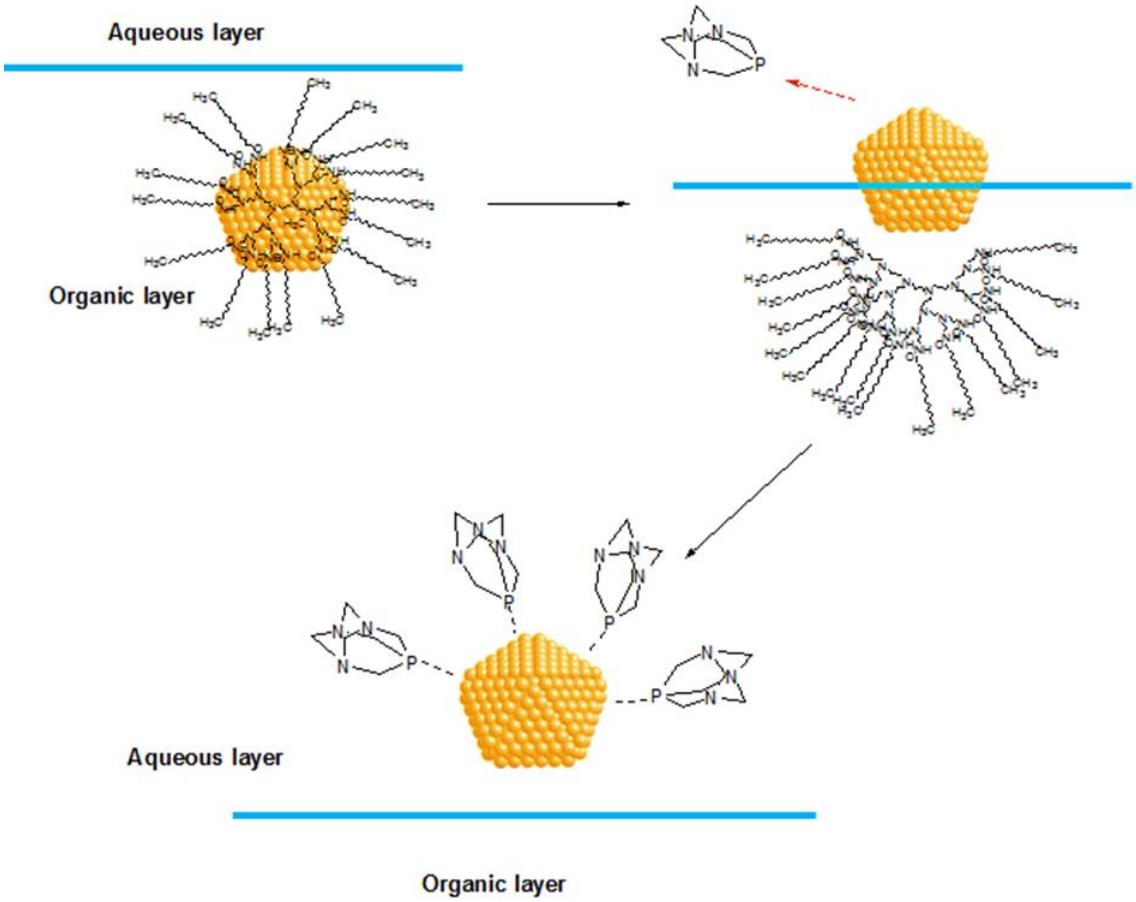

Scheme 2.5 Graphic representation of nanoparticle stabilization.

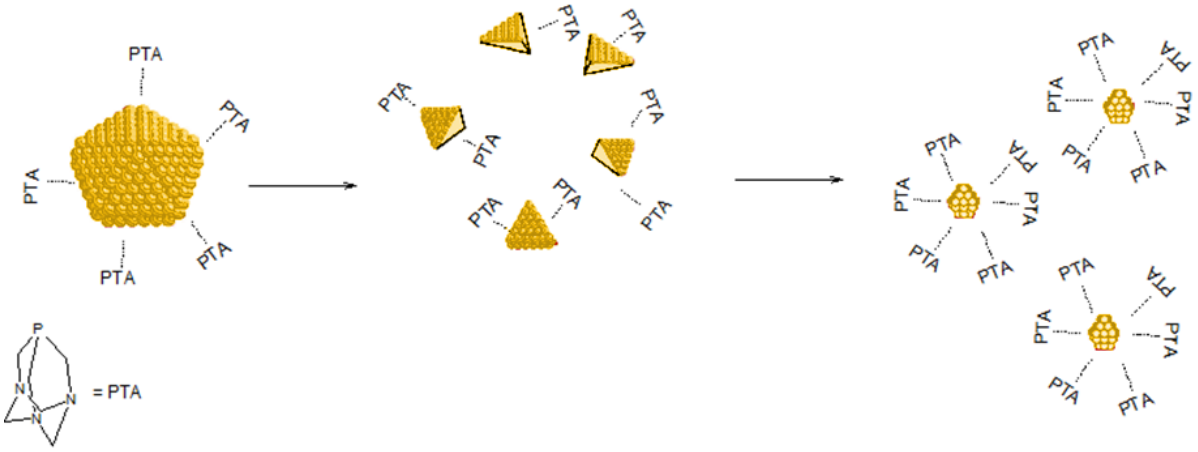

2.2.4 Extraction and Characterization of Au_{31} MPCs

For the extraction of Au_{31}, UV – Vis spectroscopy exhibits no plasmon resonance peak up to 4 h of extraction (Figure 2.11). From ICP it is evident that this is due no (after 2 h) or very low concentrations (after 4 h) of Au being present in the aqueous layer (Figure 2.9). It is only from after 8 h of extraction that nanoparticles are visible in TEM images (Figure 2.12) and a plasmon resonance peak is detected by UV – Vis spectroscopy.

The unstable nature of Au_{31} is clearly depicted in the TEM images after 8 h of extraction. Although UV – Vis spectroscopy shows a plasmon resonance peak, the TEM image shows distorted particles (Figure 2.12a). This is as a result of the energy of the electron beam affecting the unstable Au_{31} particles causing them to distort. It is only after 16 h where both concentrations of Au nanoparticles are high enough, and it is able for particles to be easily discerned, that it is possible to determine average particle size and distribution.

The instability of the Au_{31} nanoparticles is further reflected in the histogram (Figure 2.12e where two populations of nanoparticles appear to be present) and particle size distribution observed after 24 h of extraction; the particle size distribution widening from 16 to 24 h with an increase in average particle size from 8.0 nm ± 2.4 to 9.4 nm ± 4.7 thus clearly indicating agglomeration occurring.

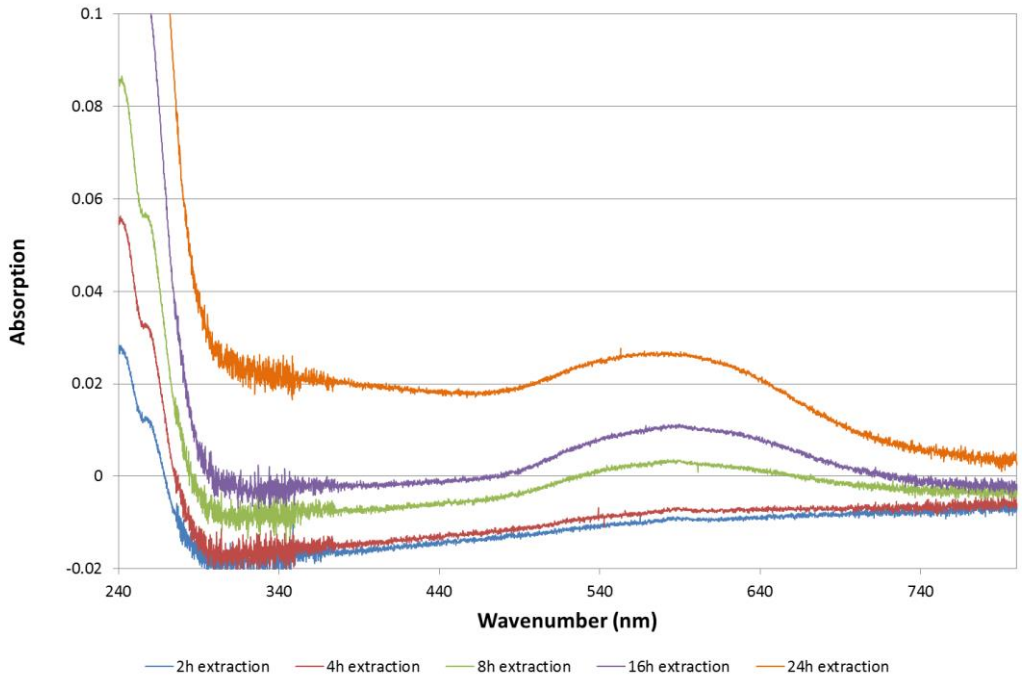

Figure 2.11 UV – vis spectra of samples taken after 2, 4, 8, 16 and 24 h of Au_{31}.

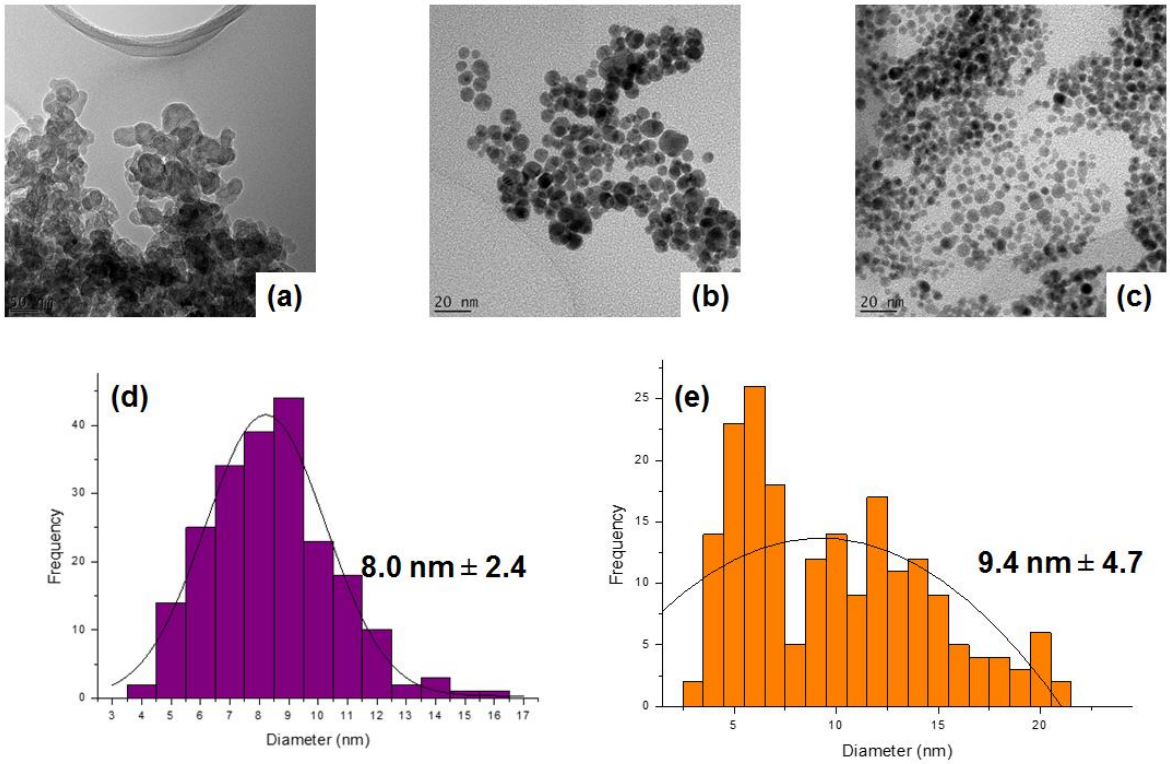

Figure 2.12. Histograms and TEM images of Au_{31} nanoparticles extracted after 8 (a), 16 (b, d) and 24 h (c, e).

A possible reason for the above could be the ease, or lack thereof, with which migration occurs from the organic to the aqueous phase. Since Au_{31} is an unstable atom cluster, it takes some time for rearrangement to a more stable Wulff polyhedron cluster as well as regular twinned seeds to occur within the dendrimer micelle in the organic layer. This is clearly depicted in Figure 2.13a and b where fused DENs having various atom stacking patterns are visible thus indicating the Wulff construction taking place. Once the more stable atom stacking arrangements are achieved (Figure 2.13c) then only are ligands able to attach and render the nanoparticles soluble in the aqueous layer.

Once migration occurs, further rearrangement in order to form more stable nanoparticles continues. The result of this is seen by the distorted particles observed after 8 h of extraction. However as time progresses, more ligand stabilized nanoparticles are formed.

The wide particle size distribution after 24 h as compared to after 16 h of extraction can be ascribed to the combination of, and continuous rearrangement of nanoparticles to more stable atom cluster sizes in the organic and aqueous phases. After 16 h mostly the nanoparticles which are stable enough to migrate from the organic phase is present. As time progresses,

there is the presence of both newly migrated nanoparticles and those which have further stabilised and agglomerated.

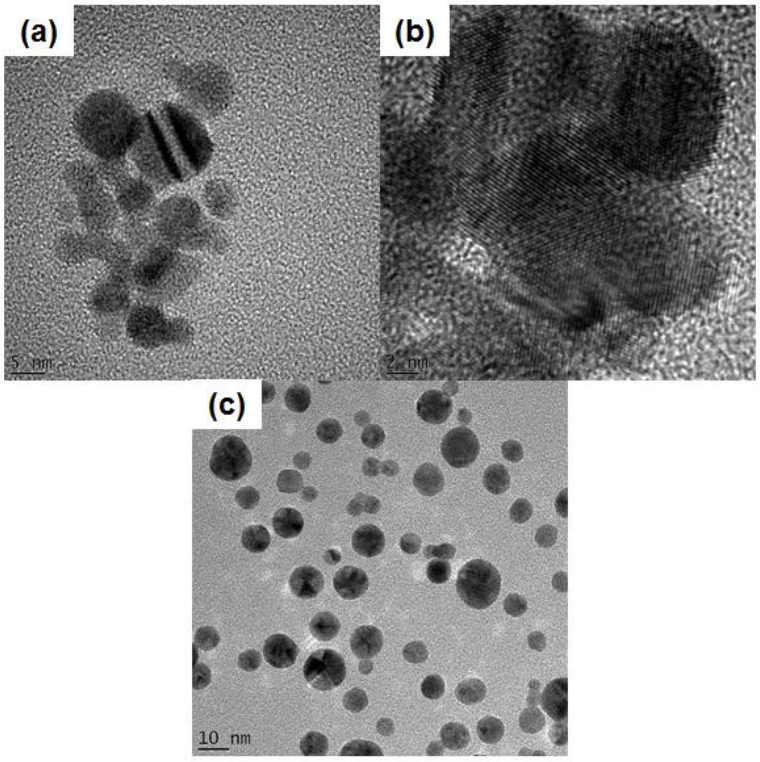

Figure 2.13 Rearrangement of Au_{31} DENs to form more stable nanoparticles.

2.2.5 Extraction and Characterization of Au_{13} MPCs

The UV – vis spectra at the various time intervals of extraction only show hints of a plasmon resonance peak for each time period although it can clearly be seen from ICP (Figure 2.9) and TEM images (Figure 2.14) that nanoparticles are present in the aqueous phase throughout extraction. This observation could be explained by considering the appearance of the aqueous layer and what is further seen in the TEM images.

Comparing the aqueous layers of Au_{55}, Au_{31} and Au_{13} (Figure 2.15) it can be seen that both the aqueous layers of Au_{55} and Au_{31} are clear solutions (the light blue, almost colourless, Au_{55} solution indicative of it containing extremely small nanoparticles with the purple Au_{31} solution indicative of the presence of larger nanoparticles). The aqueous layer of Au_{13} however clearly contains a precipitate. In the TEM images (Figure 2.16) it can be seen that most of the nanoparticles are surrounded by an organic layer. It therefore becomes clear that in addition to having PTA most likely co-ordinated to nanoparticles, nanoparticles are also surrounded by the micelle structure in the aqueous layer. Because of this, and the lower

concentration of Au extracted as compared to Au_{55} (Figure 2.9), the plasmon resonance peak is not as strongly detected by UV – vis spectroscopy.

A possible explanation as to how the micelle could end up in the aqueous layer could be related to the concentration of micelle initially present in the organic phase. It must be remembered that the micelle concentrations were varied while Au concentrations in the organic phase were kept constant in order achieve the desired Au atom cluster sizes. Thus Au_{13} would require the highest relative concentration of micelle in order to achieve the 1:13 micelle:Au ratio (as opposed to a 1:55 and 1:31 micelle:Au ratio for Au_{55} and Au_{31} respectively).

Because of the higher concentration of micelle present, localized concentrations of nanoparticles are formed. TEM images of the DENs of Au_{13} provide evidence for this with pockets of closely stacked nanoparticles clearly visible in Figure 2.16.

Extraction still occurs *via* the mechanism of hydrophobic/hydrophilic micelle conformity at the interface. However in this case, the aggregate of nanoparticles are in contact with a large surface area to the micelle while PTA co-ordinates to it simultaneously. This renders it soluble and then draws the nanoparticle aggregate into the aqueous phase while still having the micelle attached. As a result both the dendrimer micelle migrates along with the nanoparticles into the aqueous layer. The mechanism is depicted in Scheme 2.6.

The nanoparticles in the aqueous phase are now at an intermediate stage of no longer being completely encapsulated by the dendrimer micelle after having conformed, and being stabilized by the PTA ligand. Further seed growth occurs to a certain extent (up to 4.7 nm ± 1.4 from 4.0 nm ± 1.6) before the previously mentioned divide-and protect mechanism of ligand stabilization occurs resulting in a final nanoparticle size of 3.3 nm ± 1.0 after 24 h.

The DENs average size and initial extracted nanoparticle size of 3.9 nm ± 1.6 and 4.0 nm ± 1.6 are strikingly similar and is therefore perhaps a further indication of the internal dendrimer nanocomposite having been formed and subsequent stabilization of the nanoparticles by the dendrimer micelle.

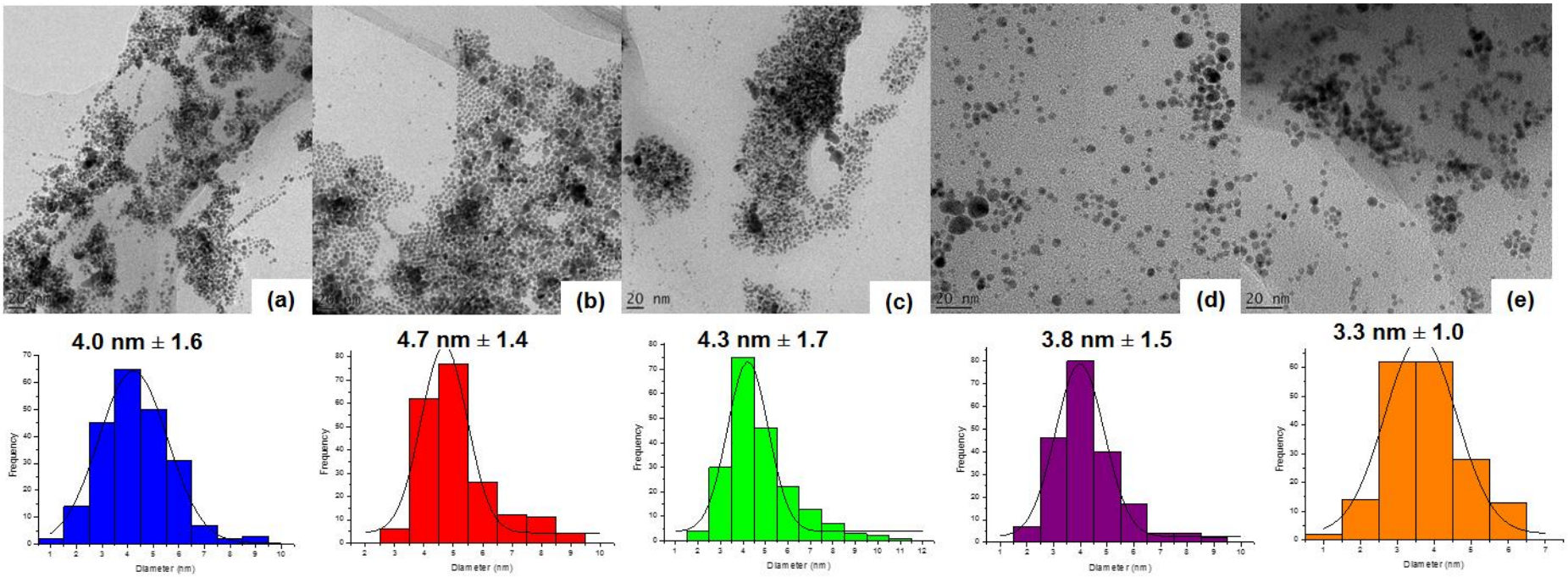

Figure 2.14 TEM images, histograms and particle size distributions of Au_{13} after 2, 4, 8, 16 and 24 h extraction (a, b, c, d and e respectively).

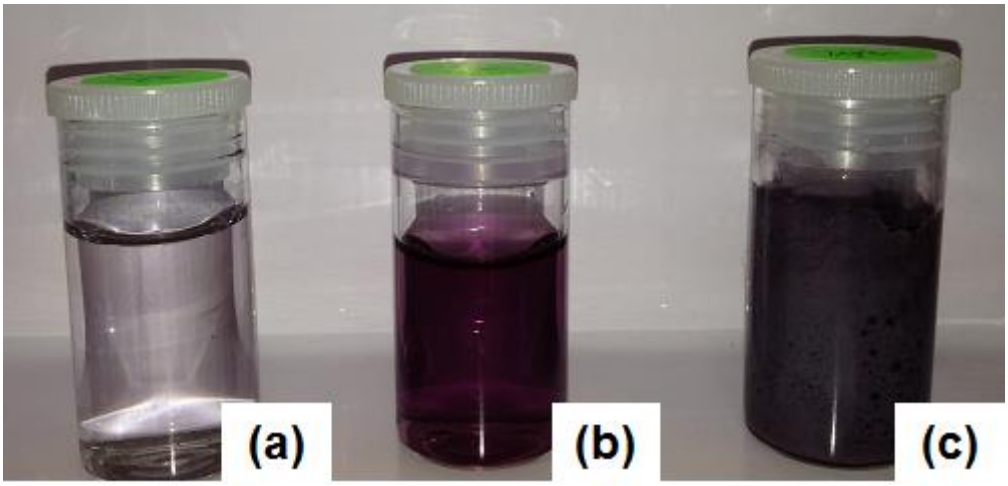

Figure 2.15 Appearance of aqueous layers containing Au_{55} (a), Au_{31} (b) and Au_{13} (c).

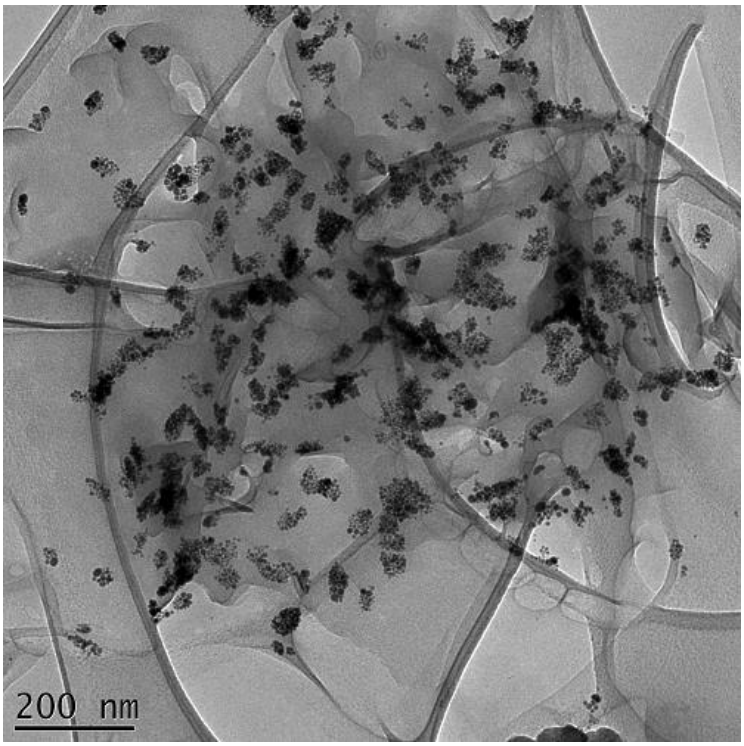

Figure 2.16 TEM image of Au_{13} DENs showing evidence of internal dendrimer nanocomposite formation.

Furthermore, the average size of the DENs and the nanoparticles extracted into the aqueous phase hint at the fact that seeds are single crystals. A particle size of 4.0 nm corresponds to a cluster composed of in the region of 492 atoms and 7 complete shells starting from Au_{13}.[30] Seed growth in the aqueous layer adds only one more shell since 4.7 nm is in the region of 642 atoms and 8 complete shells starting from Au_{13}. The final size of 3.3 nm obtained in the aqueous layer corresponds to a reduction to approximately 362 atoms and 5 complete shells.

The most stable MPC synthesised was that of Au_{55} atom clusters. These proved to be stable enough to exist at close to the size of a single 55 atom cluster. With nanoparticles formed from initial Au_{31} clusters, it was clear that rearrangement occurred in order to achieve a more stable shell configuration. The closer the starting configuration is to these "magic numbers", the more stable the nanoparticles will be albeit of larger size.

The stability of the Au_{55} nanoparticles was further emphasised due to its witnessed propensity to reduce in size as extraction time increased. This was postulated to be due to the ligand/shell configuration satisfying the criteria of closed shell noble gas configuration. This most likely lead to a "divide-and-protect" scenario resulting in decreasing nanoparticle size as more ligand coordination took place. It is thus evident, by observing the decrease in nanoparticle size with extraction time of Au_{55} clusters, that it might be possible to tailor particle size by stopping or continuing with extraction for certain lengths of time.

Furthermore, previously proposed synthesis routes to producing phosphine stabilized Au_{55} clusters are quite laborious requiring anaerobic conditions and diborane gas as a reducing agent.[21] Although subsequently developed methods are simpler, it still requires inert conditions and washing steps with various solvents.[31] The method described here in obtaining Au_{55} nanoparticles is therefore much simpler and economical.

A limitation which has been observed with the PTA ligand however is that it has a propensity to oxidize. As a result the stabilization of the nanoparticles is lost over time with TEM confirming increased particle size over time. It therefore has to be evaluated whether changing the extraction ligand from PTA to another water soluble phosphine ligand such as triphenylphosphine trisulfonate (TPPTS) will impart the same closed shell noble gas configuration which would result in the "divide-and-protect" mechanism occurring and leading to a reduction in nanoparticle size and formation of Au_{55} clusters with increased extraction time.

Scheme 2.6 Graphic representation of excess micelle migrating into aqueous layer along with nanoparticles.

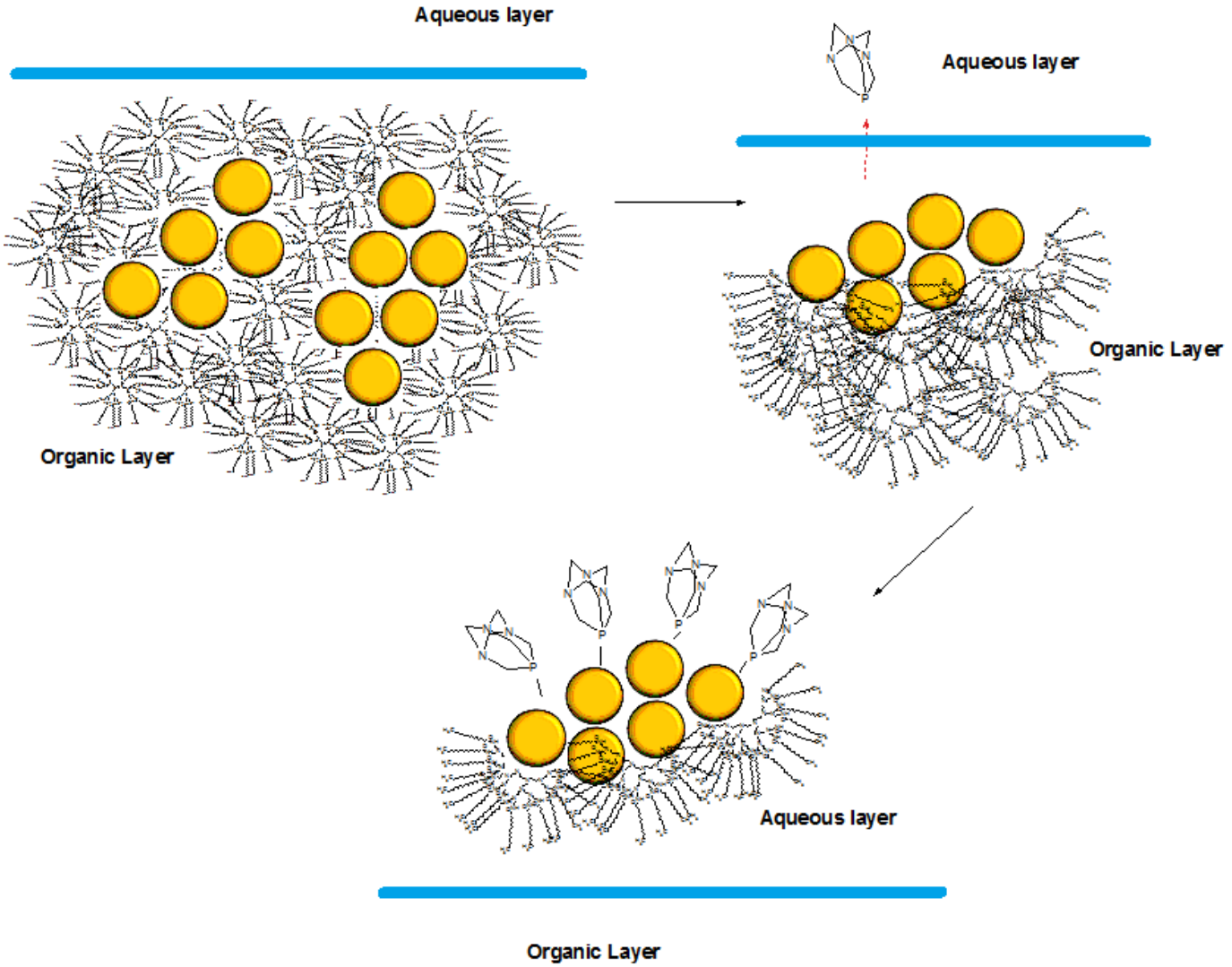

The work discussed in this chapter has been published in *Polyhedro*n and featured on the cover of the issue as shown in Figure 2.17.[32]

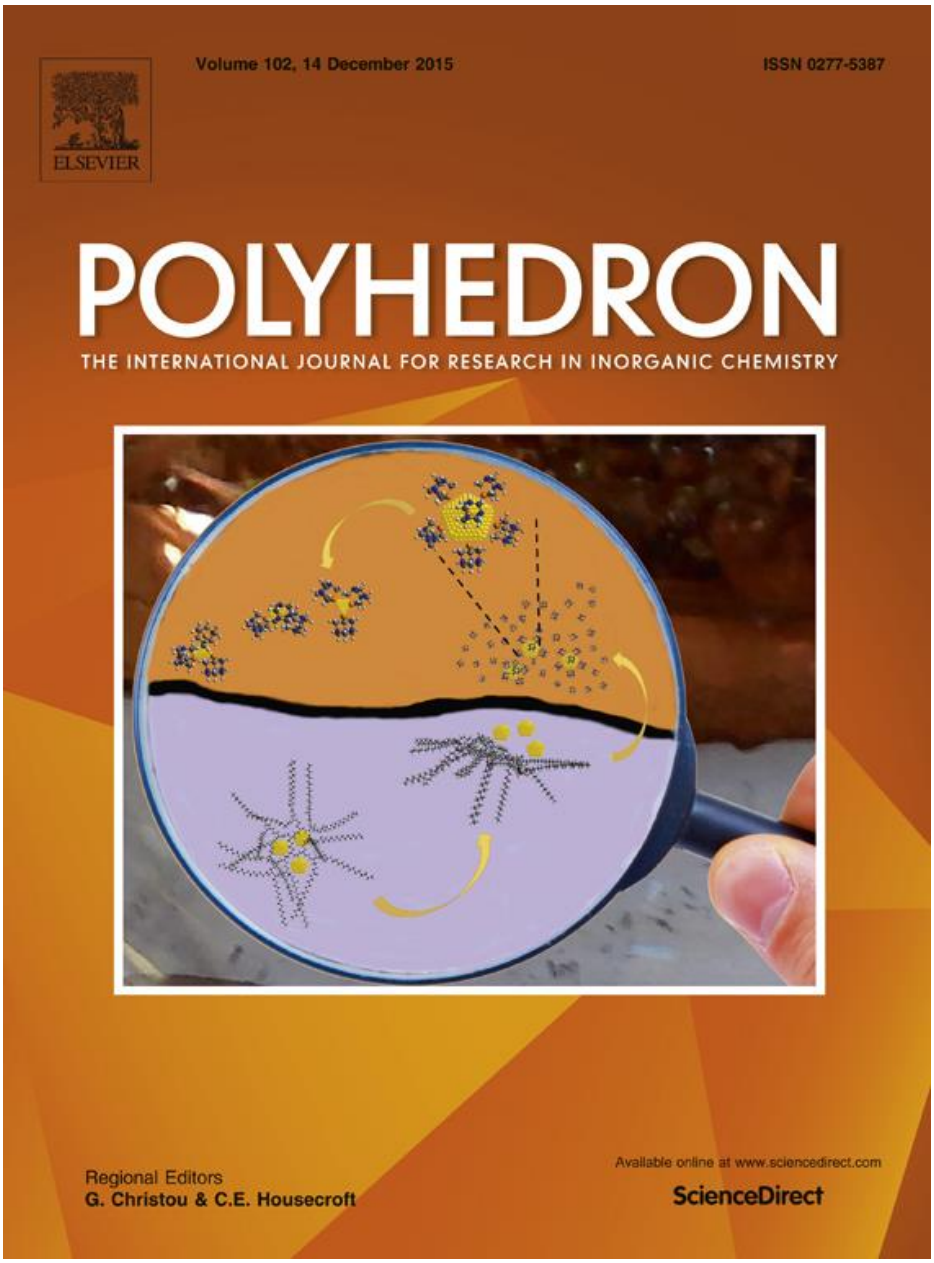

Figure 2.17 Polyhedron cover featuring work in this chapter.[32]

2.3 Summary and Conclusions

In this chapter, we have shown that using a dendrimer as a template for nanoparticle synthesis initially aids in the formation of the desired nanoparticle cluster size (by controlling the dendrimer:metal ratio), however these initial nanoparticle seeds rapidly undergo growth within the dendrimer template leading to larger than expected nanoparticle sizes.

By extracting these nanoparticles from the dendritic template using a hydrophilic ligand, we created stable monolayer protected clusters (MPCs) which gave the initially aimed for nanoparticle clusters in the case of Au_{55} after an extraction period of 24 hours. In the case of Au_{13} a similar phenomenon was observed however, due to the presence of the dendrimer micelle in the aqueous phase, the nanoparticles were stabilized by the dendrimer as well as the PTA ligand which minimised agglomeration and the limited "divide and protect" mechanism, since the nanoparticle sizes remained stable at ≈ 4 nm. It was found that the initial dendrimer:metal ratio does play a role in nanoparticle stability and subsequent extraction since formation of nanoparticle clusters which does not result in a closed shell formation (magic numbers) leads Wulff construction as seen in the case of Au_{31} nanoparticle synthesis. Wulff constructed nanoparticles form as a result of the anisotropic nature of the initially formed Au_{31} seeds which leads to a continual rearranging in order to achieve a stable closed shell configuration. This continuous rearrangement and the consequent irregular-shaped nanoparticle, hampers ligand coordination to the nanoparticle surface resulting in low extraction efficiencies.

By combining the dendrimer templated as well as the MPC method for nanoparticle synthesis, we have demonstrated a simpler and more economical procedure for Au_{55} nanoparticle synthesis.

2.4 Experimental

2.4.1 Materials

Reagent grade solvents, triethylamine and palmitoyl chloride were obtained from Merck Chemicals and used as received. Na_2CO_3, $NaBH_4$ and $HAuCl_4$ were obtained from Sigma-Aldrich and used as received. PTA was synthesised according to the method of Daigle *et al*.[33]

2.4.2 Characterization

IR was obtained using a FT-IR 200spectrometer. ^1H and ^{13}C NMR were obtained on a Varian Innova 400 MHz NMR spectrometer in deuterated chloroform. UV – Vis absorbance spectra were obtained using a GBC 920 UV-VIS spectrometer and quartz cuvettes having a path length of 1.00 cm. The spectrum of either chloroform or water was used as the background depending on the solution being analysed. TEM images were obtained using a FEI Tecnai G^2 Field Emission Gun (FEG) TEM operating at 200 kV and having a 2.5 Å point-to-point

resolution, 1.02 Å line resolution and 1.4 Å information limit. Samples were prepared by dropwise addition of the sample onto a carbon coated copper grid. Average nanoparticle sizes were determined from the TEM images using ImageJ image processing software. Au concentrations were measured on a Spectro Acros ICP-OES spectrometer.

2.4.3 Preparation of G3 PPI dendrimer micelle

THF (20 ml) was added to G3 PPI-dendr-$(NH_2)_{16}$ (0.298 g, 0.18mmol) in a round bottomed flask. Triethylamine (3ml) and palmitoyl chloride (0.86 ml, 2.85 mmol) was then added to the stirring THF/dendrimer solution and left to stir for 72h at room temperature in an attempt ensure complete reaction at the dendrimer periphery. After this time the solvent was evaporated and 30 ml diethyl ether added to the residue, refluxed for 30 min and then filtered to obtain a white residue. Na_2CO_3 (0.5 g) in 50 ml distilled H_2O was then added to the residue and the mixture refluxed for approximately 4 h. After this time the mixture was filtered, the residue washed with H_2O and dried at 60°C. A product yield of 44% (determined as a percentage of the expected yield and actual yield based on the initial mols of dendrimer started with) was obtained. The IR data compared well with that found in literature.[34]

IR obtained: amide N-H stretch (3297.1 cm^{-1}), secondary amide N-H stretch (3082.1 cm^{-1}), saturated C-H (2915.3 cm^{-1}), secondary amide C=O (2848.4cm^{-1})

For ^{1}H NMR the multiplet at 0.9 ppm due to R_2NH, the singlet at 1.27 ppm due to the C_{15} alkane chain, the singlet at 1.63 ppm due to NC-CH, and the mulitplet at 2.23 ppm due to the RCOH compares well with literature.

For ^{13}C NMR the chemical shifts at 14.3, 22.7, 24.9, 25.8, 27.4, 29.8, 31.8, 36.8, 37.9, 51.7, 52.3 and 174 ppm compare well with literature.
The absence of any stretching frequencies or chemical shifts in IR or NMR spectroscopy respectively, confirmed that complete modification of the dendrimer periphery had been achieved.

2.4.4 Preparation of Au DENs

For the preparation of Au_{55}, G3 micelle (0.01 g, 0.0018 mmol) was dissolved in 20 ml chloroform. $HAuCl_4$ (0.032 g, 0.01mmol) was then added to the micelle solution and stirred

for 10 min. $NaBH_4$ (0.01 g, 0.26 mmol) was dissolved in 0.2 ml MeOH and added to the Au/micelle solution. Reduction was carried out for 30 min. For the preparation of Au_{31} and Au_{13}, the amount of $HAuCl_4$ as well as $NaBH_4$ and volume of solvent were kept the same as for Au_{55} synthesis, with the amount of micelle being used being varied. Thus for Au_{31} the amount of micelle used was (0.018 g, 0.0033 mmol) and for Au_{13} (0.050 g, 0.0091 mmol).

2.4.5 Extraction of Au Nanoparticles

1,3,5-triaza-7-phosphaadamantane (PTA) (0.0065 g, 0.04 mmol) was dissolved in 20 ml distilled water and added to the Au DENs solution. Extraction was carried out by stirring the mixture for 24 h with UV- Vis samples taken at 2, 4, 8, 16 and 24 h of extraction time.

2.5 References

(1) Garcia-Martinez, J. C.; Crooks, R. M. *J. Am. Chem. Soc.* **2004**, *126* (49), 16170.

(2) Haridas, M.; Srivastava, S.; Basu, J. K. *Eur. Phys. J. D* **2008**, *49* (1), 93.

(3) Phillips, A. D.; Gonsalvi, L.; Romerosa, A.; Vizza, F.; Peruzzini, M. *Coord. Chem. Rev.* **2004**, *248* (11–12), 955.

(4) Dyson, P. J.; Ellis, D. J. *Adv. Synth. Catal.* **2003**, *345*, 211.

(5) Darensbourg, D. J.; Joo, F.; Kannisto, M.; Katho, A.; Reibenspies, J. H.; Daigle, D. J. *Inorg. Chem.* **1994**, *33* (2), 200.

(6) Čermák, J.; Kvíčalová, M.; Blechta, V. *Collect. Czechoslov. Chem. Commun.* **1997**, *62* (2), 355.

(7) Debouttière, P.-J.; Coppel, Y.; Denicourt-Nowicki, A.; Roucoux, A.; Chaudret, B.; Philippot, K. *Eur. J. Inorg. Chem.* **2012**, *2012* (8), 1229.

(8) Wang, Z. L. *J. Phys. Chem. B* **2000**, *104* (6), 1153.

(9) Aghlara, H.; Rostami, R.; Maghoul, A.; SalmanOgli, A. *Opt. - Int. J. Light Electron Opt.* **2015**, *126* (4), 417.

(10) Manchon, D.; Lermé, J.; Zhang, T.; Mosset, A.; Jamois, C.; Bonnet, C.; Rye, J.-M.; Belarouci, A.; Broyer, M.; Pellarin, M.; Cottancin, E. *Nanoscale* **2015**, *7* (3), 1181.

(11) Noguez, C. *J. Phys. Chem. C* **2007**, *111*, 3806.

(12) Knecht, M. R.; Garcia-Martinez, J. C.; Crooks, R. M. *Langmuir* **2005**, *21* (25), 11981.

(13) Xia, Y.; Xiong, Y.; Lim, B.; Skrabalak, S. E. *Angew. Chemie - Int. Ed.* **2009**, *48* (1), 60.

(14) LaMer, V. K.; Dinegar, R. H. *J. Am. Chem. Soc.* **1950**, *72* (11), 4847.

(15) Niu, Y.; Crooks, R. M. *Comptes Rendus Chim.* **2003**, *6*, 1049.

(16) Jiang, W.; Hibbert, D. B.; Moran, G.; Herrmann, J.; Jamting, A. K.; Coleman, V. a. *RSC Adv.* **2013**, *3* (20), 7367.

(17) Sujitha, M. V.; Kannan, S. *Spectrochim. Acta - Part A Mol. Biomol. Spectrosc.* **2013**, *102*, 15.

(18) Suman, T. Y.; Radhika Rajasree, S. R.; Ramkumar, R.; Rajthilak, C.; Perumal, P. *Spectrochim. Acta - Part A Mol. Biomol. Spectrosc.* **2014**, *118*, 11.

(19) Zhou, L.; Russell, D. H.; Zhao, M.; Crooks, R. M. *Macromolecules* **2001**, *34*, 3567.

(20) Torigoe, K.; Suzuki, A.; Esumi, K. *J. Colloid Interface Sci.* **2001**, *241*, 346.

(21) Schmid, G.; Pfeil, R.; Boese, R.; Bandermann, F.; Meyer, S.; Calis, G. H. M.; van der Velden, J. W. M. *Chem. Ber.* **1981**, *114* (11), 3634.

(22) Alvarez, M. M.; Khoury, J. T.; Schaaff, T. G.; Shafigullin, M. N.; Vezmar, I.; Whetten, R. L. *J. Phys. Chem. B* **1997**, *101* (19), 3706.

(23) Kim, Y.; Oh, S.; Crooks, R. M. *Chem. Mater.* **2004**, *16* (1), 167.

(24) Cleveland, C. L.; Landman, U.; Shafigullin, M. N.; Stephens, P. W.; Whetten, R. L. *Zeitschrift Fur Phys. D-Atoms Mol. Clust.* **1997**, *508* (1–4), 503.

(25) Lu, X.; Rycenga, M.; Skrabalak, S. E.; Wiley, B.; Xia, Y. *Annu. Rev. Phys. Chem.* **2009**, *60* (1), 167.

(26) Garcia-Martinez, J. C.; Scott, R. W. J.; Crooks, R. M. *J. Am. Chem. Soc.* **2003**, *125* (37), 11190.

(27) Schmid, G. *Chem. Soc. Rev.* **2008**, *37* (9), 1909.

(28) Schmid, G.; Emmrich, E.; Majoral, J. P.; Caminade, A. M. *Small* **2005**, *1* (1), 73.

(29) Walter, M.; Akola, J.; Lopez-Acevedo, O.; Jadzinsky, P. D.; Calero, G.; Ackerson, C. J.; Whetten, R. L.; Grönbeck, H.; Häkkinen, H. *Pnas* **2008**, *105* (27), 9157.

(30) An, K.; Somorjai, G. A. *ChemCatChem* **2012**, *4* (10), 1512.

(31) Weare, W. W.; Reed, S. M.; Warner, M. G.; Hutchison, J. E. *J. Am. Chem. Soc.* **2000**, *122* (51), 12890.

(32) Cloete, J.; Mapolie, S. F.; Malgas-Enus, R. *Polyhedron* **2015**, *102*, 469.

(33) Daigle, D. J. *Inorganic Synthesis*, 32nd ed.; Darensbourg, M. Y., Ed.; 1998.

(34) Newkome, G. R.; Shreiner, C. D. *Polymer (Guildf).* **2008**, *49* (1), 1.

Chapter 3

Evaluation of Dynamic Light Scattering (DLS) as a Technique for Size Determination of Synthesized Hydrophilic Gold Nanoparticles

---

3.1 Introduction

In Chapter 2 it was shown that there is a reduction in the size of nanoparticles extracted as time increased up to a period of 24 hours. It was hypothesised that this is due to nanoparticle stabilization by the ligand, 1,3,5-triaza-7-phosphaadmantane (PTA), occurring along twinning faults present in initially formed nanoparticles leading to smaller, more stable nanoparticles; a mechanism described as the "divide-and-protect" mechanism of nanoparticle stabilization.

The above mechanism could thus potentially result in the synthesis of nanoparticles of varying sizes. Variation in size could possibly result in varying activity or selectivity when the nanoparticles are employed as potential catalysts.[1] Thus by altering the Au:dendrimer micelle ratio, it was thought that Au atom clusters such as Au_{147}, Au_{309} *etc.* and thus varying size could be obtained.

However, attempts to vary nanoparticle size by altering the Au:dendrimer micelle ratio showed that although the proposed mechanism held for successive synthetic procedures, the nanoparticle sizes obtained for specific Au:dendrimer micelle ratios were not reproducible. As a control, the synthesis of Au_{55} was then repeated. This is illustrated in Figure 3.1 where the initial size of the extracted nanoparticles, as well as the size after 24 h, is shown. Figure 3.1a shows the results of the Au_{55} synthesis described in Chapter 2 where an initial average size of 10.5 nm ± 2.9 is obtained immediately after extraction and which reaches 1.5 nm ± 0.9 after 24 h. Figure 3.1b then shows the results of the attempted repeat where an initial average size of 47.0 nm ± 16.2 and reaches 29.7 nm ± 15.7 after 24 h of extraction. It was then hypothesised that this was due to the "divide-and-protect" mechanism not occurring efficiently due to possible differences in stirring regimes which might be affected by the use of different round-bottomed flasks and stirrers. In an attempt to address possible inefficiencies in the mechanism occurring, extraction time was increased to 48 hours.

However, no further reduction of nanoparticle size was observed. The increased extraction time in fact appeared to accelerate agglomeration and is illustrated in Figure 3.2.

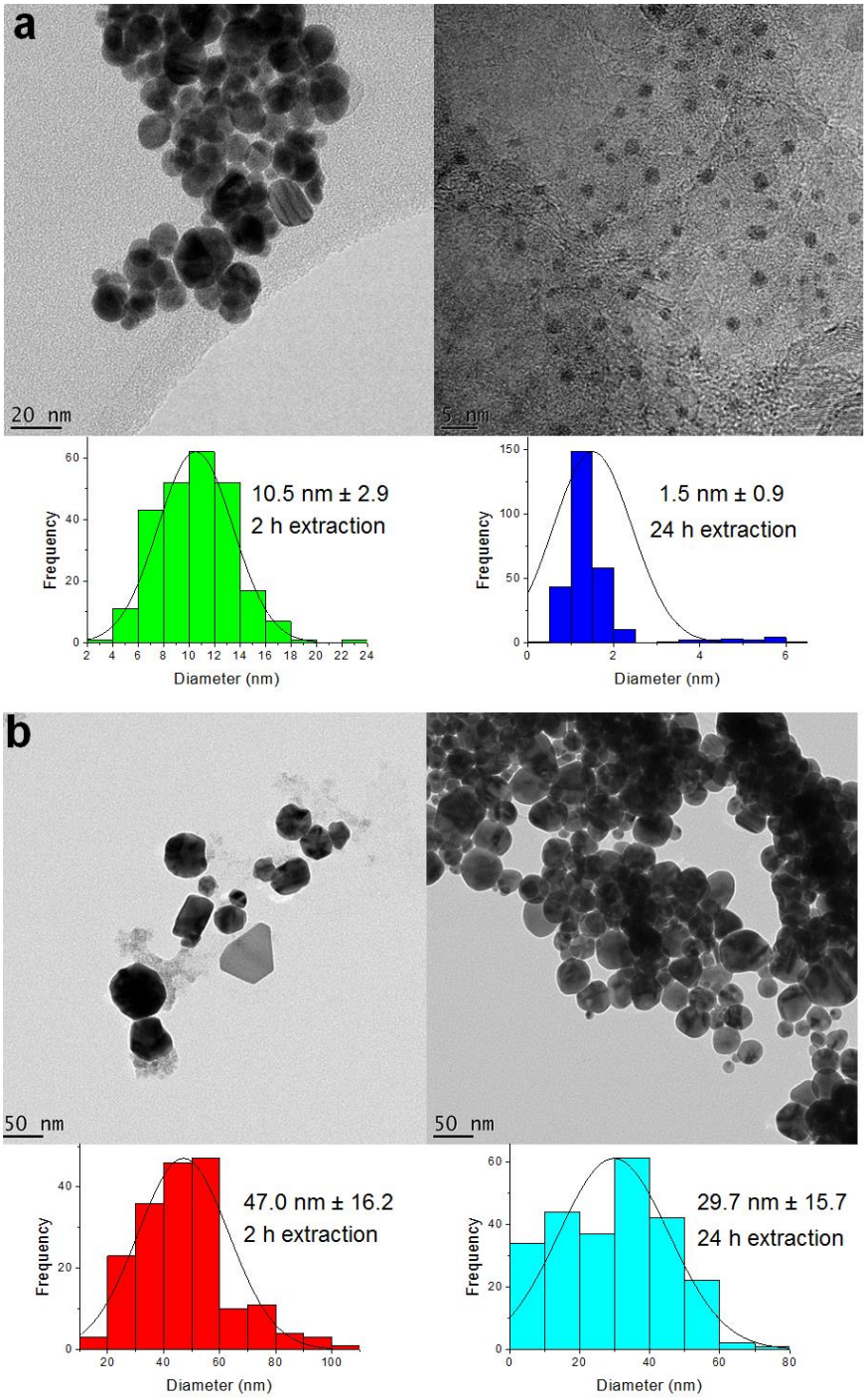

Figure 3.1 Differences in nanoparticle sizes after 2 (left) and 24 h (right) of extraction using the same synthesis method for successive synthetic attempts (**a** and **b**).

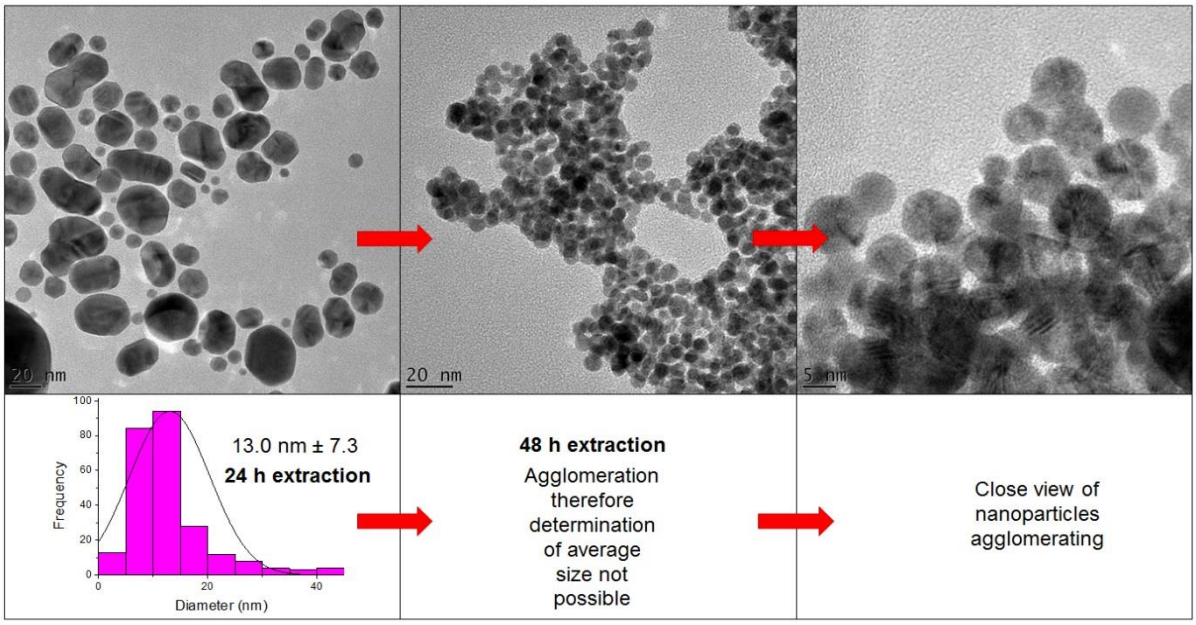

Figure 3.2 Illustration of nanoparticle agglomeration with an increase in extraction time from 24 h to 48 h.

Following the above observation, it was thus further hypothesized that increasing the ligand to gold ratio for extraction of the gold from the organic into the aqueous phase (^{31}P NMR had previously shown a chemical shift corresponding to P-Au and therefore confirmed coordination of the ligand to the Au nanoparticles), would firstly increase the efficiency of the "divide-and-protect" mechanism irrespective of changes in mixing regimes and secondly provide extra stabilization against agglomeration. Subsequently the ratio was increased from 0.4:1 to 1:1. Visually, the extraction with the increased PTA concentration appeared to be more efficient. This is illustrated in Figure 3.3 where the clear organic layer when using a 1:1 ligand to gold ratio (Figure 3.3 right) contrasts with the dark purple organic layer where a 0.4:1 ligand to gold ratio was used. This suggests that more gold was extracted using the higher ligand to gold ratio resulting in a clear organic layer. The dark purple organic layer in the case where a ratio of 0.4:1 ligand:Au was used, indicates the presence of Au nanoparticles formed during the initial reduction process and not extracted into the aqueous layer.

Figure 3.3 Appearance of organic and aqueous phases after extraction with 0.4:1 ligand to gold ratio (left) and 1:1 ligand to gold ratio (right).

Although visually the increase in ligand concentration appears to result in more efficient extraction, the nanoparticle size would usually only be known if the sample is subjected to TEM analysis. It was subsequently realized that a further possible reason for the variation in nanoparticle size might be due to differences in the time between particle formation and performing of actual TEM analysis. Up to this point in our research, it was quite common to have delays in performing TEM analysis due to the availability of facilities and therefore it was quite possible that agglomeration was occurring to various degrees during this time. We were in fact fortunate that TEM analysis for our time studies (reported in Chapter 2) could be performed within 24 h of running the experiment. The initial experiments involving the increase of the ligand to gold ratio would thus still hold, but it was now apparent that a more immediate method of nanoparticle size determination was needed to eliminate any variances in obtained sizes due to agglomeration brought about by time delays in obtaining TEM analysis. We thus embarked on a study to explore an alternative approach to probe control nanoparticle sizes.

With this in mind we explored the possibility of Dynamic Light Scattering (DLS). It is a technique which is routinely used to analyse the size and size distribution of particles with diameters ranging from a few nanometres to a few microns, and has been shown to be effective in the determination gold nanoparticle size up to 100 nm.[2,3] In particular, it has been shown to be effective in nanoparticle size determination in aqueous media in techniques developed for biosensing applications.[4,5] Hence it was thought that DLS may be suitable for measuring the size of our water soluble nanoparticles. In addition, modern commercial DLS

instruments are relatively easy to operate with low associated operating costs compared to a technique such as TEM.[3]

It was considered that even though the presence of the 1,3,5-triaza-7-phosphaadmantane (PTA) ligand in the extracted gold nanoparticle solution could perhaps result in slightly larger hydrodynamic diameters compared to those obtained through TEM, it could nevertheless have the potential of *in-situ* monitoring of nanoparticle size. In addition, one should be able to monitor the evolution of nanoparticle size during the entire nanoparticle synthesis process and not only at the end of it. It was rationalized that due to the compact nature of the PTA ligand compared to surfactant type nanoparticle stabilizing agents, the discrepancy between a potential larger hydrodynamic diameter and the actual size that would be determined by TEM would not be that great and could be factored in.[6]

3.1.1 Basic Principle of Dynamic Light Scattering

Dynamic light scattering (DLS), also known as photon correlation spectroscopy or quasi-elastic light scattering, is a technique whereby the size distribution profile of sub-micron particles in suspension or polymers in solution can be determined.[7] DLS measures the speed of particles undergoing Brownian motion and translates this into size.

Brownian motion is the random movement of particles due to collisions caused by bombardment by the solvent molecules that surround them and is influenced by particle size, sample viscosity and temperature. In general, the smaller the particle, the faster the Brownian motion and the larger it is, the slower the motion. This relationship between particle size and velocity of the Brownian motion is given by the Stokes-Einstein Equation:[8]

$$dH = \frac{kT}{3\pi\eta D}$$

(Equation 3.1)

Where dH = hydrodynamic diameter, k = Boltzmann's constant, T = absolute temperature, η = viscosity and D = diffusion coefficient

The particle size here is referred to as the hydrodynamic diameter and is defined as the diameter of a hard (solid) sphere that diffuses at the same speed as the particle or molecule being measured. The need to relate the measured size based on the Brownian motion to a

solid sphere is often a problem due to the fact that typically, particles are not spherical. This measured size which is related to a solid sphere is referred to as the equivalent spherical diameter.

The concept of the equivalent spherical diameter is illustrated in Scheme 3.1.[9] Four possibilities of the equivalent spherical diameter exists for an irregularly shaped particle. The first possibility is an equivalent sphere having a diameter with the same minimum cross length of the irregularly shaped particle (a). The second possibility is a sphere with a calculated size based on the same diffusion coefficient as the irregularly shaped particle (b). Thirdly there exists a possibility that a sphere with the same volume can be measured (c) while the fourth option is an equivalent sphere with a diameter with the same maximum cross length of the irregularly shaped particle (d). What this means is that the more regularly shaped and closer to spherical a particle is, the more accurate the size measurement using DLS will be.

Scheme 3.1 Illustration of equivalent spherical diameter.[9]

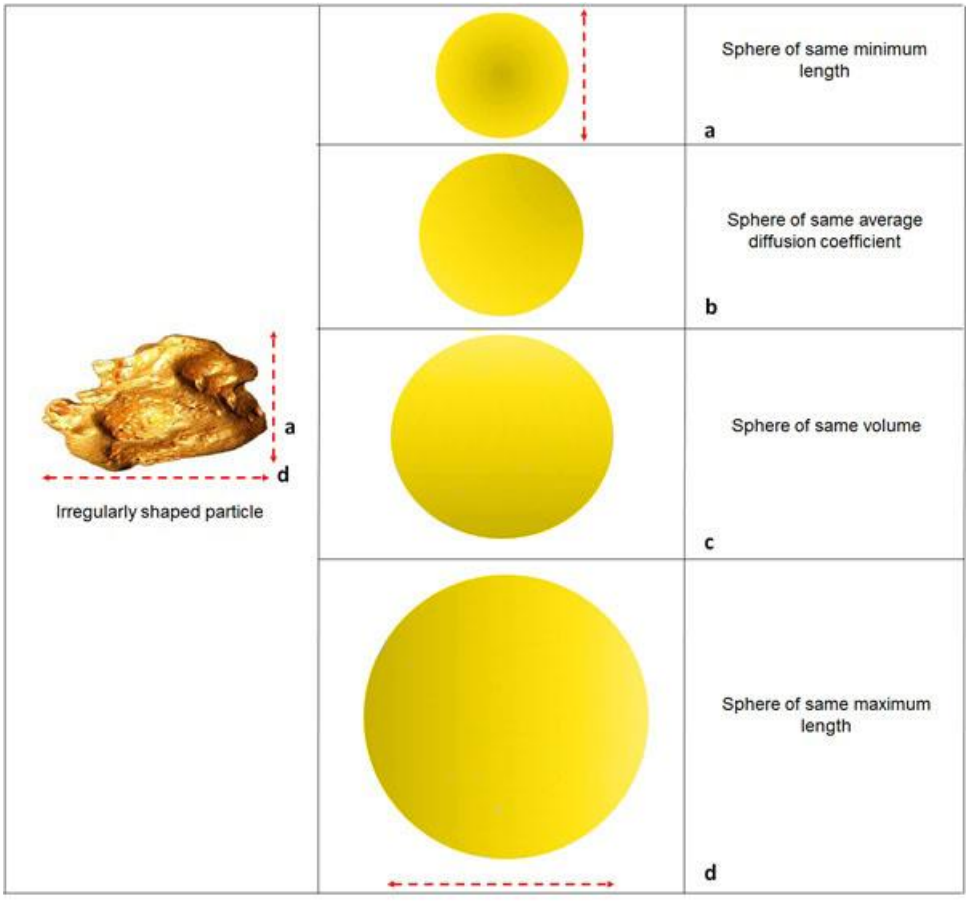

The derived hydrodynamic diameter not only depends on the main, core equivalent spherical diameter particle itself, but also on any surface structure associated with it as well as the concentration and type of any ions in the medium in which it is being measured.

The ions in a medium and their total concentration may affect particle diffusion speed, therefore altering the speed of Brownian motion could subsequently have an effect on the calculated apparent hydrodynamic diameter. Similarly, any ligand or polymer attached to the particle surface will alter the Brownian motion and hence apparent hydrodynamic diameter.

3.2 Experimental

It was attempted to determine the hydrodynamic diameters of our extracted gold nanoparticles using a Particulate Systems NanoPlus zeta/nano particle analyser (Figure 3.4a). Initially it was attempted to measure the size of extracted Au_{55} with PTA as ligand. From TEM, a particle size of 1.5 nm ± 0.9 was previously determined after 24 h of extraction. A fresh Au_{55} solution was thus prepared with 0.1 ml of the aqueous solution transferred to a disposable plastic cuvette and placed in cell holder (Figure 3.4c). This was diluted with 2.5 ml of distilled water before being placed in the DLS instrument for size analysis. For later zeta potential experiments, an auto titrater (Figure 3.4b) was connected to the DLS instrument with sample circulating from the sample vial, where pH is monitored and altered, to the DLS instrument by means of a flow cell (Figure 3.4d).

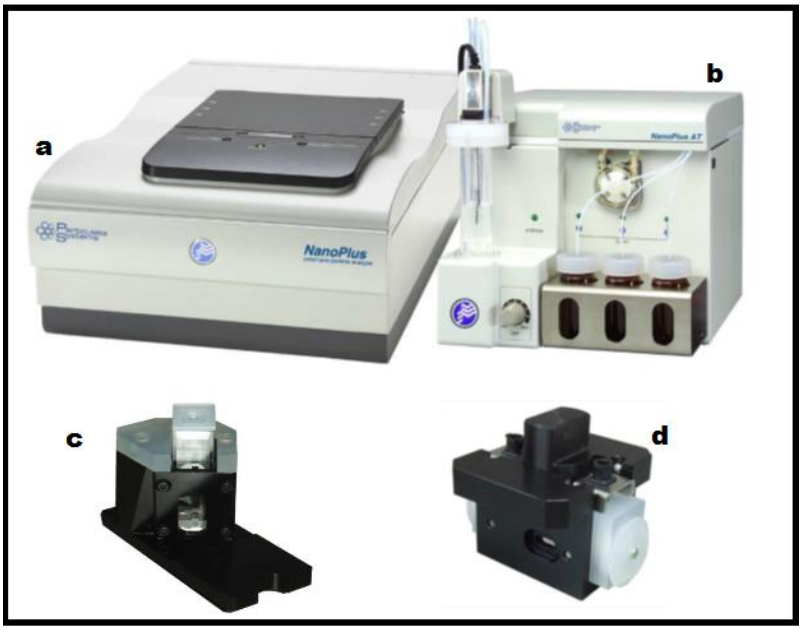

Figure 3.4 NanoPlus DLS instrument (a) with auto titrator (b) and disposable cuvette in cell holder (c) and flow cell (d).

3.3 Results and Discussion

3.3.1 Direct Measurement of Nanoparticle Size

Figure 3.5 shows the DLS analysis results for 70 accumulation times. The fitting curve of the auto correlation function (ACF) is indicative of extremely large particles (Figure 3.5a - the less the fluctuation of $G2_{(T)}$ the larger the particle size) while the fitting curve of the $Ln(G2_{(T)}-1)$ vs T plot shows that although large (Figure 3.5b), sedimentation did not occur during the accumulation time (Figure 3.5d)[10]. The observed particle size indeed showed an average of 1707.6 nm with a polydispersity index of 0.844 indicating a relatively broad distribution of particle sizes; particle size when measured by DLS being fairly monodisperse when the polydispersity index is below 0.7. This is seen in the distribution results where peak values of 20.8 nm ± 0.8, 642.5 nm ± 182 and 48479 nm ± 4962.4 (Figure 3.5c) are observed.

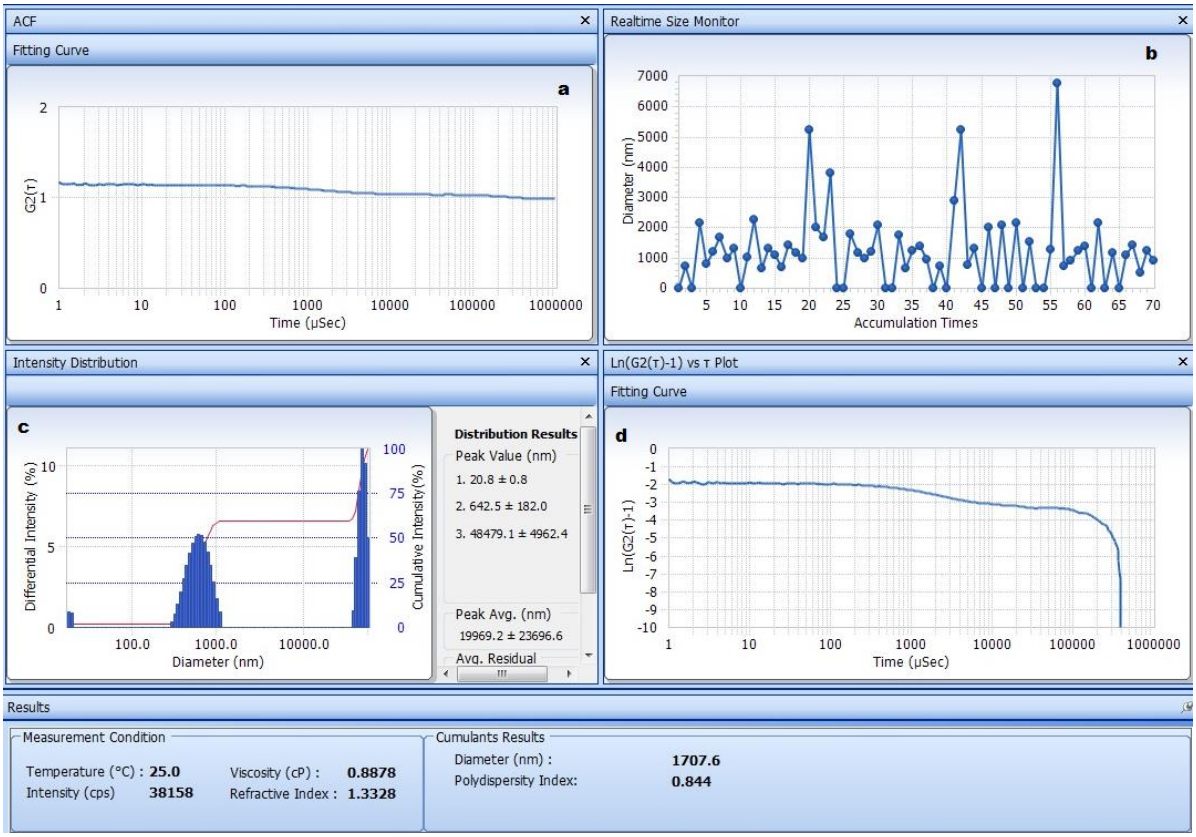

Figure 3.5 Size analysis results for extracted Au_{55} with PTA in aqueous layer.

However, repeating analysis of the same samples resulted in an average size 3134.6 nm with a polydispersity of 1.650. This extremely wide polydispersity index correlated to the distribution results of 35.2 nm ± 8.6, 891.9 nm ± 409.8 and 47085.8 nm ± 25147.8. Each subsequent repeat analysis yielded similar large average nanoparticle sizes with very broad

particle size distributions which were not even close to the 1.5 nm ± 0.9 determined from TEM.

The extremely large discrepancy between the particle sizes determined from TEM and DLS can however be rationalized when looking at the TEM images and bearing in mind the principles of hydrodynamic diameter and equivalent spherical diameter. Figure 3.6 shows an aggregate of nanoparticles with individual particles ranging approximately between 5 and 25 nm. These types of aggregates consistently appeared in multiple TEM analyses performed. These aggregates could perhaps be seen as single irregularly shaped nanoparticles with a large hydrodynamic diameter. The variation in DLS results observed could then be a result of the equivalent spherical diameter of maximum or minimum length (Figure 3.6a and b respectively) or same volume or average diffusion coefficient. Removal of aggregates were attempted through filtration, but proved unsuccessful.

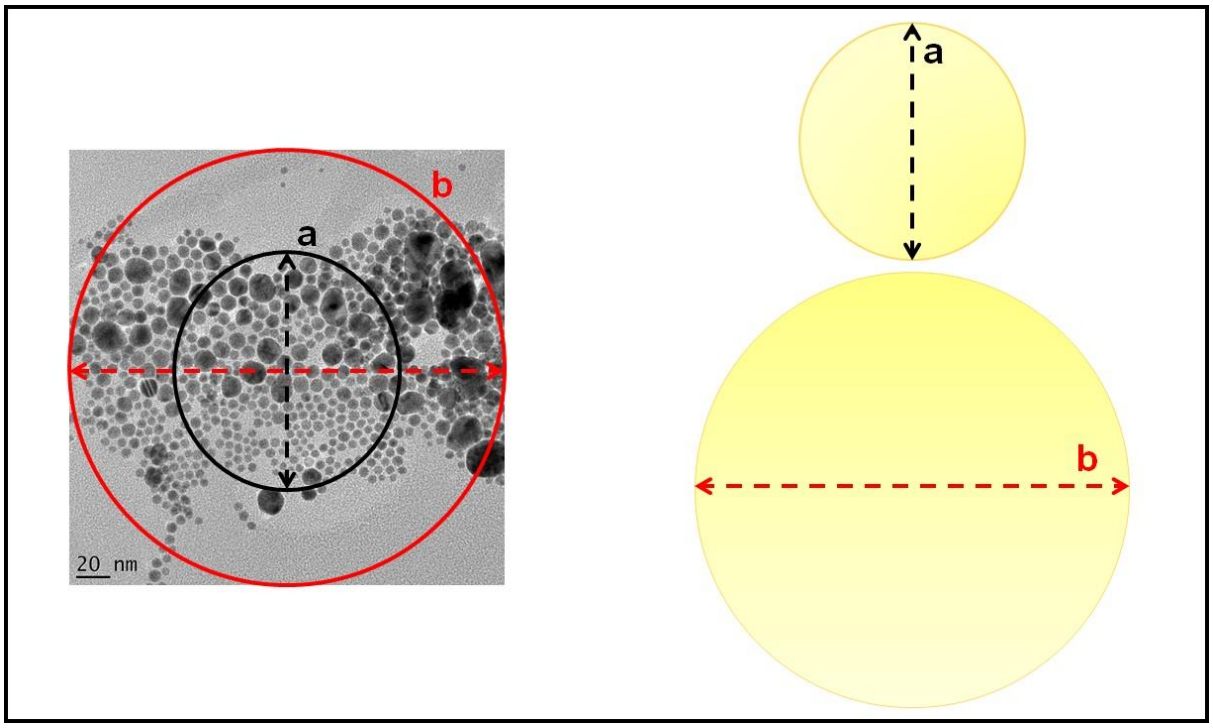

Figure 3.6 Image showing a grouping of aggregated nanoparticles which could potentially be seen as a single irregularly shaped nanoparticle with an equivalent spherical diameter of same maximum (a) or minimum length (b).

Although the example in Figure 3.6 shows that an irregularly shaped nanoparticle of maximum equivalent diameter of approximately 263 nm and minimum equivalent diameter of 133 nm, much larger aggregates have been observed. An example of this is shown in

Figure 3.7 where aggregated nanoparticles could be interpreted as isolated nanoparticles with hydrodynamic diameters of up to thousands of nanometres by DLS (highlighted areas).

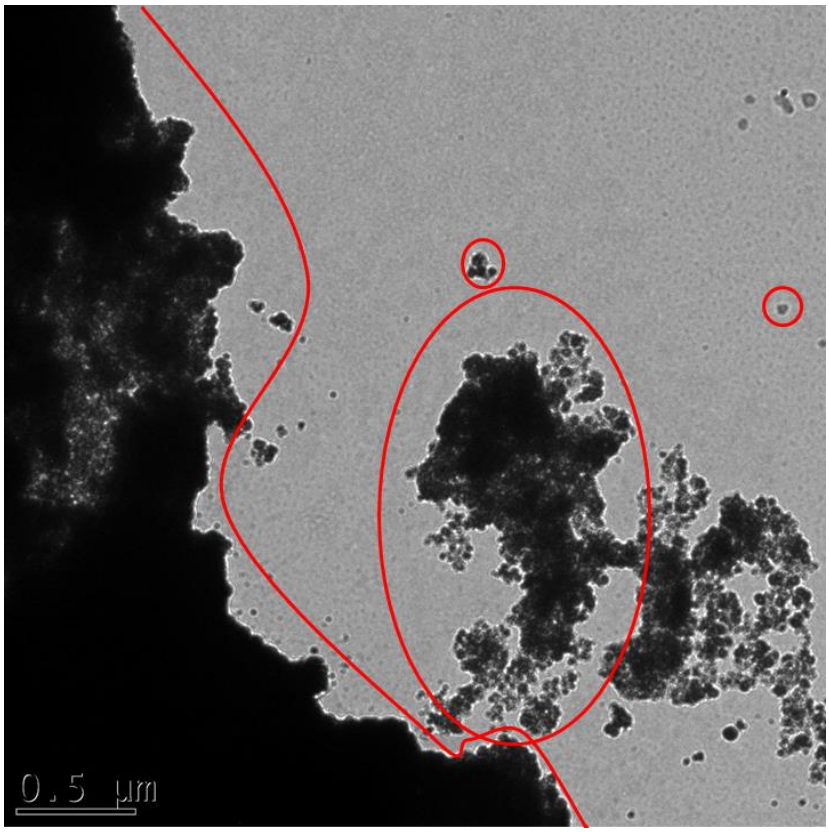

Figure 3.7 TEM image illustrating the various sizes of aggregates which could be observed as single nanoparticles with large hydrodynamic diameters by DLS.

In order to circumvent the above limitation of aggregated nanoparticles appearing as single nanoparticles with extremely large hydrodynamic diameters, changes in zeta potential brought about by changes in pH of the nanoparticle solution was evaluated. By varying the pH it was hoped that a zeta potential could be identified at which good separation of the individual particles could be achieved. In this way it was hoped to obtain a better correlation with the particle sizes determined using TEM.

3.3.1.1 Basic Principle of Zeta Potential Measurements

Colloidal articles in solution have either positive or negative charges on their surfaces. Ions in solution that have an opposite charge to that of the particle surface gather close to the surface so as to maintain the charge balance at the surface. The layer of ions immediately surrounding the particle surface is known as the Stern Layer. The concentration of the counter ions decreases with increasing distance from the surface and is found in conjunction

with oppositely charged ions which ensures the overall neutrality of the solution. This is known as the diffuse layer and together with the Stern layer constitute the diffuse electric double layer (Figure 3.8a).[11]

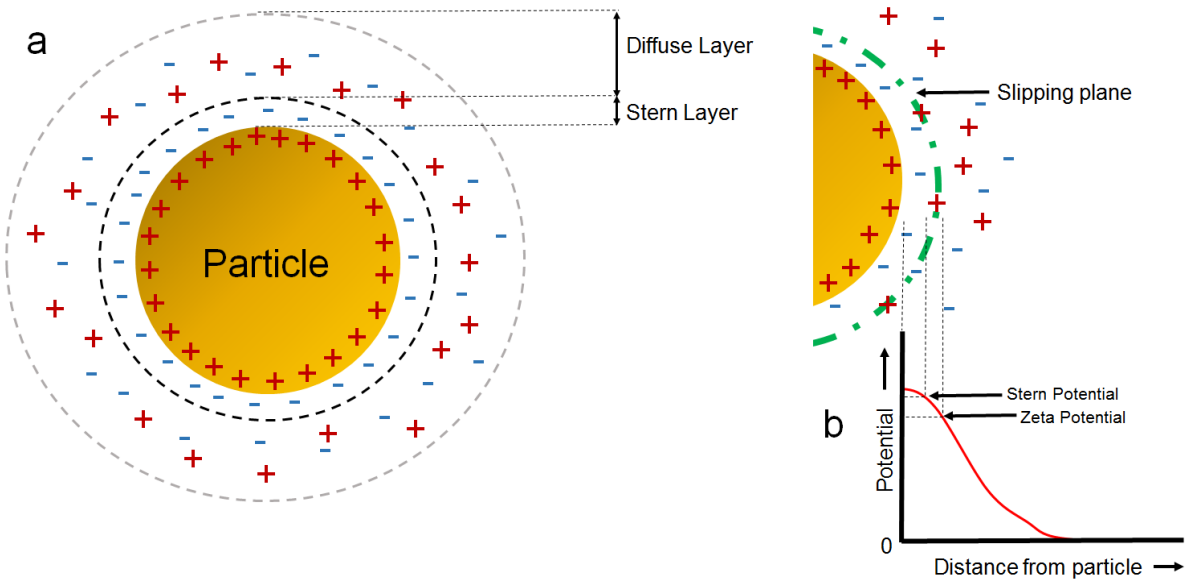

Figure 3.8 Illustration of Stern and diffuse layers constituting the diffuse double layer (**a**) and the slipping plane giving rise to the zeta potential (b).[11]

Particles undergoing Brownian motion in a liquid do not only move along with the immediate Stern layer, but would also move along with some of the diffuse layer which borders the Stern layer. This creates an intermediate border known as the slipping plane (Figure 3.8b). The difference in the Stern potential and that created by the slipping plane gives rise to the zeta potential.[12]

The further one moves from the surface of the particle, the less charged the solution becomes in the diffuse layer, and eventually becomes neutral. The greater the absolute zeta potential value, the greater the electrostatic repulsion between the particles in solution. Conversely, a zeta potential approaching zero would increase the likelihood of particles colliding and thus aggregating.

3.3.2 Measuring of Nanoparticle size following Zeta Potential Adjustment

By varying the pH, the ionic composition of the mixture is thus altered and this could influence the zeta potential. The NanoPlus instrument was thus connected to an auto-titrator which allowed for a series of analyses varying the pH from 3 to 8 to be carried out. The

software allowed for the setting of desired pH values to which the sample solution could be changed and the resultant zeta potential and particle sizes measured. Furthermore, unlike the size measurements by DLS described above using the instrument, a flow cell instead of a cuvette was used. This allowed for the sample to be circulated thereby keeping the sample volume constant. The data obtained from these measurements showed that a pH of 7 resulted in the smallest measured average particle size (3.4 nm, Figure 3.9). However the polydispersity index (11.4) was exceptionally poor implying a very wide particle size distribution.

pH	Zeta Potential (mV)	Diameter (nm)
3.05	10.04	137.9
3.91	21.18	214.9
4.91	14.15	466.8
5.94	16.72	0.0
6.91	10.40	3.4
7.92	3.91	1116.8

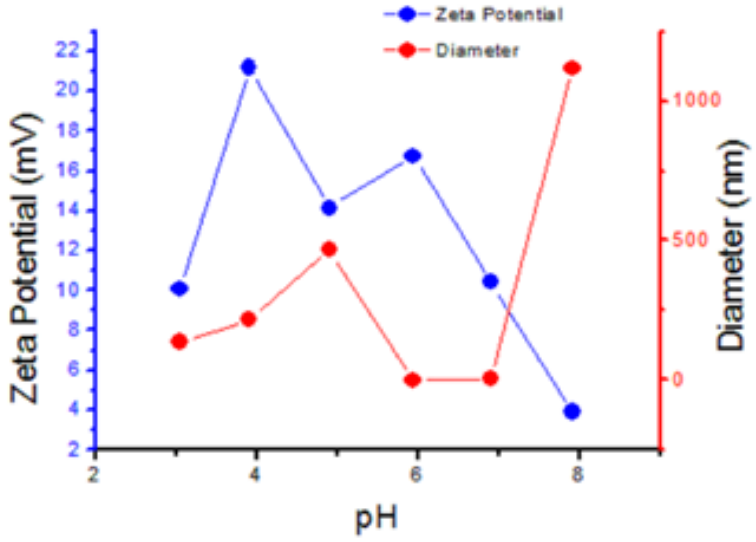

Figure 3.9 Analysis results for pH 3 to 8.

Given the results above, it was attempted to establish whether at a pH of 7 a size of close to 3.4 nm would be obtained and also whether with repeated measurements, the polydispersity index would improve (since there would be a greater probability of the Brownian motion of particles being measured and hence the size more accurately determined). However only one of the repeats (10 in total) yielded an observed particle size of 2.1 nm with a polydispersity index of 1.3. The reason for this was that the concentration of the sample had changed (due the sedimentation of aggregated particles) with only one analysis at an adequate concentration being possible.

From the image below (Figure 3.10), it is clear that the insufficient amount of data collected is due to the particles settling out of solution with some adhering to the stirrer magnet. This corresponds with the visual observations made. It can be seen that the colour of the sample solution changes from a light red colour at pH 2 to a grey/blue at pH 9. This colour change corresponds to an increase in gold nanoparticle size[13]; with the sedimented nanoparticles observed to be adhering to the stirrer bar at the end of the experiment. This therefore provides evidence for the decrease in observed nanoparticle size being due to agglomeration of particles and their settling out of solution rather than the zeta potential being altered by changes in the pH with a concomitant a change in particle size. In fact, the change in pH could most likely be affecting the ligand and decreasing its stabilization effect by for example protonation.

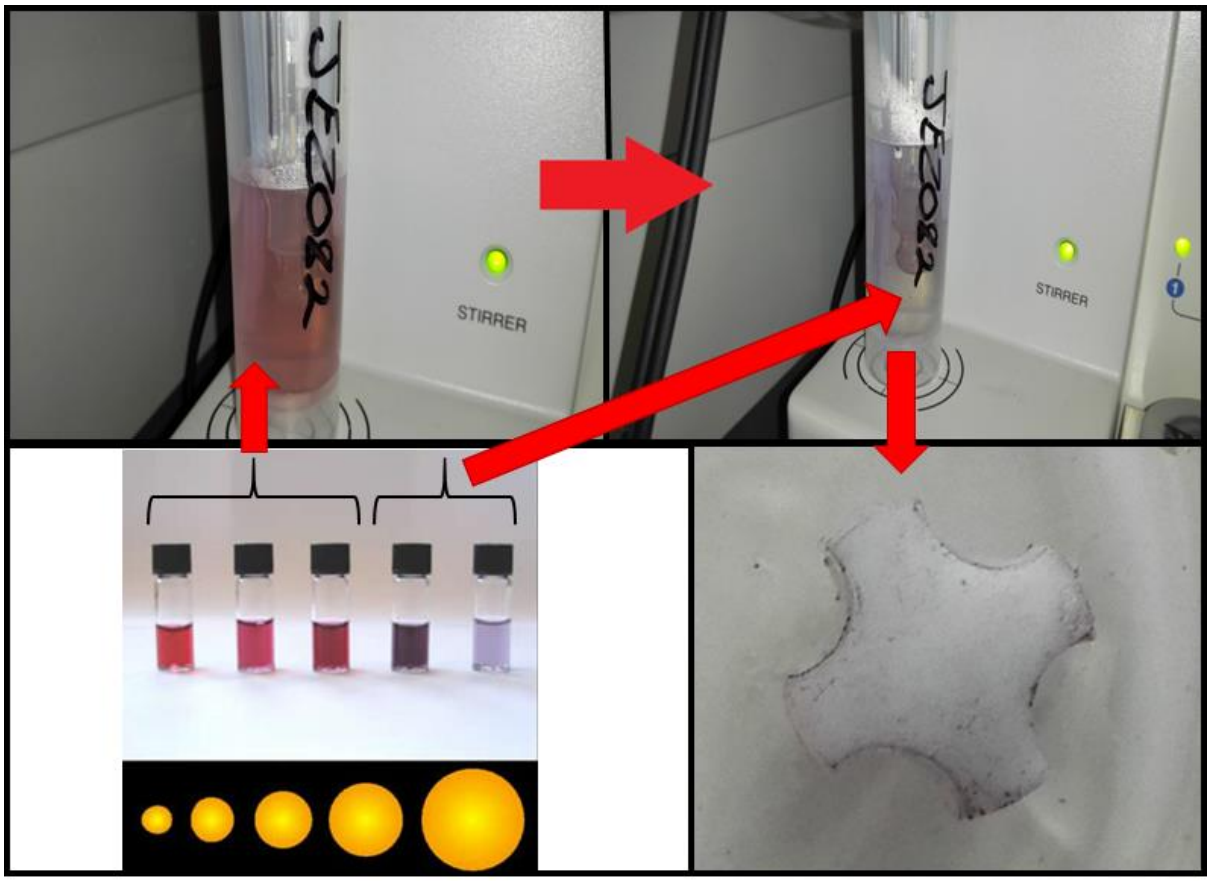

Figure 3.10 Colour change in sample solution from pH 2 to pH 9 corresponding to increase in size.[4,13–15] The agglomerated nanoparticles settled on the stirrer magnet are shown.

The apparent concentration of sample therefore would appear to be continually decreasing with time. This is essentially due to material precipitating out of solution with time. However, the results obtained do not suggest such a straight forward correlation since it was one of the

later runs in the repeatability test series which gave sufficient Brownian motion data to obtain an average size. This however might just be purely coincidental that sufficient particles are present.

From the above observations, it appears that although the pH of 7 appears to result in a zeta potential at which aggregation of particles is reversed and small average particle sizes are observed, it is actually the pH at which we have an optimum zeta potential resulting in particles agglomerating and settling out of solution onto the stirrer bar. In fact it appears that the increase in pH from 3 to 6 results in agglomeration which reaches a maximum at 6 (most agglomeration, no particles observed, insufficient data, see Figure 3.9). With increasing pH, particles are seen again starting at size 3.4 nm at pH 7 with a dramatic increase in size to 1116.8 nm at pH 8. The small particles at pH 7 are observed since they are still small enough not to have settled out of solution, while the larger particles at pH 8 are ones in the process of settling out and seen by chance.

An experiment was set up to start at pH 2 and increase to a pH of 9 in order to determine behaviour over a wider pH range. The results are shown in Figure 3.11.

A definite change in size with pH is observed. It appears that particle size increases from pH 2.1 to 2.95 and then starts decreasing at pH 3.90 and reaches a size of 4.8 nm at pH 4.91. There is then a large jump in size to 296.7 nm at pH 5.92 before decreasing to 4.2 nm and then showing no values at the pH values above this. Although at first inspection it appears that increase in pH results in a decrease in particle size, it is actually a case of particle size increasing. The large particles however settle out of solution leaving the smaller particles suspended in solution. In reality the sizes *actually* being measured are those of the latter.

The agglomeration of particles observed in the above experiments suggest that ligand stabilization of the extracted nanoparticles is not optimum. Therefore the next set of experiments were focused on increasing ligand concentration while monitoring zeta potential in order to determine if stable nanoparticles are formed.

pH	Zeta Potential (mV)	Diameter (nm)
2.10	10.17	157.0
2.95	2.99	228.1
3.90	4.86	32.5
4.91	5.17	4.8
5.92	3.82	296.7
6.91	0.03	4.2
7.90	-1.25	0.0
8.92	-1.46	0.0

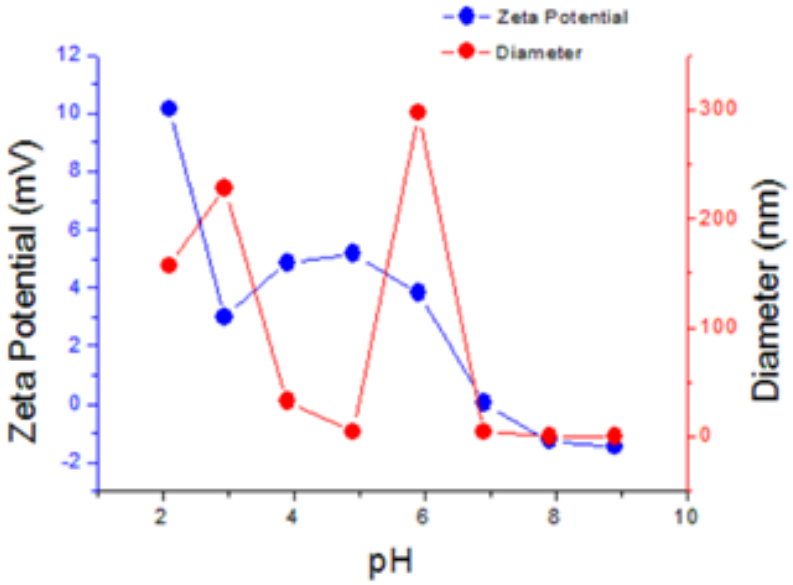

Figure 3.11 Analysis results for pH 2 to 9.

3.3.2.1 Effect of increased ligand concentration

Figure 3.12 to Figure 3.14 shows the results obtained for samples containing a 1:1 ligand:gold ratio compared to a previous sample with a 0.4:1 ligand:gold ratio.

The results for the higher ligand concentration samples appear to be repeatable with the exception of two or three outliers in particle size. It appears that the greater ligand concentration stabilises the nanoparticles to such an extent that pH hardly appears to affect the zeta potential and varies between -1 and 2 mV at most.

pH	Zeta Potential (mV)	Diameter (nm)
2.10	0.09	86.9
2.91	0.41	4.1
3.92	1.59	0.0
4.93	1.37	146.4
5.92	0.72	0.0
6.90	0.67	0.0
7.91	-0.33	0.0
8.93	-0.80	0.0

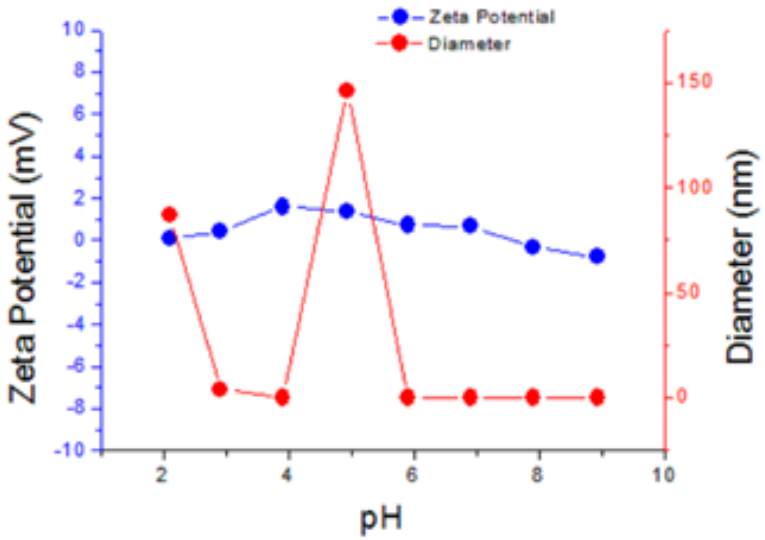

Figure 3.12 Analysis results for pH 2 to 9 with 1:1 ligand:gold ratio.

With regards to particle size, with the higher ligand concentration, particle sizes are on average much smaller and that the small sizes or zero values seen are not due to particles settling out of solution as previously observed. The larger observed sizes are most likely due to some larger agglomerates still being present, but are encountered less frequently due to the greater stabilizing effect of the higher ligand concentration. This is evident in the lack of colour changes of the solution as previously observed (Figure 3.15) and also the lack of visible particles adhered to the stirrer bar or on vial walls.

pH	Zeta Potential (mV)	Diameter (nm)
2.04	-0.71	0.0
2.96	-0.08	44.1
3.92	-0.05	4969.1
4.90	-0.02	0.5
5.91	0.74	0.0
6.90	-0.99	0.0
7.91	0.00	0.0
8.90	-0.48	46.4

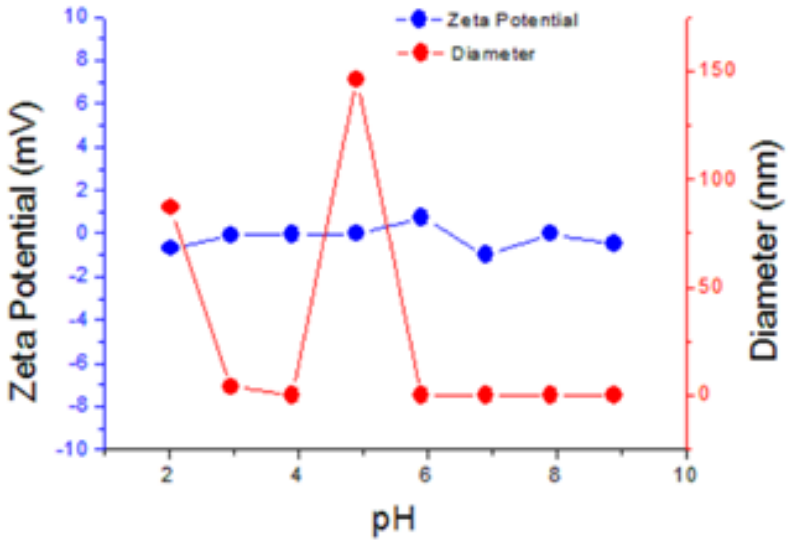

Figure 3.13 Repeat analysis results for pH 2 to 9 with 1:1 ligand:gold ratio.

Furthermore it was aimed to determine whether pH and zeta potential changed with further addition of ligand after initial extraction using a ratio of 1:0.4 Au:PTA (which was initially determined to be the optimum ratio for extraction in Chapter 2). Synthesis was carried out as per our established method of dissolving 0.01 g (0.0018 mmol) dendrimer micelle in 20 ml $CHCl_3$ followed by addition of 0.034 g (0.01 mmol) $HAuCl_4$ which is dissolved in the micelle solution. Reduction of the Au salt is then achieved by the dropwise addition of a solution of 0.01 g (0.026 mmol) $NaBH_4$ dissolved in MeOH (2.0 ml). Extraction of the formed nanoparticles was done by addition of 0.002 g (0.004 mmol) of PTA dissolved in 20 ml distilled H_2O to the $CHCl_3$ solution. The biphasic mixture was stirred for 24 h to allow for maximum extraction of the Au nanoparticles from the organic to the aqueous phase to occur.

pH	Zeta Potential (mV)	Diameter (nm)
2.10	10.17	157.0
2.95	2.99	228.1
3.90	4.86	32.5
4.91	5.17	4.8
5.92	3.82	296.7
6.91	0.03	4.2
7.90	-1.25	0.0
8.20	-1.46	0.0

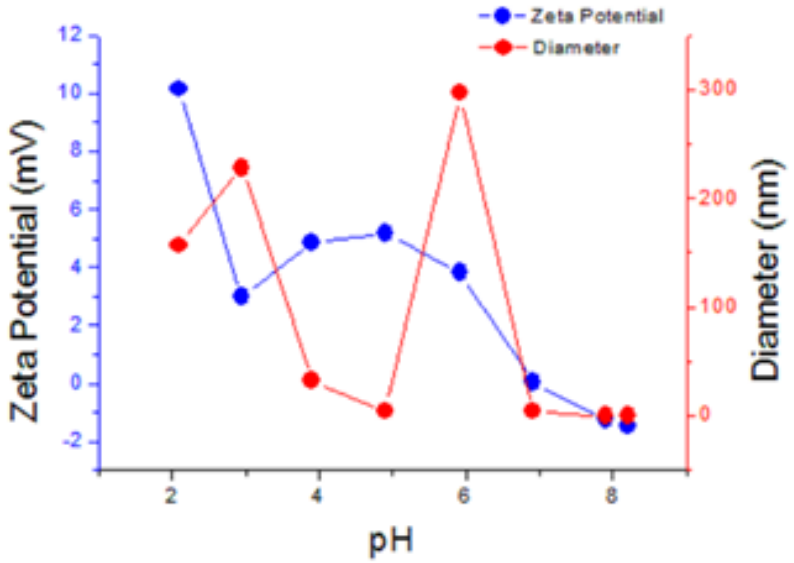

Figure 3.14 Analysis results for pH 2 to 9 (0.4:1 ligand:gold).

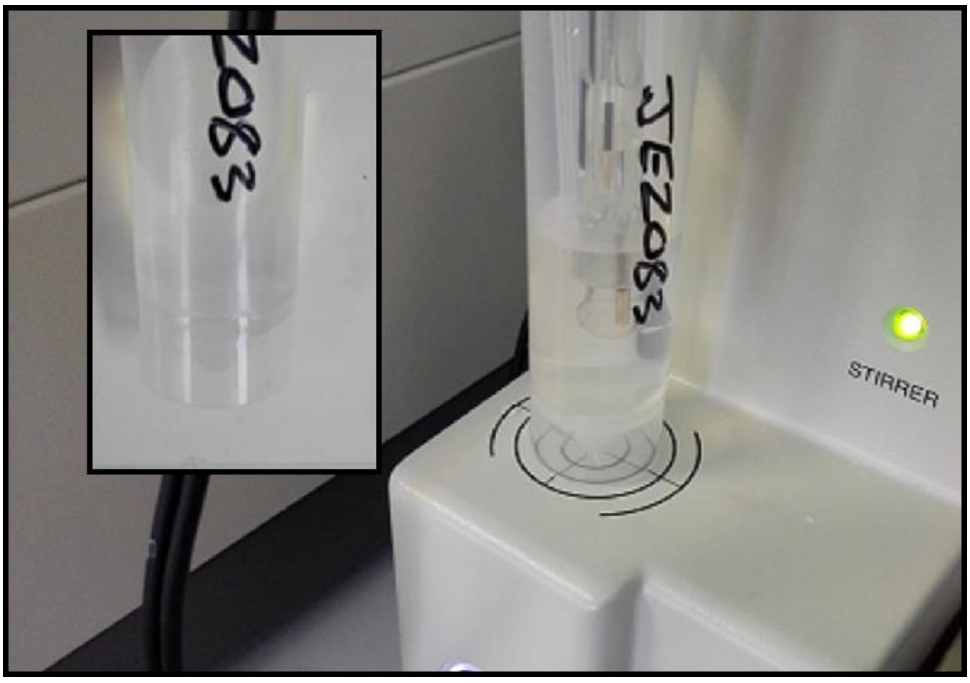

Figure 3.15 Colour of sample solution before (inset) and after analysis from pH 2 to 9.

After 24 h, most of the 20 ml aqueous layer was syringed from the top of the organic layer and placed in the sample vial of the NanoPlus instrument, after which the initial pH and zeta potential readings was taken. Subsequently further aliquots of PTA were then added and the pH and zeta potentials measured. The PTA was added in increments such that a final Au:PTA ratio of roughly 1:1 was obtained. The results are tabulated in Table 3.1 and also shown graphically in Figure 3.16.

Table 3.1 Change in pH and zeta potential with addition of PTA ligand.

Total Mass of PTA added after initial extraction (g)	pH	Zeta Potential
-	2.3	29.53
0.0021	2.98	29.58
0.0046	3.73	27.20
0.0083	5.21	23.81
0.0138	5.74	16.67
0.0186	5.96	15.20

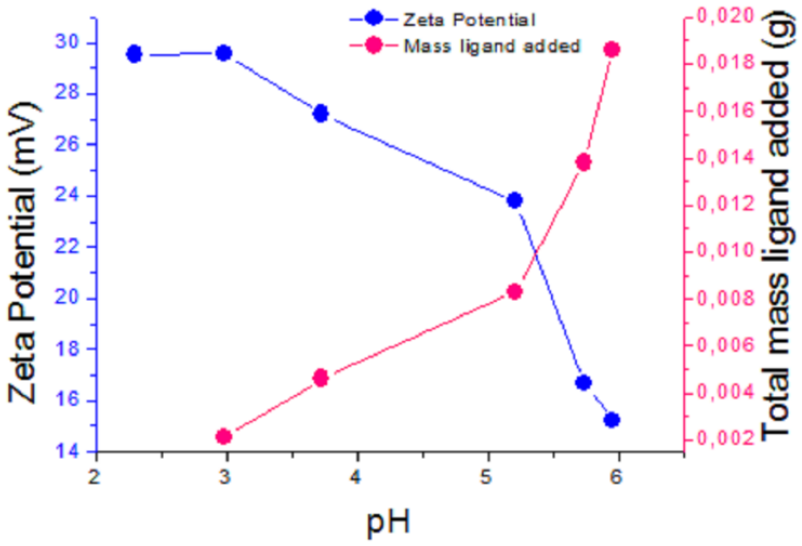

Figure 3.16 Zeta potential vs pH for successive addition of PTA after extraction.

It is clear from the above data that the addition of PTA increases the pH and lowers the zeta potential. A zeta potential which decreases would usually suggest a loss of stability of colloids and hence a greater probability of agglomeration occurring. However, with the ligand stabilized nanoparticles which are water soluble, it would suggest that the nanoparticles are becoming more soluble due to further attachment of the additional ligand to

the nanoparticle surface. In other words, the charge difference between the slipping plane and Stern potential becomes smaller due to the ligand enhancing solubility with each addition of PTA; *i.e.* the particle becomes more dissolved in the liquid with each addition of ligand and is thus better stabilized.

When starting with a 1:1 Au:PTA ratio, the zeta potential remains unchanged at close to zero with changes in pH from acidic to basic by the addition of aliquots of 0.1 M NaOH solution (Figure 3.17). This shows that the nanoparticles are stabilized and rendered completely soluble in the aqueous layer; the difference in charge between the surfaces of the nanoparticles and of the aqueous layer being more or less identical and resulting in zeta potentials very close to zero which appears unaffected by changes in pH.

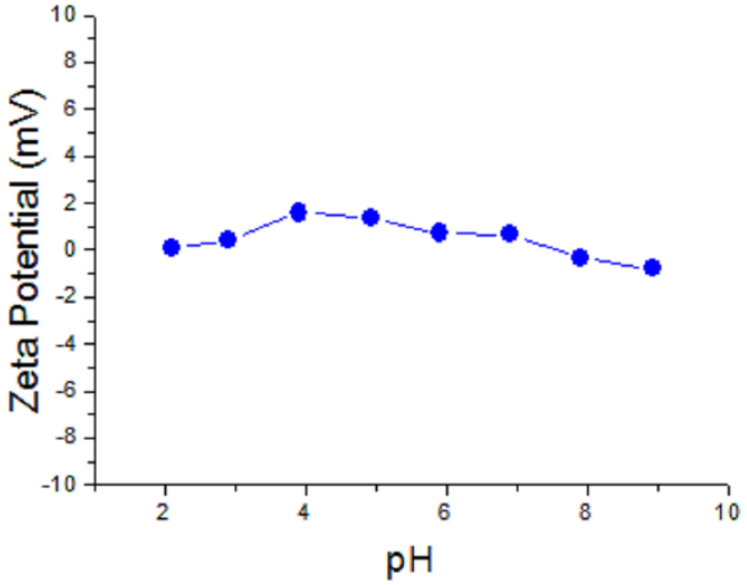

Figure 3.17 Relative constant zeta potential close to zero with changes in pH after extraction with 1:1 Au:PTA.

3.3.2.2 Effect of ligand type

A similar experiment using triphenylphosphine trisulphonate (TPPTS) as ligand was also performed. This was in order to assess whether the larger TPPTS ligand would better stabilize the nanoparticles, thereby making it possible to obtain hydrodynamic diameters of only the nanoparticle and ligand and not equivalent spherical diameters of aggregates as had been observed with PTA. The results are tabulated in Table 3.2 with Figure 3.18 showing the graphical representation of these results.

Table 3.2 Change in pH and zeta potential with addition of TPPTS ligand.

Total Mass of TPPTS added after extraction (g)	pH	Zeta Potential
-	8.88	-0.81
0.00129	10.21	-3.81
0.0263	11.56	62.56
0.0373	11.83	-0.72
0.0463	11.95	-0.01
0.0584	12.07	-1.06

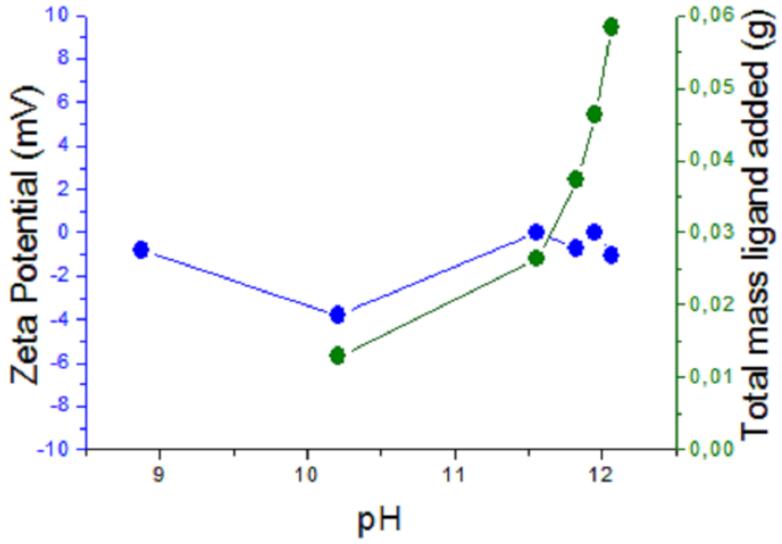

Figure 3.18 Zeta potential vs pH for successive addition of TPPTS after extraction.

It can clearly be seen that TPPTS imparts a far more basic character to the aqueous solution which is pH 8.8 after extraction compared to pH 2.3 for PTA extraction. The pH then increases with subsequent addition of TPPTS resulting in a pH of 12.07 when a 1:1 Au:TPPTS ratio in the aqueous layer is reached.

What is also evident is that the zeta potential remains relatively close to zero and therefore suggests that TPPTS renders the nanoparticles soluble in the aqueous layer more readily than PTA. Despite this observation, TEM results show that nanoparticle size evolution after extraction follows a similar path to that of when PTA is used as a ligand and appears to offer no advantage over PTA as a stabilizing ligand.

For both sets of experiments where PTA and TPPTS were incrementally added, no clear pattern in size could be observed which could be correlated to the addition of the ligand. As before, sizes ranged from below 10 nm up to greater than 1000 nm or more.

3.4 Summary and Conclusion

Initial endeavours to measure nanoparticle size using DLS resulted in observed particle sizes up to 10^3 times or more greater than those determined by TEM. This was due to the nature of the stabilized nanoparticles resulting in the hydrodynamic diameter measured being much larger than that of individual particles. Two major factors contributed to this; aggregates of nanoparticles which were being seen as single large particles and the attached ligands slowing down the Brownian motion which could be interpreted as the presence of large particles.

It was anticipated that by varying the pH and subsequent zeta potential, the aggregates would disperse and that it would thus be possible to measure particle sizes which were closer to that observed by TEM at the determined pH value. However, although it initially appeared that a pH of 7 was promising, further experiments showed that in fact agglomeration was predominating with particles settling out of solution. This suggested that perhaps ligand stabilization was not adequate under these conditions.

Experiments were then carried out firstly with an increased PTA ligand concentration where the pH was varied. This resulted in very little fluctuation of the zeta potential. With no sedimentation occurring, it suggested that the particles were thus better dissolved and not as prone to settling out of solution.

It was then intended to determine whether further addition of ligand would stabilize the nanoparticles by rendering them more soluble after extraction. Incremental addition of ligand after starting with a low PTA:Au ratio showed that the pH increased while the zeta potential decreased with further addition of ligand. Again, with no sedimentation occurring, it showed that additional PTA ligand could further stabilize nanoparticles by rendering them more soluble.

When starting with a high PTA:Au ratio, the zeta potential started at close to zero and remained constant with further addition of ligand. This indicated that a high ratio immediately stabilizes the nanoparticles and prevents agglomeration and subsequent sedimentation from occurring.

In contrast, in a similar experiment using the larger TPPTS ligand, the zeta potential started close to zero when using a low TPPTS:Au ratio. This initially indicated that in fact the larger ligand did have a greater stabilizing effect. However, subsequent TEM analysis showed that the evolution of nanoparticle size from initial extraction to the end of a 24 h period was similar to that seen for PTA as stabilizing ligand. No advantage in terms of final size obtained was thus gained by using TPPTS instead of PTA.

Therefore, although it was initially intended to use DLS as a technique to rapidly and more cost effectively measure particle size, it proved unsuitable for use with the ligand stabilized, water-soluble gold nanoparticles. Further experiments did however reveal more about how better nanoparticle stabilization could be achieved through increasing the ligand concentration. The technique was thus valuable in learning about the nanoparticle environment and therefore serves a useful aid in guiding nanoparticle synthesis strategies.

3.5 References

(1) Campbell, C. T.; Sharp, J. C.; Yao, Y. X.; Karp, E. M.; Silbaugh, T. L. *Faraday Discuss.* **2011**, *152*, 227.

(2) *Modern Methods of Particle Size Analysis*; G. Barth, H., Ed.; John Wiley & Sons, Inc.: New York, 1984.

(3) Zheng, T.; Bott, S.; Huo, Q. *ACS Appl. Mater. Interfaces* **2016**, *8* (33), 21585.

(4) Verma, M. S.; Rogowski, J. L.; Jones, L.; Gu, F. X. *Biotechnol. Adv.* **2015**, *33* (6), 666.

(5) Liu, X.; Dai, Q.; Austin, L.; Coutts, J.; Knowles, G.; Zou, J.; Chen, H.; Huo, Q. *J. Am. Chem. Soc.* **2008**, *130* (9), 2780.

(6) Benoit, D. N.; Zhu, H.; Lilierose, M. H.; Verm, R. A.; Ali, N.; Morrison, A. N.; Fortner, J. D.; Avendano, C.; Colvin, V. L. *Anal. Chem.* **2012**, *84* (21), 9238.

(7) Berne, B. J.; Pecora, R. *Dynamic light scattering :with applications to chemistry, biology and physics*; Dover Publications, Inc.: Mineola, New York, 2000.

(8) Edward, J. T. *J. Chem. Educ.* **1970**, *47* (4), 261.

(9) Jennings, B. R.; Parslow, K. *Proc. R. Soc. Lond. A. Math. Phys. Sci.* **1988**, *419* (1856), 137.

(10) Instruments, M. *Malvern Guides*. 2011, pp 1–6.

(11) Malvern Instrument Ltd. In *Zetasizer Nano Series User Manual*; 2004; p 16.2.

(12) Salopek, B.; Krasic, D.; Filipovic, S. *Rud. Zb.* **1992**, *4*, 147.

(13) http://www.webexhibits.org/causesofcolor/9 .html.

(14) Chansuvarn, W.; Tuntulani, T.; Imyim, A. *TrAC - Trends Anal. Chem.* **2015**, *65*, 83.

(15) Xie, X.; Xu, W.; Liu, X. *Acc. Chem. Res.* **2012**, *45* (9), 1511.

Chapter 4

Optimization of Nanoparticle Synthesis Methods for Improved Stabilization against Agglomeration

---

4.1 Introduction

In Chapter 3 it was attempted to utilize Dynamic Light Scattering (DLS) as a rapid and cost effective technique to measure nanoparticle size. Although it was found to be unsuitable for size measurement of the nanoparticles synthesized by the dendrimer micelle template extraction method, DLS did provide valuable information regarding nanoparticle stabilization. It was found that increasing the ligand to metal ratio resulted in an increase in solubility of the extracted gold nanoparticles in the aqueous layer. It was thus hypothesised that this increased solubility translated into better stabilization of the nanoparticles and would make the postulated "divide-and-protect" mechanism (as discussed in Chapter 2) proceed with greater efficiency and subsequently would result in consistent synthesis of gold nanoparticles closer to the desired Au_{55} cluster size of approximately 1.5 nm.

However, despite subsequent synthetic procedures utilizing the 1:1 micelle:Au ratio, the nanoparticles produced for consecutive experiments under the same conditions varied in size. These results thus indicated that nanoparticle stabilization was not the major determining factor in achieving synthesis reproducibility, but that improved control over additional synthesis parameters were required in order to improve nanoparticle synthesis reproducibility. In light of this, it was aimed to evaluate each fundamental step in the formation of the gold nanoparticles; from reduction and generation of Au^0, to the factors governing nucleation of the Au^0 atoms and further growth into nanoparticles of a particular size, as well as stabilization of the nanoparticles upon extraction from the dendrimer micelle template.

As discussed in Chapter 1, the most widely accepted mechanism of nucleation and growth is that proposed by LaMer.[1,2] By way of reminder, the mechanism is separated into three stages as depicted in Figure 4.1. The first stage is the rapid increase in the concentration of monomers. In the case of gold nanoparticle synthesis, the rapid increase in the concentration of monomers is due to the generation of Au^0 atoms upon reduction of $HAuCl_4$. The

concentration of the monomer increases until a saturation point C_{sol} is reached, after which they are no longer soluble. The concentration of monomer further increases until a critical concentration (C_{crit}) is reached where rapid nucleation occurs (stage **II**). The rate of nucleation is described as "effectively infinite". This rapid nucleation (or "burst nucleation") continues until the monomer concentration decreases and stabilizes (stage **III**).

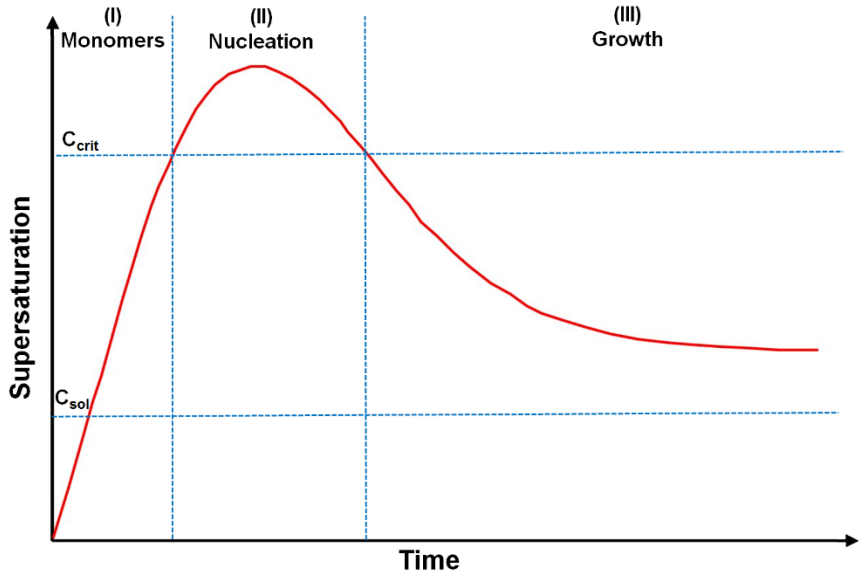

Figure 4.1 LaMer diagram schematic.

The above clearly indicates how critical the reduction step is in the synthesis process since the concentration of the monomers (*i.e.*Au^0) and the rate at which they are generated is critical to subsequent nucleation and growth. In this regard the initial concentration of $HAuCl_4$ is thus critical as it would determine the rate at which rapid or burst nucleation is reached and subsequently how large the resultant nanoparticles will initially become. Using small-angle X-ray scattering (SAXS) and X-ray absorption near-edge spectroscopy (XANES), Polte *et al* (2010) proposed that stage **I** proceeds according to 4 steps as Au^{3+} concentration decreases and Au^0 monomer concentration increases. This is illustrated in Figure 4.2. Although 4 steps are proposed, it is an extremely rapid process and, under the conditions employed by them, generation of Au^0 monomers and nucleation (*i.e.* stages **I** and **II**) occur in less than 200 milliseconds.[3,4] This observation would thus further reinforce the need to control initial gold salt concentration and reduction in order to consistently synthesise nanoparticles of a particular shape and size. Since the formation of nuclei/seeds occurs so rapidly, by having as close as possible control over reduction and initial gold salt

concentration, the consistency of these nuclei/seeds formed within the 200 millisecond timeframe could potentially be controlled with the subsequent merging of these resulting in more consistent sizes and shapes of the final nanoparticles formed.

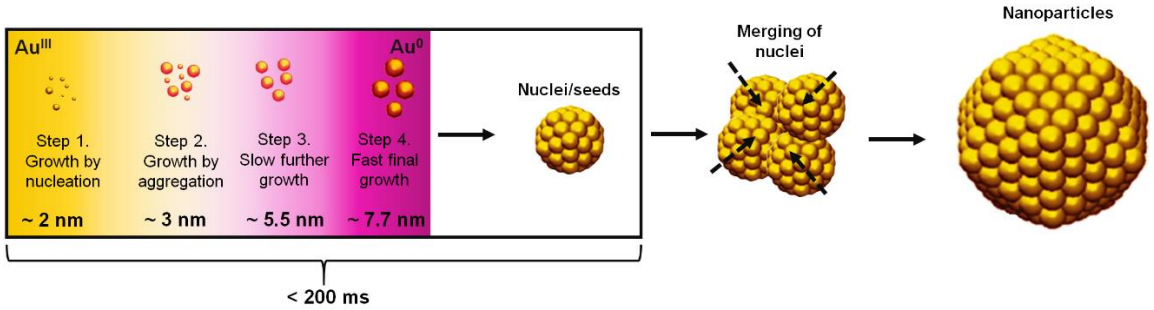

Figure 4.2 Process of gold nanoparticle formation as deduced by Polte *et al* (adapted from references 3 and 4).

As outlined in Chapter 1, nanoparticle growth proceeds either in a kinetically or thermodynamically controlled fashion, where thermodynamic growth results in the uniform growth of all crystal facets and thus the subsequent formation of spherical or near-spherical structures. With kinetic growth, the energetically preferential orientation of crystal facets favours directional growth and thus results in the formation of polyhedron shaped nanoparticles. Controlling whether thermodynamic or kinetic growth is dominant is a matter of adjusting reaction conditions. Tiny variations in growth conditions, such as sequence of addition of reducing and capping agents, and concentrations thereof, are of critical importance. However, synergistic effects of both thermodynamic and kinetic aspects is of further importance in determining final nanoparticle shape and size. Hence, due to the number of potential slight variations in reaction conditions which could result in variations in the final size and morphology of nanoparticles formed, it is extremely important to have as much as possible control over synthesis parameters.

Figure 4.3 shows TEM images of Au nanoparticles obtained for similar synthesis and extraction times under similar conditions. Coupled with this is a LaMer diagram depicting the expected shapes of nanoparticles at various times along the LaMer curve. What can be seen is a correspondence of these TEM images with nanoparticle shapes at various time periods along the LaMer diagram curve. It can thus be deduced that the inconsistency in nanoparticle shape and size which had been obtained, is due to variations in the initial rate of nucleation and growth. Considering that synthesis and extraction conditions and times were similar for each of the samples of which the TEM images are depicted, it could thus be implied that

variations could be arising in the rate of generation of monomers (*i.e.* reduction) and/or slight variations in the starting concentration of the gold salt which is subsequently reduced. The implication of these variations would be that varying rates of supersaturation are obtained which thus affects the time of onset and rate of nucleation and growth. In addition, variations in reduction and/or gold salt concentration may affect which mechanism of nucleation and growth is favoured and thus possibly also affecting the rate thereof. The effect then would be as seen in Figure 4.3 where varying shapes and sizes are obtained under similar synthesis and extraction conditions, and times.

Thus, by considering the above factors, it was attempted to control synthesis and extraction conditions in order to obtain consistent nanoparticle size and shape even if not the 1.5 nm size of a Au_{55} particle; the initial focus being on consistency of size with tailoring of the actual size to be considered thereafter.

4.2 Results and Discussion

Modifications to the Au nanoparticle synthesis procedure, described in Chapter 2, were made in order to evaluate various aspects of it in an attempt to achieve repeatability in the nanoparticle size obtained. The aspects to be evaluated were that of the reduction procedure, variations in stirring, the type of reactor vessel, the effect of reactor vessel size, and adjusting the procedure of Au nanoparticle extraction from the organic into the aqueous phase.

4.2.1 Effect of Reduction Procedure on Obtained Nanoparticle Size Repeatability

The effect of altering the reduction procedure on obtaining nanoparticle size repeatability was evaluated in round bottomed flasks. When considering previous reduction procedures, the $NaBH_4$ was dissolved in a small volume of methanol and added to the micelle/Au solution. As mentioned, this would typically be 0.01 g of $NaBH_4$ dissolved in 0.2 ml of methanol which was then added to a 20 ml micelle/Au solution. It was thought this concentrated solution of $NaBH_4$ could have resulted in some localized reduction upon addition thus contributing to the inconsistency in nanoparticle synthesis. Considering this then, the volume of MeOH was increased to 2 ml in order to get a more dilute concentration of $NaBH_4$ which would then possibly limit any localized reduction taking place.

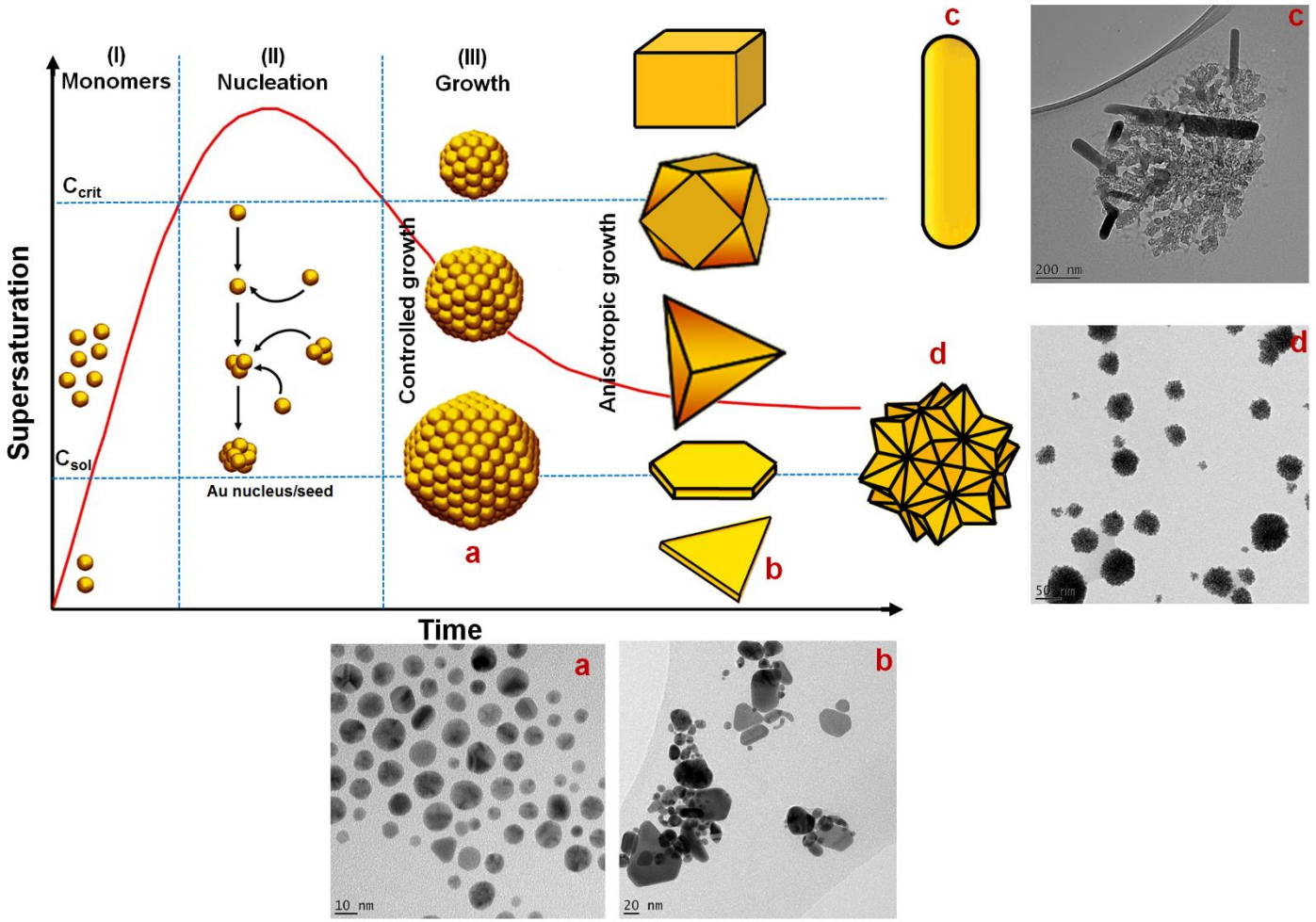

Figure 4.3 Comparison of final nanoparticle shapes obtained with shapes expected at different points in time along a LaMer diagram curve (modified from reference 5).

Furthermore, it was thought that the rate of addition of the $NaBH_4$ solution could also contribute to the synthesis inconsistency as fast addition could result in localized reduction which in turn could result in rapid growth of nanoparticles due to the high concentration of reduced Au^0 atoms being generated in a localized area.

Thus, in addition to the dilution of the $NaBH_4$, it was attempted to slowly add the reduction solution (using a dropping funnel) in order to avoid any possible localized reduction and subsequent rapid nanoparticle growth. If the rate were therefore to be controlled, it was thought that the rate of nanoparticle growth would be similar each time. It can however be seen from Figure 4.4 that, although dilution and slow reduction resulted in more uniformly shaped nanoparticles, the variation in size was still glaringly apparent for successive synthesis and extraction reactions; sizes varying between 29.7 nm ± 15.7 and 14.2 nm ± 10.8.

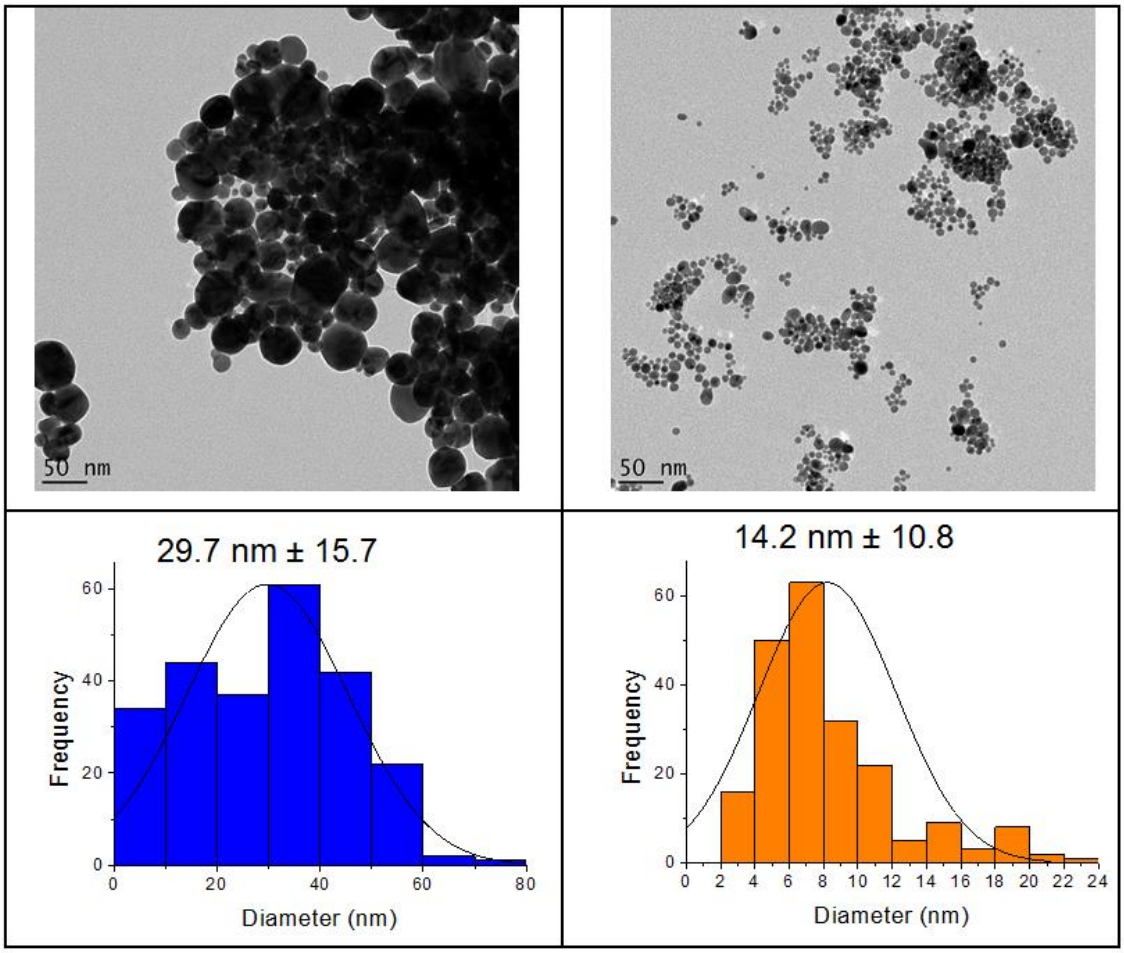

Figure 4.4 Comparison of nanoparticles synthesised using a slower addition rate of reducing agent under for successive synthesis procedures under similar conditions.

4.2.2 Effect of Reagent Measurement and Mixing Regimes on Obtained Nanoparticle Size Repeatability

From the above it could be seen that more controlled addition of the reducing agent resulted in more uniformly shaped nanoparticles, although size and size distribution still varied. A probable explanation for this, considering that reduction was similar in each case, was that there were variations in the Au and micelle concentration due to slight variances in the weighing of each for successive synthetic procedures.

At the scale of synthesis used to produce the nanoparticles up to this point, it should be considered that a difference in weighing out ± 0.0020 g of the 0.0340 g $HAuCl_4$ required, is equivalent to a variation of ± 5.9 % of the Au^0 atoms generated upon reduction. This variance in concentration of Au^0 atoms could thus contribute to the variances in the sizes of nanoparticles formed. Similarly, a difference in weighing out ± 0.0020 g of 0.0100 g of dendrimer micelle is equivalent to a ± 20 % difference in dendrimer micelle concentration and thus available stabilization for nanoparticles produced upon reduction. The variance in dendrimer micelle available for stabilization could thus result in slower or faster agglomeration in the organic phase and thus ultimately lead to variations in the final extracted nanoparticle size obtained. In a similar manner, any variation in the mass of PTA ligand in the aqueous phase could affect stabilization (negatively or positively) and subsequently final nanoparticle size.

In addition, if the retention and scaffolding properties of the dendrimer micelle are considered, it becomes apparent that stirring rate and/or efficiency could potentially contribute to the rate of nucleation and growth. Figure 4.5 shows a 3D rendering of the dendrimer micelle with a hypothetically sized and shaped nanoparticle encapsulated within it. It can be seen that orientation (a) appears to show a well encapsulated nanoparticle within a dendrimer exhibiting good retention and scaffolding properties. However, once rotated it becomes clear that encapsulation is not optimum (b and c) and that there is potential for nanoparticles to be exposed and for agglomeration to occur if orientation of dendrimer micelles are favourable. In addition, this shows a lack of potential retention ability. Up to this point, Au nanoparticle synthesis and extraction had been carried out in round bottomed flasks where different stirrer plates, different sized stirrer bars, and flasks. Although stirrer speeds were set at the same value when using different stirrers, there may have been differences in the actual stirrer speeds. Therefore, in conjunction with using different sized stirrer bars and

flasks, the subsequent potential variations in mixing regimes may have contributed the variation in nanoparticle size for consecutive synthetic procedures. This is because stirring facilitating dendrimer micelle orientations which favour agglomeration or instances where nanoparticles are not retained within them due to shearing forces caused by the stirring regime. These orientations and/or possible release of nanoparticles from the dendrimer micelle interior are most likely completely random, therefore adding to synthesis inconsistency. Therefore, in order to try and eliminate these variations, a parallel reactor system was utilized. This allowed for stirring speed to theoretically be equal across the six reactions while also maintaining a set temperature (thus eliminating temperature fluctuations which was earlier identified as a possible source of synthesis inconsistency).

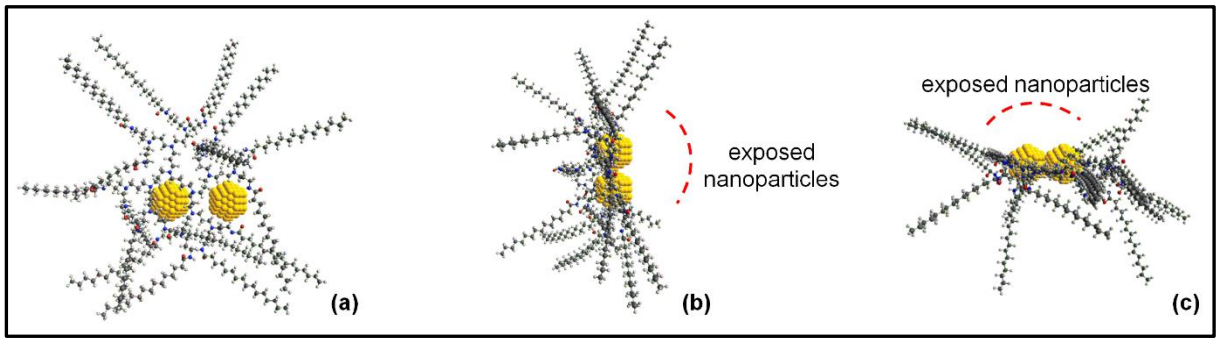

Figure 4.5 3D rendering of dendrimer encapsulated nanoparticles (of hypothetical size and shape) showing potential lack of stabilization which may facilitate some agglomeration.

In the first part of this evaluation then, weighing out of reagents into six reactor tubes of the parallel reactor, were made as close and as accurately as possible to each other (to within ± 0.0001 g). Solvents were also measured out with a pipette (as opposed to a syringe) in an attempt to further increase accuracy in the concentrations of reactants. A second set of six reactions were then performed using stock solutions of each reagent. It was thought that even if the concentrations were not completely accurate, it would however be exactly the same for each reaction and hence produce similar sized nanoparticles if having all other reaction conditions the same as well.

Secondly, in an attempt to determine the effect of mixing efficiency (which could possibly have an effect on reducing efficiency and dendrimer micelle orientation as mentioned earlier), different pairs of stirrer bars were used (Figure 4.6). In this way, pairs of reactions could be compared with each and the effect of differing mixing regimes related to each other while also being able to judge synthesis repeatability between pairs. The resulting mixing

regimes of blank runs, shown in Figure 4.7, were carried out with just chloroform and water, therefore mimicking the bi-phasic reaction environment under which nanoparticle synthesis would occur. It shows that the vortices created (which would play a role in nanoparticle formation) were roughly related to the size of the stirrer bars, but that interestingly, no pair were exactly identical.

Figure 4.6 Differences in pairs of stirrer bars used for parallel reaction

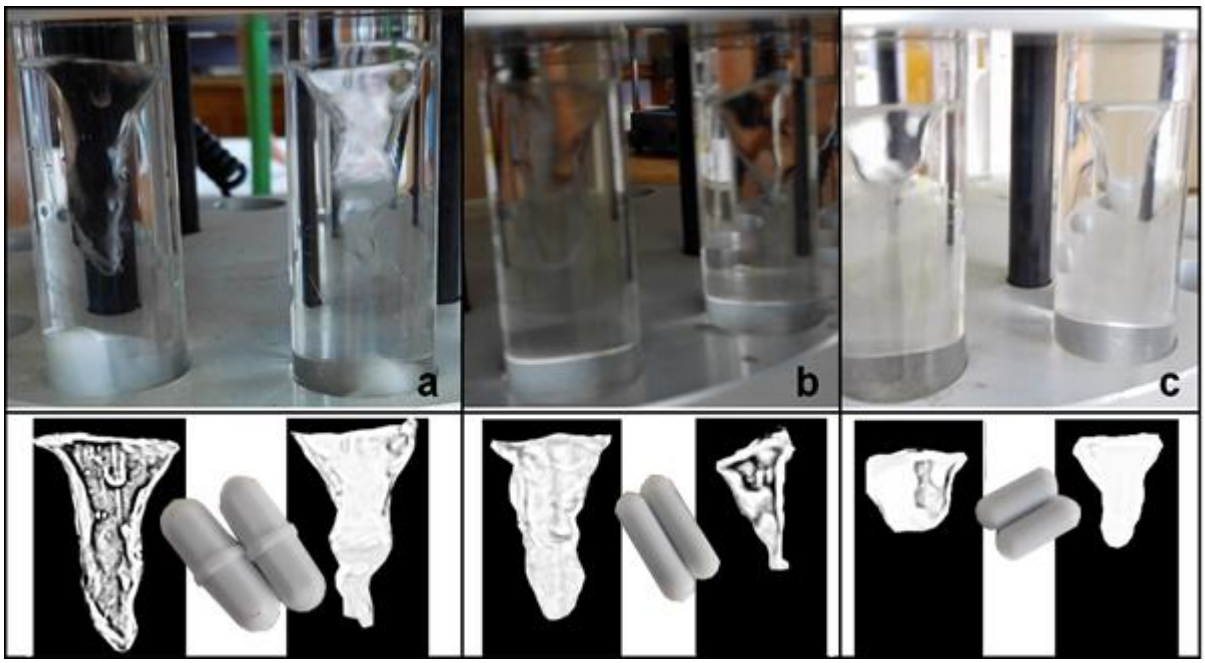

Figure 4.7 Comparison of vortices created, and thus mixing regimes, by sets of stirrer bars **a**, **b** and **c** (images manipulated to remove backgrounds thereby only highlighting vortex area).

After dissolution of the micelle and $HAuCl_4$ (JEZ092 to JEZ097 – reagents separately weighed out to within ±0.0001 g for each reaction), the reduction solution was added in a dropwise manner, as slowly as possible, such that the 2 ml was added over a period of 1 minute. Table 4.1 shows which stirrer bars were used for each pair of reactions.

Table 4.1 Reaction codes and stirrer bar pairs (individually measured reagents and solvents).

Reaction Code	Stirrer Bar Pair
JEZ092 JEZ093	
JEZ094 JEZ095	
JEZ096 JEZ097	

However, as can be seen in Figure 4.8 (shown after addition of the aqueous ligand solution), the pairs of reactions, which theoretically should have been similar in appearance, are all different. The varying colours of the organic layers allude to different sizes (and most likely varying shapes) of nanoparticles having been formed. This result shows a relationship with the above observation that none of the pairs of what should be similar mixing regimes, are actually alike.

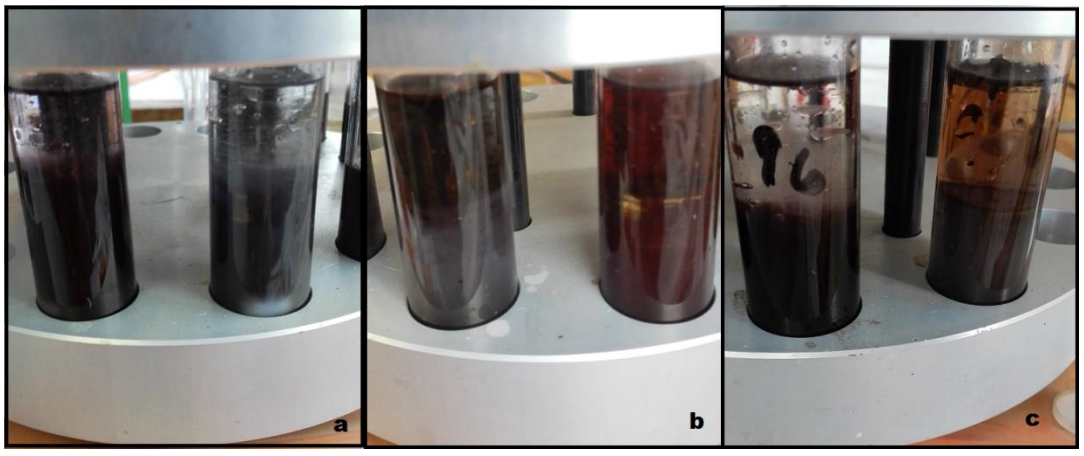

Figure 4.8 Differences in the organic and aqueous layers for each pair of reactions.

Figure 4.9 shows the UV-vis spectra of the extracted nanoparticles and the aqueous layers immediately after the 24 h extraction time and after being separated from the organic layer. Again, clear differences of pairs that should be similar are visibly apparent. As previously reported, a 1:1 Au:PTA ratio results in the masking of the plasmon resonance peak. As a result, no plasmon resonance peak is visible in Figure 4.9. However, absorption bands are visible at around 245 and 285 nm for JEZ093, JEZ095 and JEZ097. From literature there are suggestions that these might be due to gold-phosphine interactions[6]. The similarities in the absorption bands for JEZ095 and JEZ097 might suggest that similar numbers of ligand are coordinated to similarly sized and shaped nanoparticles. The difference in the absorption bands for JEZ093 compared to these may then suggest that although a similar number of ligands are coordinated, the size (and possibly shape) is different. The tentative conclusion on size and shape is based on the colour of the separated aqueous solutions; the colour of JEZ095 and JEZ097 being similarly colourless and clear with JEZ093 being a clear purple colour. Likewise then, it may be that JEZ092 has particle sizes similar to JEZ095 and JEZ097, but with a differing number of ligands coordinated. JEZ094 and JEZ096 thus have similar numbers of ligand coordinated, but with clear differences in nanoparticle size.

Transmission electron microscopy (TEM, Figure 4.10) confirms what could be deduced visually and by means of UV-vis; that no two pairs of reactions using the same pair of stirrer bars produced nanoparticles having similar average sizes and shapes. In fact none of the nanoparticles were similar in appearance except for JEZ093 and JEZ094 even though being a pair utilizing different stirrer bars. These were in fact the only two samples from which average sizes could be determined; 10.2 nm ± 3.2 and 6.8 nm ± 2.1 for JEZ093 and JEZ094 respectively.

JEZ092 produced large nanoparticles in the region of close to 100 nm while rods were also observed. JEZ095 was seen to contain even larger nanoparticles (up to 200 nm), while JEZ096 contained irregularly shaped nanoparticles suggesting formation of unstable nanoparticles. JEZ097 produced micrometre sized structures.

By comparing the TEM images to the colours of the separated aqueous layer samples in Figure 4.9, it can be seen that the clear solutions (JEZ092, JEZ095 and JEZ097) contained the extremely large gold particles, while the blue coloured solutions (JEZ092 and JEZ093) contained nanoparticles between approximately 5 and 13 nm (with JEZ093, the lighter blue

sample, containing the smaller average size). The irregularly, blob shaped nanoparticles of JEZ096 appears to have produced a light red sample.

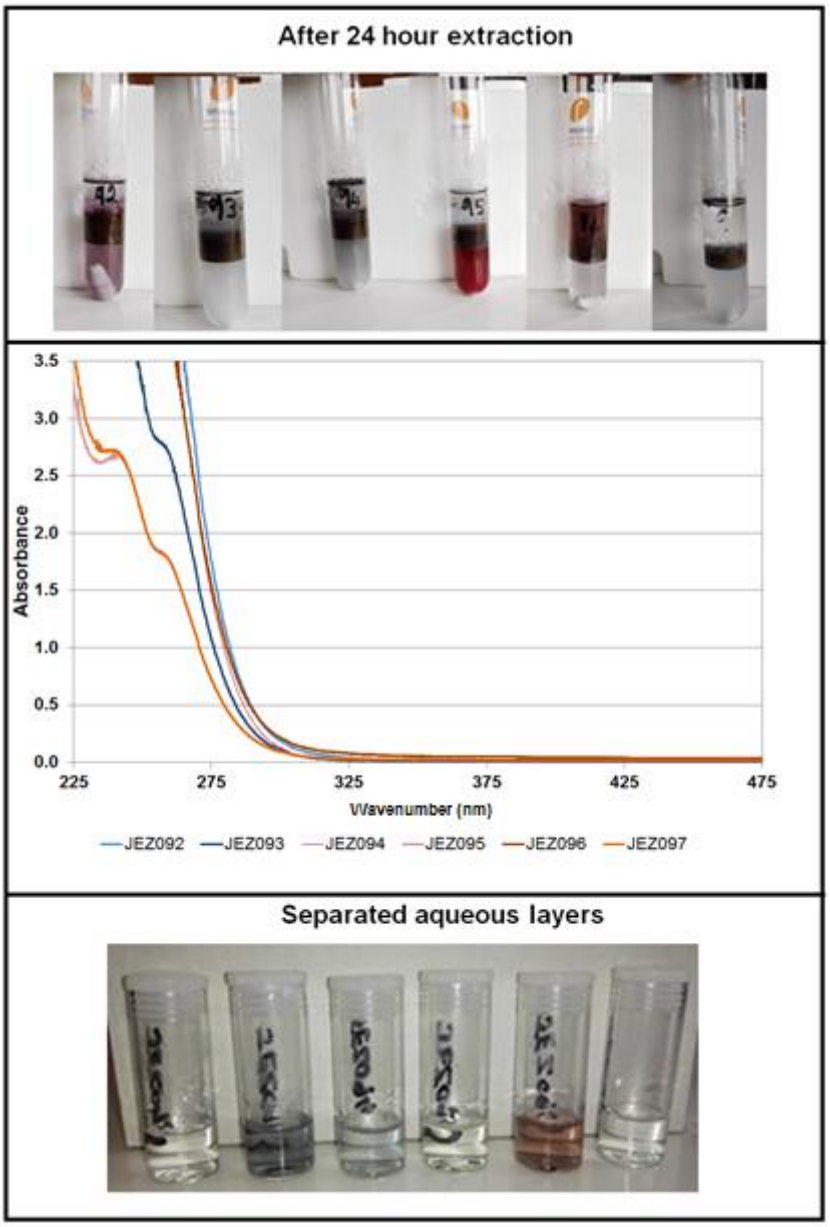

Figure 4.9 Appearance of reaction mixture after 24 h of extraction (top), appearance of the separated aqueous layer (bottom) and UV-vis spectrum of the aqueous layer.

No correlation can however be made between the nanoparticle size and the UV-vis spectra (Figure 4.9). The differences in the spectra (observed absorption bands) are then just due to the gold-phosphine interactions and not due to both interactions and size as initially speculated. The above seems to strongly suggest that differences in stirring regimes do result in varying environments where random dendrimer micelle configurations which either

facilitate agglomeration (Figure 4.11a) resulting in larger particles being extracted, or cause them to configure in such a manner so as to provide sufficient stabilization resulting in smaller nanoparticles being extracted (Figure 4.11b). Alternatively (or possibly in conjunction with) release of nanoparticles due to the shearing forces created by the stirring regime may also have occurred, resulting in unprotected nanoparticles vulnerable to agglomeration (Figure 4.12). The larger extracted nanoparticles are then not as easily stabilized by the PTA ligand in the aqueous layer thus limiting any mechanistic advantage. Conversely, smaller nanoparticles transported to the aqueous phase more readily undergoes the "divide-and-protect" mechanism thus resulting in the smaller nanoparticle sizes observed. Although the above suggests that it is the randomness of dendrimer micelle orientation which results in nanoparticle synthesis inconsistency, it was attempted to evaluate the "variation in randomness" if exactly the same solution and hence reagent concentrations were used for all reactions.

Subsequently then, JEZ098 to JEZ103 were carried out similarly to JEZ092 to JEZ097 except that a 60 ml micelle/gold solution was pre-prepared (using a pipette to measure out the volume). This was divided between the six reaction tubes using a pipette to measure 10 ml into each. Thus in this way exactly the same solution was in each of the reaction tubes. Similarly, a 6 ml $NaBH_4$ solution was prepared and added to each Au/micelle solution during the reduction step. In addition, a 60 ml solution of the PTA ligand in water was prepared and 10 ml added with a pipette to each reaction tube to effect extraction of the Au nanoparticles.

The effect of the consistency in using exactly the same solutions throughout as well as adding the reducing agent at exactly the same rate is clearly apparent from Figure 4. ***13*** with similar looking solutions obtained for JEZ098 to JEZ101 and only JEZ102 and JEZ103 having differing appearances. The visible similarities in the samples are further emphasized after separation of the aqueous layer. Although it appeared different immediately after the end of extraction, the separated aqueous layer of JEZ102 now appeared identical to JEZ098 to JEZ101; the exception still being JEZ103. Even though different in appearance, the UV-vis spectrum is however still similar to the rest.

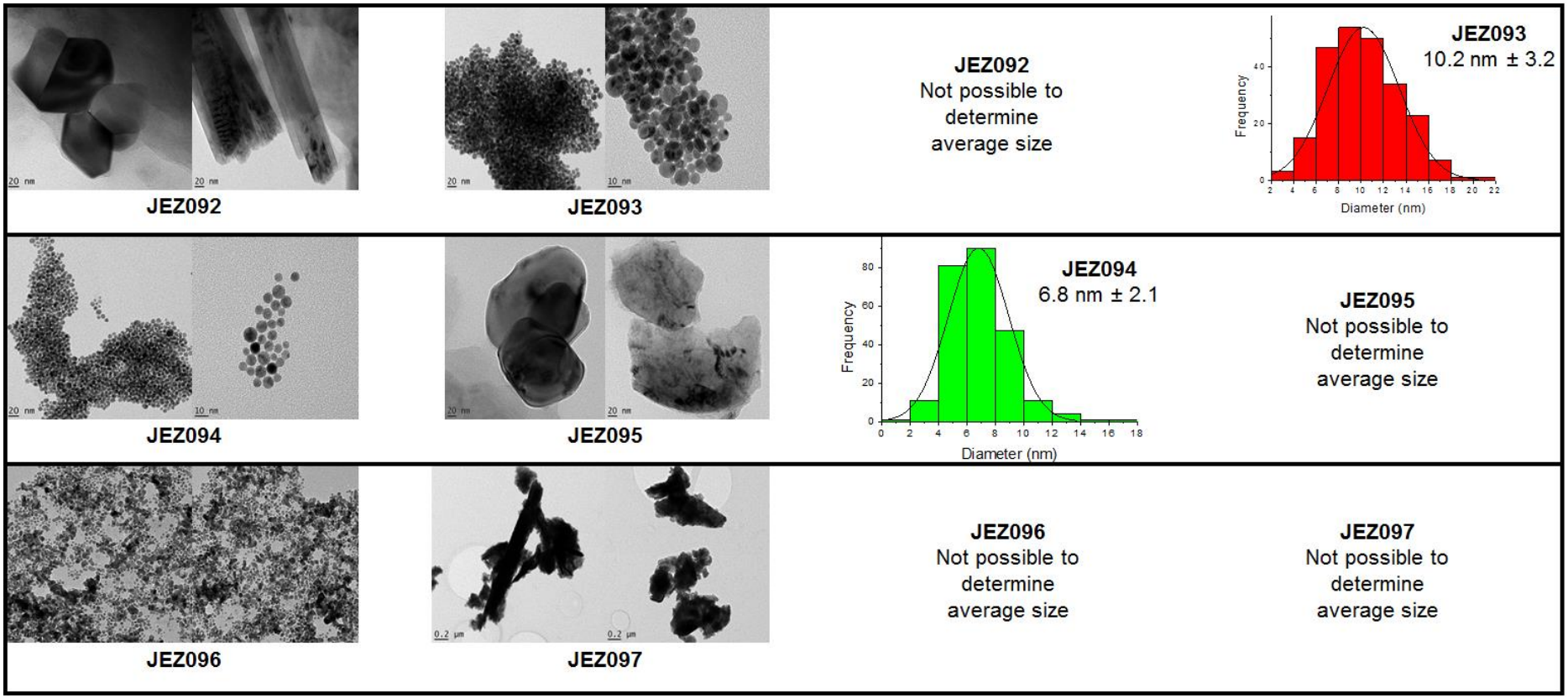

Figure 4.10 TEM images of JEZ092 to JEZ097.

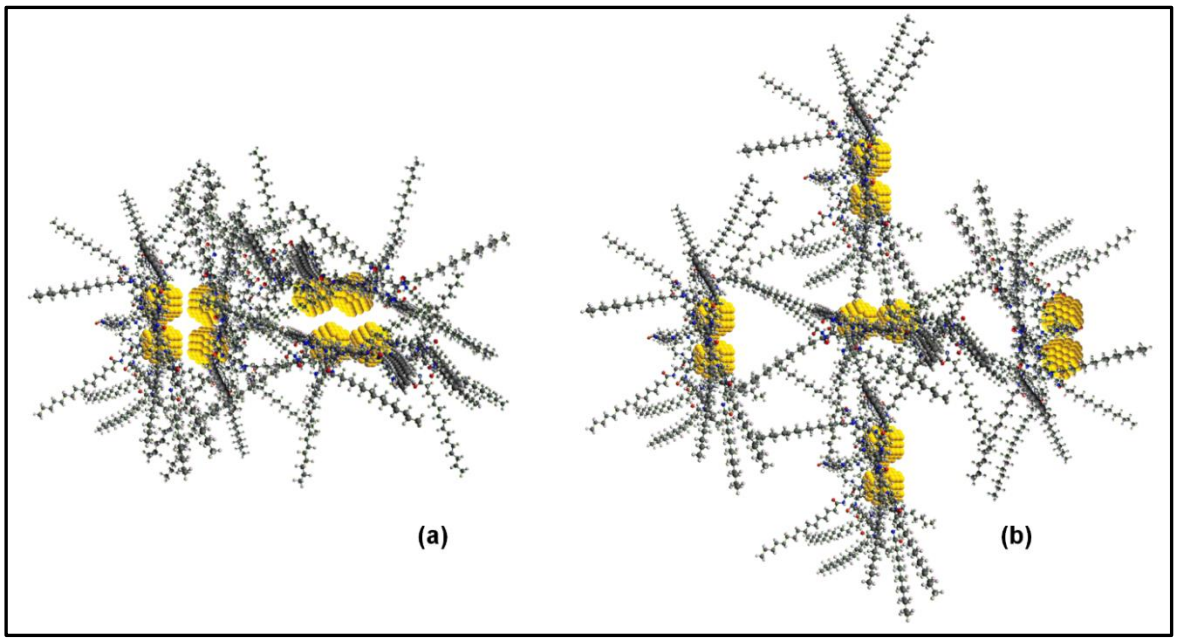

Figure 4.11 Dendrimer micelle orientations which would result in agglomeration (**a**) and stabilization (**b**).

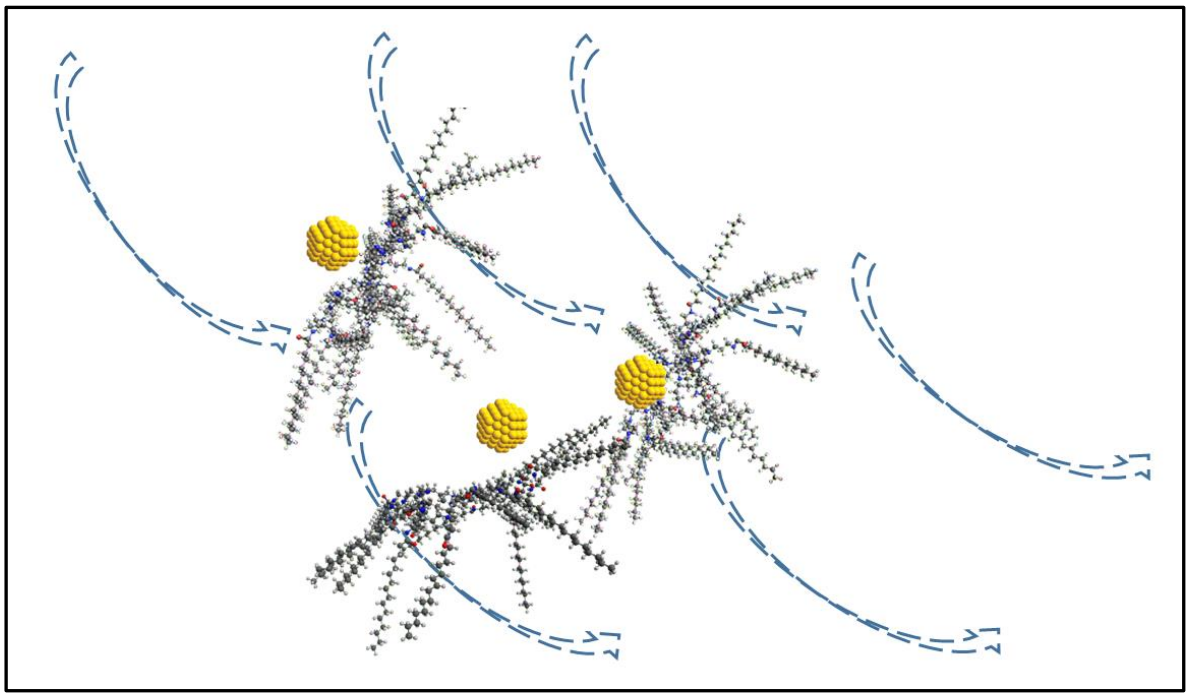

Figure 4.12 Illustration of possible shearing forces caused by mixing regime potentially resulting in release of nanoparticles from dendrimer micelle interior (dotted arrows depicting hypothetical forces being applied).

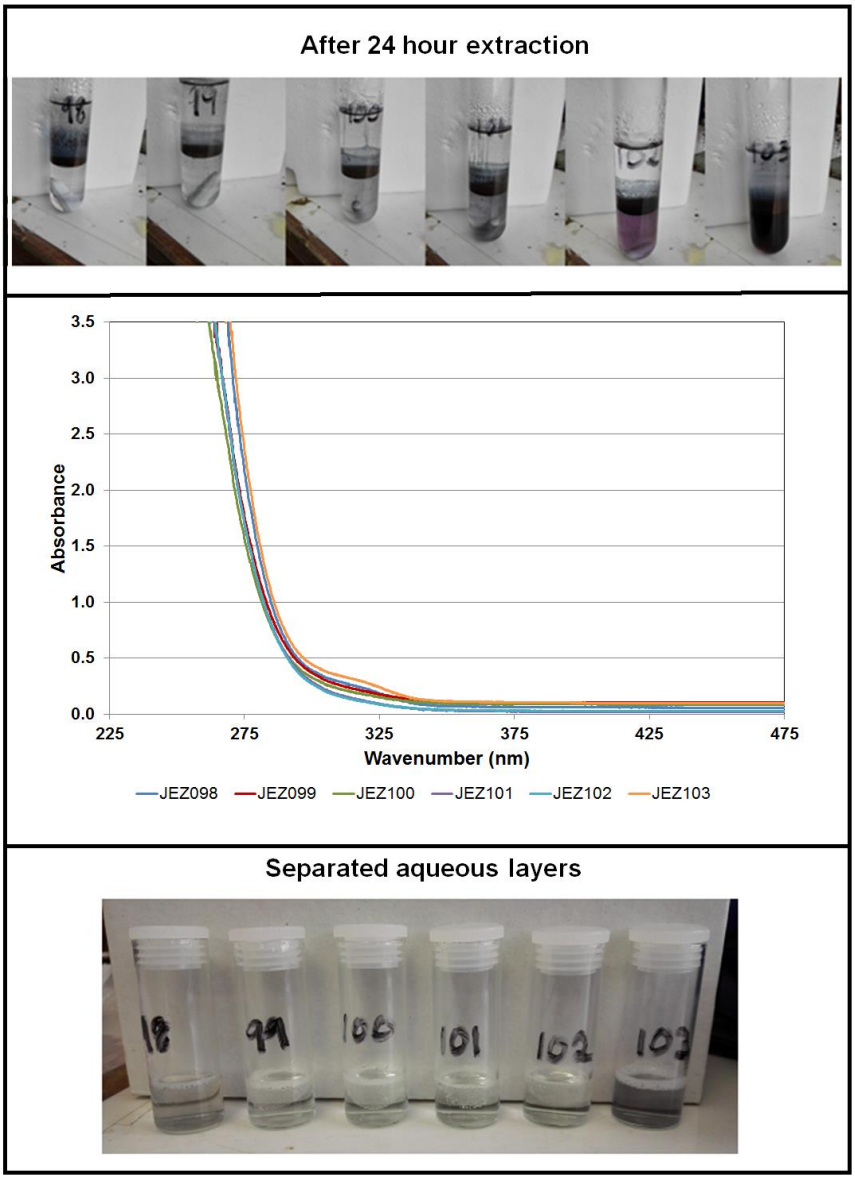

Figure 4. 13 Appearance of reaction mixture after 24 h of extraction (top), appearance of the separated aqueous layer (bottom) and UV-vis spectrum of the aqueous layer for samples prepared from stock solutions.

In contrast to the first set of experiments, average sizes for four out of the six samples could be obtained from TEM (Figure 4.14). Interestingly, the sample most different in appearance (JEZ103) yielded the smallest average nanoparticle size. The TEM images also clarify the similarities in the UV-vis spectra where it can be seen that the sizes obtained were fairly similar; being within the standard deviations of each of the samples from which an average size could be obtained. These average sizes were larger than the first set of experiments with standard deviations observed also being much broader. The broader size distributions compared to the first set of experiments indicate that nanoparticle nucleation and growth was slower (and still ongoing) and thus resulted in more countable particles compared to the

overgrown structures (resulting from rapid nucleation and growth) obtained for the majority of the first set of experiments. From the above observations, it is thus clear that where separate measuring of reagent masses and making up of solutions were done, a greater variety of nanoparticle sizes were obtained compared to where stock solutions were used. This therefore suggests that "variation in randomness" of dendrimer micelle orientation is limited when using the same solutions of reagents for successive nanoparticle synthesis procedures despite the previously observed variation in mixing regimes. It is therefore clear that although it appears that due to the architecture of the dendrimer micelle used, random orientations of it may contribute to agglomeration (or loss from the interior) or stabilization to various degrees and thus the inconsistency in nanoparticle sizes obtained. However, it appears that maintaining exact concentrations of reagents from one synthesis to another limits the variation in orientation despite differences in mixing regimes.

4.2.3 Evaluation of Custom Reactor Set-up for Nanoparticle Synthesis

The above provided positive indications as to parameters which could possibly be controlled in order to consistently synthesise the desired nanoparticles. Although each variation to the previously established synthesis and extraction procedure showed promise, it appeared that randomness in dendrimer micelle orientation still presented a challenge in controlling reproducibility of nanoparticles obtained from successive procedures. However, the randomness of orientation appeared to be limited if reagent concentrations were constant (*i.e.* use if stock solutions) for successive synthesis procedures. With this in mind, it was thought that although it was aimed to be as accurate as possible manually, using an automated system to exercise even greater control over process conditions may further limit variation in the synthesis and extraction procedure.

The effectiveness of using an automated nanoparticle synthesis system was demonstrated by Ftouni *et al* (2012).[7] They synthesised 1.8 nm gold nanoparticles with narrow size distribution by means of the Turkevich method (15 nm particles are produced under classical conditions) in high yields using a continuous flow capillary reactor. The reactor, made from commercially available items, allowed for short mixing, heating and quenching times which are critical parameters for the Turkevich method. The effectiveness of the micro-reactor compared to that of classical glassware in the synthesis of gold nanoparticles is shown in Figure 4.15.

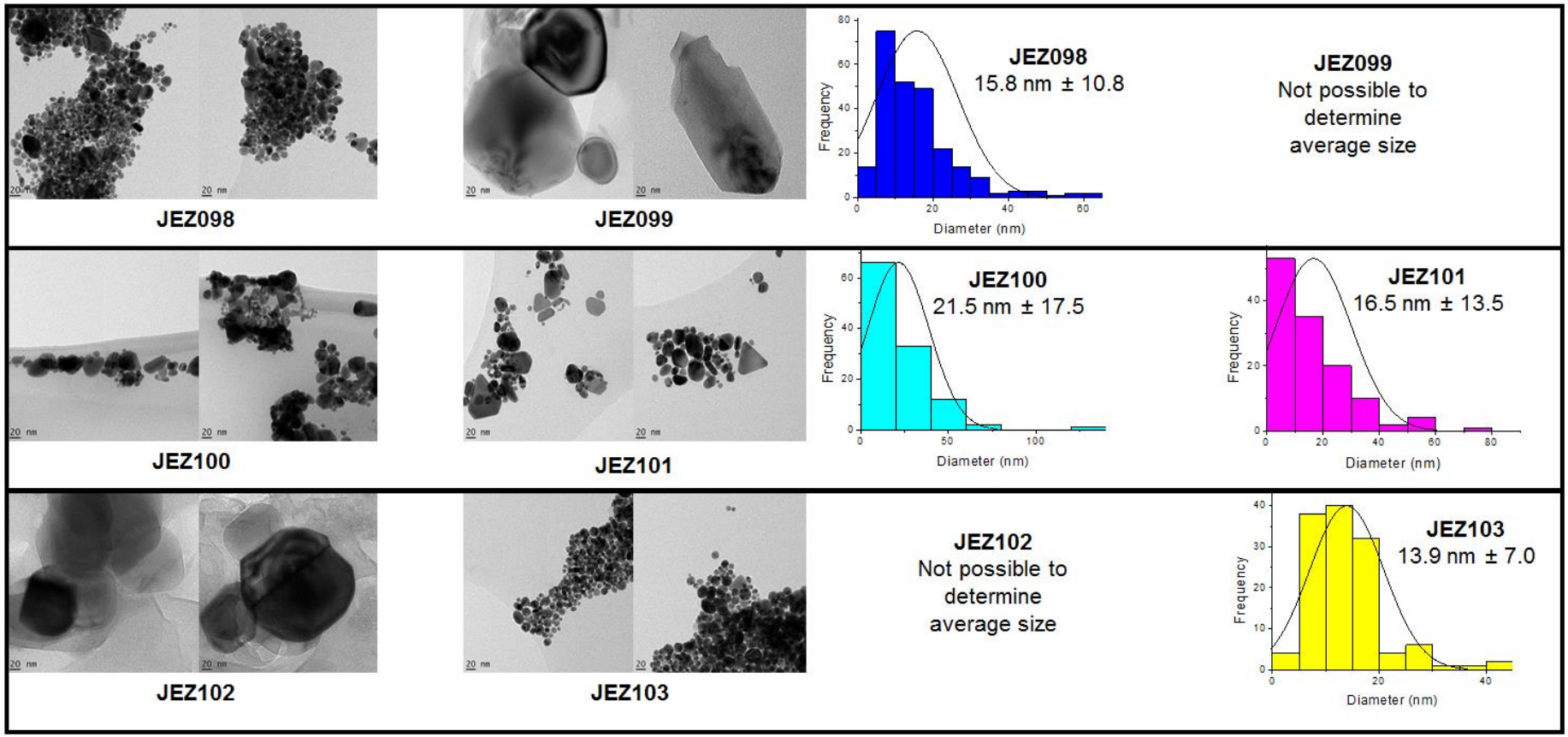

Figure 4.14 TEM images of JEZ098 to JEZ103.

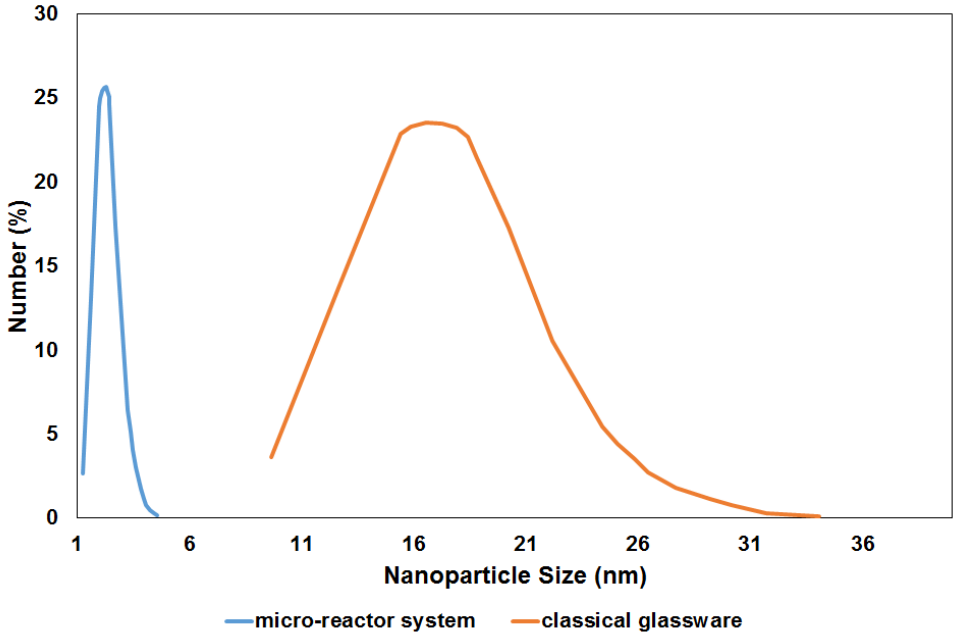

Figure 4.15 Comparison of nanoparticle size distribution (determined by dynamic light scattering) synthesized using a micro-reactor system (a) and classical glassware (b).[7]

A system was thus envisioned where the concentrations of reagents would remain constant for successive synthesis procedures, the rate of reduction could be controlled and stirring and temperature would remain constant. As such, a reactor system as depicted in Figure 4.16, was designed in-house. With this system, stock solutions of reagents could be fed to the reaction vessel with the ability to control the rate of reduction. Although the stock solutions would be manually prepared, the same solutions would be used for successive synthesis procedures thus potentially resulting in consistency in nanoparticles produced for a certain batches of pre-prepared reagent stock solutions.

Subsequently a reactor setup was commissioned with the assistance of Devos Laboratory Consultants which incorporated most of the desired aspects of the proposed setup designed by us and shown in Figure 4.16. The supplied reactor is shown in Figure 4.17 and was controlled from a control panel which allowed for the adjustment of stirrer speed, reduction solution dosing rate and temperature. What was however lacking were reservoirs for addition of the Au/micelle and PTA solutions. Although not ideal, with the volumes of Au/micelle and PTA solutions which would be required due to the volume of the reactor, it was foreseen that, providing care was taken accurately transferring the solutions as accurately as possible, any slight variations would be negligible for successive synthesis procedures.

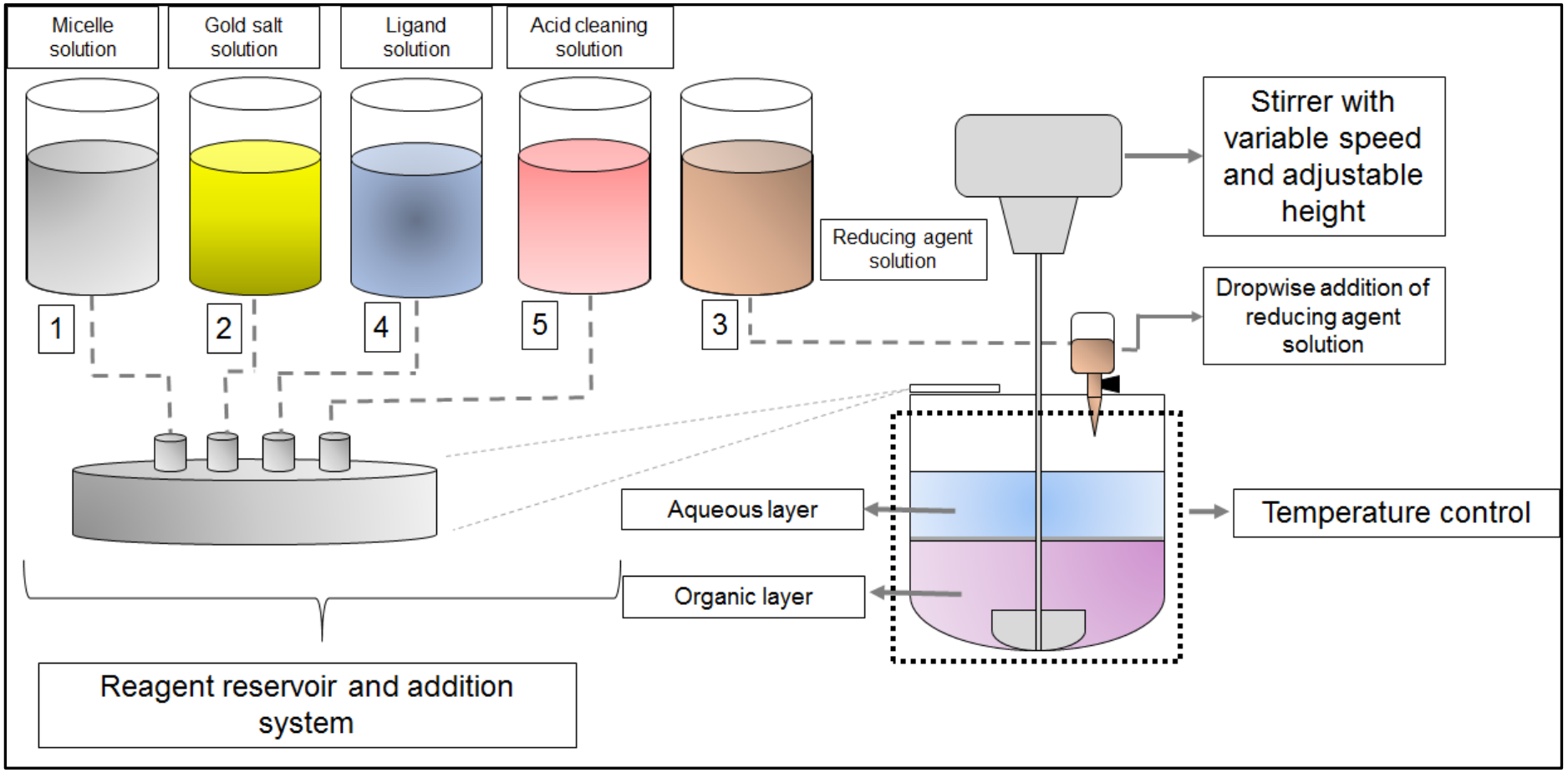

Figure 4.16 Proposed reactor setup, designed by us, in order to control synthesis parameters.

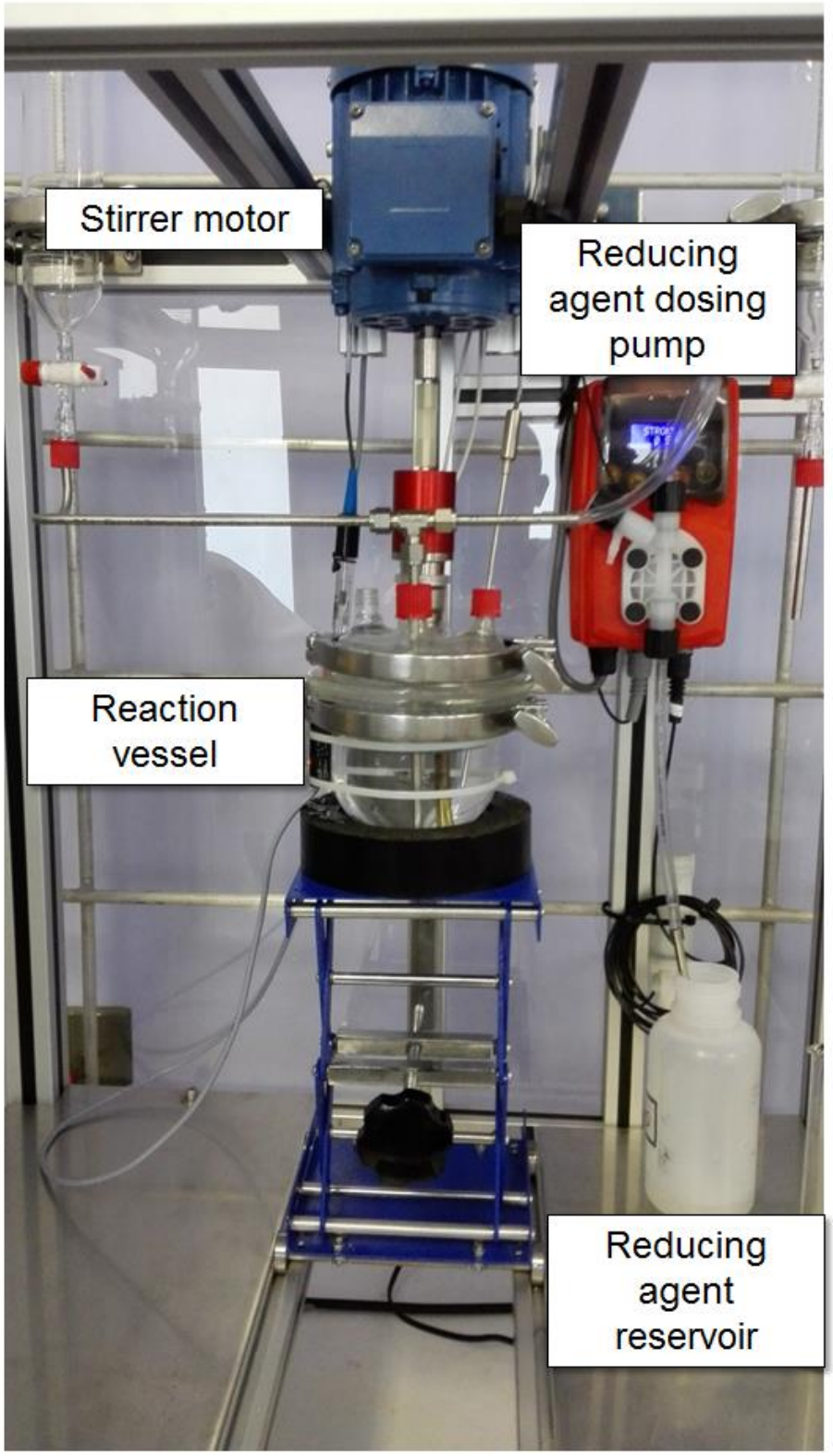

Figure 4.17 DEVOS reactor setup as realized by Dewald Vosloo of Devos Laboratory Consultants

The aim of the initial reactions were to carry out the synthesis and extraction of Au_{55} as a commissioning run for the DEVOS reactor setup. In addition, the repeatability of the synthesis method was to be tested. As such, stock solutions of the Au/micelle, reducing agent and PTA were made. Due the volume of the reaction vessel, the synthesis had to be scaled up 10 times (from 20 ml volumes of organic and aqueous to 200 ml of each for a total volume of 400 ml). Thus 400 ml each of the Au/micelle and PTA solutions and 80 ml of the reducing agent solution were prepared. This was in order for there to be sufficient solutions to carry out comparative runs using reagents with the same concentration. The scaled up masses and volumes of reagents and solvents are shown in Table 4.2.

In order to investigate extraction efficiency and nanoparticle stabilization at this larger scale, less PTA was initially used (0.5:1 PTA:Au ratio for JEZ104 and 105, and 0.3:1 PTA:Au for JEZ106 and 108 respectively). For JEZ109 and 110, the previously determined optimum ratio of 1:1 PTA:Au employed in previous small scale runs was used (see Chapter 3).

Table 4.2 Scale up of reagents and solvents.

	Original Reagent Mass (g)	**Original Solvent Volume (ml)**	**New Reagent Mass (g)**	**New Solvent Volume (ml)**
Micelle	0.01	20ml $CHCl_3$	0.1	200ml $CHCl_3$
$HAuCl_4$	0.034	Dissolved with micelle	0.34	Dissolved with micelle
$NaBH_4$	0.01	2ml MeOH	0.1	20ml MeOH
PTA	0.0008	20ml H_2O	0.008	200ml H_2O

All the above were doubled up in order to have consecutive runs using exactly the same concentration of reagents as the aim of these experiments were to test repeatability. Therefore, theoretically, consecutive pairs of runs should have yielded similar results. Thus 400 ml of micelle/Au solution, 400 ml PTA solution and 20 ml $NaBH_4$ solution were prepared.

Firstly a pump calibration was carried out. As reducing agent addition rate was thought to be the most critical parameter which needed to be controlled, consistency in the rate of addition

was for consecutive runs was crucial. Table 4.3 shows the percentage output of the pump related to the strokes per minute and the resultant volume of solvent pumped per minute. Figure 4.18 shows the resultant plots.

Table 4.3 Pump calibration values.

Pump Output (%)	Solvent	Strokes/min	ml/min
5	water	1	2.3
10	water	2	5.6
25	water	6	15.6
50	water	12	29.3
75	water	18	45.8
90	water	21	53.4
100	water	24	63.3
	Repeat		
5	water	1	2.9
10	water	2	5.6
25	water	6	18
50	water	11	32
5	$NaBH_4$ in MeOH	1	1.8
10	$NaBH_4$ in MeOH	2	3.9
20	$NaBH_4$ in MeOH	6	6.6

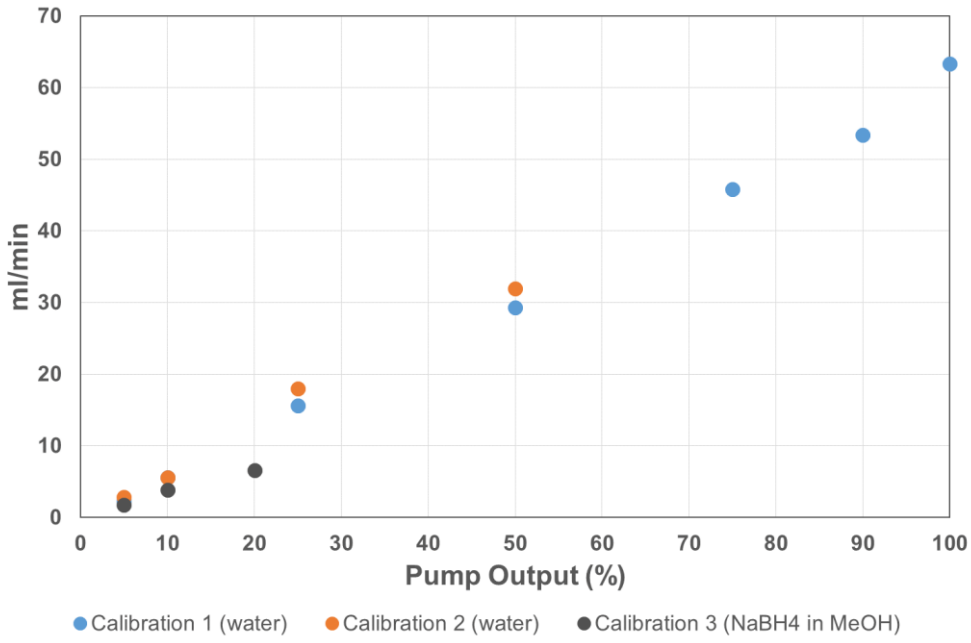

Figure 4.18 Pump calibration results.

It can be seen from the above that at up to 10 % pump output, the volume dispensed is exactly the same for water and about 30 % less for $NaBH_4$ in MeOH. What is clear is that for solvents of the same density at low pump output percentages, the volumes dispensed are quite consistent. At higher pump outputs of 25 – 50 % there is a variance of the volume dispensed of approximately 10 – 15% for a solvent of the same density. However, since the aim was to add the reducing agent at the slowest possible rate, we would be working at the lowest possible pump outputs. Thus from the above, the repeatability of the volumes dispensed at the lower pump outputs were acceptable.

The reactor conditions and reducing agent dosing rates are shown in Table 4.4. It was attempted to synthesis Au_{55} with the temperature kept constant at 30 °C with a stirring speed of 500 rpm. It was aimed to carry out reduction with a dosing rate of 1.8 ml per minute.

Table 4.4 Reactor conditions and reducing agent dosing rates.

Run Number	JEZ104	JEZ105	JEZ106	JEZ108	JEZ109	JEZ110
Au:Micelle	55	55	55	55	55	55
Temp (°C)	30	30	30	30	30	30
Stirring Speed	500	500	500	500	500	500
Pump Output (%)	5	5	5	100, 20**	5#	5#
ml/min	1.8	1.8*	1.8	24, 6	1.8	1.8

* Bubble in line resulted in slower dosing rate ** Dosing rate increased to remove bubble # new priming procedure

It however became apparent that dosing the reducing agent using an initial low pump output caused bubbles in the line. This occurred for JEZ105 and resulted in reduction taking 30 min as compared to 8 min for JEZ104 even though the same pump output was used. A bubble again appeared in the line for JEZ108. In order to remove the bubble, the rate was increased to 100 % output. This quickly pushed through the bubble after which the output was reduced to 20 %. In total however, the reduction time was similar to that JEZ106 (≈ 10 min). For JEZ109 and JEZ110, a priming procedure was employed in order to prevent the initial formation of bubbles in the line. Firstly 200 ml of distilled water was pumped at 100 % output. The pump and line were not emptied of water and was then followed by 80 ml MeOH at 100 % output. This was pumped until the pump and line were empty of MeOH. The reducing agent solution was then added to a measuring cylinder reservoir (35 ml). Upon dosing, an output of 50 % was used pumping into a waste container until 20 ml of the reducing solution was left in the measuring cylinder reservoir. Reduction was then carried out

with an output of 5 % until the measuring cylinder reservoir was empty. It was previously determined that the dead volume of the pump and lines were approximately 15 ml. By cleaning and priming the pump and lines as described above, the chances of bubbles were reduced while improving the accuracy of rate and volume of reducing agent solution dosed during reduction.

Figure 4.19 shows the appearance and TEM results of JEZ104 and JEZ105. In appearance, the aqueous layers look similar, with both organic layers appearing identical; the clear appearance suggesting good extraction had occurred despite the low concentration of PTA utilized in the aqueous layer. However TEM shows that larger nanoparticles were produced for JEZ104 (62.7 nm ± 33.1) as compared to JEZ105 (27.5 nm ± 19.3). This may indicate that the extremely slow reduction which occurred for JEZ105 compared to JEZ104 resulted in the smaller nanoparticles produced. In both cases, the size distribution is quite wide indicating that perhaps due the lower than desired PTA concentration and/or extraction time being insufficient for the larger volumes utilized, the “divide-and-protect” mechanism had not occurred optimally.

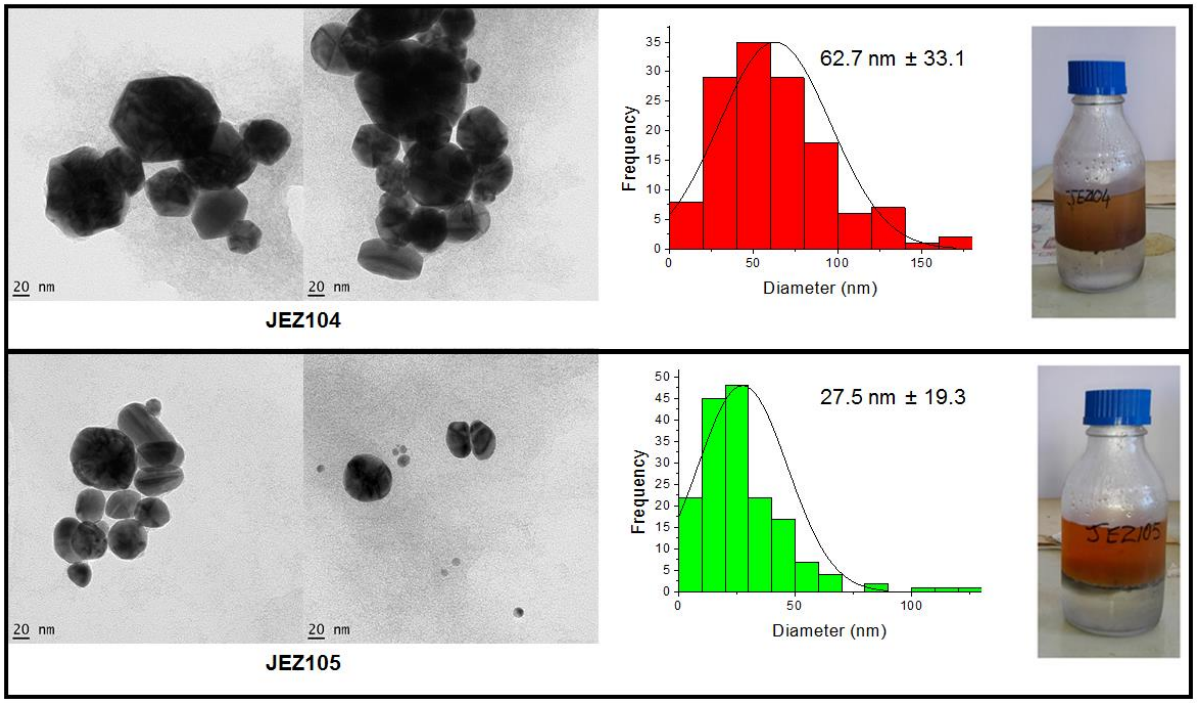

Figure 4.19 Appearance and TEM results of JEZ104 and 105 (Reaction conditions: 30°C, 500 rpm, dosing time JEZ104 = 8 min, dosing time JEZ105 = 30 min).

Figure 4.20 shows the appearance and TEM results of JEZ106 and JEZ108. Since even less PTA was used here, the inefficient extraction of Au into the aqueous layer is indicated by red colour of the organic layer for both JEZ106 and JEZ108. TEM results show similar sized nanoparticles for both (55.0 nm ± 31.6 and 49.8 nm ± 23.9 respectively). This confirms the poor extraction which occurred. Again the wide size distributions in both cases indicate that the "divide-and-protect" mechanism had not fully taken place.

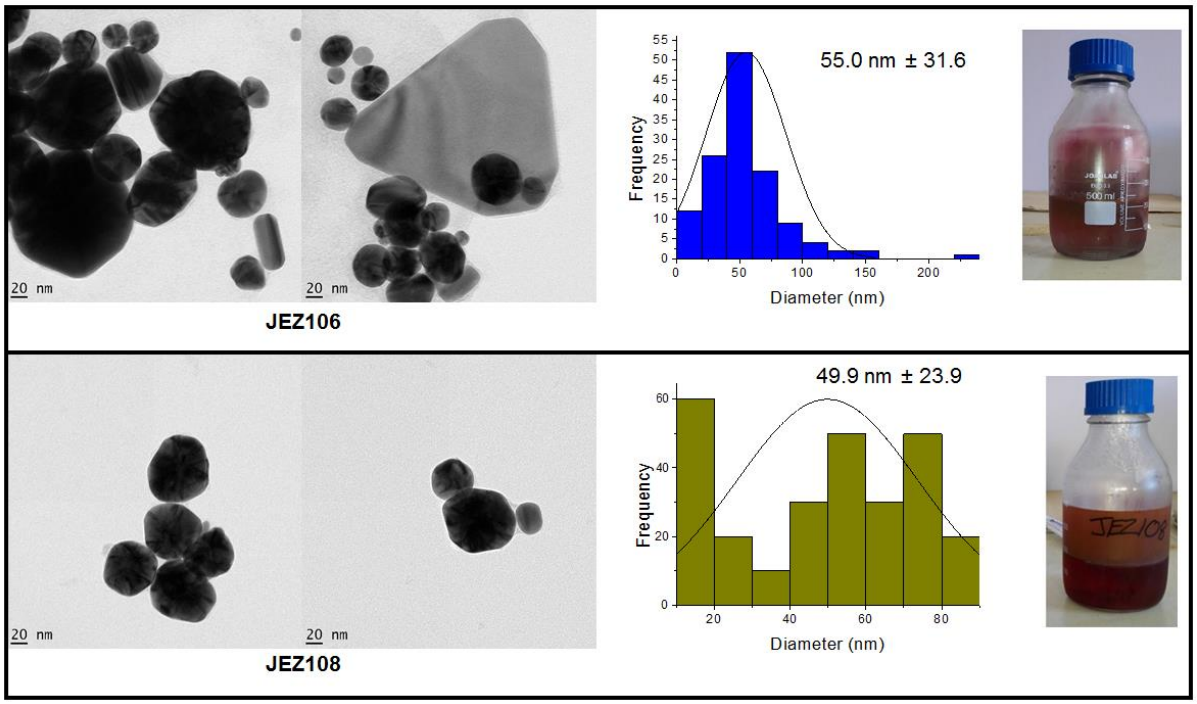

Figure 4.20 Appearance and TEM results of JEZ106 and JEZ108 (Reaction conditions: 30°C, 500 rpm, dosing time JEZ106 = 11 min, dosing time JEZ108 = 11 min, but rate of addition different – see Table 4.4).

Figure 4.21 shows the appearance and TEM results for JEZ109 and JEZ110. With the previously determined optimum concentration of 1:1 PTA:Au used (see Chapter 3), it is immediately clear that more efficient extraction had occurred due to the clear organic layers of both reactions. TEM indicates that the difference in appearance of the solutions is due to large aglomerates of gold being formed for JEZ109 and relatively monodisperse 12.3 nm nanoparticles being formed for JEZ110. In this case it appears as if an extreme example of dendrimer micelle orientation variation played a role in the different sizes obtained after using the same stock solutions and conditions.

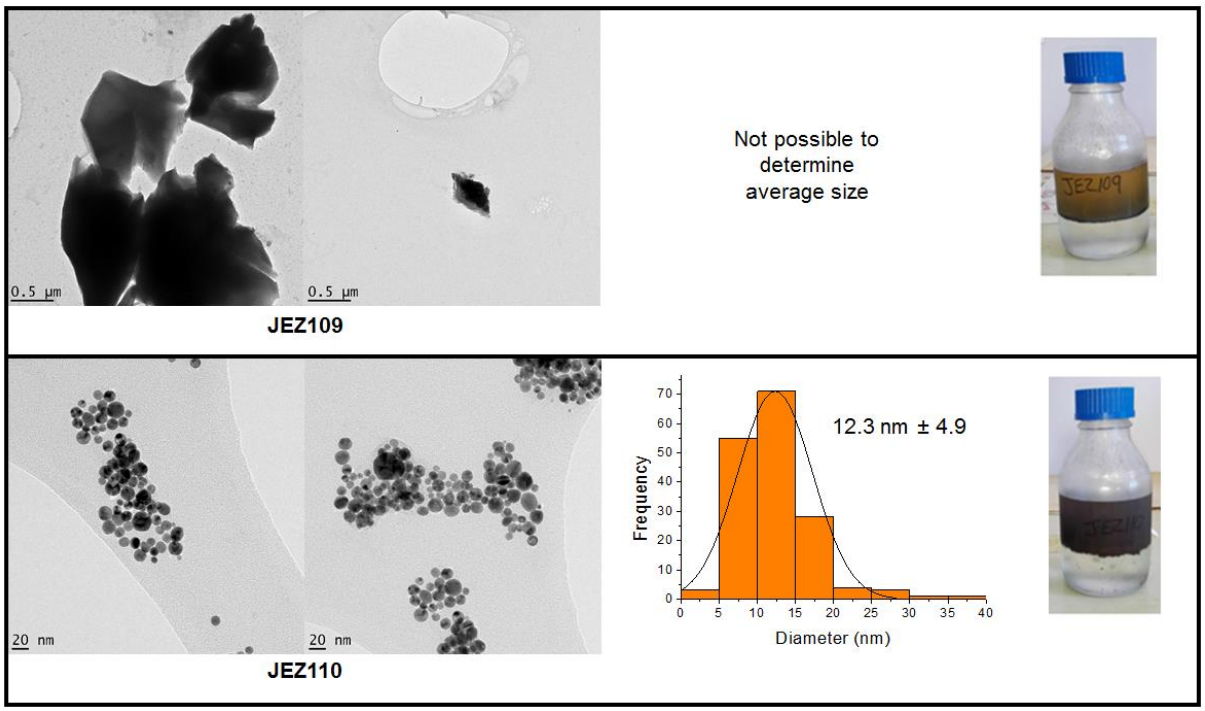

Figure 4.21 Appearance of and TEM results for JEZ109 and JEZ110.

Reactions JEZ111 and JEZ112 were set up in order to evaluate extraction into the aqueous phase over 96 h. It was previously hypothesised that due to the larger volumes of solvent and quantities of reagents used, the "divide-and-protect" mechanism may take longer to go to completion than the 24 hours previously employed. It can be seen from Figure 4.22 that for JEZ111, the nanoparticle size obtained was 28.0 nm ± 22.5. This extremely wide standard deviation could indicate that the "divide-and-protect" mechanism is perhaps at an intermediate phase, although further along than after 24 hours, and perhaps has not reached completion yet. By looking at JEZ112, it appears that it may have reached a more advanced stage of the mechanism with what appears to be concentrated areas of organic material surrounding very small particles of gold (resulting in the dark areas seen). No average particle size could however be determined due to the resolution of individual particles not being clear and subsequent difficulty in counting them. Table 4.5 summarises the nanoparticle sizes obtained for the DEVOS reactor set-up evaluations along with notable deviations (or lack thereof) for each pair of reactions. It is apparent from this that the more controlled reactor set-up method of synthesis and extraction surprisingly showed no improvement in size consistency for successive synthesis procedures. Similar randomness in nanoparticle size (and shape) for successive synthesis procedures were exhibited as was observed with the more manual previous methods. Furthermore, the increased scale of

reaction appeared to result in an increase in the average size of the nanoparticles obtained. This would seem to confirm the notion that the root cause of the synthesis inconsistency lies with the nature of the dendrimer micelle retention and scaffolding properties, or more specifically the lack thereof. Further strategies thus had to be devised to mitigate the effects presented by the structural inadequacies of the G3 PPI dendrimer micelle.

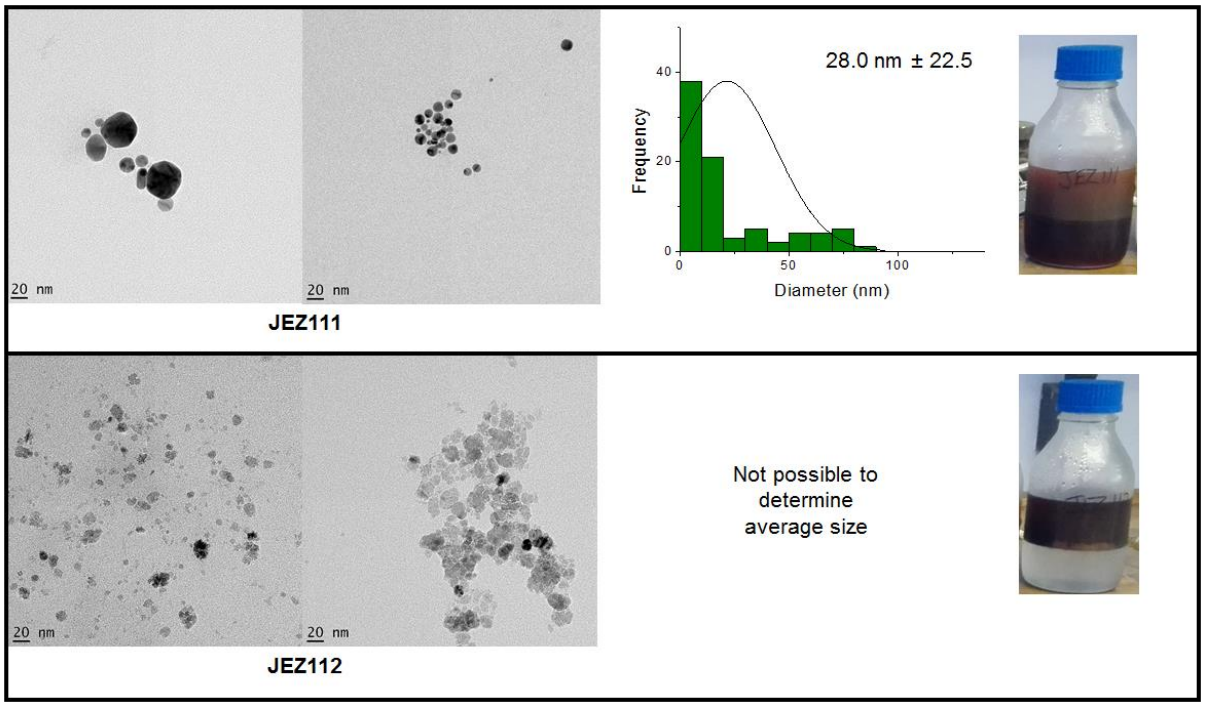

Figure 4.22 TEM results for JEZ111 and JEZ112.

4.2.4 Evaluation of modified reduction and extraction techniques

From the above results it was deduced that the most likely cause of nanoparticle synthesis inconsistency was due to the relatively poor retention and scaffolding properties of the dendrimer micelle. A method which would either aid retention of the nanoparticles within the dendrimer micelle interior or limit orientations of it which would favour agglomeration needed to be found. Therefore the next feasible solution would be to develop a strategy to arrest any potential agglomeration which would otherwise occur regardless of the dendrimer micelle architecture. In this respect therefore, it was hypothesized that by introducing the PTA ligand along with the reducing agent would immediately stabilize nanoparticles formed upon reduction and thus mitigate agglomeration due to orientations of the dendrimer micelle favouring this or loss of nanoparticles from its interior. In this way partitioning of the gold salt into the dendrimer micelle interior would still occur, therefore still fulfilling its role as a template, but PTA would immediately stabilize nanoparticles formed upon reduction and thus

potentially limit the size of the initial DENs formed. With the nanoparticles then stabilized by the water soluble PTA ligand within the hydrophilic interior of the PPI dendrimer micelle, addition of the water layer would then hopefully result in the stabilized nanoparticles diffusing to the aqueous layer from the interior of the micelle.

Table 4.5 Nanoparticle sizes obtained for DEVOS reactor set-up synthesis evaluations along with notable deviations for each pair of consecutive reactions.

Reaction Code	PTA:Au Ratio	Reaction Deviations	Nanoparticle Size (nm)
JEZ104	0.5:1	none	62.7 nm ± 33.1
JEZ105	0.5:1	Slower reducing agent addition	27.5 nm ± 19.3
JEZ106	0.3:1	none	55.0 nm ± 31.6
JEZ108	0.3:1	Faster reducing agent addition	49.9 nm ± 23.9
JEZ109	1:1	Revised pump priming procedure	Micron-sized agglomerates
JEZ110	1:1	Revised pump priming procedure	12.3 nm ± 4.9
JEZ111	1:1	96 h extraction time	28.0 nm ± 22.5
JEZ112	1:1	96 h extraction time	Non-discreet nanoparticles

A further aspect which had not been considered previously was addition of the aqueous layer upon initiation of nanoparticle extraction from the organic layer. To date, PTA was dissolved in water and this solution added to the stirring organic DENs solution. As proposed by the mechanism in Chapter 2, this would result in contortion of the dendrimer micelle extremities at the organic/aqueous interface and release of the nanoparticle from its interior and eventual migration from the organic phase to the aqueous phase. However, no controlled manner of addition of the aqueous PTA solution had been practiced; the addition usually having been

done by directly pouring or syringing the aqueous solution to the organic phase with no consideration to rate of addition.

It was thus proposed that the controlled infusion of the aqueous solution through the organic solution was applied instead of the previous single addition of the aqueous layer to initiate nanoparticle extraction. This would serve a two-fold purpose. Firstly it would minimize any localized extraction points which could result in localized aggregation of extracted nanoparticles. It was thought that this may be a contributing factor to the variation in nanoparticle sizes obtained previously. The concept is illustrated in Figure 4.23 where the infusion of water into the organic layer (a) is shown compared to once off single addition. It can be seen that theoretically, hydrophilic nanoparticles would most likely be transported in a more disperse manner when water is diffused into the organic layer whereas large aggregations which are then transported from the organic layer could occur when a single addition of water is made.

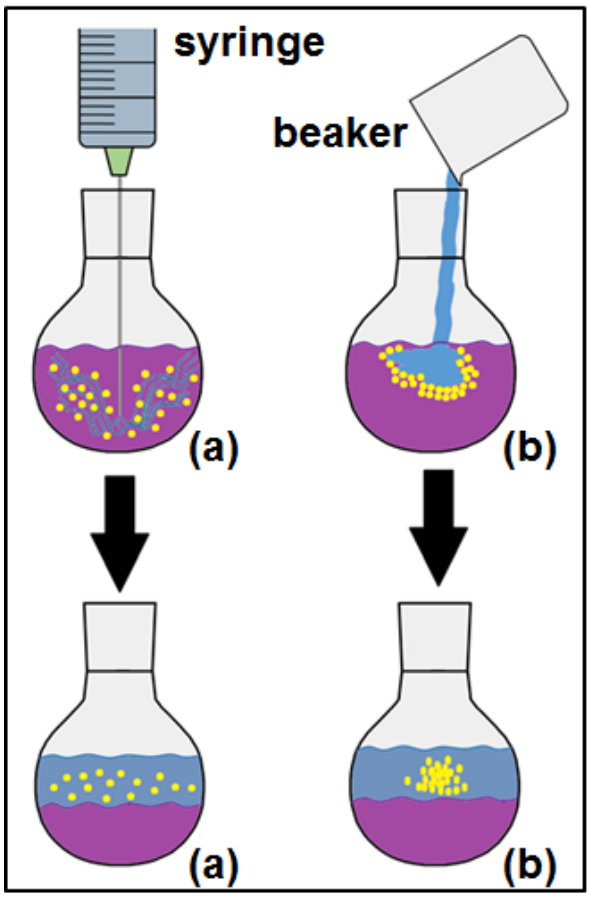

Figure 4.23 Illustration showing infusion of water into the organic layer (a) compared to a single addition of water (b).

The importance of control of addition of the aqueous phase becomes apparent when considering the work of Schwenke *et al* (2014) in modelling the assembly of nanoparticles at liquid interfaces due to crowding and ordering[8]. They showed that local ordering nanoparticles ($<\Psi_6>$) increases as the fraction of the interface covered by nanoparticles (ϕ) increases (Figure 4.24). The rate of this varies relative to the rate of adsorption or packing (Γ) of nanoparticles from the bulk which increases with increasing nanoparticle concentration. Related to this is the relaxation time t_a which increases with interface coverage ϕ *i.e.* ordering of nanoparticles at the interface is dependent on the concentration of nanoparticles and the rate at which they aggregate to lower their surface energy ($\Gamma = t_a^{-1}$). Therefore there is a rapid filling of the interface by higher surface energy nanoparticles which plateaus as aggregation (adsorption or packing) lowers this energy after which adsorption starts once more. Hence by controlling the addition of the aqueous phase, Γ is controlled thus minimizing the probability of localized absorption or packing.

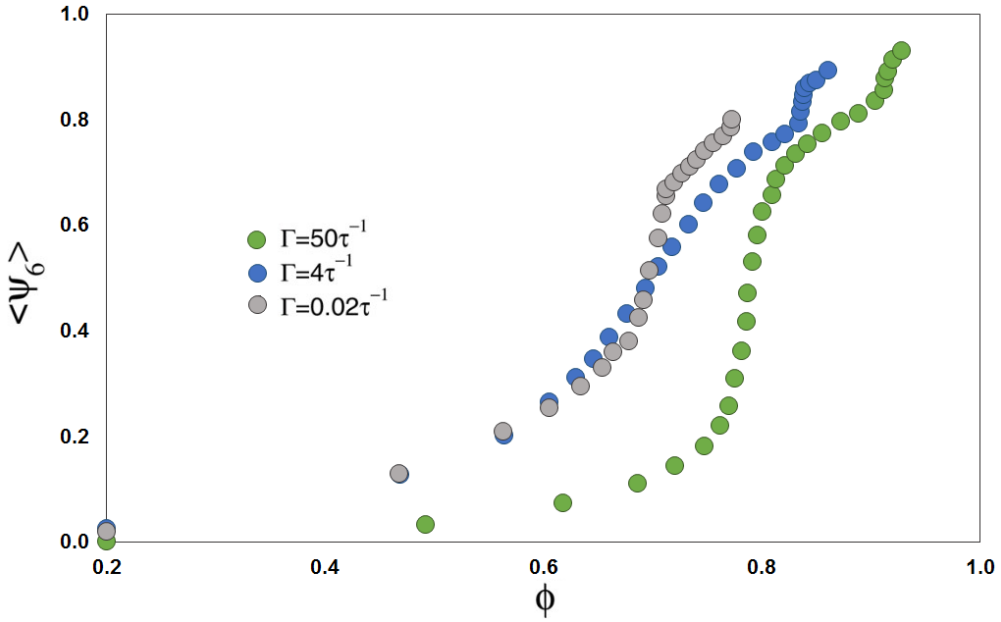

Figure 4.24 $<\Psi_6>$ as a function of surface coverage ϕ a monodisperse system at varying rates of adsorption (Γ).[8]

The hypothesis was subsequently first tested using the DEVOS reactor setup. The PTA was subsequently dissolved along with the $NaBH_4$ in MeOH before addition at approximately 2 ml/min to the Au/micelle was made. In order to further limit any possible fast nucleation and growth of the gold nanoparticles, 200 ml of water was dosed through the organic layer at 50 % pump output (12 strokes/min; ≈ 30 ml/min) as soon as physically possible upon the

completion of reduction. This therefore represented a further modification to the procedure where previously stirring was continued for a period of time after addition of the reducing agent which was done in order to try and ensure complete reduction. However, this strategy may have instead resulted in nanoparticle growth. Thus, in order to limit nanoparticle growth, extraction was immediately initiated. The TEM results of the modified synthesis method using the DEVOS reactor can be seen in Figure 4.25 with DENs having an average size of 5.93 nm ± 2.64 being formed. At the end of the extraction period, PTA stabilized nanoparticles with an average size of 4.75 nm ± 1.38 were obtained. This is almost 3 times smaller than the previous smallest size obtained using the DEVOS reactor setup. What is furthermore apparent is the general uniformity of shape for both DENs and extracted nanoparticles.

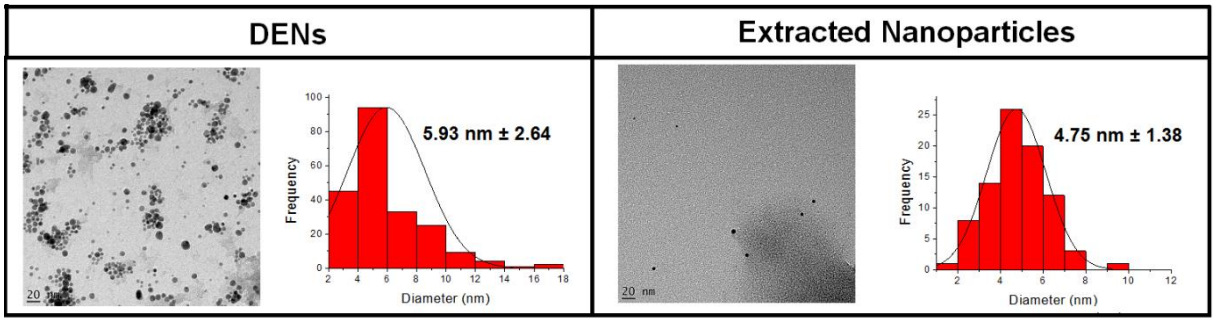

Figure 4.25 TEM results for DEVOS reactor setup utilizing $NaBH_4$/PTA co-addition and controlled extraction procedure.

To test repeatability of the modified procedure, synthesis and extraction was carried out on the original scale (20 ml organic and aqueous phases in 50 ml round-bottomed) the experiments had initially been carried out at. As such, synthesis was carried out in a round bottomed flask with the water infused through the organic layer using a syringe (as depicted in Figure 4.23). From Figure 4.26 it can be seen that an average size of 2.28 nm ± 1.64 was obtained after 24 h of extraction. Again there is evidence for the proposed "divide-and-protect" mechanism with DENs size being 4.87 nm ± 1.87. This also represents the smallest average nanoparticle size obtained since our initial synthesis of 1.5 nm particles. Compared to results obtained from the reactor setup, the smaller scale again produced the smaller nanoparticles, thus demonstrating the effect of scale on final nanoparticle size.

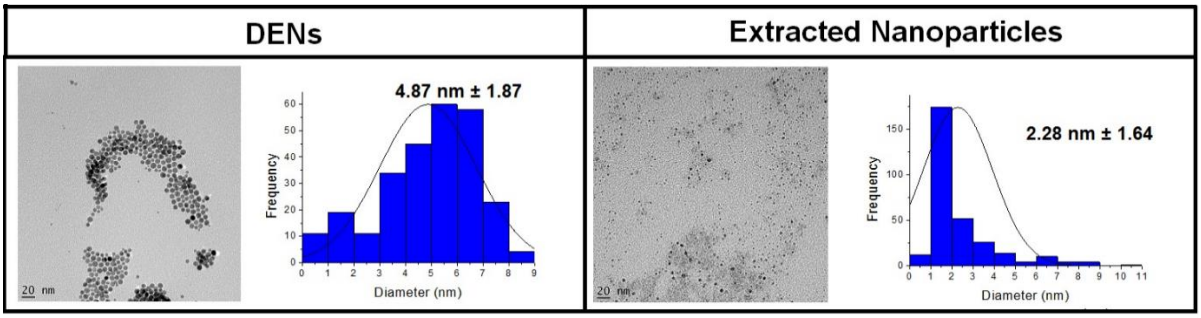

Figure 4.26 TEM results for 20 ml organic and aqueous phases in 50 ml round-bottomed flask utilizing $NaBH_4$/PTA co-addition and controlled extraction procedure.

Further validation of the repeatability of the method was obtained when it was applied by other members of the research group. Table 4.6 summarizes the TEM results subsequently obtained. The intended aim of the experiments for which the results were obtained, was to tailor the nanoparticle size by adjusting the Au^{3+}:dendrimer ratio (as also discussed in Chapter 2). Thus it was aimed to synthesize Au_{13}, Au_{55}, Au_{147} and Au_{309} by varying the Au^{3+}:dendrimer ratios accordingly. Although the eventual nanoparticle sizes obtained were not what would be expected of those particular cluster sizes, what is apparent is that firstly, the nanoparticle sizes obtained increased or decreased with the Au^{3+}:dendrimer ratios used and also that nanoparticle sizes for successive synthesis procedures using the same ratios, were reproducible.

Table 4.6 TEM results for nanoparticles synthesised by other research group members using modified method.

Sample name	Au^{3+}:G3 Dendrimer ratio	Diameter (nm)
LUC-6	13	6.77 ± 3.45
LUC-7	13	7.22 ± 1.56
LUC-17	55	17.30 ± 5.92
LUC-16	55	16.98 ± 9.23
LUC-35	147	35 ± 8.26
LUC-50	309	50 ± 9.46

* The sample name contains the nanoparticle size prefixed by LUC *e.g.* LUC-x: x= diameter calculated and rounded off.

Modifications applied to the synthesis method were thus successful in not only considerably reducing the size of the nanoparticles formed, but also in producing particles of relatively

uniform shape. What is also evident is that the proposed “divide-and-protect” mechanism is still apparent with nanoparticles reducing in size and polydispersity after extraction. Subsequent reactions further demonstrated reproducibility of the method with sizes consistently in the size range obtained in Figure 4.26. The method also proved successful when using triphenylphosphine trisulphonate (TPPTS) as ligand where an average nanoparticle size of 2.55 nm ± 1.2 was obtained.

The next proposed strategy was to try and aid stabilization of the nanoparticles formed after reduction. Barring utilizing a higher generation dendrimer micelle which would exhibit greater retention and scaffolding ability, it was hypothesized that adding the hydrophilic ligand usually dissolved in the aqueous phase and assists in extraction of nanoparticles from the organic phase along with the reducing agent might aide stabilization directly after reduction. Along with this, addition of the aqueous layer was also modified to prevent any localized agglomeration during extraction. This strategy proved successful with nanoparticles close to the desired 1.5 nm consistently being produced by following this method. Again, the method was further validated through application of the revised procedure by additional group members where nanoparticles of consistent sizes were repeatedly obtained.

4.3 Conclusion

In conclusion, the work outlined in this chapter does not invalidate what was learnt in Chapter 2 regarding the mechanisms of nanoparticle synthesis and extraction. It does however introduce measures which allows for greater control over the Au nanoparticle synthesis procedure and hence consistent reproducibility in the size and, to a certain extent, shape of nanoparticles produced. In fact, the measures introduced resulting in the positive results achieved, were guided by the results and proposed mechanisms from Chapter 2 and what was learnt about the nanoparticle environment and stabilization in Chapter 3.

It should further be noted that the nanoparticle sizes achieved using the modified synthesis methods may be even smaller than measured. Studies on nanoparticle stability toward agglomeration were conducted and showed that this does occur over time. However, as with the inconsistency in nanoparticle size previously obtained, there was inconsistency in the rate at which this occurred. Nonetheless, with the modified procedure, even though a delay in obtaining TEM data results in a larger nanoparticle size being determined, the agglomeration

appears to be constant. Therefore, even with agglomeration occurring, it is still possible to achieve consistency in terms of nanoparticle size.

4.4 Experimental

4.4.1 Characterization

Parallel reactions were carried out using a Radleys Carousel 12 Plus Reaction Station™ with reaction tubes have a working volume of 5- to 20 ml. UV – Vis absorbance spectra were obtained using a GBC 920 UV-VIS spectrometer and quartz cuvettes having a path length of 1.00 cm. The spectrum of either chloroform or water was used as the background depending on the solution being analysed. TEM images were obtained using a FEI Tecnai G^2 Field Emission Gun (FEG) TEM operating at 200 kV and having a 2.5 Å point-to-point resolution, 1.02 Å line resolution and 1.4 Å information limit. Samples were prepared by dropwise addition of the sample onto a carbon coated copper grid. Average nanoparticle sizes were determined from the TEM images using ImageJ image processing software. Au concentrations were measured on a Spectro Acros ICP-OES spectrometer.

4.4.2 Synthesis of Au Nanoparticles

When utilizing a round bottomed flask, G3 poly(propylene imine) dendrimer micelle (0.01 g, 0.0018 mmol) was dissolved in 20 ml chloroform. $HAuCl_4$ (0.032 g, 0.01mmol) was then added to the micelle solution and stirred for 10 min. $NaBH_4$ (0.01 g, 0.26 mmol) was dissolved in 0.2 ml MeOH and added to the Au/micelle solution. Reduction was then carried out for 30 min. For parallel reactor evaluations the volumes and masses were halved due to the size of the reactor tubes. For the DEVOS reactor set-up these increased 10 fold in order to ensure stirrer blades were below the surface of the bi-phasic reaction mixture therefore facilitating adequate mixing.

Extraction of the nanoparticles from the aqueous layer was carried out by dissolving 1,3,5-triaza-7-phosphaadamantane (PTA) (0.0065 g, 0.04 mmol) in 20 ml distilled water and adding it to the Au DENs solution. The biphasic mixture was then stirred for 24 h. Again these volumes and masses were increased or decreased relative to round bottomed flask method values depending on the reactor system used.

4.5 References

(1) LaMer, V. K.; Dinegar, R. H. *J. Am. Chem. Soc.* **1950**, *72* (11), 4847.

(2) LaMer, V. K. *Ind. Eng. Chem.* **1952**, *44* (6), 1270.

(3) Polte, J.; Ahner, T.; Delissen, F.; Sokolov, S.; Emmerling, F.; Thunemann, A. F.; Kraehnert, R. *J. Am. Chem. Soc.* **2010**, *132*, 1296.

(4) Polte, J.; Tuaev, X.; Wuithschick, M.; Fischer, A.; Thuenemann, A. F.; Rademann, K.; Kraehnert, R.; Emmerling, F. *ACS Nano* **2012**, *7* (7), 5791.

(5) An, K.; Somorjai, G. A. *ChemCatChem* **2012**, *4* (10), 1512.

(6) *Optoelectronic Properties of Inorganic Compounds*; Roundhill, D. M., Fackler, J. ., Eds.; Springer Science+Business Media: New York, 1999.

(7) Ftouni, J.; Penhoat, M.; Addad, A.; Payen, E.; Rolando, C.; Girardon, J.-S. *Nanoscale* **2012**, *4* (15), 4450.

(8) Schwenke, K.; Isa, L.; Del Gado, E. *Langmuir* **2014**, *30* (11), 3069.

Chapter 5

Catalytic Evaluation of Synthesized Hydrophilic Gold Nanoparticles in the Transformation of Styrene

---

5.1 Introduction

Catalytic reactions carried out in water offers great advantages in terms of green chemistry since, as a solvent, it is both inexpensive and environmentally benign. In addition, using water as a solvent has the potential to accelerate reaction rates and enhance reaction selectivities. This holds true even when reactants are sparingly soluble or insoluble in water. In addition, the low solubility of oxygen in water can facilitate air-sensitive, but moisture tolerant transition metal catalysis in open air.[1]

It was shown in Chapter 3 that the 1,3,7-triazaphosphaadamantane (PTA) ligand rendered the synthesized nanoparticles soluble in water, with nanoparticle solubility increasing with increased ligand concentration. The resulting aqueous solution of nanoparticles could thus potentially be utilized as an inexpensive and environmentally benign catalyst solution with accelerated reaction rates and enhanced selectivities.

One such reaction it could potentially catalyse, is the oxidation of alkenes. One of the possible products of this reaction is the epoxide derivative of the alkene. These epoxides are important in the chemical industry as they are required for the synthesis of several different types of fine chemicals, agricultural chemicals and pharmaceuticals.[2] In particular, the catalytic oxidation of styrene produces benzaldehyde, which is an important chemical widely used in medicine, the production of dyes, synthetic flavours, synthetic aroma compounds and as additives in resins.[3] As such, numerous examples of studies related to the catalytic oxidation of alkenes (most notably styrene), using transition metal catalysts, appear in literature and include the use of gold and specifically gold nanoparticles.[4–9] In addition, the effectiveness of water as solvent in the oxidation of styrene has also previously been demonstrated.[3,10]

Consequently it was aimed to evaluate the catalytic activity of our water soluble gold nanoparticles in the oxidation of styrene. Along with water acting as a benign solvent and

further attempting to abide by the principles of green chemistry, oxidants which are potentially not hazardous or produce toxic by-products, such as hydrogen peroxide (H_2O_2) and *t*-butyl-hydroperoxide (TBHP), were utilized. Commercial oxidation of alkenes is commonly carried out by ozonolysis or stoichiometric oxidation using potassium permanganate ($KMnO_4$), potassium bichromate ($K_2Cr_2O_7$) and chromic acid (H_2CrO_4) amongst others.[11] Although they are very selective and high yielding, ozone (O_3) has the potential to be highly explosive while Cr_2O_3 and MnO_2 by-products are potentially harmful to the environment due to its toxicity.[12–14] On the other hand, H_2O_2 produces only water as a by-product while TBHP produces *t*-butanol which can easily be recovered and has value as a gasoline blending component.[15,16]

Figure 5.1 shows the possible products which may be obtained from the oxidation of styrene.[16] Styrene oxide and benzaldehyde have been shown to be the major products formed, with further oxidation of styrene oxide producing phenylacetaldehyde, benzoic acid and 1-phenylethane-1,2,-diol.[2,16–18]

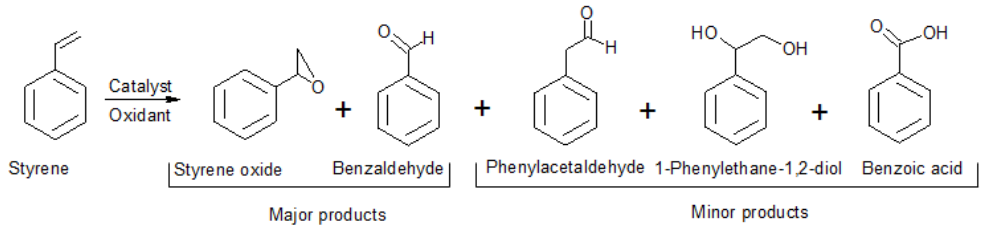

Figure 5.1 Possible products obtained from the catalytic oxidation of styrene in the presence of H_2O_2.[2,16–18]

The examples of styrene oxidation catalysed by gold nanoparticles cited in references 4,5 and 7–9, were aimed at controlling selectivity to produce either styrene oxide or benzaldehyde, and was motivated by the observations of Turner *et al* (2008) showing extremely high activity toward styrene oxidation by nanoparticles smaller than 2 nm supported on boron nitride.[19] They found that nanoparticles with a mean size of 1.5 nm (comprised of approximately 55 Au atoms) exhibited the highest activity while those larger than 2 nm were completely inactive. Subsequent studies thus focused on the effect of varying the cluster size Au_n below $n = 55$ (where n is the number of gold atoms in a cluster) on selectivity. With the insight gained from these studies, Gao *et* al (2010) as well as Lin and Pei (2014) then attempted to elucidate the mechanism of styrene oxidation on the surface of gold nanoclusters where n ranged from 16 to 55 using density functional theory (DFT) calculations.[20,21] They

found that the most likely reason for variation in selectivity was due to the formation of varying sizes of oxametallacycle intermediate structures on different gold cluster sizes.

The critical role of the support material of the Au nanoparticle is highlighted in the findings of Wang *et al* (2013), who found that contrary to what was previously observed, gold nanoparticles greater than 2 nm in size were indeed catalytically active for the oxidation of styrene. Compared to the results of Turner *et al*,[19] whose Au nanoparticles were supported on boron nitride or silica, Wang and co-workers found that sizes of between 20 – 150 nm supported on amino functionalized, porous polydivinyl benzene were highly active for styrene oxidation.[6] Their results suggested that Au^0 or Au^{3+} sites on the surfaces of nanoparticles larger than 2 nm were not active sites for styrene oxidation, but rather that Au^+ sites were. It was proposed that this is due to the nature of the particular Au/support interaction resulting in Au^+ sites having similar Au/substrate binding energies to that of binding sites on Au_{55} supported on silica. Furthermore, the amino functionalized polydivinyl benzene supported nanoparticles showed no leaching as was observed for the Au_{55}/SiO_2 catalysts. In addition, the former also exhibited superior recyclability. It was found that the amino functionalized polydivinyl benzene supported nanoparticles showed no decrease in activity even after being recycled 7 times, whereas the Au_{55}/SiO_2 catalysts lost activity after being recycled twice due to leaching and subsequent aggregation of the Au_{55} nanoparticles.

Whereas the examples cited above evaluated the catalytic activity of Au nanoparticles on various supports, in our catalytic system the nanoparticles are not supported but only protected by a relatively compact ligand (compared to aliphatic type ligands). In addition, our catalyst system also differs from the above since our nanoparticles are not a colloidal suspension, but are rendered soluble in water by the PTA ligand. As mentioned above, different supports affected the catalytic performance of nanoparticles of various sizes and, as such, it could be expected that our unsupported, water soluble catalytic system might exhibit other differences in terms of activity when compared to systems reported in the literature. Catalytic evaluations were thus planned whereby the organic substrate would be simply added to the aqueous catalyst solution. The bi-phasic environment produced when adding the organic substrate to the aqueous catalyst solution, creates an organic/aqueous interface as compared to a solid/liquid or solid/gas interface for a supported heterogeneous catalyst. However, because the nanoparticles are soluble in the aqueous environment, it would thus be in the same phase as potential oxidants such as H_2O_2. Additionally, the use of a potential

oxidant such as TBHP which is organic in nature yet miscible with water, puts us in the realm of bi-phasic catalysis with the presence of a phase-transfer catalyst. A further possible advantage is that, as is the case with heterogeneous systems, the potential exists for easy recovery of the catalyst for recycling unlike conventional homogeneous catalysts.

Given the accepted properties of homogeneous catalysts in terms of good activity and selectivity, it was envisaged that our catalysts could perhaps also show these characteristics. In addition, since we would be operating under biphasic conditions, recyclability would also be a possibility. With this in mind, we set out to evaluate the catalytic activity of the synthesized water soluble gold nanoparticles (as discussed in Chapter 4) in the oxidation of styrene, using H_2O_2 and TBHP as oxidants. A further aspect which could potentially influence the catalyst performance is the effect of nanoparticle size. In previous chapters the quest for synthesizing nanoparticles with similar sizes consistently was described. This was achieved by tailoring several of the synthesis parameters. Hence, it became possible to evaluate the effect of nanoparticle size on activity and selectivity. From this possible activity and selectivity information gained from the catalytic evaluations, and knowledge of tailoring nanoparticle sizes, specific product ranges could potentially be targeted based on nanoparticle size and reaction conditions.

5.2 Results and Discussion

By tailoring nanoparticle synthesis parameters, we could consistently obtain nanoparticles of similar size, as well as a series of nanoparticles of different average sizes. The catalytic activity of the various sized nanoparticles could then be compared. Five batches of nanoparticles, which were synthesized on a relatively large scale (200 ml of aqueous catalyst solution) in the custom-made synthesis reactor set-up described in Chapter 4, were subsequently utilized in catalysis evaluations. As can be seen from Figure 5.2 and Table 5.1, the nanoparticles synthesized ranged in size from 55.0 nm ± 31.6 to 8.5 nm ± 3.2.

Table 5.1 Nanoparticle batch codes and their respective sizes

Nanoparticle Batch Name	Nanoparticle Size
JEZ106	55.0 nm ± 31.6
JEZ108	49.9 nm ± 23.9
JEZ111	28.0 nm ± 22.5
JEZ110	12.3 nm ± 4.9
JEZ121	8.5 nm ± 3.2

What is further noticeable about these nanoparticles as seen in Figure 5.2, and which may potentially impact catalytic performance, is that there is a range of size distributions as well as differences in shape. In particular, the larger nanoparticles utilized (JEZ106, JEZ108 and JEZ111) have large size distributions as well as a mixture of spherical, triangular and polygonal shapes. The smaller nanoparticles (JEZ110 and JEZ121) on the other hand, have narrower size distributions and appear to be mostly spherical in shape. As described in Chapter 4, the variation in nanoparticle shape and size obtained was due to variations applied in the synthesis procedure involving the rate of reduction and the addition of the PTA ligand.

With the variation in the nature of the nanoparticles described above, it might therefore be expected that the smaller nanoparticles with narrower size distribution would be more active due to their higher surface area, as well as be more selective in the oxidation products formed as a result of their more uniform shape and thus potentially more uniform surface morphology.[22–24] Conversely, the larger nanoparticles might be expected to be less active and less selective due to their lower surface area and variations in surface morphology as a result of their varying shapes. The UV-vis spectra of each of the aqueous catalyst solutions are shown in Figure 5.3 and reveal the surface plasmon resonance bands resulting from the nanoparticles in solution. As discussed in Chapter 2, absorption bands due to the surface plasmon response varies as a result of differences in size and shape of nanoparticles as well as their environment. Therefore the broad and varying position and intensity of the plasmon resonance peaks observed for JEZ106, JEZ108 and JEZ111 (Figure 5.3), are indicative of the broad size distributions and varying shapes of nanoparticles in each batch of aqueous catalyst solution.[25–27] For JEZ110 and JEZ121, the plasmon resonance peaks are not visible due to the presence of the larger concentrations of PTA present and is thus an indication of enhanced stabilization (as discussed in Chapter 3) resulting in the smaller size of these nanoparticles.

The metal concentration of the catalyst solutions were determined using inductively coupled plasma optical emission spectroscopy (ICP-OES). This showed that the concentration of Au in each of the aqueous catalyst solutions were between 66.2 and 68.5 ppm and therefore having an average concentration of 67.4 ppm ± 0.9 (Table 5.2). This means that, on average, approximately 4.2 % of the originally added Au^{3+} reduced to Au^{0} in the organic phase, was extracted to the aqueous phase (see Section 5.5 Experimental). These results show that despite variations in synthetic procedures, the extent of extraction of nanoparticles into the aqueous phase was fairly comparable in each case. In light of the ICP-OES results, catalyst

loading was therefore determined based on the volume of the aqueous Au catalyst solution, and with concentrations of Au in each batch being similar, it was possible to utilize similar volumes of catalyst solution in order to achieve similar metal loadings. Preliminary catalytic evaluations revealed 10 ml of the aqueous catalyst solution to provide the best styrene (0.018 mol, 2ml) conversion. This was based on the 5 to 20 ml working volume of the multi-tube parallel reactor set-up employed for the catalytic evaluations (Figure 5.4 – Radleys Carousel 12 Plus Reaction Station™ fitted with a compatible Heidolph EKT Hei-Con digital temperature control unit). The 10 ml volume of aqueous catalyst solution therefore translated into a catalyst loading of 0.0034 mmol (0.67 mg) as shown in Table 5.2.

The utilization of the multi-tube parallel reactor set-up enabled the simultaneous evaluation of individual nanoparticle sizes under the same set of reaction conditions. Reaction temperature was set using the digital temperature control unit. The temperature control unit then regulated the heating of the bottom section of the carousel. Regulation of temperature was based on the measurement of water temperature in the sealed temperature measurement tube (see Figure 5.4) with heating rate controlled by the temperature input setting control. Evaporation was prevented by the cooling of the top of the reaction tube by means of water circulating through the cooling section of the carousel. Stirring rate was set at setting 9 of the stirring speed input setting control, with similarly sized and shaped stirrer bars being used in each tube to try and ensure similar mixing for each parallel reaction.

Upon completion of reaction a specified reaction time, the reaction tubes were cooled in an ice-bath (so as to prevent possible evaporation of organic material) before the tube caps were removed and the top organic product/substrate layer separated from the aqueous catalyst layer. The organic layer was then filtered (to remove any potential particulate matter such as agglomerated Au) using a 0.45 µm syringe filter in preparation for gas chromatographic (GC) analysis. The filtered organic layer was transferred to a 2 ml GC vial to which 0.1 ml *p*-xylene internal standard was added and sealed with a crimp GC vial top. Styrene conversion was defined as a percentage of the difference in the initial and final amount of styrene divided by the initial amount of styrene ($X_{styrene}$ (%) $= \left[\frac{C_{sty(i)} - C_{sty(f)}}{C_{sty(i)}}\right] x$ 100 %).

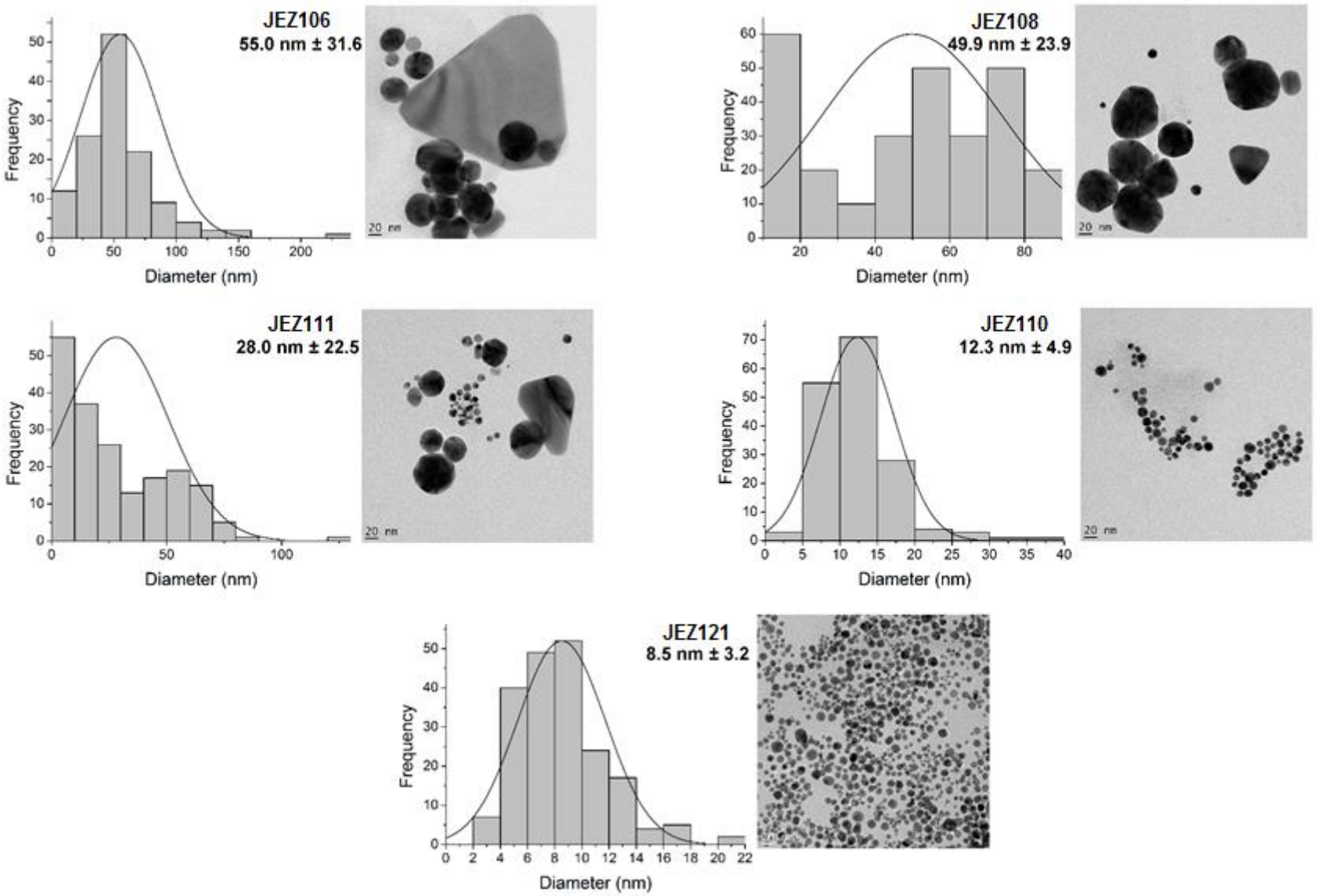

Figure 5.2 Nanoparticles utilized for catalysis evaluations.

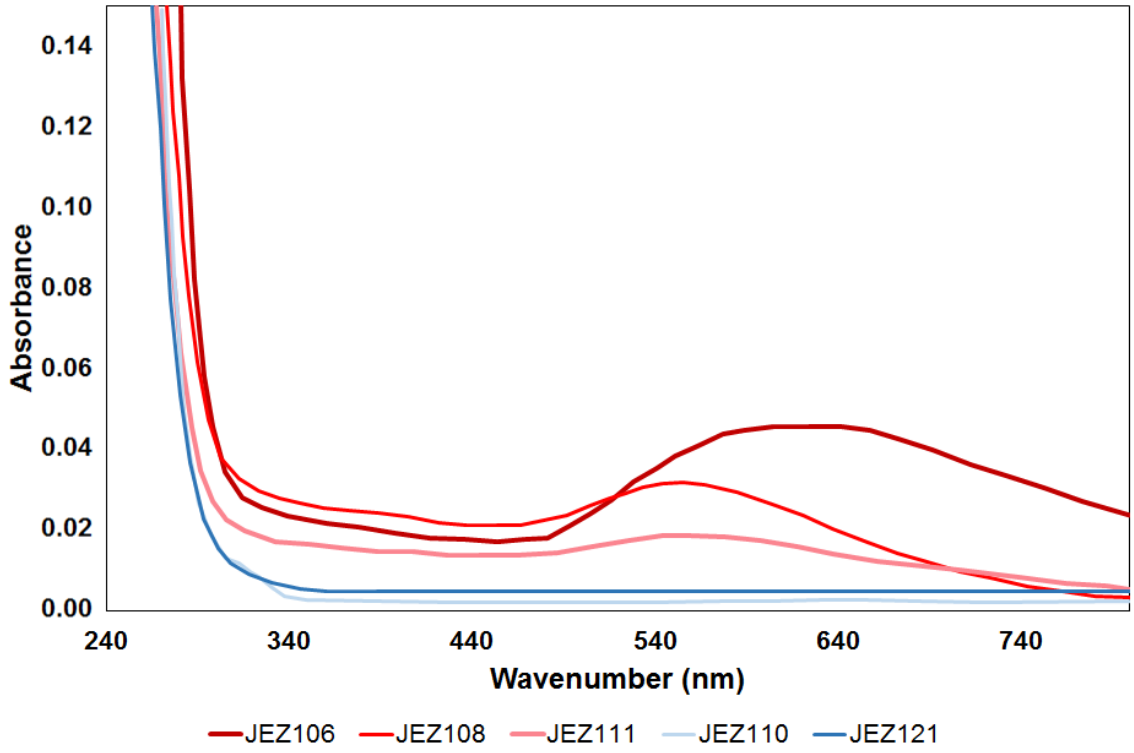

Figure 5.3 UV-vis spectra of aqueous nanoparticle solutions utilized for catalysis evaluations.

Table 5.2 Au concentration as determined by ICP-OES of Au nanoparticle solutions and subsequent metal loadings based on 10 ml volume utilized for catalytic evaluations.

	JEZ106	JEZ108	JEZ111	JEZ110	JEZ121	Average
Concentration (ppm)	67.1	66.2	66.7	68.5	68.3	67.4
Metal Loading (mg)	0.67	0.66	0.67	0.69	0.68	0.67
Metal Loading (mmol)	0.0034	0.0034	0.0034	0.0034	0.0034	0.0034

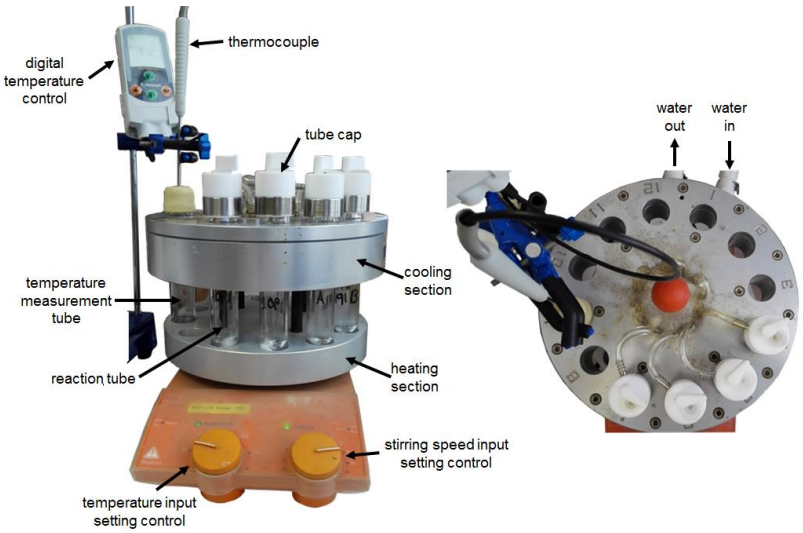

Figure 5.4 Multi-tube parallel reactor set-up.

The various reaction parameters evaluated to probe their effect on catalyst activity and selectivity was the effect of time, temperature and nature of oxidizing agent. The first parameter evaluated was that of time, with reactions carried out at 1-, 3- and 24 h. The temperature utilized was 70 °C which was based on what has generally been reported on in literature (as an example see references 16 and 18 and further references therein). What was immediately and strikingly evident from GC analysis (monitoring the decrease of styrene) was that maximum substrate conversion appeared to have been achieved after 1 h on stream. In addition it was also noted that nanoparticle size had no significant effect on conversion rates. The reaction conditions and styrene conversion results are tabulated in Table 5.3, with styrene conversion results summarized in Figure 5.5.

Table 5.3 Comparison of styrene conversion at times of 1-, 3- and 24 h for a range of nanoparticle sizes (styrene conversion reported as an average of duplicate runs).

Catalyst Name	Nanoparticle Size	Time (h)	Styrene Conversion (%)
JEZ106	55.0 nm ± 31.6	1	92.8
JEZ108	49.9 nm ± 23.9	1	92.9
JEZ111	28.0 nm ± 22.5	1	92.7
JEZ110	12.3 nm ± 4.9	1	92.8
JEZ121	8.5 nm ± 3.2	1	92.7
JEZ106	55.0 nm ± 31.6	3	92.7
JEZ108	49.9 nm ± 23.9	3	92.7
JEZ111	28.0 nm ± 22.5	3	92.1
JEZ110	12.3 nm ± 4.9	3	93.2
JEZ121	8.5 nm ± 3.2	3	92.9
JEZ106	55.0 nm ± 31.6	24	92.7
JEZ108	49.9 nm ± 23.9	24	92.4
JEZ111	28.0 nm ± 22.5	24	93.1
JEZ110	12.3 nm ± 4.9	24	93.0
JEZ121	8.5 nm ± 3.2	24	92.7

Reaction conditions: 0.0034 mmol Au; 70 °C; Oxidant = H_2O_2

With maximum styrene conversion seemingly reached after 1 h, it was aimed to determine whether at shorter reaction times the effect of nanoparticle size became apparent. Thus catalytic evaluations were additionally carried out at 15- and 30 min. The styrene conversion results are shown in Table 5.4 and summarized in Figure 5.6.

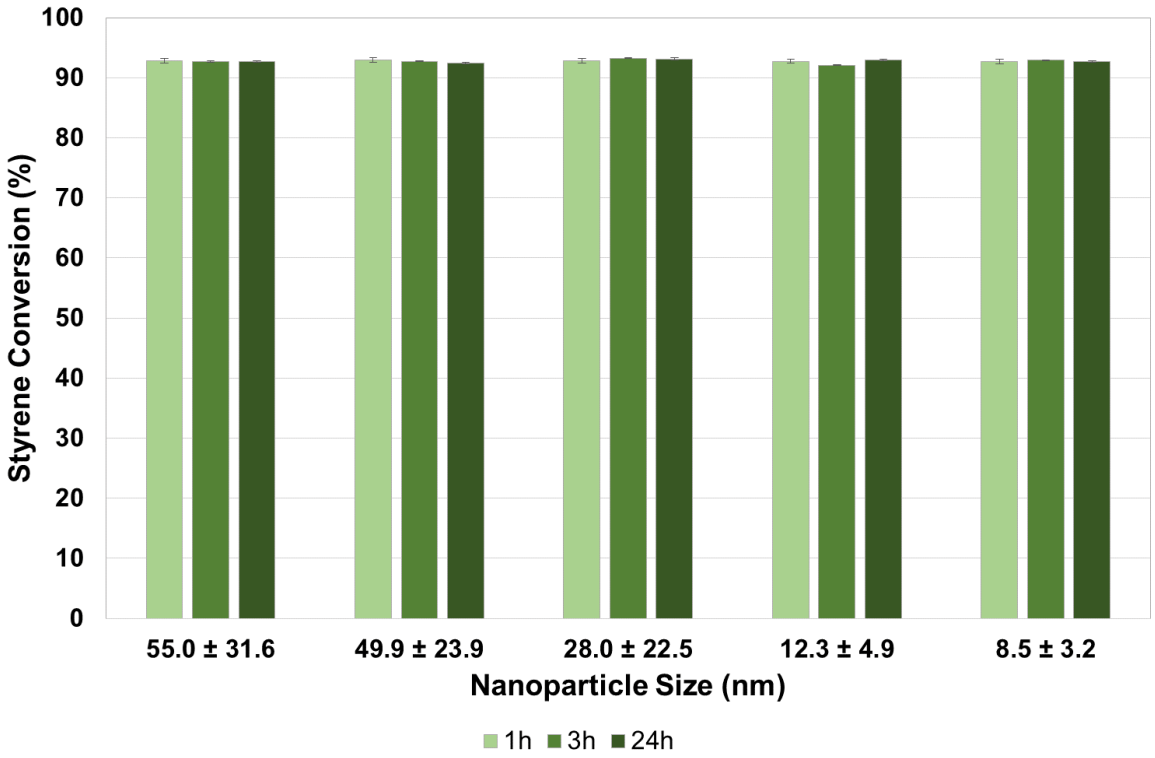

Figure 5.5 Effect of time on styrene conversion (varying nanoparticle size at Au loading of 0.0034 mmol, 70 °C, H_2O_2 as oxidant).

Table 5.4 Comparison of styrene conversion at times of 15 and 30 min for a range of nanoparticle sizes (styrene conversion reported as an average of duplicate runs).

Catalyst Name	Nanoparticle Size	Time (min)	Styrene Conversion (%)
JEZ106	55.0 nm ± 31.6	15	33.8
JEZ108	49.9 nm ± 23.9	15	33.5
JEZ111	28.0 nm ± 22.5	15	36.9
JEZ110	12.3 nm ± 4.9	15	35.9
JEZ121	8.5 nm ± 3.2	15	35.7
JEZ106	55.0 nm ± 31.6	30	50.2
JEZ108	49.9 nm ± 23.9	30	48.9
JEZ111	28.0 nm ± 22.5	30	51.9
JEZ110	12.3 nm ± 4.9	30	50.5
JEZ121	8.5 nm ± 3.2	30	51.0

Reaction conditions: 0.0034 mmol Au; 70 °C; Oxidant = H_2O_2

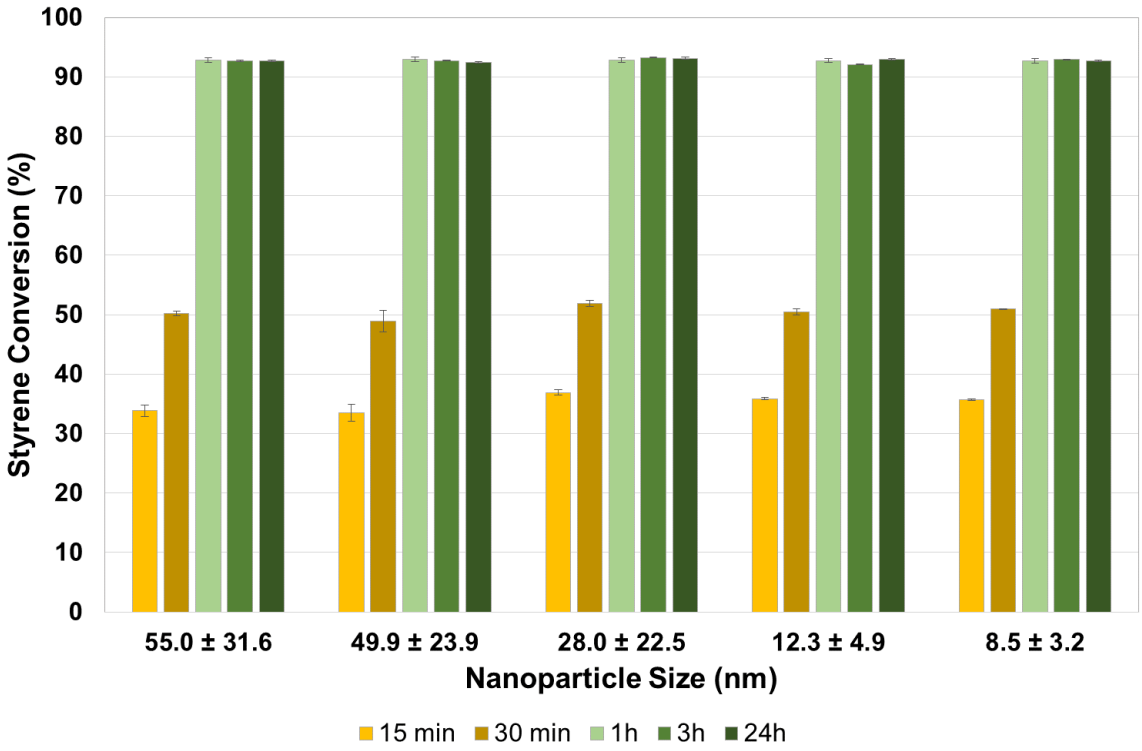

Figure 5.6 Effect of time on styrene conversion at 15 and 30 min compared to times above of 1 h and above (varying nanoparticle size at Au loading of 0.0034 mmol, 70 °C, H_2O_2 as oxidant).

These results show that after 15 min, conversion of styrene to other products is between 33- and 37 %. At these lower conversions there does appear to be some correlation with nanoparticle size. Where the larger nanoparticles (JEZ106 and JEZ108) are utilized, the styrene conversions achieved are 33.8- and 33.5 % respectively. The styrene conversion then increases slightly to between 35.7- and 36.9 % utilizing the smaller average sized nanoparticles (JEZ111, JEZ110 and JEZ121). However, since the styrene conversion only increases by up to 4 %, the correlation between nanoparticle size and styrene conversion after 15 min is by no means conclusive. Furthermore it can be seen from Table 5.4 and Figure 5.6 that after 30 min, styrene conversion reaches approximately between 49- and 52 %. Again, this is a very small variance from which no correlation between nanoparticle size and styrene conversion can be made.

Focusing on the product selectivity resultant from the observed styrene conversion, a further unexpected result was the formation of a white precipitate (see Figure 5.7). From GC analysis of the mother liquor, benzaldehyde was the only oxidation product detected in solution albeit in trace amounts which increased from just above 0.02 mass percent after 1 h to a maximum approaching approximately 0.10 mass percent (Figure 5.8). No oxidation products were

observed for reactions shorter than1 h. As with styrene conversion, there also appeared to be no difference in selectivity when varying nanoparticle size. The selectivity toward the white precipitate obtained between 1 and 24 h of reaction (as calculated by GC analysis) correlated to the styrene conversion obtained *e.g.* a 93 % conversion would correspond to an approximate 92.9 % weight percentage (relative to the initial mass of styrene) of the white precipitate. This was confirmed by isolating (by means of evaporation) the white precipitate and it was found that, as a percentage of the initial amount of styrene subjected to catalysis, the amount of white product isolated corresponded to the styrene conversion obtained.

Another observation, as shown in Figure 5.7 is that the white precipitate appeared to be less abundant up to 1 h of reaction (imparting only a cloudiness to the reaction mixture), despite styrene conversion being similar to what was obtained after 3- and 24 h. Where the precipitate was not as abundant however *i.e.* at lower styrene conversions, the mass of the precipitate isolated did not correlate to the conversion; varying between 34- and 55 %. The visible differences, the amount of precipitate isolated as well as the F-test results, adds to the evidence that intermediates had formed within the first hour thus resulting in the similar mean conversion results after 1 h as for the longer reaction times. What this implies overall is that the majority of the styrene is consumed after 1 h, which then undergoes further transformation to the white product observed thereafter at increased reaction times.

Figure 5.7 Appearance of reaction mixture after 1 h (left) and appearance after 24 h (right – appearance similar after 3 h).

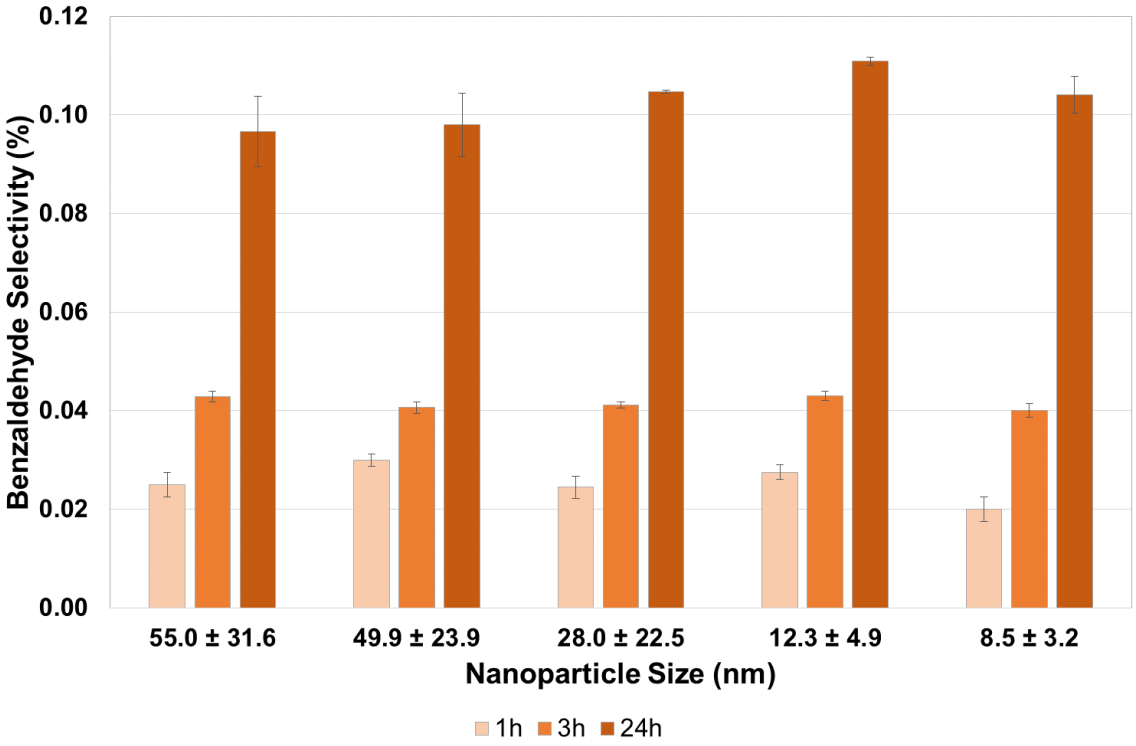

Figure 5.8 Effect of time on benzaldehyde selectivity with increased reaction time for nanoparticles of varying size.

However, before any mechanisms of product formation could be proposed, identification of the unexpected precipitate was imperative. Based on the appearance of the isolated material (a flaky, brittle, white material with traces of purple colouring most likely due to the gold nanoparticles encapsulated within – Figure 5.9) it was hypothesized that instead of the formation of oxidation products, the styrene had polymerized to form polystyrene.

Figure 5.9 Appearance of material isolated from aqueous layer of reaction mixture.

To test the hypothesis, it was thought that firstly infrared (IR) spectroscopy, followed by proton nuclear magnetic resonance (^{1}H NMR) spectroscopy and gel permeation chromatography (GPC) would provide sufficient information to confirm polystyrene formation. Before actual characterization of the material, it was thought that removal of the trace amounts of nanoparticles would be necessary since the presence of them may have skewed analysis results. This was to be done by dissolving the polystyrene and placing it in a centrifuge to separate the nanoparticles from the polystyrene. From literature, it was found that polystyrene should be highly soluble in tetrahydofuran (THF) and chloroform.[28] The isolated material was indeed found to be highly soluble in both and this therefore served as preliminary evidence pointing to the fact that it was polystyrene.

After subsequent dissolution of the material in chloroform and centrifugation for one hour, it was possible to separate the nanoparticles (which had aggregated in a clump at the tip of the centrifuge tube) by decanting the polystyrene solution. The chloroform was then removed by evaporation to leave a pure white flaky material. This was then subjected to attenuated total reflectance (ATR) IR analysis; of which the resultant spectrum is shown in Figure 5.10 below. Comparing it to literature, the presence of the bands due to the aromatic C-H stretching vibration (3030-3080 cm^{-1}), aromatic C-H combination frequency overtones (2000-1650 cm^{-1}), aromatic C-C bond stretching vibration (1625-1475 cm^{-1}), and aromatic C-H deformation vibrations (1250-900 and 900-650 cm^{-1}) were present.[29] This was therefore the first evidence of the white precipitate being polystyrene.

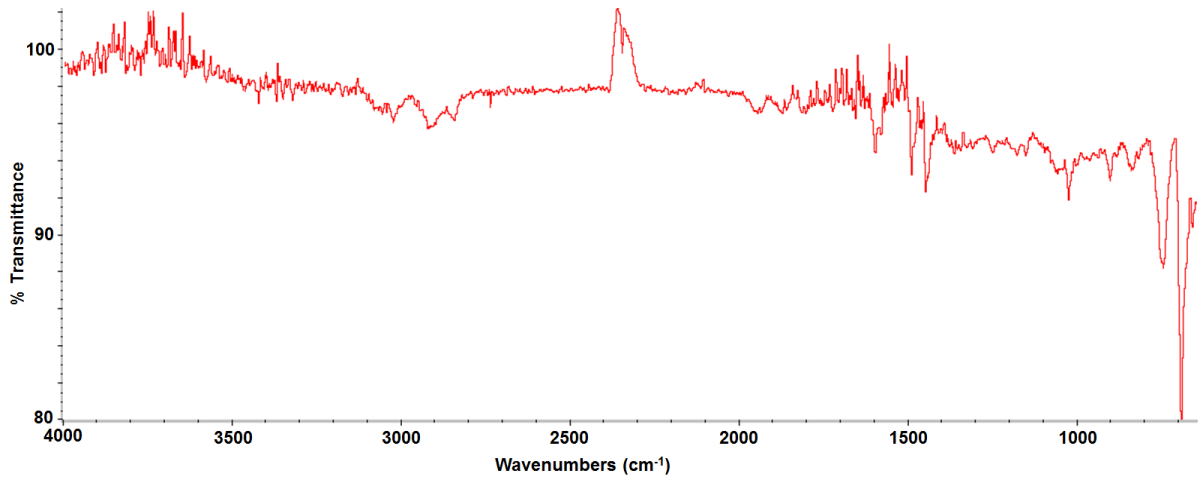

Figure 5.10 ATR-IR of isolated material.

Further evidence of the product being polystyrene was obtained from ^{1}H NMR (Figure 5.11). Multiplets for Ar-H protons were found in the region between 6 and 8 ppm with chemical shifts of –CH- protons of the backbone of the polymer chain found in the region between 3.5 and 5.5 ppm while that of the $–CH_2-$ units were found between 1 and 2.5 ppm. These chemical shifts corresponded well with those reported in literature.[30]

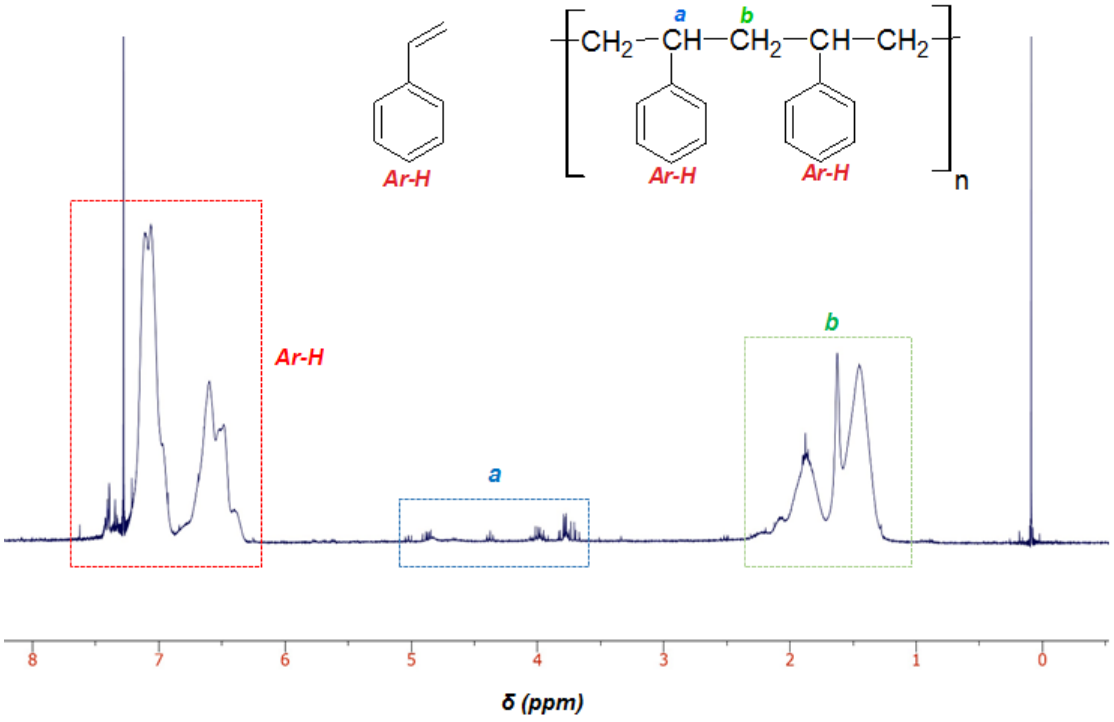

Figure 5.11 ^{1}H NMR spectrum of isolated material confirming it to be polystyrene.[30]

To confirm the polymeric nature of the white precipitate, and therefore confirm that polystyrene was indeed formed, GPC was carried out. The GPC chromatogram is shown in Figure 5. ***12*** along with the resultant peak table (Table 5.5).

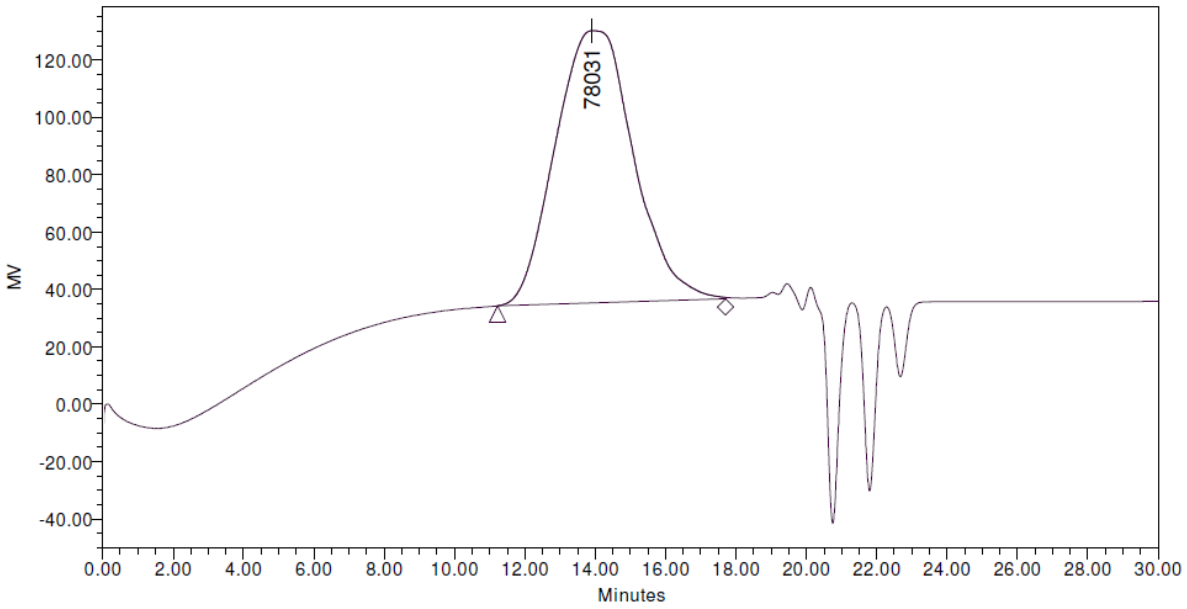

Figure 5. 12 GPC chromatogram of white precipitate.

Table 5.5 Relative GPC peak table of white precipitate.

M_n	M_W	M_P	M_Z	M_{Z+1}	M_W/M_n	M_Z/M_W	M_{Z+1}/M_W
31916	120722	78031	290939	494787	3.8	2.4	4.0

* M_n = Number average molecular weight, M_W = Weight average molecular weight, M_P = Molecular weight of highest peak, M_Z and M_{Z+1} = Higher average molecular weights
*Units = Daltons
*M_W/M_n = Polydispersity Index

It can be seen from the above GPC results that a weight average molecular weight (M_W) of 120722 was obtained. With a number average molecular weight (M_n) of 31916, a resultant relatively large polydispersity index of 3.8 was obtained. The large polydispersity index, coupled with high average molecular weights (M_Z and M_{Z+1}) values of 290939 and 494787, is an indication that polymerization is rapid and not very controlled. Rapid polymerization is supported by the previous styrene conversion results showing that a maximum conversion had been reached by the end of the first hour of reaction.

Having now confirmed the major, previously unidentified product to be polystyrene, it was attempted to determine the mechanism by which styrene polymerization occurs under the conditions employed. It was already seen that for reaction time of up to 1 h, the reaction mixture was turbid, but without heavy precipitate, although styrene conversion is still similar. The fact that for up to an hour of reaction time no heavy precipitate was present, may suggest

that the products formed during the initial stages are perhaps lower molecular weight polystyrene. In light of this, it was proposed to test whether a reduction in reaction temperature would possibly limit polystyrene formation. The reaction conditions and styrene conversion results for the temperature variation experiments are tabulated in Table 5.6 with the styrene conversion results also summarized in Figure 5.13. It can be seen that there appears to be very little difference in styrene conversion as a result of variation in temperature over a 24 h period. Only a 3 – 4 % increase in styrene conversion is observed at 70 °C as compared to reactions performed at 30- and 50 °C.

Table 5.6 Comparison of styrene conversion at 30-, 50- and 70 °C over 24 h for a range of nanoparticle sizes (styrene conversion reported as an average of duplicate runs).

Catalyst Name	Nanoparticle Size	Temperature (°C)	Styrene Conversion (%)
JEZ106	55.0 nm ± 31.6	30	89.2
JEZ108	49.9 nm ± 23.9	30	89.2
JEZ111	28.0 nm ± 22.5	30	89.4
JEZ110	12.3 nm ± 4.9	30	89.6
JEZ121	8.5 nm ± 3.2	30	89.0
JEZ106	55.0 nm ± 31.6	50	88.8
JEZ108	49.9 nm ± 23.9	50	89.3
JEZ111	28.0 nm ± 22.5	50	89.2
JEZ110	12.3 nm ± 4.9	50	88.8
JEZ121	8.5 nm ± 3.2	50	89.6
JEZ106	55.0 nm ± 31.6	70	92.7
JEZ108	49.9 nm ± 23.9	70	92.4
JEZ111	28.0 nm ± 22.5	70	93.1
JEZ110	12.3 nm ± 4.9	70	93.0
JEZ121	8.5 nm ± 3.2	70	92.7

Reaction conditions: 0.0034 mmol Au; Oxidant: H_2O_2

Since relatively high conversions were obtained even at the lower temperatures of 30- and 50 °C over 24 h, it was decided to evaluate the effect of temperature over shorter time periods. Since one of the most notable aspects of all the results thus far is the fact that there appears to be no difference in styrene conversion relative to nanoparticle size, the effect of temperature over shorter reaction times of 30- and 60 mins were evaluated using only the smallest nanoparticle size. As can be seen from Table 5.7 and Figure 5.14, at temperatures of 30- and 50 °C styrene conversions of approximately 36 % were obtained at 30- and 60 mins. A clear

difference in conversion with time was however seen at 70 °C, where styrene conversion increased from 50.5 to 92.7 % after 30- and 60 mins respectively. Clearly then, 70 °C was the best temperature for activity in this case. These results correspond to those obtained after 24 h where at 30- and 50 °C a slightly lower conversion was observed.

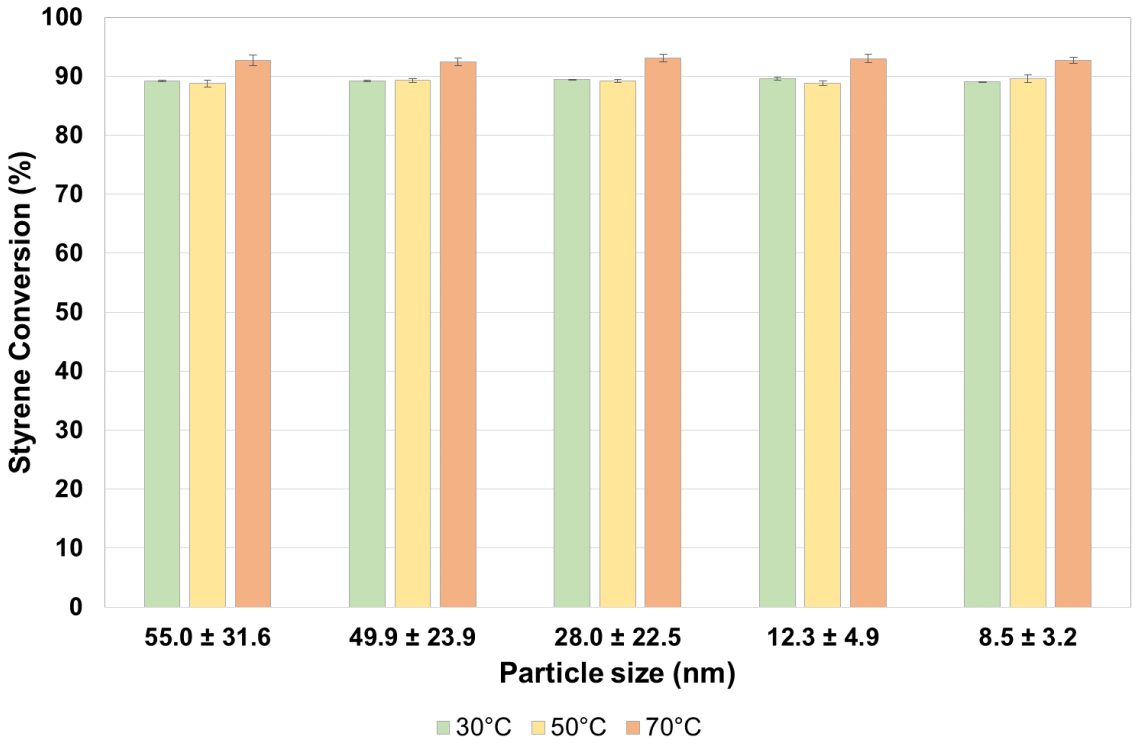

Figure 5.13 Styrene conversion as a function of temperature (reaction time: 24 h).

Table 5.7 Effect of temperature at reaction times of 30 and 60 mins (styrene conversion reported average of duplicate runs).

Time	Temperature (°C)	Styrene converted (%)
30min	30	36.8
60min	30	35.0
30min	50	35.9
60min	50	35.5
30min	70	50.5
60min	70	92.7

Reaction conditions: 0.0034 mmol Au; Nanoparticle size: 8.5 nm ± 3.2; Oxidant: H_2O_2

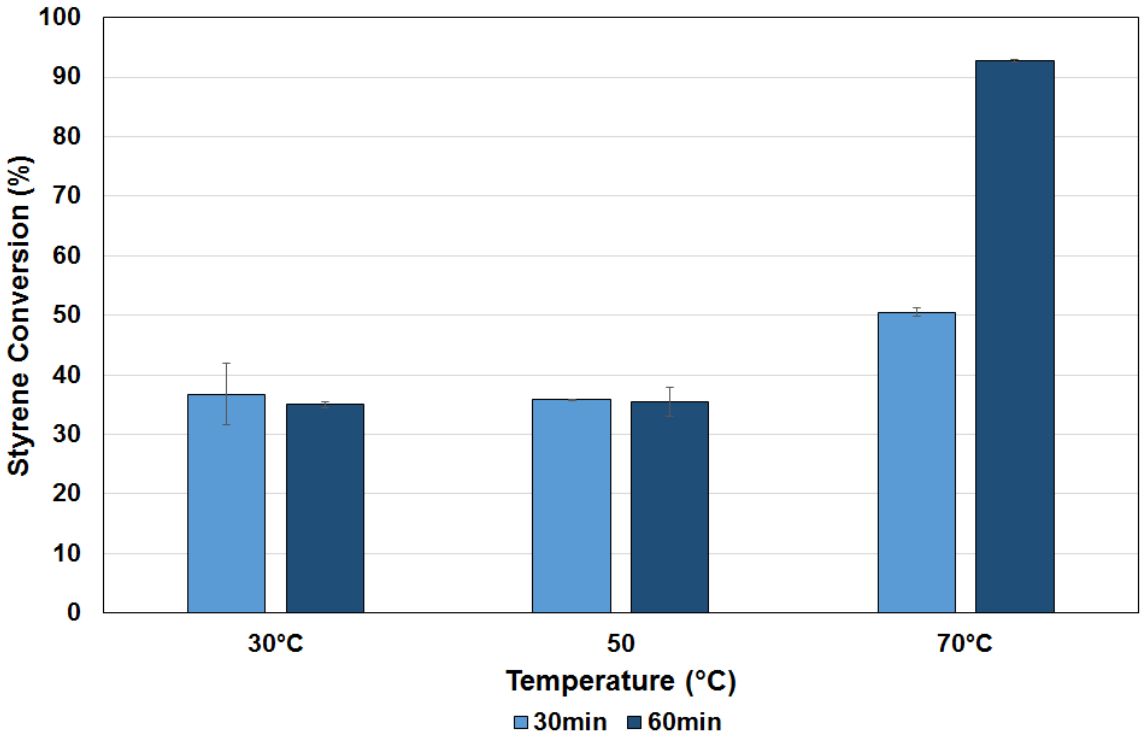

Figure 5.14 Effect of temperature at reaction times of 30 and 60 mins.

In terms of selectivity, no oxidation products were seen to have formed at 30 and 50 °C according to GC analysis, with approximately 35 % selectivity toward the polymeric material obtained after 30- and 60 mins and increasing to approximately 89 % after 24 h. Similarly, at 70 °C, selectivity to the polymeric material correlated to the styrene conversion at 30 and 60 mins with approximately 0.1 mass percent of benzaldehyde observed after 60 min.

As mentioned, there appeared to be no difference in styrene conversion and selectivity relative to nanoparticle size at 24 h. In addition, only trace amounts of benzaldehyde was observed at high conversions, with selectivity favouring polystyrene and approximately corresponding to the obtained conversion. A possible reason for the apparent lack of nanoparticle size effect on styrene conversion and selectivity is that we may be dealing with an auto-polymerization process. Although styrene is known to self-polymerize, the batch of monomer utilized in all the reported evaluations contained 50 ppm of the stabilizing agent 4-*tert*-butylcatechol, to prevent, or at least, minimize self-polymerization. Even if the stabilizer had been ineffective, the rate of self-polymerization in the absence of any stabilizer normally occurs at a rate of 0.1 % per hour at 60 °C and 2 % per hour at 100 °C.[31] Thus based on this data, and assuming a linear relationship between the rate of self-polymerization and

temperature, styrene conversion of approximately 0.5 % per hour would be expected at 70 °C in the absence of stabilizer, and would result in an approximate 12 % conversion after 24 h. Furthermore, light also did not appear to enhance any self-polymerization as no styrene conversion was observed when this was investigated. Age of the styrene also showed no effect on self-polymerization when comparing a 3-year-old batch and a newly acquired one. In addition, the presence of any residual Au or other possible contaminants such as Cu or Fe, which could facilitate styrene polymerization were mitigated by thorough washing of glassware and stirrer bars in acid baths.

However, in our case we observed that styrene conversions of up to 93 % were obtained after 1 h at 70 °C. This is clearly indicative of a catalytic effect, but as there appeared to be no influence on catalytic activity based on nanoparticle size, a component in the reaction system other than the Au nanoparticles may have been acting as the catalyst; the most likely candidate at this point possibly being H_2O_2. The polymerization process could thus proceed according to Scheme 5.1 based on the dissociation of H_2O_2 to form HO• radicals which would then initiate polymerization.[32,33]

Scheme 5.1 Proposed styrene polymerization mechanism with H_2O_2 as radical initiator.[32,33]

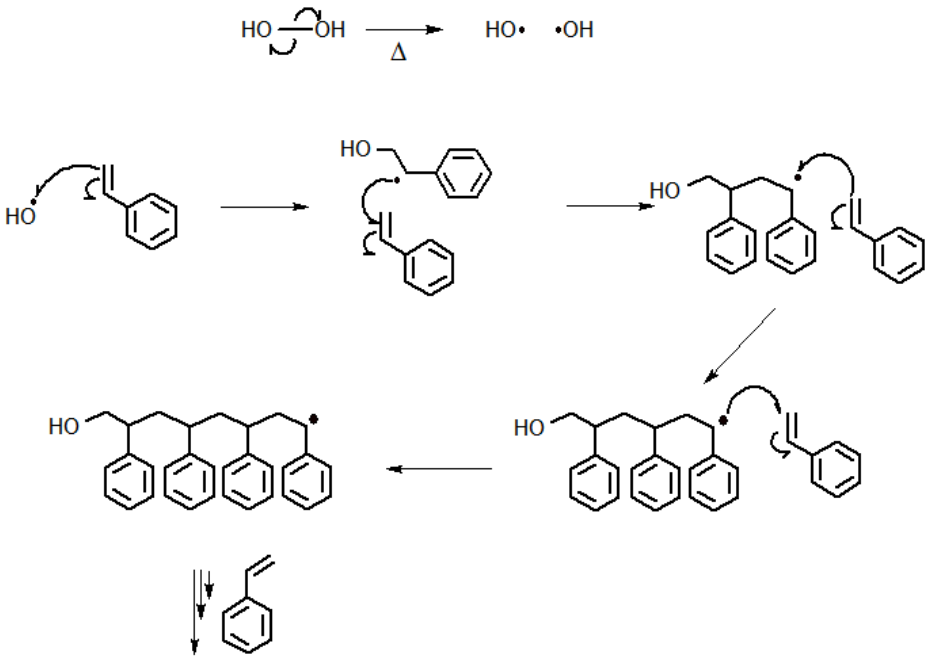

At 70 °C, H_2O_2 could readily dissociate in water to form H_2O and O_2.[33] Previously reported styrene conversion results (Figure 5.5 and Figure 5.13) appear to support this hypothesis,

since even at the relatively low temperature of 30 °C, an approximate 90 % styrene conversion was achieved. Increasing the temperature then also appears to accelerate H_2O_2 dissociation since it was seen that at 70 °C, approximately 93 % conversion was already obtained within an hour.

The above proposed HO• radical initiator mechanism does not include any involvement of the Au catalyst and therefore provides a possible explanation as to why nanoparticle size appears to have had no effect on styrene conversion.

However, the contribution of the catalyst playing some role in the polymerization process could not be discounted. As such, catalysis evaluations were performed in the absence of H_2O_2, in order to determine the role of the Au nanoparticles in the catalytic process. This was done at 70 °C over 1, 8 and 24 h. The results of these catalytic evaluations are tabulated in Table 5.8 and summarized in Figure 5.15.

Table 5.8 Styrene conversion over 1, 8 and 24 h where no H_2O_2 was added (styrene conversion reported as an average of duplicate runs).

Catalyst Name	Nanoparticle Size	Time (h)	Styrene Conversion (%)
JEZ106	55.0 nm ± 31.6	1	89.3
JEZ108	49.9 nm ± 23.9	1	89.7
JEZ111	28.0 nm ± 22.5	1	89.4
JEZ110	12.3 nm ± 4.9	1	89.3
JEZ121	8.5 nm ± 3.2	1	89.6
JEZ106	55.0 nm ± 31.6	8	89.6
JEZ108	49.9 nm ± 23.9	8	89.6
JEZ111	28.0 nm ± 22.5	8	89.0
JEZ110	12.3 nm ± 4.9	8	89.0
JEZ121	8.5 nm ± 3.2	8	89.0
JEZ106	55.0 nm ± 31.6	24	93.1
JEZ108	49.9 nm ± 23.9	24	93.0
JEZ111	28.0 nm ± 22.5	24	93.1
JEZ110	12.3 nm ± 4.9	24	93.1
JEZ121	8.5 nm ± 3.2	24	93.0

Reaction conditions: 0.0034 mmol Au; 70 °C; No H_2O_2 added

From the these results it can be seen that within the first hour, and up to 8 h, styrene conversion of between 89 and 90 % was achieved in the absence of any H_2O_2 (hence the

reaction system consisting only of catalyst and styrene). With these styrene conversions obtained in the absence of H_2O_2, it can thus be concluded that the major contributor catalysing styrene polymerization is in fact the water soluble Au catalyst.

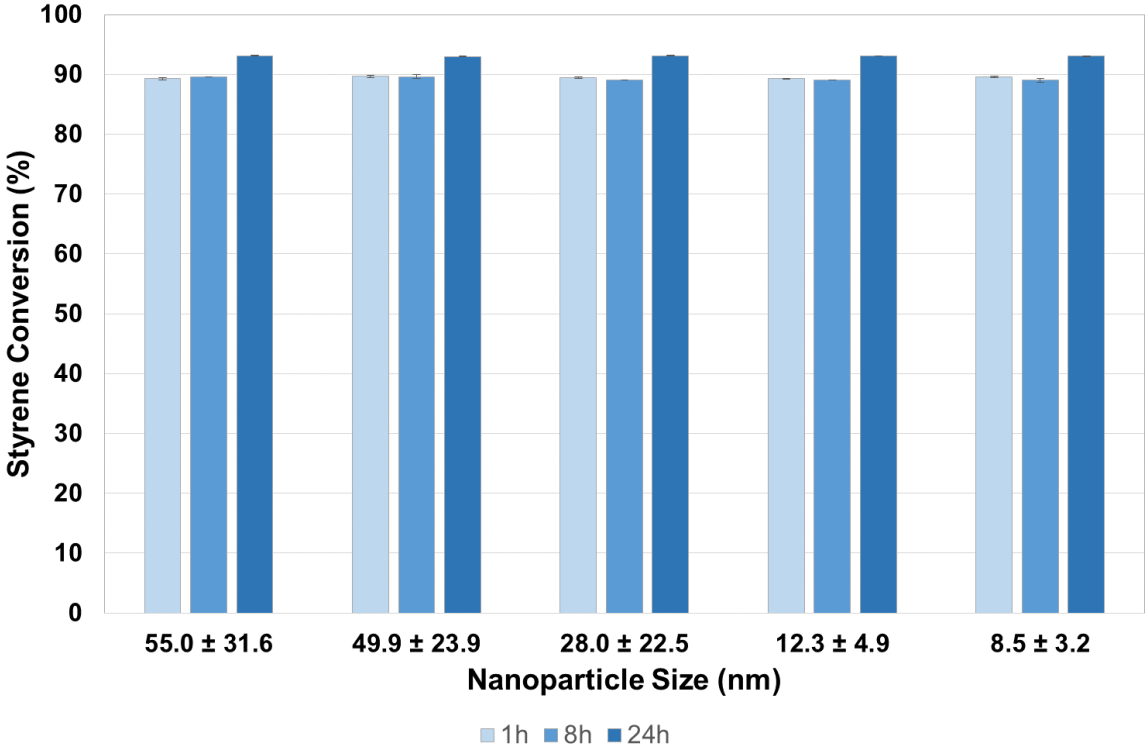

Figure 5.15 Styrene conversion at 1, 8 and 24 h for experiments in the absence of H_2O_2.

To confirm the major catalytic role played by the aqueous Au in the polymerization of styrene, evaluations were carried out in the absence of any catalyst or H_2O_2. This should of course, in theory, have resulted in no styrene conversion occurring. However, as can be seen in Table 5.9 and Figure 5.16, styrene and water stirred in the reactor tube resulted in an unexpected conversion of between 27- and 29 % as determined by GC analysis. This was obtained after 1 h of reaction time at 30-, 50- and 70 °C. In order to ascertain whether the observed conversion was as a result of the aqueous environment, styrene was stirred under the same conditions in the absence of either catalyst, water or H_2O_2 at 70 °C. Again however, against expectation, styrene conversion was observed.

Table 5.9 Styrene conversion results in the absence of catalyst (styrene conversion reported average of duplicate runs).

Temperature (°C)	Mixture	Styrene Conversion (%)
30	Styrene+Water	28.0
50	Styrene+Water	28.6
70	Styrene+Water	27.8
30	Styrene	28.1
50	Styrene	27.4
70	Styrene	28.7

Reaction conditions: No catalyst; 5 ml styrene; 5 ml water; No H_2O_2 added; 1 h reaction time

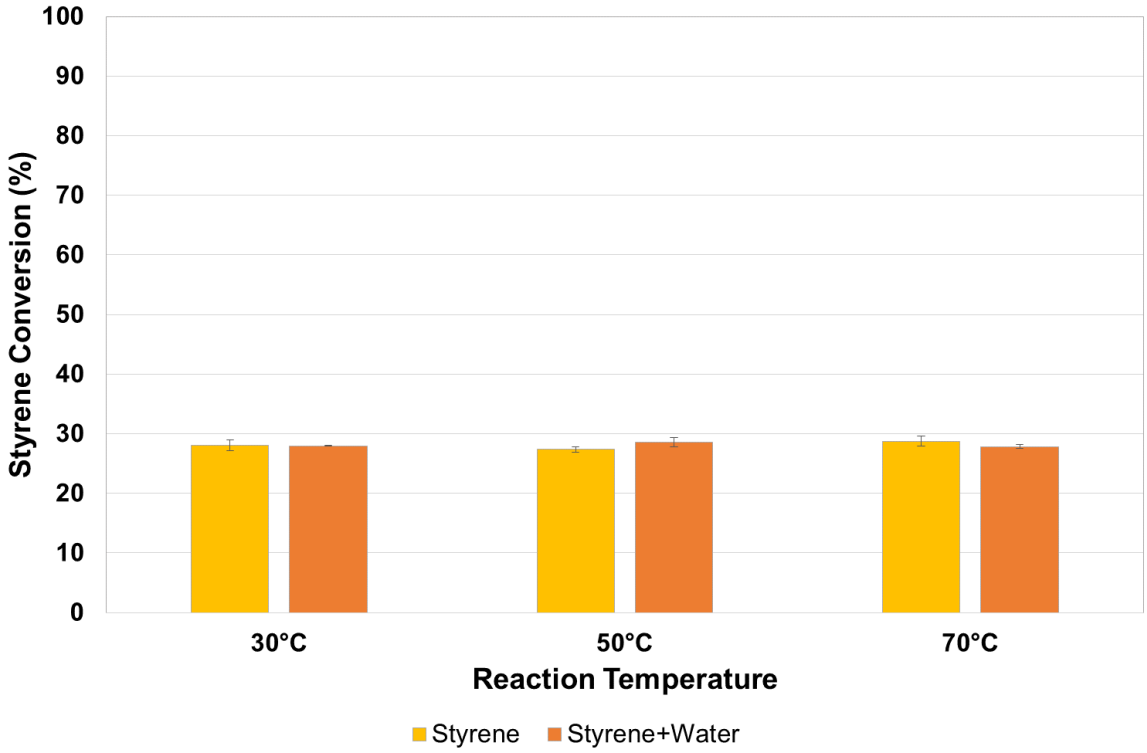

Figure 5.16 Comparison of styrene conversion for reactions containing no catalyst at 30, 50 and 70 °C.

Although styrene conversion, as determined by GC analysis, was observed in all cases, visual changes in the reaction mixture (as in signs of turbidity) were only observed for reactions at 70 °C (and even then it was slight). This turbidity was removed upon syringe filtration (to prevent any possible polymeric material from fouling the GC column) in the preparation of samples for GC analysis, but could be indicative of the early stages of polymer formation. Where no turbidity was witnessed at lower temperatures, the styrene conversion as determined by GC analysis, may have been due to initial oligomerization that may have occurred. As no extra peaks were observed in the resultant GC chromatogram, these

oligomers were most likely also removed upon syringe filtration. The portion of the samples which were not filtered, were retained for analysis. However, the unfiltered material isolated for analysis (ATR-IR and ^{1}H NMR) was insufficient to conclusively confirm the presence of polymeric or oligomeric material.

In work done by Khuong *et al* (2005), density functional theory (DFT) calculations show that the most likely mechanism of styrene self-polymerization is *via* the Mayo mechanism depicted in Scheme 5.2.[31] Here radical formation proceeds through the Diels-Alder dimerization of styrene where after molecule-assisted homolysis between the dimer and a third styrene moiety generates monoradical initiators which initiate polymerization.

Scheme 5.2 Mayo mechanism of styrene self-polymerization.[31]

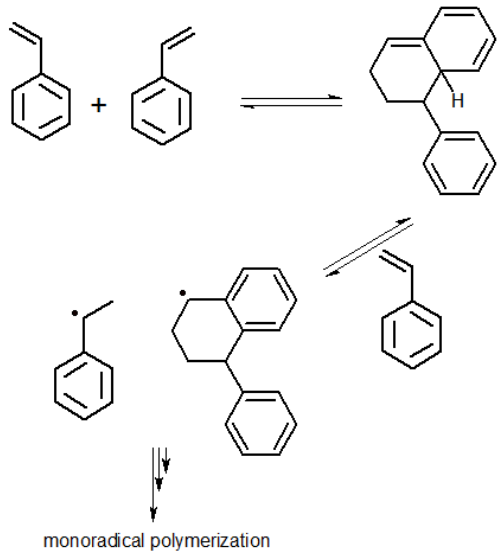

Providing conclusive evidence for the above mechanism however proved challenging. Isolating any of the material, be it polymer/oligomer or the dimer intermediates proposed in Scheme 5.2 was difficult due to their low concentrations. Analysis of any miniscule amount of material which could however be scraped together, proved inconclusive due to any sample signal being lost in baseline noise (in ATR-IR for example). However, what was apparent was that the styrene evaluated, by itself or combined with water, changed colour and acquired a clear yellow appearance. The intensity of this yellow colour change appeared to increase with an increase in temperature (Figure 5.17). With this in mind, it was anticipated that some information regarding the nature of potential intermediates or products formed may be gleaned by subjecting the samples to UV-vis spectroscopy.

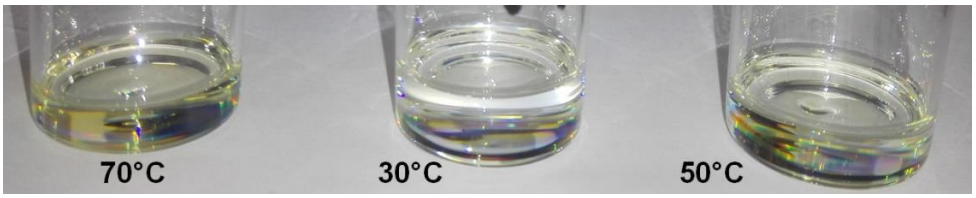

Figure 5.17 Differences in yellow colour intensity of styrene isolated after reactions at 30-, 50- and 70 °C in the absence of catalyst.

Resultant UV-vis spectra showed a clear difference for samples obtained at 30-, 50- and 70 °C (Figure 5.18). It can be seen that firstly the spectra differ from both styrene and polystyrene, thus clearly indicating differences in the concentration of intermediate species. At 30 °C it can be seen that a weak adsorption band in a similar region to that of the one present for styrene at approximately 390 nm is present. In addition to this a weak, broader band is visible in the region of approximately 435 nm. With an increase in temperature to 50 °C, the bands at 390 and 435 nm increase in intensity, thus possibly indicating an increase in the concentration of the intermediate species present. This increase in intensity corresponds to the increase in intensity of the yellow colour of the organic layer at 50 °C compared to 30 °C. At 70 °C, the two bands appeared to have transformed into a distinct, broad band at approximately 416 nm. If it is assumed that the above mentioned Mayo mechanism is occurring, the spectra could be indicative of firstly low concentrations of the Diels-Alder intermediate being formed at 30 °C, followed by an increase in its concentration at 50 °C. The broad band formed at 416 nm could then be the initial formation of oligomers after generation of the monoradical initiators.

Thus it is clear that there is self-polymerization which contributes between approximately 27- and 29 % to the overall styrene conversion. However, despite the apparent self-polymerization, it is clear that the water soluble Au is the major contributor to styrene polymerization. This is clearly demonstrated in Figure 5.19 where the presence of catalyst is shown to increase styrene conversion by approximately 60 % compared to where it is absent under the same reaction conditions (no H_2O_2, 70 °C, 1 h).

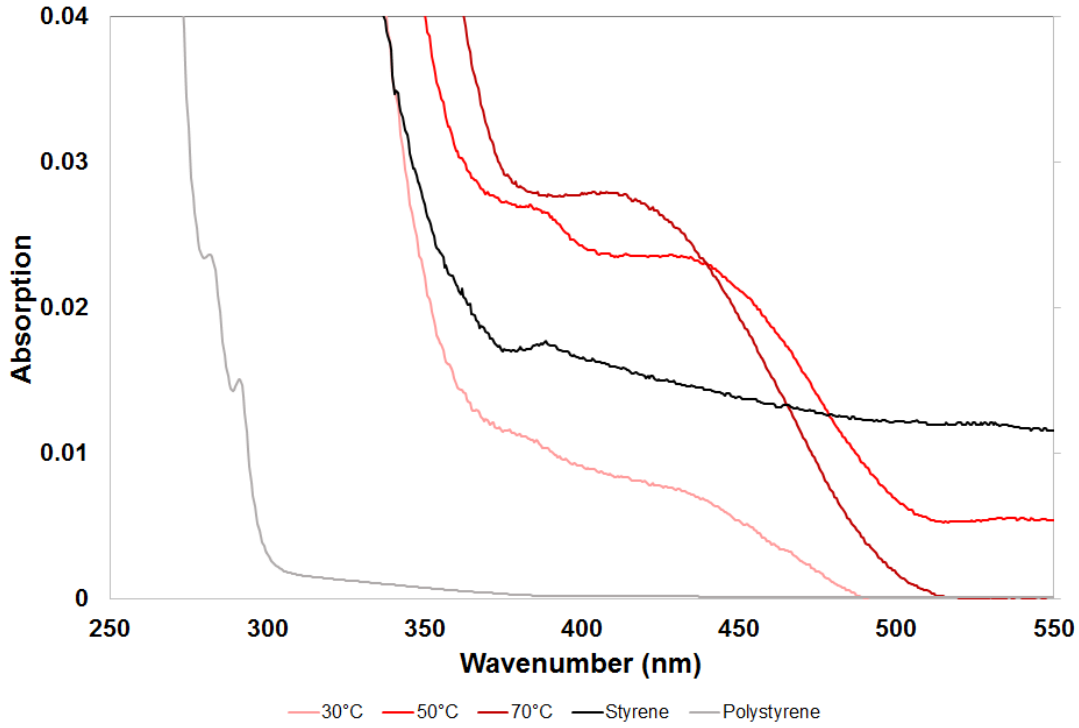

Figure 5.18 Differences in UV-vis spectra obtained at 30, 50 and 70 °C (shades of red) compared to styrene (black) and polystyrene (grey).

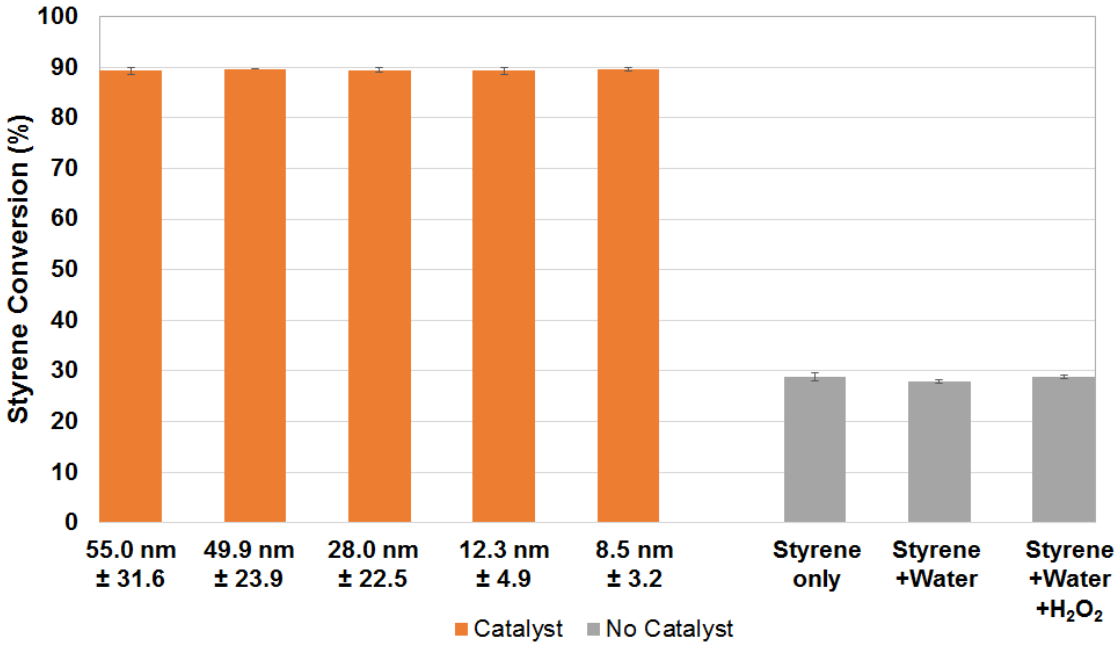

Figure 5.19 Styrene conversion in the presence and absence of aqueous Au catalyst (no H_2O_2, 70 °C, 1 h).

In terms of selectivity, in all of the above evaluations in the absence of catalyst, no oxidation products were formed. This is an indication then that the catalyst does enable the formation of benzaldehyde, but since styrene polymerization is clearly favoured, it only forms in trace amounts reaching a maximum in the region of 0.1 weight percent after 24 h at 70 °C (Figure 5.8).

It has been tentatively demonstrated that the water-soluble Au nanoparticles are primarily responsible for styrene polymerization occurring as opposed to the formation of radical initiators from H_2O_2 as proposed in Scheme 5.1. However, when looking at catalysis evaluations where H_2O_2 was present, it can be seen that at 70 °C the styrene conversion is consistently higher by approximately 2 to 3 % after 1 h of reaction compared to where it is absent (Figure 5.20). Evidently then, there is a small contribution towards styrene conversion by H_2O_2 in the first hour of reaction. In the absence of H_2O_2 the same conversion of between 92 to 93 % is however still reached after 24 h.

In order to evaluate what the contribution of H_2O_2 would be during the first hour of reaction, a mixture of firstly styrene and H_2O_2 was stirred at 70 °C for 1 h in the absence of any catalyst. It was found that styrene conversion similar to those in the absence of catalyst was obtained (27.1 %). The combination of styrene, water and H_2O_2 also produced a similar conversion result of 28.8 %. The results of the addition of H_2O_2 in the absence of catalyst is summarized in Figure 5.21. What this indicates is that H_2O_2 contributes to styrene conversion only in the presence of catalyst; acting as a co-catalyst to increase styrene conversion by between 2 and 3 % during the first hour. This admittedly is a very small increase and may not be conclusive evidence, but appears to be consistently occurring.

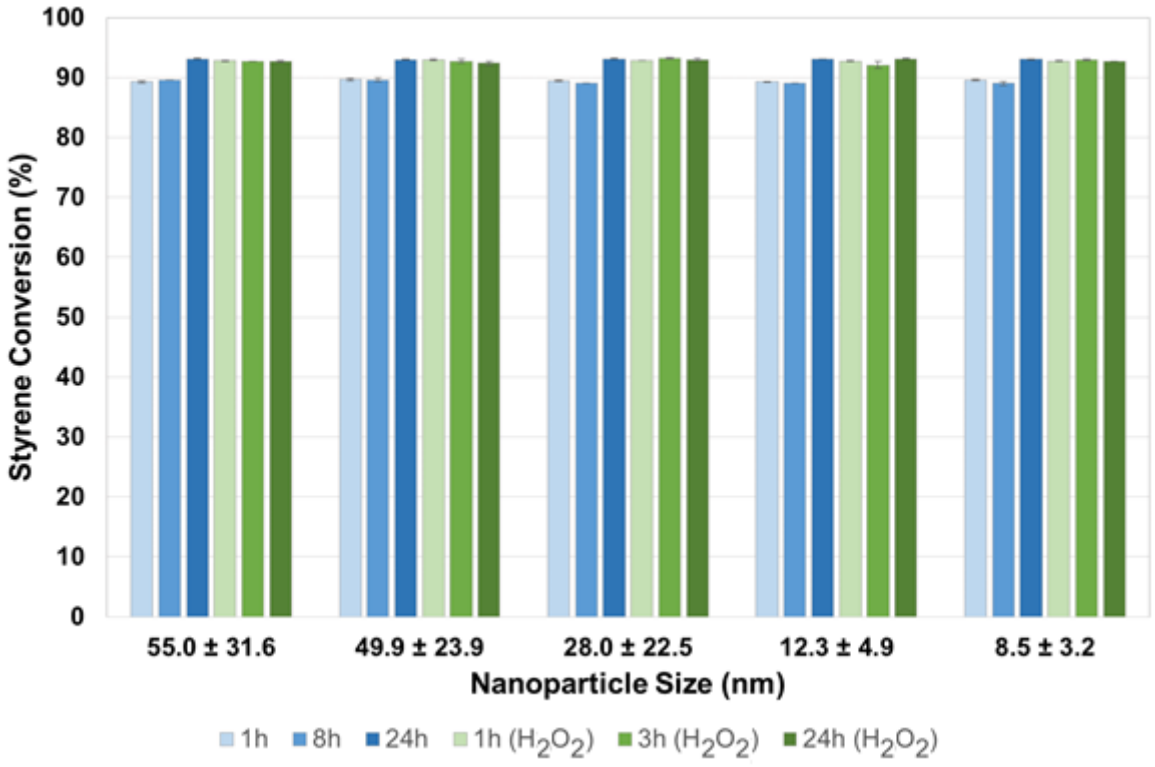

Figure 5.20 Comparison of styrene conversion with H_2O_2 excluded (blue bars) and added (green bars) at varying reaction times at 70 °C.

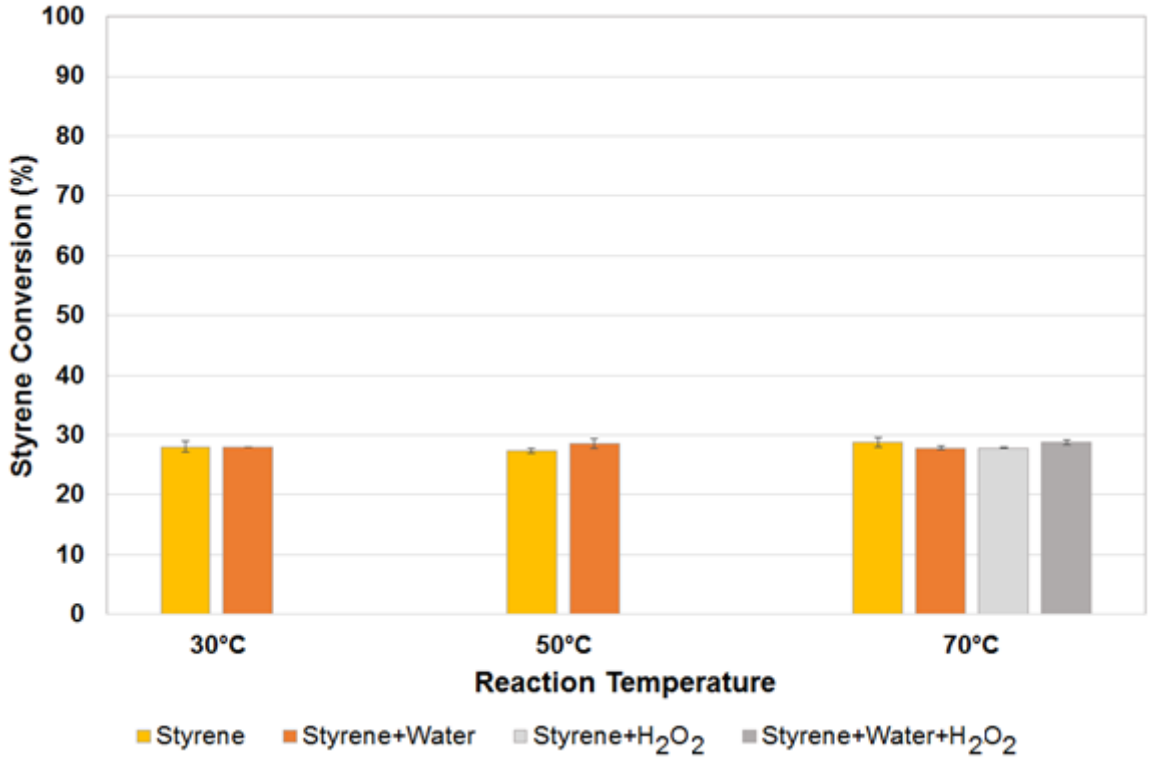

Figure 5.21 Comparison of styrene conversion in the absence of catalyst and addition of H_2O_2 at 70 °C.

The potential role of H_2O_2 in the polymerization process could be facilitated by the water soluble Au nanoparticles according to following equation[33,34]:

$$Au^{n+} + H_2O_2 \rightarrow Au^{n+1} + HO\bullet + HO^-$$

The HO• radical formed in this way would then contribute towards polymerization as depicted in Scheme 5.1.

With evidence that the catalyst overwhelmingly favours styrene polymerization, and possible suggestions that it also catalyses the dissociation of H_2O_2 to form radical initiators resulting in a small increase in styrene conversion, it was apparent that H_2O_2 was limited in its ability as an oxidizing agent (hence the trace amounts of benzaldehyde being observed). It was thus investigated whether, despite the observed propensity of the catalyst for styrene polymerization, the utilization of a stronger oxidizing agent such as *tert*-butyl hydroperoxide (TBHP)[35] might result in an increase in benzaldehyde production. The results of attempted oxidation using TBHP as potential oxidant is shown in Table 5.10 and summarized in Figure 5.22. In all cases a comparison with H_2O_2 is made.

Table 5.10 Comparison of styrene conversion in the presence of TBHP and H_2O_2 (styrene conversion reported as an average of duplicate runs).

Catalyst Name	Nanoparticle Size	Potential Oxidant	Styrene Conversion (%)
JEZ106	55.0 nm ± 31.6	TBHP	92.8
JEZ108	49.9 nm ± 23.9	TBHP	93.2
JEZ111	28.0 nm ± 22.5	TBHP	93.1
JEZ110	12.3 nm ± 4.9	TBHP	92.9
JEZ121	8.5 nm ± 3.2	TBHP	93.0
JEZ106	55.0 nm ± 31.6	H_2O_2	92.7
JEZ108	49.9 nm ± 23.9	H_2O_2	92.4
JEZ111	28.0 nm ± 22.5	H_2O_2	93.1
JEZ110	12.3 nm ± 4.9	H_2O_2	93.0
JEZ121	8.5 nm ± 3.2	H_2O_2	92.7

Reaction conditions: 0.0034 mmol Au; 70 °C, 24 h

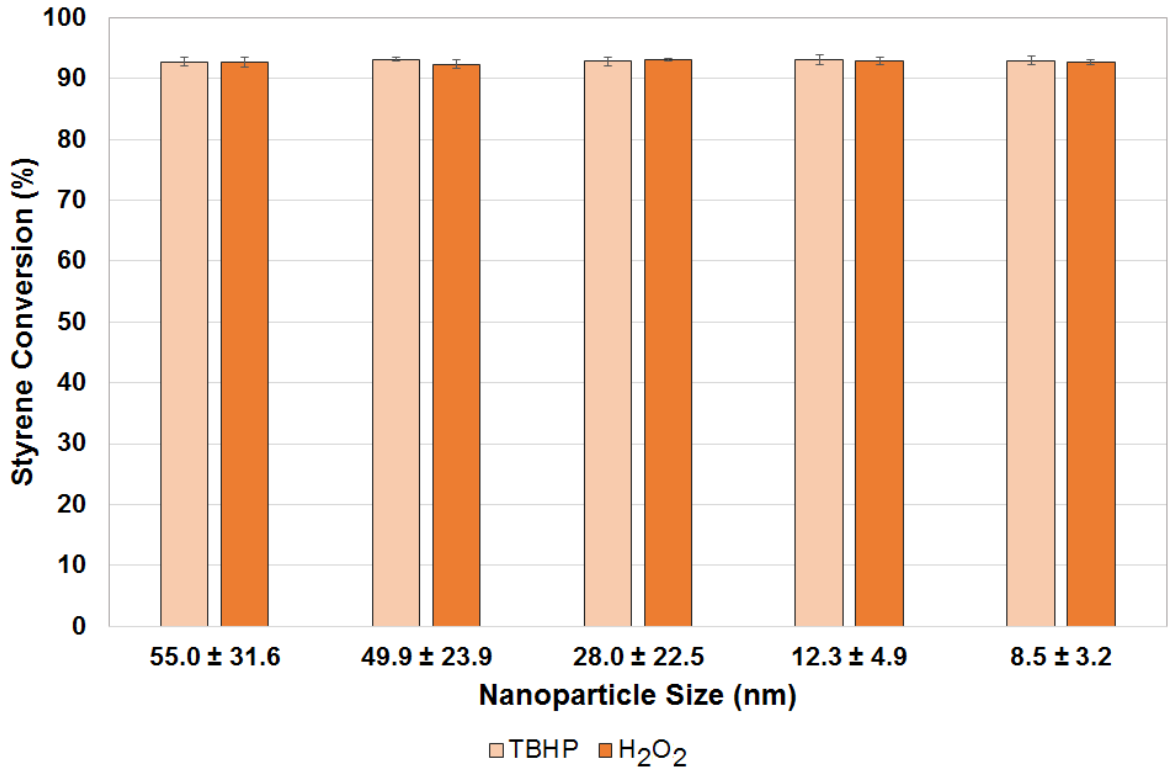

Figure 5.22 Comparison of styrene conversion using TBHP and H_2O_2 as potential oxidant.

As can be seen from the above results, the use of TBHP resulted in similar styrene conversions as when H_2O_2 was used under the same reaction conditions. What did however differ is the nature of the material obtained at the end of the reaction period of 24 h. We had previously confirmed that the material obtained when using H_2O_2 was polystyrene. When using TBHP, the material isolated at the end of the reaction differed in physical appearance in that it was not a white flaky, brittle material, but a soft, colourless gum-like material. ATR-IR however indicated that this gum-like material was also some sort of polystyrene-like material; showing transmittance bands at similar wavenumbers as polystyrene (Figure 5.23). GPC results indicated that the gum-like nature of the isolated material was due to its lower molecular weight (Table 5.11). Again, no oxidation products were formed.

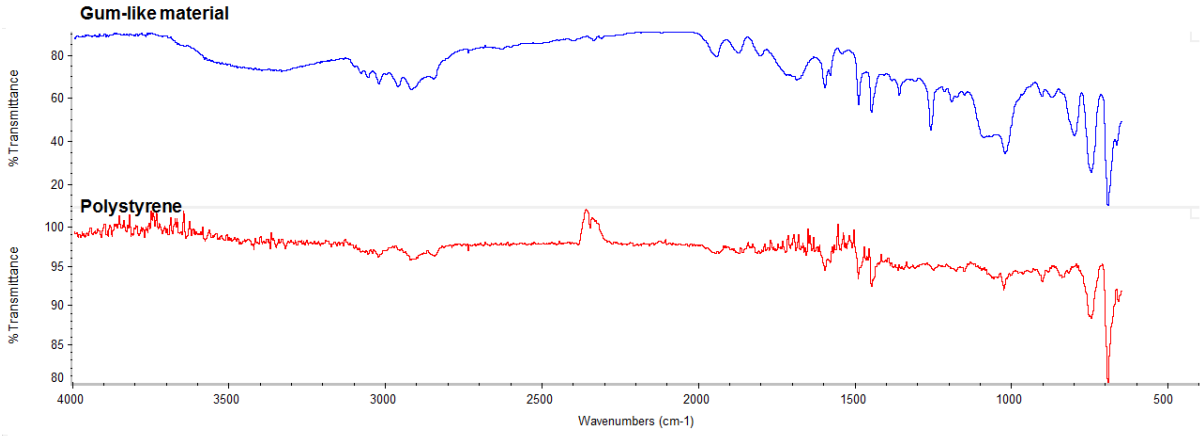

Figure 5.23 Comparison of ATR-IR spectra of gum-like material obtained when using TBHP as oxidant and that of polystyrene.

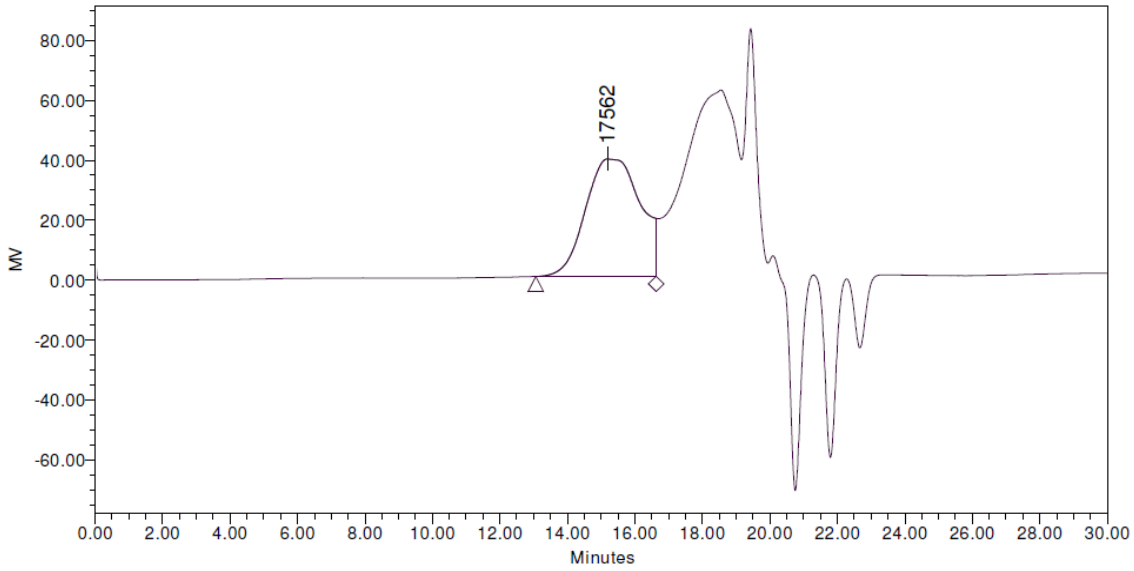

Figure 5.24 GPC chromatogram of gum-like polymer obtained when using TBHP.

Table 5.11 Relative GPC peak table comparing polymer obtained using H_2O_2 (solid) and TBHP (gum)

Polymer	M_n	M_W	M_P	M_Z	M_{Z+1}	M_W/M_n	M_Z/M_W	M_{Z+1}/M_W
Solid	31916	120722	78031	290939	494787	3.8	2.4	4.0
Gum	10788	19096	17562	33315	52869	1.8	1.7	2.8

*Unit for M_n, M_W, M_P, M_Z, M_{z+1} = Daltons; M_W/M_N = Polydispersity Index

The above observation regarding the differences in the nature of the polystyrene formed (*i.e.* polystyrene selectivity) when using TBHP compared to H_2O_2 therefore prompted a further

comparison of the polystyrene selectivity produced when using either TBHP or H_2O_2 as additive or in their absence (reaction in air). In addition, it was aimed to evaluate whether nanoparticle size contributed to any changes in polystyrene selectivity. As a result GPC results were obtained of polymer samples as tabulated in Table 5.12. The results are also shown in Figure 5.25 to Figure 5.27.

Table 5.12 Comparison of polystyrene properties obtained using different nanoparticle sizes and additives.

Additive	Nanoparticle Size	Mn	Mw	PDI
Air	8.5 nm ± 3.2	38181	116559	3.1
	28.0 nm ± 22.5	77381	296334	3.8
	55.0 nm ± 31.6	97601	302469	3.1
H_2O_2	8.5 nm ± 3.2	37274	119107	3.2
	28.0 nm ± 22.5	94118	242585	2.6
	55.0 nm ± 31.6	184698	356114	1.9
TBHP	8.5 nm ± 3.2	10306	18367	1.8
	28.0 nm ± 22.5	9768	18140	1.9
	55.0 nm ± 31.6	2238	3517	1.6

Reaction conditions: 0.0034 mmol Au; 70 °C, 24 h

What is evident is that there is a marked difference in the nature of the polystyrene when using TBHP compared to H_2O_2 and in the absence of any additive. This is therefore a clear indication that that the mechanism of polymerization when using TBHP is distinctly different compared to when using H_2O_2 or in the absence of any additive. In addition, unlike with styrene conversion, a clear difference in selectivity is in fact seen as a function of nanoparticle size.

Comparing the selectivity in the absence of additives and using H_2O_2, it seen that a corresponding trend of an increase in polymer molecular weight with an increase in nanoparticle size is obtained which can be attributed to a decrease in surface area. As previously deduced, the catalyst was confirmed to be the major contributor to styrene polymerization occurring. With the observed increase in polymer molecular weight with decreasing surface area, it appears that at higher surface area, there are more radical initiator sites therefore a greater proportion of styrene becomes associated with these sites instead of being incorporated into a growing polymer chain. Conversely, at lower surface areas, less radical initiator sites are available which then results in more styrene being incorporated into

the polymer chain and consequently resulting in the higher molecular weight polymers observed. However, it is seen that when H_2O_2 is used, M_n is larger at the larger nanoparticle sizes after being similar at the smallest size. This alludes to the fact that at higher surface areas, the H_2O_2 contributes to polymerization *via* the mechanism proposed in Scheme 5.1. H_2O_2 also appears to result in better PDI values as particle size increases. This again alludes to the fact that as surface area decreases, H_2O_2 increases its contribution towards polymerization. As the amount of H_2O_2 is similar when added with each nanoparticle size, the increased contribution of H_2O_2 towards polymerization results in lower PDI values as surface area decreases. Therefore, although in terms of styrene conversion H_2O_2 only provides a 2 – 3 % increase, it has a greater influence in increasing the molecular weight of the polymer formed and also leading to more monodisperse material.

The contribution of H_2O_2 to polymerization is confirmed when considering M_w values of polymers produced in the absence of it. In the absence of H_2O_2, M_w appears to level off to values around 300000 when employing nanoparticles of 28.0 nm ± 22.5 and above. However when H_2O_2 is present, at the larger nanoparticle size of 55.0 nm ± 31.6, and therefore lower surface area, the peroxide appears to contribute towards polymerization *via* the mechanism proposed in Scheme 5.1.

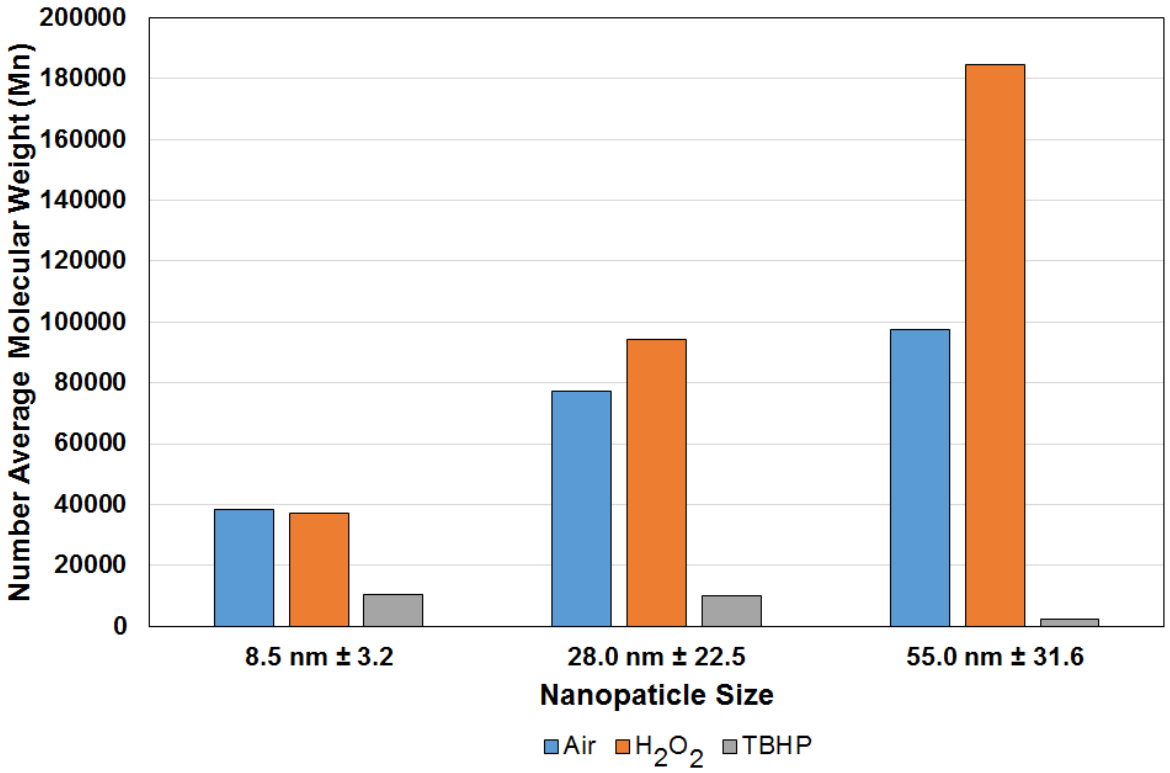

Figure 5.25 Number average molecular weight comparison (M_n) of polystyrene produced using different additives for varying nanoparticle sizes.

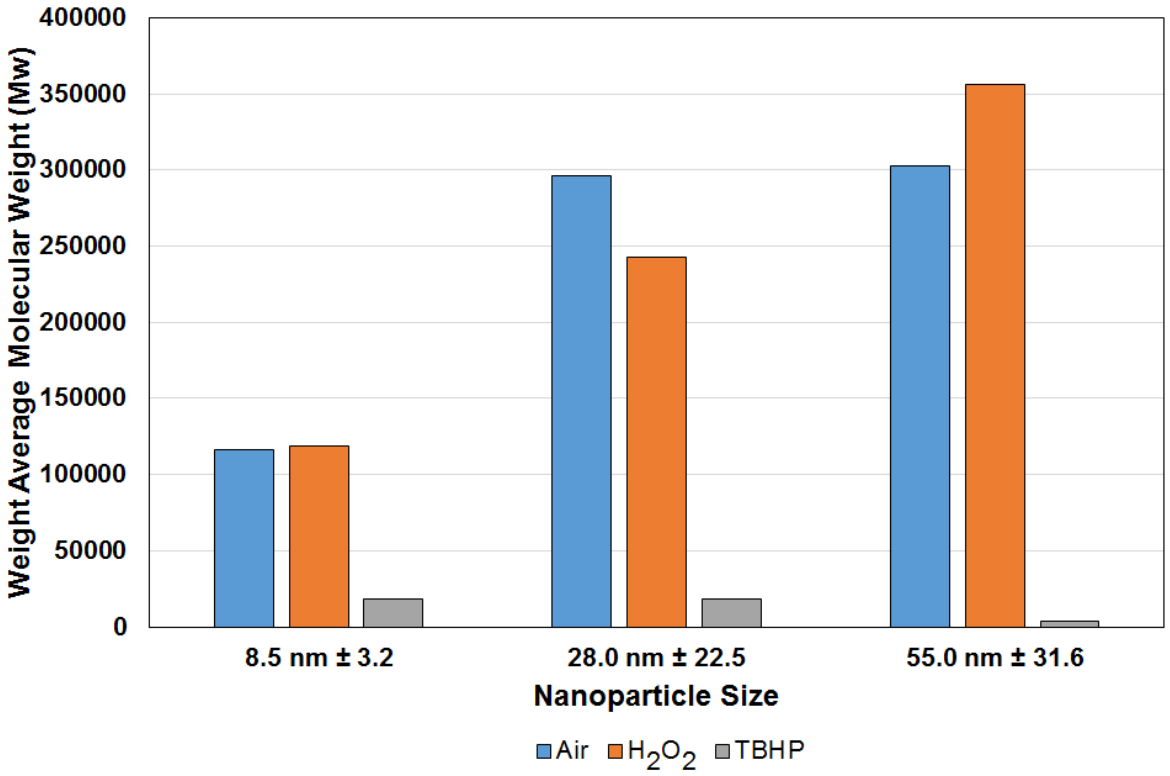

Figure 5.26 Weight average molecular weight comparison (M_w) of polystyrene produced using different additives for varying nanoparticle sizes.

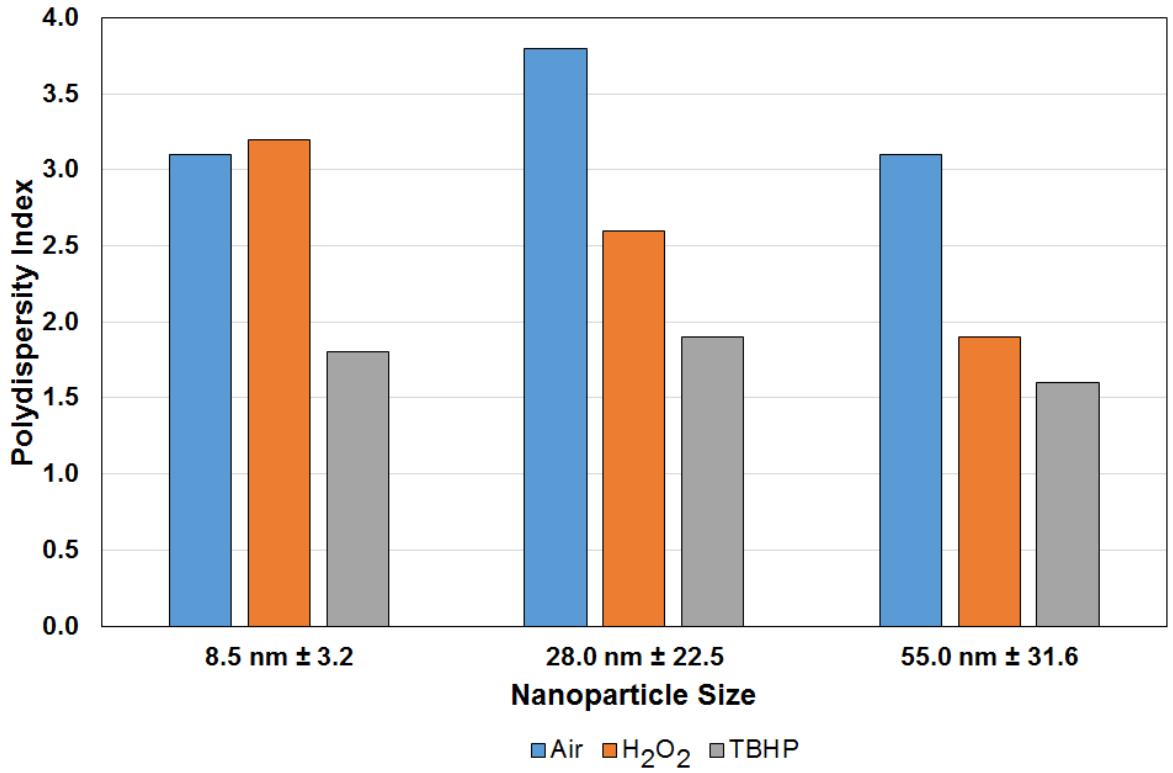

Figure 5.27 Polydispersity index (PDI) comparison of polystyrene produced using different additives for varying nanoparticle sizes.

The lower molecular weight and more monodisperse nature of the polymer obtained when using TBHP indicated that polymerization when using TBHP was more controlled and formed polystyrene with shorter, but more consistent chain lengths. This observation hints at the mechanism at play when using TBHP; the shorter polystyrene chain lengths and lower polydispersity index suggests that a type of living (also known as controlled) free radical polymerization (LFRP) is taking place. This is supported by the fact that the polydispersity index of 1.8 is closer to the range of 1.2 to 1.3 for this type of polymerization in literature as compared to polydispersity indexes above 3.0 where H_2O_2 or the absence of any oxidant is utilized.[36]

LFRP is where a potentially reactive polymer species goes through alternating activated and deactivated states. In the activated state a monomer is able to be added, while in the deactivated state the reactive end of the polymer species is blocked, by for example, a halogen, stable nitroxyl or transition metal compound. The blocked polymer remains dormant until it is reactivated by means of heat or chemical means. A number of these activation/deactivation cycles allow for the polymer chains to grow slowly and

simultaneously.[37] The various steps of this process as proposed by Kruse *et al* (2003) in modelling studies which they undertook, are depicted in Scheme 5.3.[38]

Scheme 5.3 Steps in the living free radical polymerization of styrene (adapted from ref. 38).

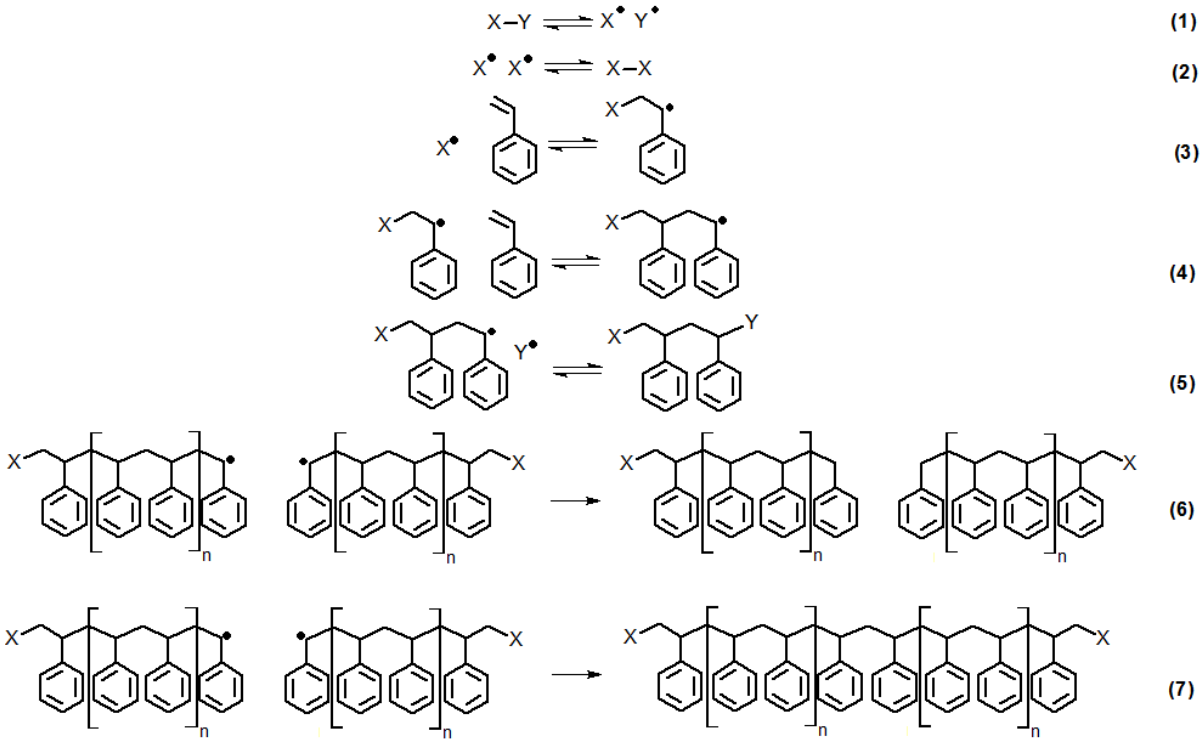

According to Scheme 5.3, the first step in the LFRP process is bond fission of an initiator X-Y, and reversible recombination thereof. A second step involves the reversible recombination/fission of X• radicals which were generated in the first step. Next would be the addition of the initiator to the monomer (step 3), followed by reversible propagation/de-propagation (step 4). A possible step to follow this may be the reversible coupling/de-coupling of Y• radicals (step 5). Chain growth is then terminated by means of radical recombination (step 6) or disproportionation (step 7).

Thus in our catalytic studies, where TBHP was utilized as an attempted oxidant, the role of the TBHP would be in the reversible blocking of the reactive end of a developing polystyrene chain. This subsequently facilitates the activation/deactivation cycles which allows for slow chain growth. The subsequent reaction steps before chain termination by recombination or disproportionation are shown in Scheme 5.4.

Scheme 5.4 Proposed LFRP of styrene with TBHP as initiator.

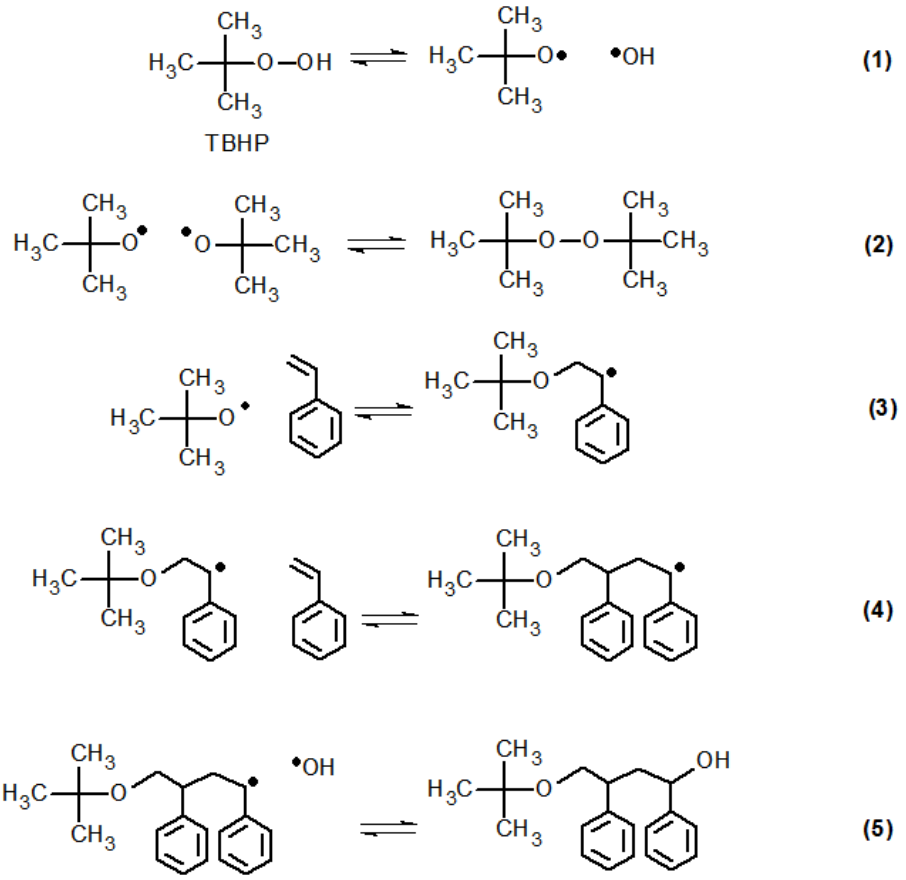

In an attempt to provide evidence for the proposed role of TBHP, the styrene conversion at shorter reaction times of 30 and 60 mins using TBHP, H_2O_2 and in the absence of additive, were evaluated. Since styrene conversions in the region of 90 % were obtained when doing these evaluations over 24 h, it was thought that more insight might be gained into the mechanisms of polymerization at shorter reaction times using these additives and in their absence. The results of these evaluations are shown in Table 5.13 and Figure 5.28.

Table 5.13 Comparison of styrene conversions at 30 and 60 min when using H_2O_2 or TBHP as additive as well as in their absence (styrene conversion reported average of duplicate runs).

Additive	Time	Styrene converted (%)
H_2O_2	30min	34.0
TBHP	30min	66.2
Air	30min	34.8
H_2O_2	60min	92.7
TBHP	60min	67.0
Air	60min	89.6

Reaction conditions: 0.0034 mmol Au; 70 °C

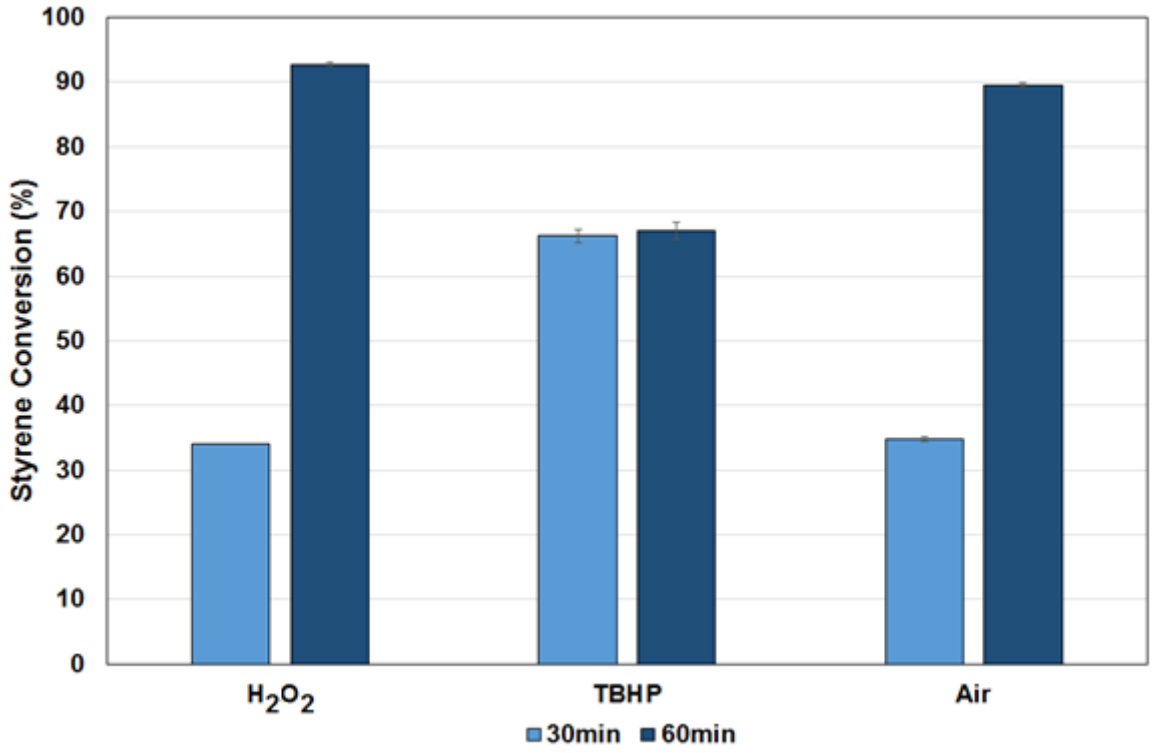

Figure 5.28 Comparison of styrene conversions at 30 and 60 min when using H_2O_2 or TBHP as additive as well as in their absence.

What is immediately apparent is that there is similar styrene conversions at 30- and 60 mins of between 66- and 67 % when using TBHP. As previously observed, this increases to approximately 92 % after 24 h and is similar to that obtained when using H_2O_2 and without any additive. The similar conversions when using H_2O_2 and in its absence after 30- and 60 mins again confirms that H_2O_2 plays a very minor role in styrene conversion.

In addition to the differences in conversion when utilizing TBHP as compared to H_2O_2 or in the absence of any additive, there is also an observed difference in selectivity when utilizing TBHP. It can be seen from Figure 5.29 and Table 5.14 that in addition to the presence of oxidation products benzaldehyde and styrene oxide, there are also other compounds eluting. GC coupled to a mass spectrometer (GC-MS) confirmed the presence of benzaldehyde and styrene oxide with the previously unknown peaks being confirmed to be due to TBHP associated with the organic substrate (Figure 5.30). This therefore alludes to the mechanism proposed in Scheme 5.4. The variation in elution times of the TBHP seen in Figure 5.29 suggests that it is associated with varying lengths of styrene units.

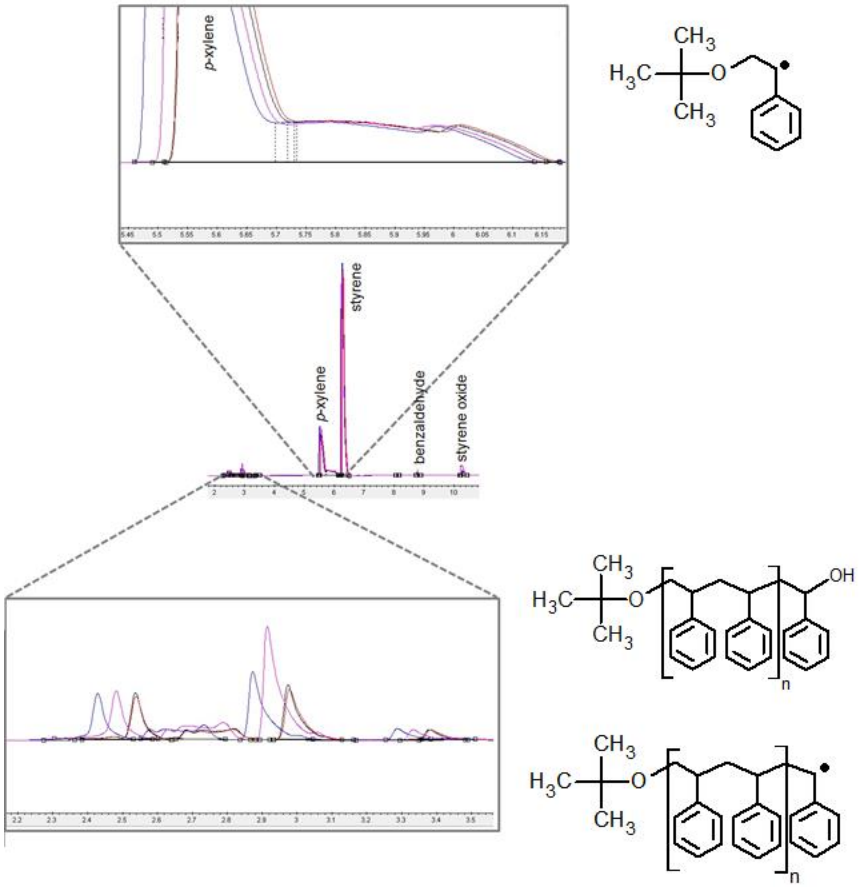

Figure 5.29 GC chromatogram showing extra compounds eluting along styrene and oxidation products benzaldehyde and styrene oxide.

Table 5.14 Benzaldehyde and styrene oxide selectivity when using TBHP as additive at 20 and 60 mins reaction time (selectivity reported average of duplicate runs).

	Benzaldehyde mass %	**Styrene Oxide mass %**
30 min	0.0055	0.0176
60 min	0.0096	0.0315

Reaction conditions: 0.0034 mmol Au; 70 °C

Therefore, neither H_2O_2 nor TBHP fulfil their intended purposes of being oxidizing agents. Whereas H_2O_2 appears to have a minimal effect on overall styrene conversion (only appearing to increase conversion by 2- to 3 % during the first hour of reaction at 70 °C) or selectivity of the polystyrene formed, TBHP on the other hand appears to influence the polydispersity index of the resultant polymer.

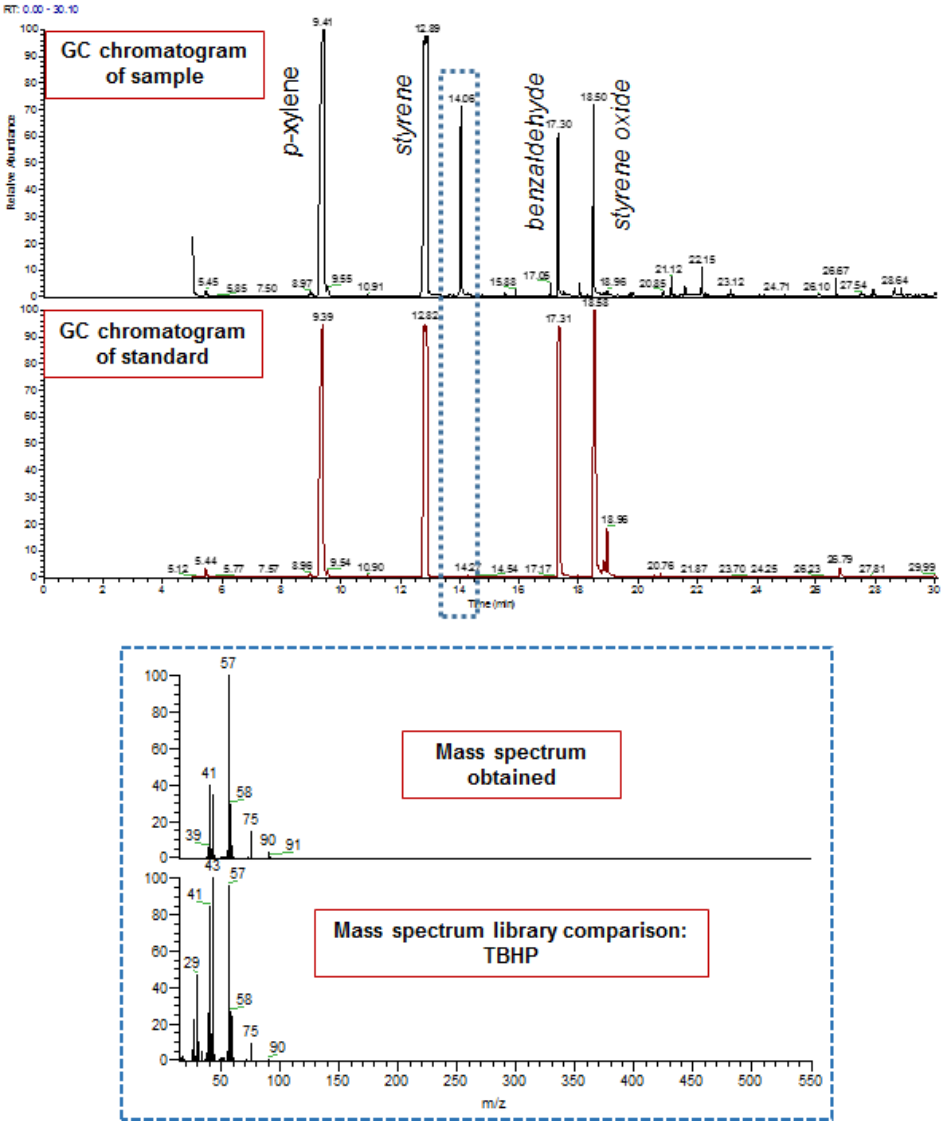

Figure 5.30 GC-MS results confirming TBHP to be associated with substrate.

In summary, from all of the performed catalysis evaluations, a number of unexpected/interesting observations were made. The initial aspect which roused interest, and was against expectation, was the almost complete absence of the targeted oxidation products although styrene conversion consistently approached or exceeded 90 %. The reason for this was that, as was eventually determined, styrene was being polymerized to form polystyrene instead of being oxidized by our hydrophilic gold nanoparticle system.

A further aspect was that there appeared to be no effect of Au nanoparticle size on styrene conversion. Each size evaluated resulted in similar conversions under the same set of reaction conditions. It was initially hypothesized that the lack of influence of nanoparticle size on conversion was that the intended oxidant, H_2O_2, was catalysing the polymerization of styrene.

However, subsequent investigations revealed that this was not the case and that indeed the aqueous Au catalyst was primarily responsible for the conversion of styrene. This was despite evidence of a contribution to styrene conversion due to self-polymerization. There was however evidence of the effect of nanoparticle size on selectivity as shown from resultant GPC results (Figure 5.25 to Figure 5.27) where M_n, M_w increased with an increase nanoparticle size, while PDI decreased with increasing particle size. This was however only the case in the absence of any additive and when using H_2O_2. Where TBHP was used as an additive, M_n, M_w and PDI remained comparatively lower.

The lack of nanoparticle size effect on styrene conversion, despite evidence that the aqueous Au plays the primary catalytic role in polymerization, will be addressed in the following section where a mechanism is proposed which can account for this anomaly.

5.3 Proposed overall catalytic reaction mechanism

Irrespective of catalyst size, it has been observed that rapid polymerization of styrene occurs at the expense of oxidation. The major question thus arising from the above results would be how the reaction mechanism differs in this catalytic system to favour styrene polymerization over oxidation? One major difference is that the nanoparticles employed here are not supported and are thus not a colloidal suspension, but instead completely soluble in an aqueous medium. This could perhaps be the major reasons for the difference in behaviour observed as compared to that in literature.

As a first step in rationalising what the absence of a support material might impart resulting in the catalyst system favouring polymerization rather than oxidation of styrene, we need to consider the mechanism of styrene oxidation proposed by Lin and Pei (2014) based on density functional theory (DFT) calculations.[21] Of interest is their H_2 promoted epoxidation mechanism as shown in Figure 5.31. This is because here, there is the coordination of H_2 and O_2 to the surface of a gold nanoparticle surface. Under the correct conditions and depending on the catalyst/support interactions resulting in favourable binding energies, H_2 and O_2 could possibly be derived from H_2O as we observed similar catalytic results when either using H_2O_2 or in its absence. The eventual outcome is the formation of water and an oxygen atom attached to the catalyst surface which is available for epoxide formation. This type of scenario may well be occurring in the catalyst system employed here. It must be remembered that even though less than 0.5 % of benzaldehyde was detected, it has still indeed formed.

Furthermore, on closer inspection it can be seen that at 70 °C over 24 h, there even appears to be a slight effect of nanoparticles size (if one considers Figure 5.32) on benzaldehyde selectivity where decreasing nanoparticle size seems to result in an increase in its selectivity. However this observation is far from being definitive to be able to draw any conclusions on the mechanism of the extremely minor benzaldehyde product formation.

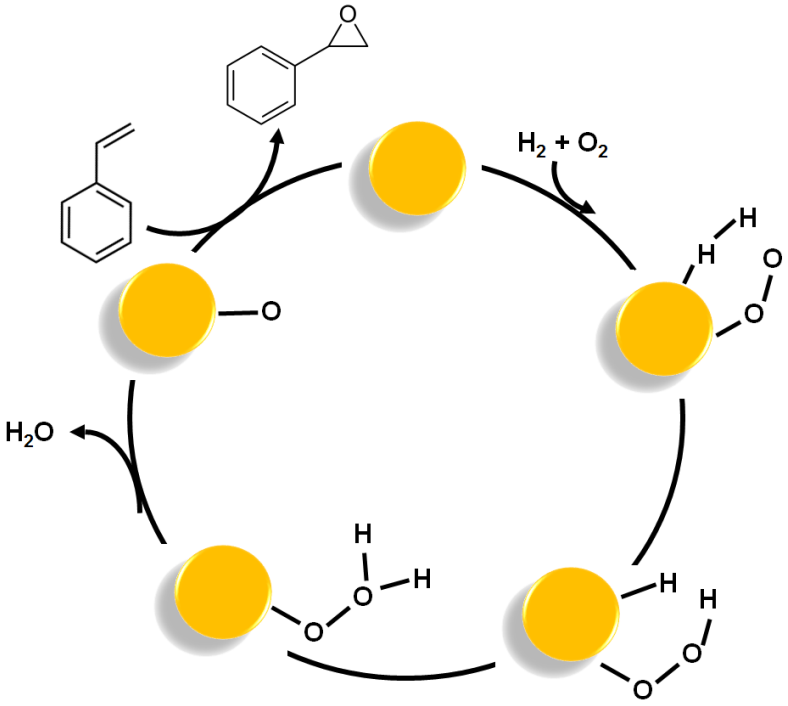

Figure 5.31 H_2 promoted epoxidation mechanism proposed by Lin and Pei.[21]

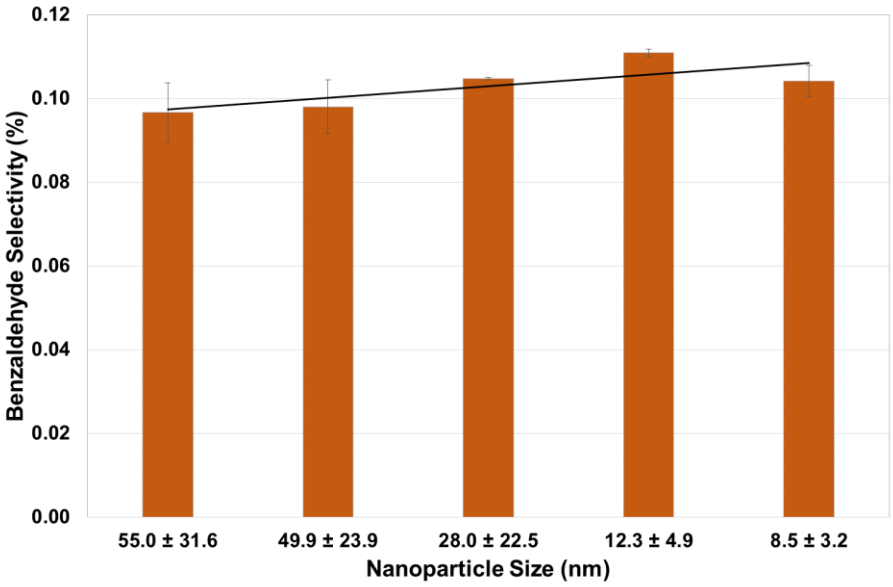

Figure 5.32 Possible influence of nanoparticle size on benzaldehyde selectivity.

However, the overwhelmingly major product has been shown to be polystyrene. Depending on conditions, selectivities of between approximately 90- and 94 % were consistently observed. It was demonstrated that this was due mainly to the presence of the catalyst. The question would then be how the catalyst would initiate polymerization?

While rationalizing that H_2O_2 may not be acting as an oxidizing agent, it was also thought unlikely to be the primary source of free radical initiators. A more likely scenario may then be that aqueous Au nanoparticles catalyses the Mayo mechanism depicted in Scheme 5.2. A possibility it that the aqueous nanoparticles could be catalysing the formation of the Diels-Alder dimer, which results in monoradical formation and subsequent polymerization, perhaps by acting as a Lewis acid.

It is known that Lewis acids can act as catalysts for Diels-Alder reactions.[39] The mechanism is shown in Scheme 5.5 (MX_n = metal halide Lewis acid). The oxygen of the dienophile carbonyl functionality coordinates to the Lewis acid thus rendering the dienophile more electrophilic and hence more reactive towards the diene. In addition it has been shown that reaction rates are further enhanced when using catalytic amounts of a Lewis acid in water.[40,41]

Scheme 5.5 Mechanism of the Lewis acid catalysed Diels-Alder reaction (MXn = metal halide Lewis acid).[39]

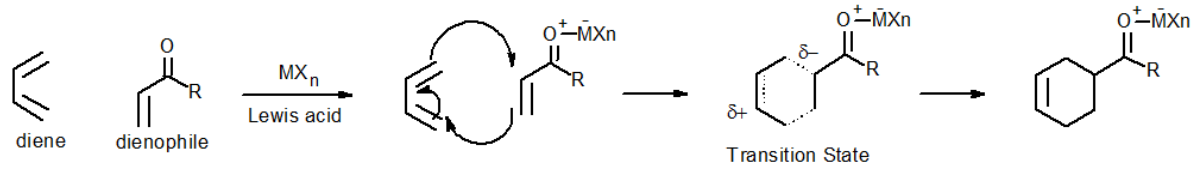

Now, if one considers the energy-dispersive X-ray spectroscopy (EDX) spectrum of the synthesized Au nanoparticles, there is evidence of an abundance of Cl on their surfaces (Figure 5.33). These Au-Cl sites on the surface of the nanoparticle are artefacts of the $HAuCl_4$ reduction process during synthesis and may now potentially act as Lewis acids.

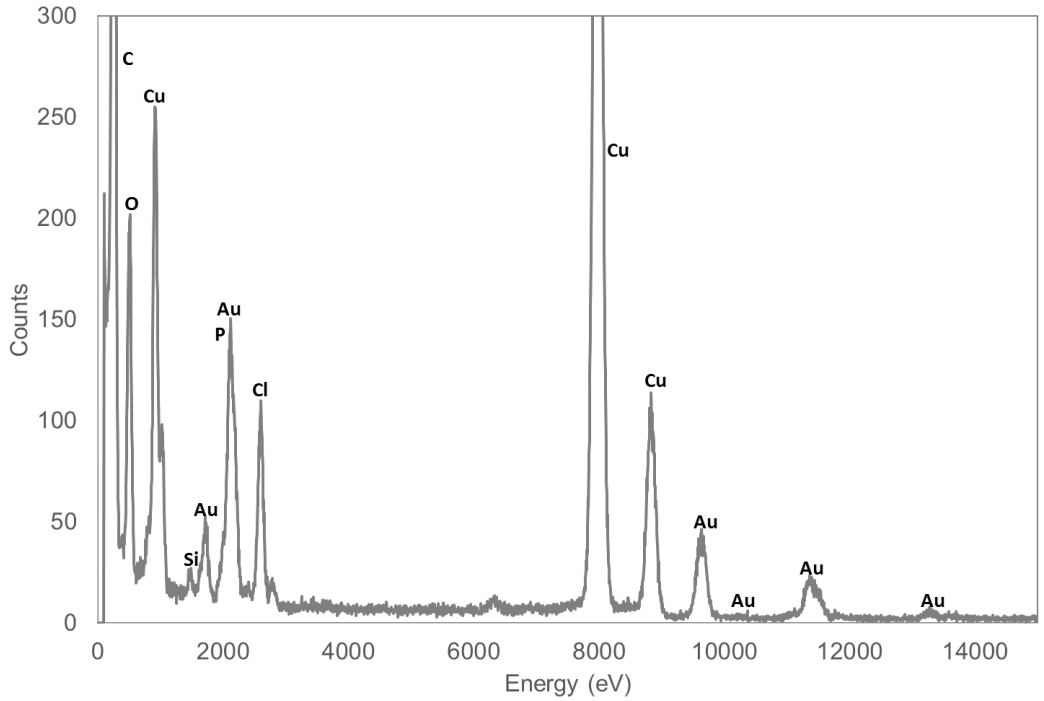

Figure 5.33 EDX of synthesized Au nanoparticles showing presence of chlorine (Cu, C, O, P and Si present due to TEM grid composition).

With the reaction further also taking place in an aqueous environment, the styrene dimerization process of the Mayo mechanism is further accelerated. From here, radical initiation and then polymerization could occur.

However, the limitation faced here is the nature of the dienophile. If it is proposed that the Mayo mechanism forms the Diels-Alder dimer, both the diene and dienophile would be styrene moieties and would therefore lack a carbonyl oxygen to which the Lewis acid can coordinate. On the other hand, if a Diels-Alder addition were to occur between a styrene and benzaldehyde moiety (the Diels-Alder addition of benzaldehyde and a diene having been demonstrated in literature),[42] this could be catalysed by Au-Cl sites on the surface of the nanoparticle acting as Lewis acids. The proposed mechanism is shown in Scheme 5.6.

Scheme 5.6 Proposed mechanism of Diels-Alder addition between a styrene and benzaldehyde moiety catalysed by Au-Cl sites acting as Lewis acids.

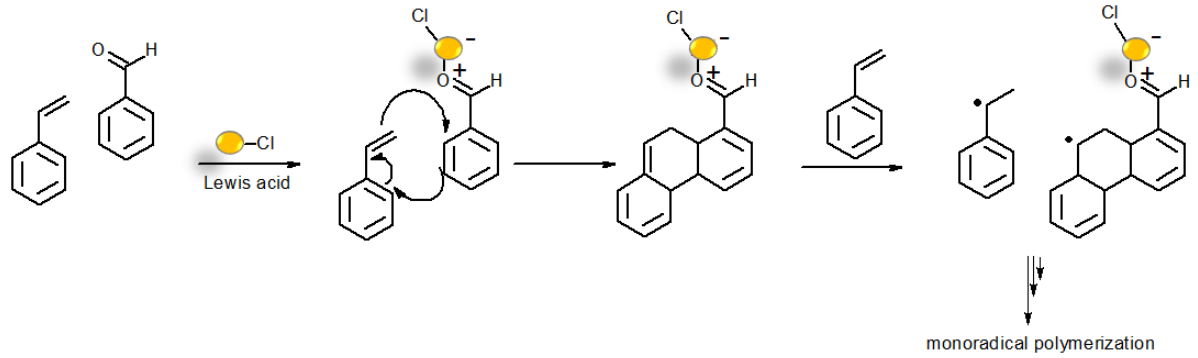

The implication of the above proposed mechanism then is that oxidation is indeed occurring, but that the benzaldehyde formed is being consumed through the Lewis acid catalysed Diels-Alder addition with styrene which subsequently initiates radical polymerization. The trace amounts of benzaldehyde observed at the end of the reaction may thus be remnants of what had been initially formed and subsequently consumed as depicted in Scheme 5.6. This hypothesis is supported where TBHP is used as additive. It was seen that at 30- and 60 mins reaction time, benzaldehyde and styrene oxide are present, but is not detected after 24 h. Figure 5.7 could be held as further support for this hypothesis where the lack of polystyrene after 1 h of reaction compared to 3- and 24 h is observed although similar high conversions are obtained. This may indicate that benzaldehyde which had formed is in the process of undergoing Diels-Alder addition and in the process of eventually forming polystyrene.

The Lewis acid catalysed addition of benzaldehyde and styrene also provides a plausible reason as to why polymerization was seen to occur in the absence of either H_2O_2 or TBHP. Formation of the benzaldehyde dienophile would still be possible by means of some oxidation of styrene by atmospheric or dissolved oxygen. This would then allow for the mechanism in Scheme 5.6 to occur.

With proposed styrene polymerization occurring in the manner proposed in Scheme 5.6, it may also suggest why nanoparticle size appears to have no effect on conversion. All that is needed for polymerization to occur is for radical initiation to be kick started. Once this has happened, the polymer chain will then grow. Incorporation of styrene moieties into the polymer chain is thus not dependent on having to coordinate to the catalyst surface. This is depicted in Figure 5.34. Therefore, even the lower comparative surface area of the larger

nanoparticles utilized during the catalyst evaluations may have been sufficient to catalyse initial Diels-Alder addition and subsequent radical initiation to occur leading to polymerization. Similarly, the amount of benzaldehyde required would also not necessarily need to be overly abundant; a sufficient amount to coordinating to Lewis acid sites to initiate subsequent radical formation and polymerization would be adequate.

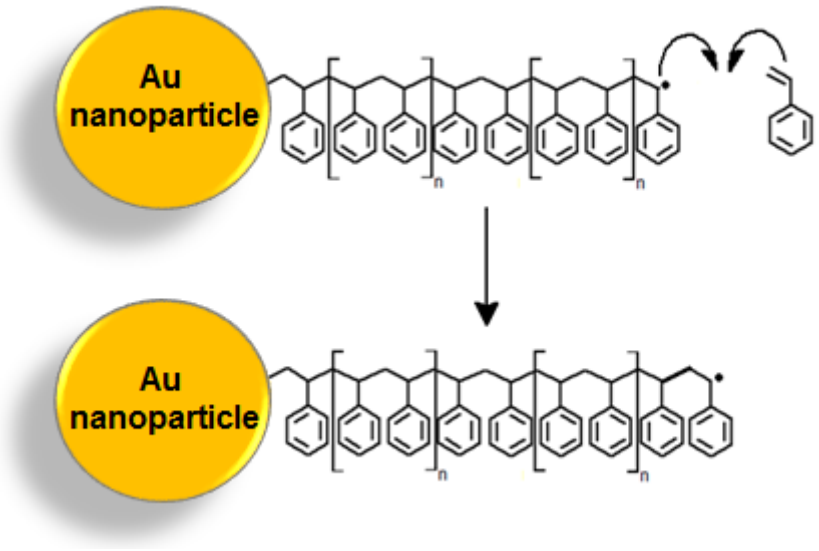

Figure 5.34 Incorporation of styrene moieties into the polymer chain illustrating the independence of polymerization on catalyst surface area.

With various mechanistic aspects having been addressed, based on various observations from the catalytic evaluations of the aqueous Au nanoparticles and information from literature, we are now in a position to propose an overall mechanistic pathway for the observed styrene polymerization and the percentage contribution of each aspect. This is comprised of four aspects as depicted in Scheme 5.7; the contribution of styrene self-polymerization (A), the primary role of the catalyst in styrene polymerization in the absence of additives (B), and the effect of the presence of either H_2O_2 (C) or TBHP (D) on the polymerization process.

Scheme 5.7 Flow chart of various aspects of the overall polymerization mechanism (percentages indicate contribution to overall polymerization).

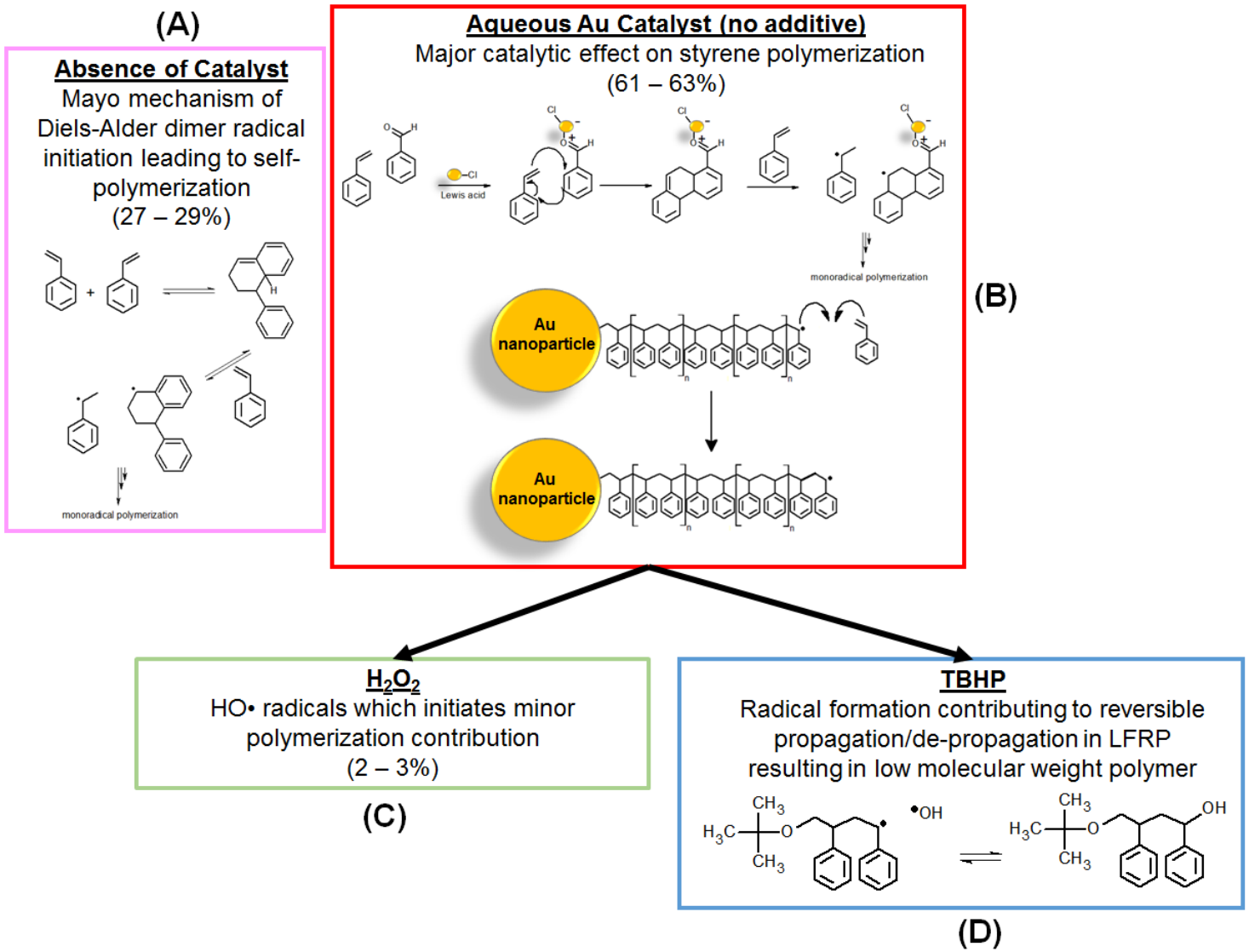

5.4 Conclusions

Initial catalysis evaluations revealed the unexpected formation of polystyrene instead of the anticipated styrene oxidation products; with benzaldehyde being found only in trace amounts. Furthermore, styrene conversion did not appear to be dependent on nanoparticle size. The focus was then shifted to the understanding of why, at the conditions employed, polymerization of styrene was favoured.

Conditions were subsequently varied in order to ascertain whether more of the desired oxidation products could be formed and polymerization limited. The first variable investigated was that of temperature. However it was found that selectivity to polystyrene was still favoured at the expense of oxidation products. It was then hypothesized that polymerization was not being catalysed by the aqueous Au nanoparticles, but instead by the intended oxidant, H_2O_2. This was thought to possibly occurring by the dissociation of to form HO• radicals which would then initiate polymerization.

Catalysis evaluations were subsequently carried out in the absence of H_2O_2. High conversions in the region of 90 % were however still observed which resulted in it being clear that polymerization activity was indeed due to the Au catalyst. H_2O_2 was found to have a minor contribution of around 2 to 3 % which indicated that some radical formation due to its dissociation did occur.

In order to confirm Au catalyst activity, it was omitted in the following set of evaluations; the hypothesis here being that no conversion would be observed. However, contrary to expectation, styrene conversion just below 30 % was observed. It was thus clear that self-polymerization, mostly likely *via* the Mayo mechanism of Diels-Alder styrene dimer formation initiating radical polymerization. However, the presence of the catalyst yielded an approximate 60 % increase in conversion thereby confirming its major contribution to the observed activity.

The next step was to ascertain whether a different oxidant would result in an increase in oxidation products with TBHP subsequently being evaluated. However, once again polymerization was overwhelmingly favoured. What changed however, was the nature of the polystyrene isolated in the presence of TBHP. Compared to when H_2O_2 was used or omitted,

the polystyrene obtained was of a lower molecular weight and polydispersity index. The conclusion here was that TBHP was dissociating to form radicals which would facilitate the living/controlled free radical polymerization process thus resulting in the lower molecular weight polystyrene.

The mechanism whereby the catalyst was facilitating polymerization was reasoned to be due to it acting as a Lewis acid catalysing Diels-Alder addition of styrene and benzaldehyde. This would work on the assumption then that oxidation had indeed occurred and that the products thereof had been consumed in the addition process. This resulted in what appeared to be only trace amounts of benzaldehyde having been formed.

In evaluating whether linear alkenes such as 1-pentene and 1-octene would also undergo polymerization under the conditions employed for polystyrene production, no conversion was observed. If the proposed mechanism in Scheme 5.6 holds, the reason for this could be two-fold. Firstly, since no conversion was observed, it means that no oxidation of the mono-olefins to form aldehydes occurred and alludes to the lower reactivity of these olefins as compared to styrene.[43] Secondly, even if some oxidation to form aldehydes did occur, with the olefins evaluated not being dienes, a Diels-Alder addition could not occur and therefore would prevent the proposed mechanism in Scheme 5.6 from proceeding. In a manner then, the lack of conversion, and absence of polymerization when using 1-pentene and 1-octene, adds support to the proposed mechanism.

One of the suggested benefits of our aqueous Au nanoparticle catalyst system discussed in the introduction (Section 5.1), was that it could be utilized as a bi-phasic catalyst and hence had the potential to be recycled. However, due to the polystyrene which had formed, the catalyst became incorporated within the polymer and proved difficult to separate without large scale agglomeration of the nanoparticles occurring. This was evident when the polystyrene was dissolved in THF or chloroform and subjected to centrifugation. This resulted in large, purple coloured Au agglomerates being discernible.

It will further be of interest if other transition metal nanoparticles synthesized in the same could be utilized in other catalytic process. An example of this could be the synthesis of Rh nanoparticles for use in hydroformylation.

5.5 Experimental

In order to determine metal loading, ICP-OES analysis was performed. This was carried by sampling 5 ml of the aqueous Au solution. This was followed by removal of water by means of evaporation to leave only gold. This was then re-dissolved in 2 ml *aqua regia* (3:1 mixture of concentrated HCl:HNO_3) which was then diluted to 5 ml with water.

Styrene was added to the gold catalyst solution before addition of oxidant (H_2O_2 or tert-butyl hydroperoxide) and heating to the desired temperature. The concentration of the gold in solution was determined by the efficiency of extraction from the organic layer (using ICP) with metal loading for catalysis subsequently determined by the volume of the aqueous solution. In initial catalysis reactions, gold concentration in the catalyst solutions were extremely low (due to the synthesis and extraction procedure of the gold nanoparticles not being optimized as described in previous chapters) therefore requiring larger volumes of the aqueous catalyst solution. Preliminary reactions were therefore carried out in 50 ml round bottomed flasks (to accommodate potential larger volumes of aqueous catalyst solution with possible metal loading increases) fitted with a reflux condenser. However, once nanoparticle extraction was optimized, it allowed for smaller volumes to be utilized while achieving higher metal loadings. This subsequently allowed for the utilization of a multi-tube parallel reactor which enabled multiple parallel catalytic evaluations to be carried out.

Styrene conversion and oxidation product formation was measured using a Varian 9000 polar gas chromatograph. Before each set of catalysis evaluations, response factors of styrene, and possible oxidation products benzaldehyde and styrene oxide (which would, according to literature, most likely be the major products), relative to the *p*-xylene internal standard were calculated. Response factors ($\frac{K_i}{IS}$) were calculated from the average of seven analyses with varying concentrations of each component using the equation:

$$\left(\frac{K_i}{IS}\right) = \frac{C_k A_{IS}}{C_{IS} A_i}$$

(Equation 5.1)

Where $\left(\frac{K_i}{IS}\right)$ = calculated relative responsive factor

C_k = known concentration (g/ml) of component in sample

C_{IS} = concentration (g/ml) of internal standard added to sample

A_i = component area in sample chromatogram

A_{IS} = internal standard area in chromatogram

Styrene was varied between 8 and 92 % of the total vial volume with benzaldehyde and styrene oxide being varied between 0 and 42 %. This was done in order to mimic, to an extent, the low to high conversion of styrene and the formation of oxidation products from zero to approximately equal volume percentages.

The unknown concentration of a component, C_i, was calculated using the equation:

$$C_i = \frac{C_{IS}\left(\frac{K_i}{IS}\right)A_i}{A_{IS}}$$

(Equation 5.2)

5.6 References

(1) Li, C.-J.; Chen, L. *Chem. Soc. Rev.* **2006**, *35* (1), 68.

(2) Noh, J. H.; Patala, R.; Meijboom, R. *Appl. Catal. A Gen.* **2016**, *514*, 253.

(3) Cai, X.; Wang, H.; Zhang, Q.; Tong, J. *J. Sol-Gel Sci. Technol.* **2014**, *69* (1), 33.

(4) Zheng, Y.; Zhang, X.; Yao, Y.; Chen, X.; Yang, Q. *RSC Adv.* **2015**, *5* (128), 105747.

(5) Zhu, Y.; Qian, H.; Zhu, M.; Jin, R. *Adv. Mater.* **2010**, *22* (17), 1915.

(6) Wang, L.; Zhang, B. S.; Zhang, W.; Zhang, J.; Gao, X. H.; Meng, X. J.; Su, D. S.; Xiao, F. S. *Chem. Commun.* **2013**, *49* (33), 3449.

(7) Liu, J.; Krishna, K. S.; Losovyj, Y. B.; Chattopadhyay, S.; Lozova, N.; Miller, J. T.; Spivey, J. J.; Kumar, C. S. S. R. *Chem. - A Eur. J.* **2013**, *19* (31), 10201.

(8) Sharma, A. S.; Shah, D.; Kaur, H. *RSC Adv.* **2015**, *5* (53), 42935.

(9) Zhu, Y.; Jin, R.; Sun, Y. *Int. J. Hydrogen Energy* **2013**, *38* (36), 16716.

(10) Pardeshi, S. K.; Pawar, R. Y. *J. Mol. Catal. A Chem.* **2011**, *334* (1–2), 35.

(11) Zaidman, B.; Kisilev, A.; Sasson, Y.; Garti, N. *J. Am. Oil Chem. Soc.* **1988**, *65* (4), 611.

(12) Koike, K.; Nifuku, M.; Izumi, K.; Nakamura, S.; Fujiwara, S.; Horiguchi, S. *J. Loss Prev. Process Ind.* **2005**, *18* (4–6), 465.

(13) Tavares, K. P.; Caloto-Oliveira, Á.; Vicentini, D. S.; Melegari, S. P.; Matias, W. G.; Barbosa, S.; Kummrow, F. *Ecotoxicol. Environ. Contam.* **2014**, *9* (1), 43.

(14) Singh, S. P.; Kumari, M.; Kumari, S. I.; Rahman, M. F.; Mahboob, M.; Grover, P. *J. Appl. Toxicol.* **2013**, *33* (10), 1165.

(15) Rezaeifard, A.; Farshid, P.; Jafarpour, M.; Moghaddam, G. K. *RSC Adv.* **2014**, *4* (18), 9189.

(16) Titinchi, S. J. J.; Von Willingh, G.; Abbo, H. S.; Prasad, R. *Catal. Sci. Technol.* **2015**, *5* (1), 325.

(17) Wang, A.; Jing, H. *Dalton Trans.* **2014**, *43* (3), 1011.

(18) Qi, Y.; Luan, Y.; Yang, M.; Wang, G.; Tan, L.; Li, J. *Appl. Surf. Sci.* **2014**, *293*, 359.

(19) Turner, M.; Golovko, V. B.; Vaughan, O. P. H.; Abdulkin, P.; Berenguer-Murcia, A.; Tikhov, M. S.; Johnson, B. F. G.; Lambert, R. M. *Nature* **2008**, *454* (7207), 981.

(20) Gao, W.; Chen, X. F.; Li, J. C.; Jiang, Q. *J. Phys. Chem. C* **2010**, *114* (2), 1148.

(21) Lin, S.; Pei, Y. *J. Phys. Chem. C* **2014**, *118*, 20346.

(22) Laosiripojana, N.; Assabumrungrat, S. *Chem. Eng. Sci.* **2006**, *61* (8), 2540.

(23) Gregor, C.; Hermanek, M.; Jancik, D.; Pechousek, J.; Filip, J.; Hrbac, J.; Zboril, R. *Eur. J. Inorg. Chem.* **2010**, No. 16, 2343.

(24) Wunder, S.; Lu, Y.; Albrecht, M.; Ballauff, M. *ACS Catal.* **2011**, *1* (8), 908.

(25) Wiley, B. J.; Im, S. H.; Li, Z. Y.; McLellan, J.; Siekkinen, A.; Xia, Y. *J. Phys. Chem. B* **2006**, *110*, 15666.

(26) Noguez, C. *J. Phys. Chem. C* **2007**, *111*, 3806.

(27) Chakraborty, S.; Joshi, P.; Shanker, V.; Ansari, Z. A.; Singh, S. P.; Chakrabarti, P. *Langmuir* **2011**, *27* (12), 7722.

(28) García, M. T.; Gracia, I.; Duque, G.; Lucas, A. de; Rodríguez, J. F. *Waste Manag.* **2009**, *29* (6), 1814.

(29) León-Bermúdez, A.-Y.; Salazar, R. *CT&F - Ciencia, Tecnol. y Futur.* **2008**, *3*, 157.

(30) Wright, T.; Chirowodza, H.; Pasch, H. *Macromolecules* **2012**, *45* (7), 2995.

(31) Khuong, K. S.; Jones, W. H.; Pryor, W. A.; Houk, K. N. *J. Am. Chem. Soc.* **2005**, *127* (4), 1265.

(32) Norrish, R. G. W.; Brookman, E. . *Proc. R. Soc. Lond. A. Math. Phys. Sci.* **1939**, *171* (945), 147.

(33) Denisov, E. T.; Denisova, T. G.; Pokidova, T. S. *Handbook of Free Radical Initiators*; John Wiley & Sons, Inc., 2003; Vol. 7.

(34) Baxendale, J. H. *Adv. Catal.* **1952**, *4* (C), 31.

(35) Zhang, J.; Wang, Z. Z.; Wang, Y.; Wan, C.; Zheng, X.; Wang, Z. Z. *Green Chem.* **2009**, *11* (12), 1973.

(36) Grubbs, R. B.; Dean, J. M.; Bates, F. S. *Macromolecules* **2001**, *34* (25), 8593.

(37) Goto, A.; Fukuda, T. *Macromolecules* **1997**, *30* (17), 5183.

(38) Kruse, T. M.; Souleimonova, R.; Cho, A.; Gray, M. K.; Torkelson, J. M.; Broadbelt, L. J. *Macromolecules* **2003**, *36* (20), 7812.

(39) Snider, B. *Acc. Chem. Res.* **1980**, *13* (9), 426.

(40) Otto, S.; Bertoncin, F.; Engberts, J. B. F. N. *J. Am. Chem. Soc.* **1996**, *118* (33), 7702.

(41) Reymond, S.; Cossy, J. *Chem. Rev.* **2008**, *108*, 5359.

(42) Simonsen, K. B.; Svenstrup, N.; Roberson, M.; Jorgensen, K. A. *Chem. Eur. J.* **2000**, *6* (1), 123.

(43) Mizuno, N.; Yamaguchi, K.; Kamata, K. *Coord. Chem. Rev.* **2005**, *249*, 1944.

Chapter 6

Summary and Future Work

6.1 Summary and Conclusions

In this thesis, we discussed the facile synthesis of gold nanoparticles using a combination of dendrimer encapsulated nanoparticle and monolayer protected cluster (DEN-MPC) synthetic methods. Nanoparticles were formed within a generation three poly(propylene imine) (PPI) dendrimer micelle, which was soluble in an organic medium, and subsequently extracted in an aqueous medium, where it was stabilized by the water-soluble 1,3,5-triaza-7-phosphaadamantane (PTA) ligand. Optimization of this method allowed us to obtain a range of hydrophilic gold nanoparticle sizes using the same synthetic principles. It also allowed us to obtain consistent nanoparticle sizes for consecutive reactions utilizing the same synthetic method. Although the sizes obtained were not specifically the size of the cluster corresponding to the Au:dendrimer micelle ratio utilized, the obtained sizes were consistent.

In Chapter 1, a brief overview of the reactivity of gold nanoparticles was given, which highlights the attractiveness of these materials for use in various applications. Methods of gold nanoparticle synthesis were then focused on and it was shown that many of these methods is quite complex or only produced nanoparticles of a specific size. The aims and objectives in trying to address some of the shortcomings of the discussed synthetic methods, are then proposed.

Subsequently, Chapter 2 discusses the synthesis of gold nanoparticles using a combined DEN-MPC method. Utilizing this, method we were able to synthesize, amongst others,Au_{55} nanoparticles in a simpler and more economical manner as compared to many procedures cited in the literature. Furthermore, by attempting to control nanoparticle size during synthesis, mechanisms of nanoparticle extraction and size evolution could be formulated and was also discussed.

In an attempt to further study the mechanisms proposed in Chapter 2, dynamic light scattering (DLS) was explored as a more rapid and economical option to track nanoparticle growth instead of transmission electron microscopy (TEM) which had been the most

commonly used method previously. However, it was found that the information obtained using DLS differed significantly to that obtained when using TEM. Nonetheless, valuable knowledge was gained in relation to factors influencing the stability of our hydrophilic gold nanoparticles.

From the results obtained in Chapter 3, it became evident that, in addition to Au:dendrimer micelle ratios and concentrations, many other factors were at play in determining final nanoparticle size and stability. Therefore in Chapter 4, we discussed and evaluated several variations in the previously established nanoparticle synthesis procedure. Factors such as synthesis vessel type, stirring rate; and reduction and extraction procedures were varied in a quest to obtain an optimal method for nanoparticle formation/synthesis. Once this had been achieved, the nanoparticles were utilized as a catalyst in the transformation of styrene and this was discussed in Chapter 5.

In Chapter 5, we initially set out to oxidize styrene by utilizing our hydrophilic gold nanoparticles in a biphasic catalyst system. However, we found that polymerization of the styrene preferentially occurred instead of the desired formation of oxidation products. Therefore, in this chapter, we further hypothesized on the mechanisms resulting in the domination of the polymerization process under the conditions employed in our catalytic evaluations.

6.2 Proposed Future Work

6.2.1 Recycling of the Dendrimer Micelle

An aspect which could be potentially further investigated is the recyclability of the dendrimer micelle template. Our preliminary attempts at simply re-using the organic layer (*i.e.* addition of $HAuCl_4$ to the used organic layer and reducing it) did not result in formation of the desired nanoparticles. This is due to the possibility that reducing agent from the initial process is still present and is influencing the reduction step when utilizing the recycled organic layer. Similarly, trace amounts of gold in the organic layer could also be present which would influence the Au:dendrimer micelle ratio and hence influence nanoparticle growth. Thus in order to re-use the dendrimer micelle, potential methods such as ultra-filtration could be investigated in order to purify the organic layer.

6.2.2 Recycling of the Aqueous Gold Catalyst

In the attempted oxidation of styrene, it was thought that the aqueous gold catalyst could potentially easily be recovered by separating the aqueous phase from the organic product phase. However, due to the formation of polymer utilizing our specific catalytic system, we were unable to separate the two phases. However, the concept of biphasic catalysis using the aqueous catalysts we, is still feasible in cases where the products obtained are soluble in the organic phase. Hence future work could entail looking at other catalytic processes such as hydroformylation; if we synthesize rhodium nanoparticles using the same method. The method could thus potentially be used to synthesize a range of hydrophilic nanoparticles of different metals such as Pt, Pd, Cu, *etc.* which are tailored to specific catalytic applications.

6.2.3 Evaluation of Different Stabilizing Ligands

It has been observed that our gold nanoparticles do agglomerate over extended periods of time. Therefore future studies could also entail evaluating other water-soluble ligands for stabilizing the extracted nanoparticles in the aqueous phase, which would result in a longer storage life.

6.2.4 Applications of Gold Nanoparticle Containing Polystyrene

A further avenue of study could be focussed on finding applications for the gold laced polystyrene. One such example is the work done by Gu and co-workers (2014) who used gold core-polystyrene shell nanoparticles in investigating the development of surface plasmon amplification by stimulated emission of radiation (SPASER) as an optical source of tuneable wavelength.[1]

What the observed polymerization also shows is that there are interesting intrinsic electronic properties of the nanoparticles synthesized and extracted which require further understanding.

6.3 References

(1) P. Gu, D. J. S. Birch and Y. Chen, *Methods Appl. Fluoresc.*, 2014, **2**, 024004.